Exploring the conditions for the occurrence of volcanic lightning

Caron E.J. Vossen

München 2022

Exploring the conditions for the occurrence of volcanic lightning

Caron E.J. Vossen

Dissertation zur Erlangung des Doktorsgrades
an der Fakultät für Geowissenschaften
der Ludwig–Maximilians–Universität
München

vorgelegt von
Caron E.J. Vossen
aus Bunnik, Niederlande

München, den 8. März 2022

Erstgutachter: PD Dr. Corrado Cimarelli

Zweitgutachter: Professor Dr. Donald B. Dingwell

Tag der mündlichen Prüfung: 13. Juni 2022

Thunder is good, thunder is impressive; but it is lightning that does the work.

- Mark Twain

Table of contents

List of Figures

List of Tables

Preamble

Chapter 2 of this dissertation is published in a peer reviewed journal, Chapter 3 is under review at a peer reviewed journal and Chapter 4 is in preparation for standalone publication. My scientific contributions to two individual studies are presented in Chapter 5 (in preparation for standalone publication) and Chapter 6 (published in a peer reviewed journal). The content of these publications has not been altered for this dissertation, but adapted for format and consistency of the overall thesis design. The full references of the papers are the following:

Vossen, C. E. J., Cimarelli, C., Bennett, A. J., Geisler, A., Gaudin, D., Miki, D., Iguchi, M., and Dingwell, D. B. (2021). Long-term observation of electrical discharges during persistent Vulcanian activity. *Earth and Planetary Science Letters*, *570*, 117084. https://doi.org/10.1016/j.epsl.2021.117084.

Vossen, C. E. J., Cimarelli, C., Bennett, A. J., Schmid, M., Kueppers, U., Ricci, T., and Taddeucci, J. The electrical signature of mafic explosive eruptions at Stromboli volcano, Italy. *Under review at Scientific Reports*.

Vossen, C. E. J., Cimarelli, C., Cigala, V., Haarer, I., Stoiber, W., Barrancos, J., Kueppers, U., Schmid, M., and Bennett, A. J. Linking electrical activity to explosive eruption styles during the 2021 Cumbre Vieja eruption. *In preparation for standalone publication*.

Genareau, K., Cimarelli, C., Prata, A. T., Stern, S., **Vossen, C. E. J.**, and Dingwell., D. B. Ash versus ice abundance controls lightning polarity in volcanic plumes. *In preparation for standalone publication*.

Von der Linden, J., Kimblin, C., McKenna, I., Bagley, S., Li, H. C., Houim, R., Kueny, C. S., Kuhl, A., Grote, D., Converse, M., **Vossen, C. E. J.**, Stern, S., Cimarelli, C., and Sears, J. (2021). Standing shock prevents propagation of sparks in supersonic explosive flows. *Communications Earth & Environment*, *2*(1), 1-9. https://doi.org/10.1038/s43247-021-00263-y.

Author contributions

Chapter 2: C.C. designed the study, administered the project and provided supervision. A.J.B., C.E.J.V. and A.G. provided the methodology and designed the software of the sensors. M.I. provided logistical support. C.E.J.V., C.C. and D.G. installed the sensors. C.E.J.V., C.C. and D.M. carried out maintenance of the sensors and collected the data. C.E.J.V. developed the volcanic lightning detection algorithm, carried out the formal analysis, visualised the results and wrote the original draft. C.E.J.V., C.C., A.J.B., A.G., D.G., M.I. and D.B.D. contributed to the discussion and revised the manuscript. Funding was acquired by C.C. and D.B.D.

Chapter 3: C.C. and C.E.J.V. designed the study. C.C. administered the project and provided supervision. A.J.B. and C.E.J.V. provided the methodology and designed the software of the sensors. C.E.J.V., C.C., M.S. and U.K. installed the sensors. C.E.J.V., C.C., M.S., U.K., T.R. and J.T. carried out maintenance of the sensors and collected the data. C.E.J.V. processed and analysed the data, visualised the results and wrote the original draft. All authors contributed to the discussion and revised the manuscript. Funding was acquired by C.C.

Chapter 4: C.C. and C.E.J.V. designed the study. C.C. administered the project and provided supervision. A.J.B. and C.E.J.V. provided the methodology and designed the software of the sensor. C.C., U.K. and J.B. installed the sensor. C.E.J.V., J.B., C.C., M.S. and U.K. carried out maintenance of the sensor and collected the data. C.E.J.V. and V.C. recorded the thermal data and provided the software to process the thermal data. I.H. and W.S. processed the thermal data, built a database of standard atmospheric conditions for the entire eruption and together with C.E.J.V. visualised the weather data. C.E.J.V. processed and analysed the electrical data, visualised the results and wrote the original draft. C.C. revised the manuscript. All authors contributed to the discussion. Funding was acquired by C.C.

Chapter 5: K.G. and C.C. designed the study. C.C. supervised the project. C.C., S.S. and C.E.J.V. provided the methodology. D.B.D. provided the resources. C.E.J.V., S.S., K.G. and C.C. carried out and analysed the rapid decompression experiments. S.S. and C.E.J.V. visualised the results of the experiments. A.P. carried out the formal analysis of the satellite data and visualised the results. K.G. wrote the original draft. All authors contributed to the discussion and revised the manuscript. Funding was acquired by C.C. and D.B.D.

Chapter 6: J.v.d.L. and J.S. conceived the decompression shots at Special Technologies Laboratory and Ludwig-Maximilians-Universität (LMU) München to identify Mach disk tracers. C.K. and I.M. designed the decompression experiment at Special Technologies Laboratory. C.K., I.M., J.v.d.L., and J.S. operated and analysed the Special Technologies Laboratory experiments. R.H. developed the HyBurn compressible fluid dynamics code. S.B. adapted the HyBurn compressible fluid dynamics code to the experiment geometry. H.C.L. implemented the immersed boundaries in HyBurn needed to capture the full geometry. D.G. and A.K. validated the HyBurn code for the explosive flow conditions. J.v.d.L. ran HyBurn on high performance computing resources and analysed the outputs. C.S.K. analysed the simulation outputs with the Bolsig+ Boltzmann solver to determine ionisation rates. M.C. evaluated particle charging mechanisms. J.v.d.L., C.C., and J.S. designed the experiments at LMU München. C.E.J.V., S.S., J.v.d.L., J.S., and C.C. operated and analysed the LMU München experiments. J.v.d.L. wrote the original draft. All authors contributed to the discussion and revised the manuscript.

Summary

Although volcano monitoring has been improving rapidly in the last decade, the detection and monitoring of volcanic ash plumes is still challenging, despite its apparent threat to people and infrastructures. The detection of volcanic lightning during explosive eruptions offers a promising tool in the portfolio of volcano monitoring techniques, as volcano lightning is readily generated upon ejection of tephra in the atmosphere and it can be detected instantaneously and remotely also in conditions of adverse weather and poor visibility. Volcanic lightning is generated in the volcanic plume and therefore can reveal properties of its source that are difficult to investigate directly. Besides indicating the presence of volcanic particles in the atmosphere, the amount, magnitude and discharge rate of volcanic lightning might therefore provide insights into the dynamics of explosive eruptions. For this, a deeper understanding of the conditions required for volcanic lightning to occur, is needed for a wide range of eruption styles, magnitudes and compositions.

During an explosive volcanic eruption, electrification of the eruption column, and the subsequent charge separation and formation of charge clusters, generates volcanic lightning. Several plume electrification mechanisms have been proposed: silicate particle charging (electrification through fragmentation and particle collisions), ice nucleation (if the ash plume reaches sufficiently high altitudes, typically coinciding with isotherms colder than -10 °C), the interaction with (sea)water and natural radioactivity.

Three types of volcanic lightning have been distinguished based on their timing with respect to the explosion onset, their location in the plume and the length and duration of the discharge: vent discharges (also known as Continual Radio Frequency), near-vent volcanic lightning and plume volcanic lightning. In recent years, regional and global lightning detection networks have detected volcanic lightning during major eruptions using very low to very high frequency (VLF-VHF) antennas. However, these networks are limited in the detection of smaller explosive events that do not generate sufficient high-current electrical discharges. In contrast, local arrays of VHF antennas provide high spatial and temporal resolution, but these instruments are expensive and data-intensive.

In this study, a new type of lightning detector, the electrostatic Biral Thunderstorm Detector (BTD), was extensively tested at three active volcanoes, Sakurajima in Japan (Chapter 2), Stromboli in Italy (Chapter 3) and Cumbre Vieja on La Palma island, Spain (Chapter 4). The BTD has proven to be capable of detecting near-vent and plume volcanic lightning during a wide variety of explosive eruptions. A volcanic lightning detection algorithm was developed in Python, described in detail in Chapter 2 and Appendix A, to automatically identify electrical discharges. This algorithm was fine-tuned for each location, as the empirical thresholds depend on the distance between the sensor and the active vent, the local noise level and the magnitude of the explosive eruptions.

Long-term electrical monitoring (1.5 years) at Sakurajima allowed to compare the electrical activity generated by hundreds of ash-rich explosions of Vulcanian eruption style and dacitic composition (Chapter 2). An overall increase in the number of electrical discharges, the sum of neutralised charge and the maximum electrical discharge rate was observed with increasing plume height, likely the result of an increase in the mass eruption rate. Similar observations were made during mafic explosions ejecting variable amounts of ash, lapilli and incandescent bombs at Stromboli. Only weak electrical activity was detected during the mild Strombolian explosions, while strong movements of charge and tens to hundreds of electrical discharges were detected during the larger-scale explosions, in particular during a Strombolian paroxysmal event (Chapter 3). The 2021 Cumbre Vieja eruption provided the unique opportunity to link variations in the electrical activity to changes in the eruption style based on thermal and visual surveillance (Chapter 4). High-voltage electrical discharges, similar to the electrical activity detected at Sakurajima and Stromboli, were recorded during strong ash emissions, while weak ash emissions generated faint discharges that remained unidentified by the detection algorithm. Bursts of continuous low-voltage discharges of variable duration were detected during gas jetting, Strombolian activity and lava fountaining with relatively minor amounts of ash. These results show that the characteristics of the electrical signals, in particular the number of discharges, their magnitude and the discharge rate, may indicate the eruption magnitude and style for individual explosions (Chapters 2 and 3) or throughout a whole eruption (Chapter 4). In addition, the onset of volcanic lightning and movement of charge can mark the inception of the explosion, aiding the monitoring of active volcanoes (Chapters 2 and 3). Moreover, the electrical signal detected by the BTD can yield information on ash cloud direction, ash fall and consecutive explosion pulses, providing additional information on the evolution of the eruption that are not determined by conventional lightning detection instruments.

Based on the comparison of plume height and atmospheric temperature profiles, it was concluded that silicate particle charging is the dominant plume electrification mechanism during these relatively small-scale explosive eruptions, as the plume either does not exceed atmospheric freezing levels or is not sustained long enough for sufficient ice nucleation to occur and play a key role in the plume charging (Chapters 2 and 4). This further proves the effectiveness of detecting ash emissions by monitoring the occurrence of volcanic lightning.

The results of this study show that explosive eruptions of variable magnitude (tens of metres to 8.4 km plume height), different eruption styles (mild Strombolian explosions, Strombolian paroxysmal events, ash venting, lava fountaining and Vulcanian activity) and different magma compositions (from dacite to more mafic magma) all produce detectable electrical activity. This holds promise for monitoring explosive activity at any volcano using volcanic lightning. The distinct electrical signatures detected during this study, which are directly related to the eruption style and magnitude, will help set the basis for building a database of volcanic lightning and may be used to provide near real-time estimates of eruption parameters in the future.

Additionally, this study contributed to studying electrical discharges in volcanic jets analogues during rapid decompression experiments inside a Faraday Cage (FC) at Ludwig-Maximilians-Universität (LMU) of Munich, Germany.

The effect of volcanic ash and ice on the polarity of electrical discharges was investigated (Chapter 5). The results showed that ash introduced a surplus of negative charge into the FC, which led to a prevalence of negative cloud-to-ground (CG) discharges. On the other hand, ice introduced positive charge into the FC and produced predominantly positive CG discharges. Moreover, fewer electrical discharges occurred if ice was present, presumably because of a thin layer of water forming on the surface of the ice particles as a result of collisional melting, inhibiting the plume electrification. These results are consistent with the observations of five volcanic eruptions, which generated CG events of prevalent negative polarity, with a greater proportion of positive CG events for those eruptions that produced large amounts of volcanogenic ice. These findings suggest that it is plausible that the percentage of positive CG events may provide a means to quantify the relative amount of volcanogenic ice nucleation in the eruption plume.

Lastly, the effect of a standing shock wave on the occurrence of electrical discharges was examined (Chapter 6). Explosive eruptions can produce shock waves, which are caused by the sudden release of overpressured gases within the erupting magma, creating supersonic flows. Rapid decompression experiments showed that electrical discharges are favoured upstream of a standing shock wave, where the flow expands supersonically. Standing shock waves during volcanic explosive eruptions are rarely observed in nature, most likely due to presence of particles in the expanding flow perturbing or inhibiting their formation. Nonetheless, it is possible that Continual Radio Frequency (vent discharges that occur in the gas-thrust region at the inception of the explosion) is regulated by the shock flow, which could provide insight into the pressure and particle content of the explosive flow.

Chapter 1

Introduction

1.1 Motivation

Active volcanoes are associated with serious hazards, both socially and economically. Consequences of volcanic eruptions in the past involve, e.g. casualties, damage to infrastructure, loss of cultivated land and loss of revenue for airlines due to in-flight ash encounters. For this reason, efforts to monitor volcanoes have increased significantly in the last few decades (Sparks et al., 2012; Pallister and McNutt, 2015).

Movement of magma towards the Earth's surface can result in seismicity, ground deformation and the release of volcanic gases. In order to recognize these precursory signals, several instruments can be deployed to detect changes within the volcanic plumbing system.

Most monitoring networks include seismometers to detect ground motion. Understanding these signals helps volcano observatories interpret the underlying volcanic processes and may help us prepare for a possible impending eruption (Wassermann, 2012; McNutt and Roman, 2015).

Acoustic sensors are used to detect infrasound (acoustic sound waves at frequencies < 20 Hz). Both processes within the plumbing system, such as the ascent of magma (Garcés and McNutt, 1997; Fee and Matoza, 2013), as well as different processes during a volcanic eruption can produce acoustic signals (Fee and Matoza, 2013; De Angelis et al., 2019). These signals facilitate detecting, locating and characterising volcanic eruptions, as well as provide information on several eruption parameters (Fee and Matoza, 2013; De Angelis et al., 2019).

Magma injection/withdrawal typically results in changes of the gravimetric and magnetic fields (Carbone et al., 2006; Del Negro and Napoli, 2004; Napoli et al., 2008) and in ground deformation (Dzurisin, 2006). Ground deformation can be measured by tiltmeters (e.g. Rebscher et al., 2000; Gambino and Cammarata, 2017), strainmeters (e.g. Agustsson et al., 2000; Aloisi et al., 2018), dilatometers (e.g. Aloisi et al., 2020; Bonaccorso et al., 2021), Global Positioning Systems (GPS) (e.g. Peltier et al., 2010; Aloisi et al., 2018, 2020), and through radar images made by ground- and satellite-based synthetic aperture radar interferometry (InSAR) (e.g. Peltier et al., 2010; Morales Rivera et al., 2017).

The chemical composition of plumes, fumaroles, degassing soil and geothermal waters can provide information on the degassing magma in the shallow plumbing system, of which CO_2 and SO_2 are two of the most important chemical components (Pallister and McNutt, 2015; Aiuppa et al., 2021). Remote sensing techniques to measure SO2 fluxes at volcanoes include both ground-based and satellite-based instruments, such as UV cameras and differential optical absorption spectroscopy (DOAS) systems (Tamburello et al., 2011), the Ozone Monitoring Instrument (OMI) (Carn et al., 2017) and the Atmospheric Infrared Sounder (AIRS) (Prata and Bernardo, 2007).

Although each of these monitoring instruments provides valuable information, they all share the limitation that their signals do not provide information on the emission of volcanic ash. Therefore, active volcanoes are often monitored using visual surveillance, through ground-based thermal and visible imaging, helicopter flights, drones, Unmanned Aerial Vehicles (UAVs), and satellite images. These observations not only inform us of an eruption, but can also help map lava flows and track volcanic plumes in real-time. However, some volcanoes are too remote, inaccessible or simply underfunded to carry out sufficient visual surveillance or monitoring. Also satellites often lack the desired revisit period or resolution and require clear weather to provide immediate warning at the start of an eruption. Nonetheless, volcanic ash can pose a threat to the local population or air traffic and demands for improved early warning systems of volcanic ash emissions.

One promising method of detecting ash emissions instantaneously and remotely is through electrical monitoring. Volcanic lightning is frequently observed during explosive volcanic eruptions (Cimarelli and Genareau, 2021). Since it is generated within the eruption column and its frequency is correlated to the amount of volcanic ash ejected, the detection of volcanic lightning offers a reliable indication for the presence of ash. In addition, lightning can be detected up to thousands of kilometres (Behnke and McNutt, 2014), providing the prospect of a safe and near real-time monitoring system at (remote) volcanoes. However, to ascertain the detection of volcanic lightning as a suitable volcano monitoring tool, a deeper understanding of the conditions required for volcanic lightning to occur, is essential. In particular, the generation of electrical activity and its evolution throughout the course of the eruption need to be investigated for a wide range of explosive eruption styles and magnitudes.

Figure 1.1: A meteorological thunderstorm over Comala, Mexico, in July 2020. Many cloud-to-ground and a few intracloud lightning flashes are visible in this single photograph, which is a compilation of 42 photographs. Courtesy of Hernando Rivera. Reproduced with permission of the copyright holder.

1.2 Lightning physics in thunderstorms

Due to their ability to generate lightning discharges, volcanic plumes have been sometimes referred to as “dirty thunderstorms” due to the first order similarities (size, updraft velocity, convection, presence of water vapour and hydrometeors) between thunderclouds and ash-rich eruptive columns. However, despite the apparent similarities between thunderstorm and volcanic lightning, the microphysics acting in volcanic plumes and thunderclouds cannot be fully assimilated and several conditions for the generation of electrical discharges in volcanic plumes are still elusive. For this reason, the well established literature on lightning physics in thunderstorms (Rakov and Uman, 2003) provides a solid starting point to further our understanding of volcanic lightning. The basic mechanisms of lightning generation in thunderclouds is here briefly summarised for the common scenario in which a lightning strike occurs between the cloud and the earth’s surface, also known as cloud-to-ground (CG) lightning (Figure 1.1).

Necessary condition towards the formation of lightning is charge separation in clouds. Charge generation in thunderclouds is mainly caused by collisions between graupel, ice particles and supercooled water droplets (Williams, 1989; Boerner, 2019). These collisions allow electrons to break free. Typically the smaller particles become positively charged and the larger particles negatively charged (Boerner, 2019), although the local temperature in the thundercloud can cause a charge reversal (Williams, 1989). The ascent of ice particles and other small cloud particles through the cloud and the gravitational settling of larger particles, such as graupel, will lead to charge separation within the thundercloud. These processes commonly result in an electrical (PNP) tripole structure, involving a mixed-phase region of negative charge in the lower portion of the cloud, a positively charged ice-rich upper portion and a more localised positively charged lower boundary (Figure 1.2) (Williams, 1989; Boerner, 2019). This charge separation, achieved over the vertical extension of the thundercloud, creates an electric field strong enough to overcome the breakdown resistance of air, thus promoting lightning. The more charge is built up, the stronger the electric field. Also turbulence within the thundercloud can increase the electric field by clustering charged particles closer together (Cooray, 2015).

If there is sufficient negative charge in the lower portion of the cloud, the electrons in the earth’s surface are repelled deeper into the earth, making the earth’s surface positively charged. Once the electric field is strong enough, a conductive path between the negatively charged bottom of the thundercloud and the positively charged surface will be created. Under standard atmospheric conditions, the electric field needs to exceed the critical value of $2.8x10^6$ V/m to allow electrical breakdown of air (Cooray, 2015). Although this critical value decreases with height, the maximum electric field measured in thunderclouds is typically much lower (100-150 kV/m) than what is required to initiate lightning (Rakov, 2013; Cooray, 2015). Two mechanisms that can locally enhance the electric field to initiate lightning have been suggested: streamers forming from hydrometeors and relativistic runaway breakdown (high-energy collisions of cosmic ray particles colliding with atmospheric nuclei creating an avalanche of runaway electrons) (Rakov, 2013; Boerner, 2019). This enhanced electric field will start to break down the surrounding air by separating it into positive ions and electrons, also known as air ionisation. The

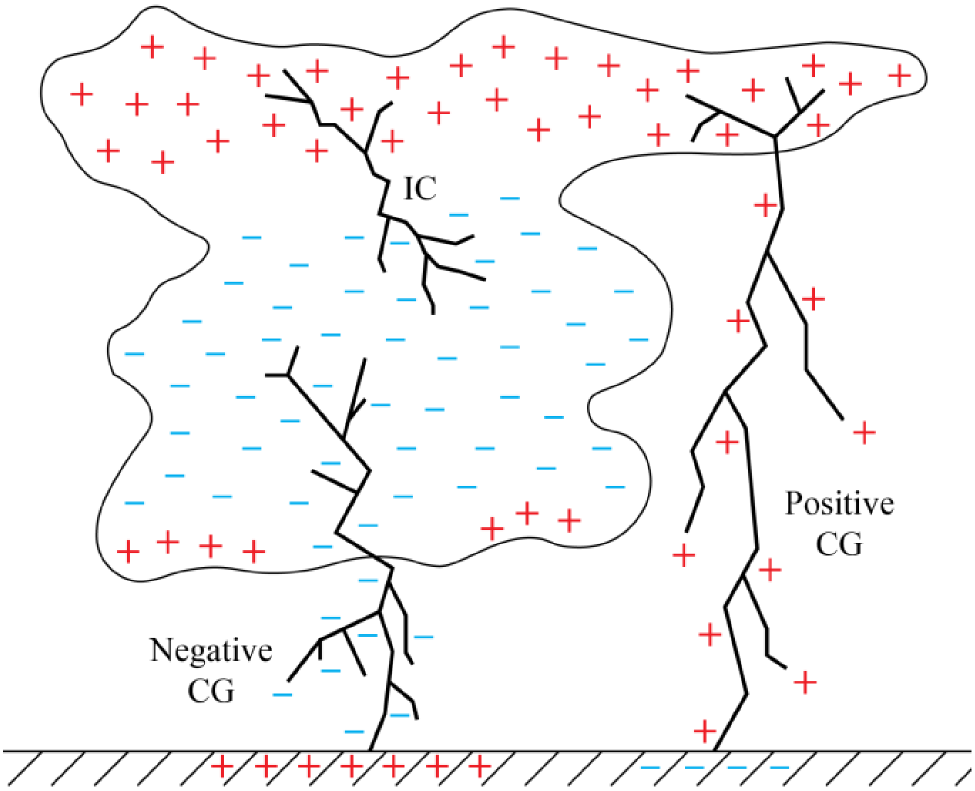

Figure 1.2: Schematic diagram of a thundercloud (not to scale) with a positive-negative-positive (PNP) tripole charge structure and intracloud (IC) and positive/negative cloud-to-ground (CG) lightning. Drawing made by the author.

ionised air, or plasma, is a lot more conductive than before ionisation, which allows the electrons to move freely and thus electrical current to flow. Many different paths of ionised air are created, which are known as stepped leaders (Cooray, 2003). The stepped leaders follow the path of least resistance, which is dependent on several factors, such as the shape of the electric field, the presence of impurities in the air and even the curvature of the earth's surface in case of large-scale thunderstorms. As soon as stepped leaders start to come in the vicinity of the earth's surface, the electric field will start to affect objects on the earth's surface. As a response, those objects will form connecting leaders pointing towards the thundercloud (Cooray, 2003). The first stepped leader to connect to one of the connecting leaders will form the conductive path between the thundercloud and the earth. Subsequently, the return stroke carries near ground potential upwards towards the cloud, creating a strong electrical current that neutralises the leader charge (Rakov, 2013). The flash that is observed during the return stroke is caused by the enormous amount of heat that is generated during the flow of current (Rakov, 2013). The heat causes the air to expand rapidly, creating a shockwave, audible as thunder. This initial strike is typically followed by secondary leaders and subsequent return strokes (Cooray, 2003, 2015; Rakov, 2013).

The lightning polarity depends on the type of charge transferred (Cooray, 2015). The scenario above described the occurrence of negative CG lightning (Figure 1.2), as negative charge was brought from the cloud to the ground, which accounts for about 90% of all CG lightning (Boerner, 2019). If the wind spreads out the positively charged upper portion of the thundercloud, the anvil, far enough that it is exposed to the ground, positive charge can travel to the earth's surface in the form of +CG lightning (Figure 1.2) (Boerner, 2019). There are many other types of thunderstorm lightning besides CG lightning. About 90% of all lightning occurs within clouds, known as intracloud (IC) lightning (Figure 1.1) (Boerner, 2019). This usually occurs between the negatively charged lower portion and the positively charged upper region of the thundercloud (Figure 1.2) (Cooray, 2003; Boerner, 2019). Lightning can also occur between clouds, referred to as inter-cloud or cloud-to-cloud (CC) lightning. Beyond the troposphere other forms of lightning can occur, which will not be discussed here.

Figure 1.3: Volcanic lightning during an eruption at Colima volcano, Mexico, in January 2017. The clear night sky proves that the lightning is produced by the volcanic eruption. Courtesy of Hernando Rivera. Reproduced with permission of the copyright holder.

1.3 Volcanic lightning

Volcanic lightning is a common phenomenon during explosive volcanic eruptions (Figure 1.3). The first written record of volcanic lightning, as far as known, was made by Pliny the Younger during the catastrophic eruption of Mount Vesuvius, Italy, which destroyed Pompeii and Herculaneum in 79 AD. He wrote (Gilman et al., 2007):

> *"... a black and dreadful cloud bursting out in gusts of igneous serpentine vapour*
> *now and again yawned open to reveal long fantastic flames,*
> *resembling flashes of lightning but much larger."*

Although volcanic lightning tends to be reported more often during the night than during daylight (McNutt and Thomas, 2015), awareness of this phenomenon has increased significantly over the last two decades (Cimarelli et al., 2022). At the end of 2012, volcanic lightning had been observed and/or detected during 394 eruptions at 152 volcanoes (McNutt and Thomas, 2015), almost twice as high compared to a few years earlier (McNutt and Williams, 2010). The 1963 Surtsey (Anderson et al., 1965), 2010 Eyjafjallajökull (Bennett et al., 2010; Arason et al., 2011), 2015 Calbuco (Van Eaton et al., 2016), 2015-2016 and 2018-2019 Sakurajima (Aizawa et al., 2016; Cimarelli et al., 2016), 2017 Bogoslof (Van Eaton et al., 2020), 2018 Fuego (Schultz et al., 2020), 2018 Krakatoa (Prata et al., 2020), 2020 Taal (Tripathy-Lang, 2020) and 2021 Cumbre Vieja (Chapter 4) eruptions are only a few examples that produced an abundance of volcanic lightning.

1.3.1 Plume electrification mechanisms

Similar to thunderstorms, the formation of volcanic lightning starts with charge generation and subsequent gravitational separation inside the volcanic plume. Several plume electrification mechanisms have been proposed, although the complexity and continuous development of volcanic plumes make it impossible to determine the relative contributions of each process. In general, ash particles are the main component in the generation of charge instead of ice particles, graupel and supercooled water droplets. Fracto-electrification typically occurs within the gas-thrust region of the volcanic plume and involves the emission of charged species from the freshly fractured surfaces of ash particles created upon fragmentation (Figure 1.4) (Dickinson et al., 1988; James et al., 2000). Tribo-electrification occurs both in the gas-thrust region and the convective region of the plume (Figure 1.4). Here, electrons transfer from one ash particle to the other when they create friction upon collision (e.g. Lacks and Levandovsky, 2007; Cimarelli et al., 2014; Gaudin and Cimarelli, 2019; Méndez Harper et al., 2021). A combination of these two processes is also possible, where emission of charged species is caused by friction instead of fracturing (Nakayama and Hashimoto, 1992). Fracto- and tribo-electrification are typically dominant in ash-rich explosive events that do not reach freezing levels.

If there is sufficient water in the plume and the plume is sustained at high altitudes for tens of minutes to hours, ice nucleation and riming can play an important role as an electrification mechanism as well (Figure 1.4) (Prata et al., 2020; Van Eaton et al., 2020). At temperatures between -13 and -23 °C (Durant et al., 2008), ash particles can become effective catalysts for ice nucleation (Maters et al., 2019, 2020), although the exact temperature at which volcanic nuclei become activated varies slightly depending on the nucleation mode (Durant et al., 2008), chemical composition, crystallinity and mineralogy (Genareau et al., 2018; Maters et al., 2019, 2020). McNutt and Williams (2010) did not find any latitudinal dependence on the occurrence of volcanic lightning. This would suggest that the water content of the erupting magma is more important in the generation of volcanic lightning than the entrainment of meteorological water. Other plume electrification processes include the interaction with (sea)water (Björnsson et al., 1967; Büttner et al., 1997; James et al., 2008) and, to a lesser extent, natural radioactivity

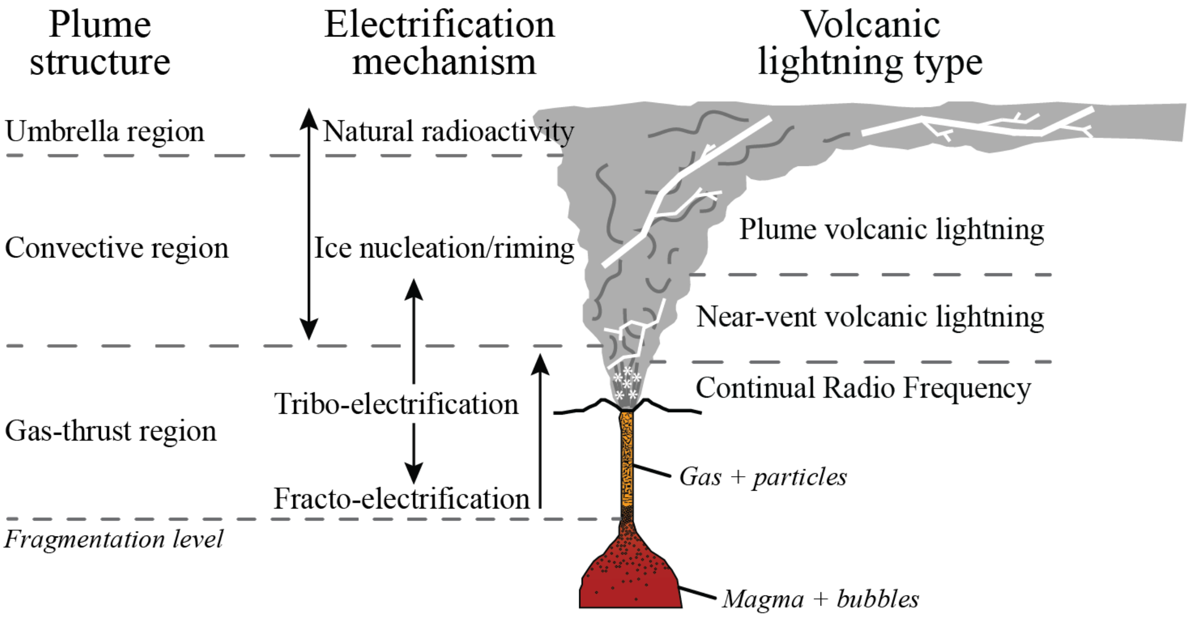

Figure 1.4: Sketch of volcanic plume (not to scale). Plume electrification mechanisms and different types of volcanic lightning are indicated with respect to different regions of the plume. Modified after Cimarelli and Genareau (2021).

(Figure 1.4) (Clement and Harrison, 1992; Aplin et al., 2014; Nicoll et al., 2019).
There has been some debate on the charge structure of volcanic plumes. Rapid decompression experiments showed that the particle size distribution, together with the inertia of the particles and the turbulence caused by the entrainment of air, are important for the separation of charge and the formation of charge clusters (Cimarelli et al., 2014; Gaudin and Cimarelli, 2019). Behnke et al. (2013) suggested that the gas-thrust and convective regions of volcanic plumes consist of disorganised charge clusters due to the turbulence, which evolve into a horizontal stratified structure at higher altitudes. Based on electric potential gradient measurements, a dipole structure was inferred at Sakurajima volcano, Japan, with a positively charged upper region consisting of gas and aerosols and a negatively charged lower region consisting of fine ash particles (Lane and Gilbert, 1992; James et al., 1998). Miura et al. (2002) suggested a tripole structure, with an additional positively charged region at the bottom consisting of coarse ash particles that clustered there after gravitational settling. Although the eruption dynamics and the constantly evolving plume structure do not allow for a universal model (Cimarelli and Genareau, 2021), similarities with the charge structure of meteorological thunderstorms are evident.

1.3.2 Types of volcanic lightning

Three types of volcanic lightning have been classified by Thomas et al. (2010) based on their timing relative to the eruption onset, their location within the volcanic plume and their length. Vent discharges are very high frequency (VHF) signals, also known as Continual Radio Frequency (CRF), that occur in the gas-thrust region at the inception of the explosion (Figure 1.4) (Thomas et al., 2007, 2010; Behnke et al., 2018). The CRF signature, a large cluster of radio frequency sources over the timespan of seconds or tens of seconds, differs from the VHF signature of lightning flashes, which typically are shorter (tens to hundreds of milliseconds), intermittent events alternated with periods with no discharges (Behnke et al., 2021; Smith et al., 2021). For this reason, the vent discharges are hypothesised to be cold plasma discharges, a form of streamer breakdown, and officially do not fall under the term "volcanic lightning" (Behnke et al., 2018, 2021). CRF has not been observed during meteorological thunderstorms and thus is a unique phenomenon for explosive volcanic eruptions, which can aid volcano monitoring. However, a single CRF pulse has an average width of 50 ns and a length up to 4 metres (Behnke et al., 2021), hence requiring a detector with a very high sampling rate, such as a Lightning Mapping Array (further discussed in Section 1.3.4). Smith et al. (2021) found that vent discharges only occur during explosive volcanic eruptions above a certain magnitude (large eruptive volume and high rise velocity), while volcanic lightning has been detected during smaller explosions as well.

Near-vent volcanic lightning occurs within the transition of the gas-thrust region into the convective region of the plume (Figure 1.4, 1.5 and 1.6) (Thomas et al., 2010). They typically have lengths of tens of metres to a few kilometres (Figure 1.4) and durations up to 30 ms (McNutt and Thomas, 2015). Both the CRF and the near-vent discharges can be used as an ash early warning system, as these discharges typically occur at the onset of the eruption (Cimarelli and Genareau, 2021).

Figure 1.5: Near-vent and plume volcanic lightning during the 2010 Eyjafjallajökull eruption in Iceland. Courtesy of Marco Fulle - www.stromboli.net. Reproduced with permission of the copyright holder.

Plume volcanic lightning is most similar to thunderstorm lightning, as it can have lengths ranging between hundreds of metres to more than 10 kilometres (Figure 1.5) and have a duration of 10 ms to 1 s (McNutt and Thomas, 2015). This type of volcanic lightning occurs after the plume has developed further, within the convective and umbrella regions minutes after the eruption onset (Figure 1.4) (Thomas et al., 2010). Even after the plume has detached from the crater, plume volcanic lightning can still occur. This makes it suitable for ash nowcasting, where the ash cloud is tracked based on the location of lightning flashes (Cimarelli and Genareau, 2021).

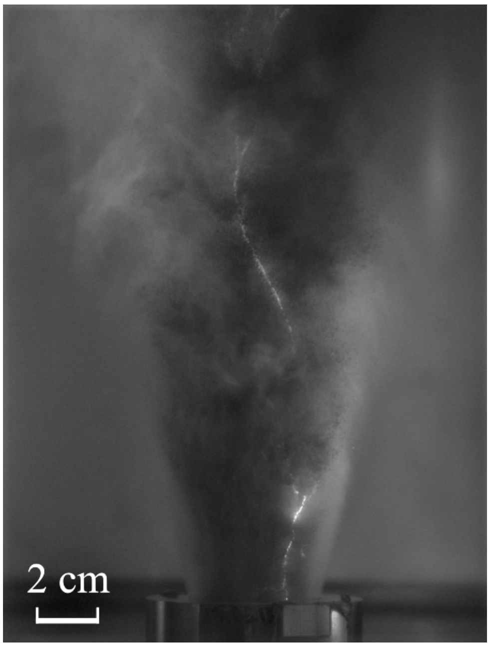

Figure 1.6: Single frame of high-speed video taken at 10,000 fps showing an electrical discharge (≥19 cm length) during a rapid decompression experiment of fine particles carried out by Cigala (2017). Reproduced with permission of the copyright holder.

1.3.3 Controls on volcanic lightning

There is still a lot to be discovered about what controls the occurrence of volcanic lightning and the underlying charging mechanisms. Both the eruption dynamics and external factors, such as water and ice, influence the generation of volcanic lightning. These parameters have been investigated through field measurements and experimental simulations.

Influence of eruption dynamics

The gas-thrust region of a volcanic eruption can be simulated under controlled conditions by performing shock-tube experiments, where a mixture of gas and particles is ejected upon rapid decompression (originally developed by Alidibirov and Dingwell (1996)). These experiments can generate electrical discharges (Figure 1.6), which can be detected using a Faraday cage (Cimarelli et al., 2014; Gaudin and Cimarelli, 2019; Stern et al., 2019). The results of different experiments showed that the proportion of fine particles is positively correlated to the number of discharges (Cimarelli et al., 2014; Gaudin and Cimarelli, 2019), while the magnitude of the discharges is linearly correlated to the initial overpressure and the total eruptive mass (Gaudin and Cimarelli, 2019). During these experiments, electrical discharges occurred as long as there was overpressure at the vent and were confined to the region of rarefaction, an under pressurised upstream region of the flow (Méndez Harper et al., 2018; Gaudin and Cimarelli, 2019). Méndez Harper et al. (2018) suggested that these conditions promote the occurrence of vent discharges in nature as well.

Little is known about the influence of the temperature of the erupting magma on the electrical activity of volcanic eruptions. Rapid decompression experiments were carried out by Stern et al. (2019) to investigate this. The results showed a higher number of smaller discharges at raised temperatures (up to 320 °C), likely related to faster charging and more efficient discharging due to increased turbulence. Méndez Harper et al. (2020) found that tribo-electrification at increased temperatures (up to 40 °C) resulted in lower surface charge densities. More research is needed to explore the effect of temperature further.

In general, the electrical activity increases with the magnitude of the eruption. Field measurements revealed an increase in the total number of discharges with increasing plume height (for plume heights $>$ 5 km, Behnke et al. (2014)) and maximum acoustic pressure (Cimarelli et al., 2016). Plume height is strongly dependent on the mass eruption rate (MER) (Settle, 1978), which in turn affects the amount of tribo-electrification in the plume (Méndez Harper and Dufek, 2016). Also the discharge rate increases with plume height (Bennett et al., 2010; Behnke et al., 2014), while changes in discharge rate can be the result of either changes in MER (Hargie et al., 2019) or enhanced plume electrification due to ice nucleation at higher altitudes (Behnke et al., 2014). Note, however, that most of these observations were obtained during ash-rich major eruptions that often reached altitudes at which ice nucleation occurs, leaving a knowledge gap regarding the electrical activity produced by the lower magnitude spectrum of explosive eruptions. In addition, little is known about how changes in the eruptive activity, such as plume collapse or a shift in eruption style, affects the electrical activity.

Influence of external water and ice

The interaction of magma with external water enhances the explosivity of a volcanic eruption. High water contents can result in vigorous plume electrification and lightning through ice nucleation if the plume is sustained and reaches sufficient altitudes, as was observed during the 2016-2017 Bogoslof eruption (Van Eaton et al., 2020) and the 2018 Anak Krakatau eruption (Prata et al., 2020). However, the amount of lightning detected before the plume reaches atmospheric freezing levels, is often low in these cases (Arason et al., 2011; Van Eaton et al., 2020). Although this may be partially due to near-vent electrical activity falling below the detection limit of the sensors (Van Eaton et al., 2020), these findings are consistent with the results of rapid decompression experiments carried out by Stern et al. (2019). They found that the total amount of neutralised charge decreases with increasing concentration of water in the sample. This may be the result of charge clusters being too far apart due to a wider jet opening angle or because of the higher conductivity of ash and/or the humid air. On the other hand, tribo-electrification experiments showed that external water coats the surface of the ash particles, inhibiting charge transfer (Méndez Harper et al., 2020). Hence, liquid water might have an inhibiting effect on the occurrence of volcanic lightning, while the presence of ice particles enhances it (Stern et al., 2019).

Besides the water content, atmospheric temperatures and the entrainment of cold air into the plume over time determine whether ice nucleation occurs. McNutt and Williams (2010) did not find a latitudinal dependence in the occurrence of volcanic lightning, suggesting that the initial water content of the erupting magma plays a bigger role in the generation of volcanic lightning than the entrainment of meteorological water. Durant et al. (2008) found that volcanic ice nuclei typically become activated between temperatures of -13 °C and -23 °C. Genareau et al. (2018) tested the importance of bulk composition and mineral abundance on the effectiveness of volcanic ash being a catalyst for ice nucleation. In the immersion mode, where ice nucleates after a solid particle is immersed in a supercooled water droplet, the composition and mineral content did have an effect on the ice nucleation site density. In addition, the smallest grain size, thus the particle with the largest proportion of surface area, was found to be the most efficient to nucleate ice (Genareau et al., 2018). Maters et al. (2019) found a positive correlation between crystallinity and the ice-nucleating activity of ash. Hence, the chemical composition, crystallinity and mineralogy of the erupting magma might influence the efficiency of ice nucleation at high altitudes. This may be further affected by the interaction with hot magmatic gases, such as H_2O, SO_2 and HCl, within the convecting plume (Maters et al., 2020).

Although it is evident that certain parameters either hinder or enhance the generation of volcanic lightning, in nature (and sometimes even during laboratory experiments) it often remains difficult to separate the individual effects of these parameters on the electrical activity.

1.3.4 Volcanic lightning detection

Lightning emits electromagnetic radiation over a wide range of frequencies, including the visible spectrum (Cimarelli and Genareau, 2021), but is strongest in the radio spectrum (Figure 1.7) (Bennett, 2017). These emissions are used to detect volcanic lightning, both through satellite-based and ground-based methods. These detections are typically combined with other measurements, such as visual and thermal imagery, seismic and infrasound measurements, mass eruption rates, ash distribution and grain size, plume heights and atmospheric vertical profiles, to put the electrical activity in context with the underlying eruption dynamics.

Satellite-based detection

A lightning flash causes a momentary optical change, which can be detected using a single channel, near-infrared optical transient detector from space. This method is applied by detectors such as the Geostationary Lightning Mapper (GLM) on the Geostationary Operational Environmental Satellite (GOES-16 and GOES-17 of the GOES-R series) and the Lightning Imaging Sensor (LIS) on the International Space Station (ISS). Schultz et al. (2020) showed that the GLM successfully detected lightning flashes during the 2018 eruption of Volcán de Fuego, Guatemala, including total optical energy and flash length. This method provides, however, a lower limit on the number of lightning flashes, as the opaqueness of volcanic plumes obscures volcanic lightning. For this reason, Schultz et al. (2020) suggested that a combined approach of satellite-based and ground-based detectors would provide a more robust dataset for volcanic lightning.

Additional information on the eruption can be provided by satellites, such as the plume height, ash nowcasting, the volcanogenic ice mass, the effective radius of ice particles and concentrations of SO_2 (Prata et al., 2020), which can aid the understanding of volcanic lightning and the underlying plume electrification mechanisms.

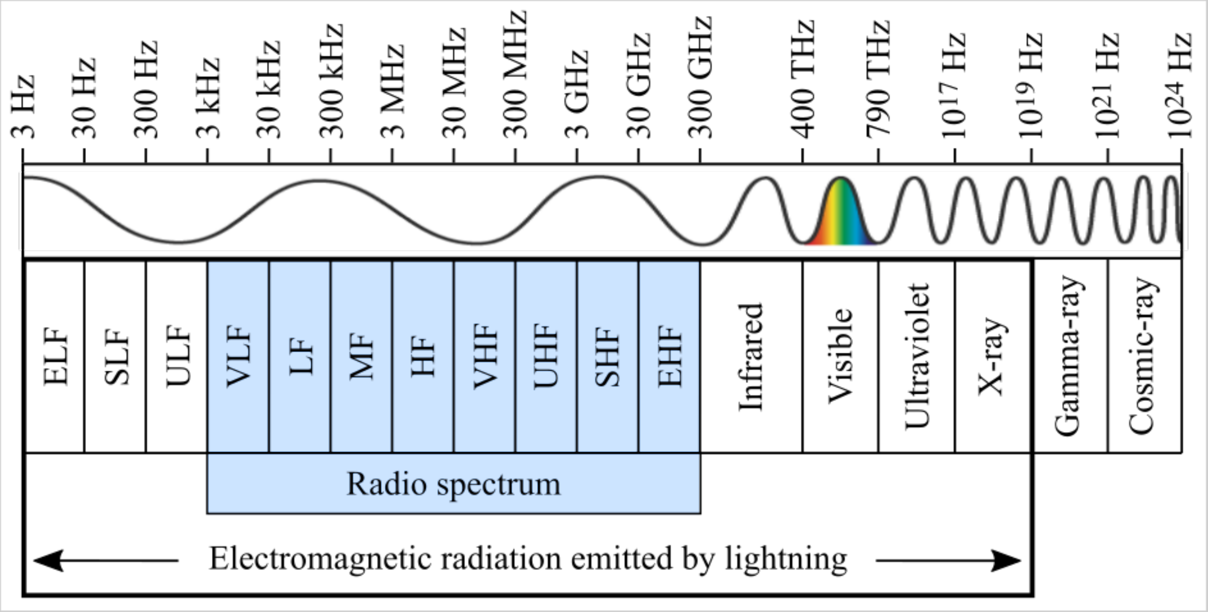

Figure 1.7: The electromagnetic spectrum, showing the frequency range, together with the corresponding band abbreviations, in which lightning emits radiation. ELF = extremely low frequency, SLF = super low frequency, ULF = ultra low frequency, VLF = very low frequency, LF = low frequency, MF = medium frequency, HF = high frequency, VHF = very high frequency, UHF = ultra high frequency, SHF = super high frequency, EHF = extremely high frequency. Diagram made by the author.

Ground-based detection

In the last decade, regional and global thunderstorm networks have demonstrated they can detect and locate volcanic lightning during major eruptions within the very low (VLF) to very high frequency (VHF) range using common thunderstorm detectors (Table 1.1). In particular, plumes reaching altitudes at which ice nucleation becomes an important electrification mechanism, generate high-current plume volcanic lightning that can be detected at great distances (100s-1000s km). A few successful examples of the four leading networks on this topic are mentioned here. The Arrival Time Difference Network (ATDnet) operated by the UK Met Office reported volcanic lightning during the 2010 Eyjafjallajökull eruption in Iceland (Figure 1.5) (Bennett et al., 2010; Arason et al., 2011, 2013). Also the Global Volcanic Lightning Monitor of the World Wide Lightning Location Network (WWLLN) detected lightning during this eruption (Behnke and McNutt, 2014), as well as during the 2015 Calbuco eruption in Chile (Van Eaton et al., 2016). The datasets of WWLLN and Vaisala GLD360 Global Lightning

Detection were combined to study volcanogenic ice nucleation, volcanic lightning and its thunder during the 2016-2017 Bogoslof eruption in Alaska (Haney et al., 2018, 2020; Van Eaton et al., 2020). Similarly, Earth Networks Total Lightning Network (ENTLN) measured lightning at Bogoslof (Lapierre et al., 2018), in addition to the 2018 Anak Krakatau eruption in Indonesia (Figure 1.8) (Prata et al., 2020) and the 2020 Taal eruption, Philippines (J. Lapierre, pers. comm.). An advantage of this method is that the data relies on widespread existing networks, and hence does not require a fast response to implement a network at the first sign of unrest at a volcano. However, these networks are often limited in the detection of smaller and more frequent ash-rich eruptions, which do not produce sufficient high-current lightning, due to the scattered geographical distribution of their sensors.

Table 1.1: The frequency range of commonly used lightning detection systems for the detection of volcanic lightning

System	**Frequency**	**Band**
LMA	60-66 MHz	VHF
ENTLN	1 Hz - 12 MHz	ELF-HF
GLD360	300 Hz - 48 kHz	ULF-LF
WWLLN	6-18 kHz	VLF
ATDnet	13.7 kHz	VLF
BTD (*this study*)	1-45 Hz	ELF-SLF

LMA = Lightning Mapping Array, ENTLN = Earth Networks Total Lightning Network, GLD360 = Global Lightning Detection, WWLLN = World Wide Lightning Location Network, ATDnet = Arrival Time Detection Network, BTD = Biral Thunderstorm Detector. The full names of the frequency bands can be found in the caption of Figure 1.7.

For high spatial (1-10 m) and temporal (nanoseconds) resolution, local arrays of VHF antennas, called Lightning Mapping Array (LMA) sensors (Table 1.1), are used on-site (Thomas et al., 2004, 2010). LMA sensors have very high sample rates (> MS/s), allowing the documentation of the propagation of a single discharge (Thomas et al., 2007; Behnke et al., 2013, 2014). The location and time of a lightning event can be determined using the time-of-arrival difference of an electrical signal at different stations within the array (Behnke et al., 2013). With this, a three-dimensional map of volcanic lightning, including vent discharges, during the course of an eruption can be built. This map can give valuable information on charging mechanisms, the charge structure of the plume and the influence of changes in the eruption dynamics on volcanic lightning (Behnke et al., 2013, 2014). However, a drawback is that these sensors are

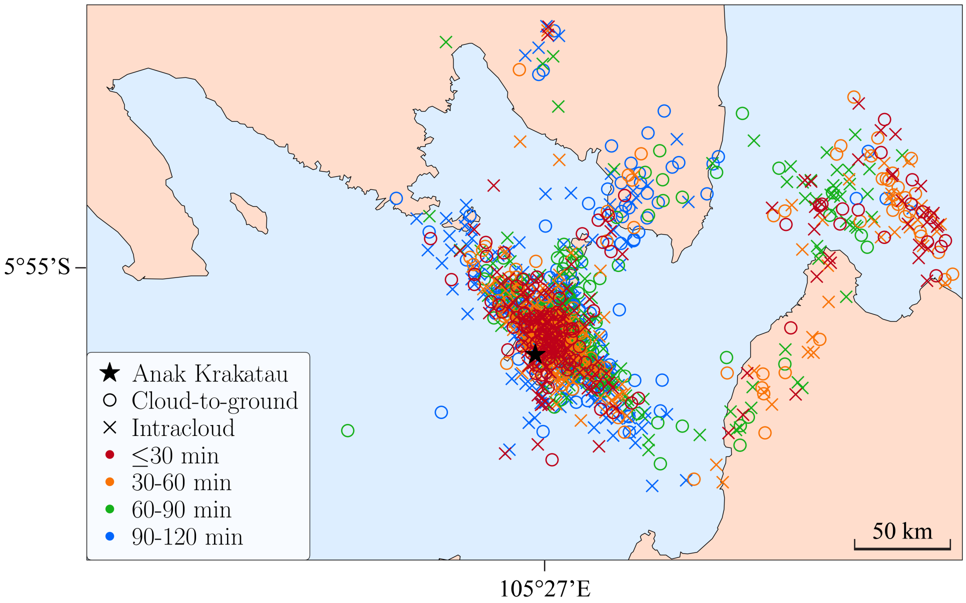

Figure 1.8: Cloud-to-ground and intracloud lightning flashes detected and located by ENTLN within the first two hours of the 2018 Anak Krakatau (star symbol) eruption in Indonesia. Modified after Cimarelli and Genareau (2021).

expensive and data-intensive, which makes them more suitable for short deployments rather than long-term volcano monitoring. Another disadvantage is that VHF antennas require a direct line-of-sight to the crater. A crater rim can scatter electrical signals, resulting in a weak signal at the antenna (Behnke et al., 2018), or can entirely prevent electrical signals from reaching the antenna, leaving any signals below the crater rim undetected (Behnke et al., 2013, 2021).

Other ground-based detection of volcanic lightning include videography, magnetotelluric, seismic and infrasound measurements. Aizawa et al. (2016) and Cimarelli et al. (2016) detected near-vent volcanic lightning at Sakurajima volcano, Japan, using a combination of normal and high-speed videography and magnetotelluric (MT) stations. These combined methods provided important constraints on the nature of lightning, although having limitations. MT stations assume the discharge occurs vertically, and therefore cannot accurately locate lightning events, while videography is limited to visible flashes that occur around or within the plume (Aizawa et al., 2016).

Similar to meteorological lightning, volcanic lightning produces thunder. Haney et al. (2018) recorded volcanic thunder during the 2016-2017 Bogoslof eruption in Alaska using a microphone array. They found that volcanic thunder can be distinguished at frequencies above 20 Hz, while at lower frequencies it is likely masked by eruption noise. Besides volcanic thunder, electromagnetic pulses can produce glitches in infrasonic records (Anderson et al., 2018; Haney et al., 2020). Also seismometers can detect lightning strikes and its accompanied thunder (Hinzen, 2012). Volcanic lightning was recorded as spikes or simultaneous gain ranging at several seismometers during the 1992 eruption of Mount Spurr in Alaska, most likely caused by electric currents being induced in the seismometer cable (McNutt and Davis, 2000).

This study

In this study, a new type of thunderstorm detector is tested for the first time at active volcanoes. Both the prototype as well as the commercial version of the Biral Thunderstorm Detector BTD-200, hereafter referred to as BTD, have been employed (Figure 1.9). This sensor detects the slow variation in the electrostatic field resulting from charge neutralisation due to an electric discharge (Bennett, 2017). Although the sensor measures the displacement current (V/m/s), the output of the antennas is provided as a measured voltage, which is proportional to the induced current.

The BTD consists of two antennas (Figure 1.9). The primary antenna is composed of an aluminium sphere that sits at the top of the antenna. The secondary antenna, sitting directly below the primary antenna, is a disc plate, which is shielded by a black cap. The position and surface area of the antennas result in a higher sensitivity for the primary antenna compared to the secondary one. In addition, the installation site and its surroundings also influence the antennas' sensitivity, as they affect the electrostatic "form factor". This form factor depends on the slope of the ground at the installation site, as well as the height and vicinity of nearby objects. In the case of a flat, open installation site and assuming a uniform vertical ambient electric field, the amplitude of the primary and secondary signals differ by a factor of ∼10. Regardless of the lower sensitivity, the secondary antenna is a valuable addition to the sensor, as it allows the discrimination of electrical discharges from signals caused by impact transients, such as charged precipitation or ash fall. As the primary antenna is exposed, precipitation or ash fall produces a transient change in the electric field upon impact, whilst the charge flows to the ground. Simultaneously, the shielded secondary antenna detects a current of opposite polarity due to its close proximity (Bennett, 2013). Hence, while electrical discharges produce signals of identical polarity, impact transients can be disregarded based on their opposite polarities (Bennett, 2013).

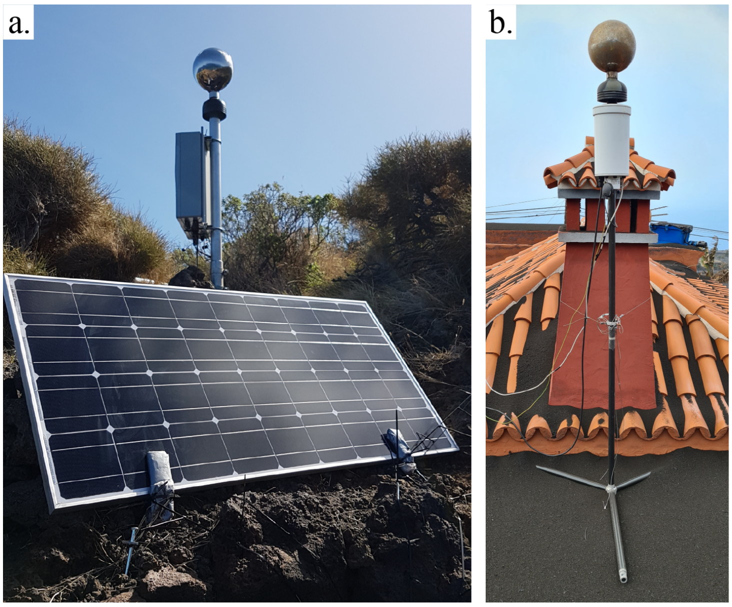

Figure 1.9: ***a)*** *Prototype of the BTD-200 powered by a 100W solar panel and a 12V 40Ah DC battery.* ***b)*** *The BTD-200, plugged into the mains power. The aluminium sphere at the top is the primary antenna, while the secondary antenna is shielded by the black cap below. The metal housing (grey and white in panels* ***a*** *and* ***b****, respectively) holds the electric board and the data logger. Pictures were taken by the author.*

Meteorological lightning can be reliably and routinely detected up to 35 km distance from the BTD, and even up to 100 km distance for larger lightning events. The BTD can be powered by the mains power or by a 100W solar panel and a 12V 40Ah DC battery in remote areas (Figure 1.9a). The BTD is manufactured with a SD card to log the data. During this study, however, the data logger was replaced by a Banana Pi and GPS to have more storage capacity and automatic GPS synchronisation. The sensor records at a sample rate of 100 Hz, which makes it suitable for long-term monitoring. While this sample rate is sufficient to detect near-vent and plume volcanic lightning, CRF signals fall below the detection limit of the BTD due their short ($\sim$50 ns) duration (Behnke et al., 2021). Also differences in time-of-arrival of lightning events at multiple sensors (within 100 km radius) will not be visible in the data at such a low sample rate. This means that it is not possible to locate lightning flashes. For meteorological lightning, the measured voltage can be converted into an estimated distance, assuming the charge moment and an installation site correction factor (Bennett, 2013), but more research is needed before this can be done for volcanic lightning as well. However, it might be possible to make a distinction between nearby volcanic lightning (at a known source location) and distant thunderstorm lightning, by analysing the intensity of the signal recorded at each sensor. In addition to the electrostatic form factor, the signal intensity is determined by the distance between the sensor and the lightning event. While the difference in distance greatly affects the signal intensity during nearby lightning, it is negligible for distant lightning, resulting in similar signal intensities at each sensor (assuming identical electrostatic form factors).

A great advantage of the BTD over the commonly used very low to very high frequency thunderstorm detectors is the frequency range in which it measures. Electromagnetic emission of lightning is strongest within the radio spectrum, but its detection may be complicated by interference caused by anthropogenic activity (Behnke et al., 2013; Bennett, 2017). To avoid this, the BTD measures within the extremely to super low frequency range (1-45 Hz, Table 1.1), which remains unaffected by anthropogenic radio emissions (Bennett, 2017). Another advantage of measuring within the quasi-electrostatic range is that the BTD does not require a direct line-of-sight to the active crater, as the electric field lines bend around the conductor, in this case the earth's surface (Tzur et al., 1985). This will allow instantaneous detection of electrical activity at the onset of an eruption, regardless of any obstruction, such as a crater rim. Besides volcanic lightning, the BTD is able to detect movement of charge and ash fall at the sensor, providing additional information on the evolution of electrical activity generated by the eruption.

1.4 Aims of this study

This study aimed at investigating the conditions for the occurrence of volcanic lightning during a variety of eruption styles, magnitudes and compositions, using a new type of detector.

Most of our knowledge on volcanic lightning is derived from laboratory experiments or field measurements during ash-rich major eruptions ($>$10 km plume height). The electrical activity of relatively small eruptions, however, remains understudied, as these events often go undetected by regional and global thunderstorm networks. For this reason, the first part of this study focused on demonstrating the effectiveness of the electrostatic Biral Thunderstorm Detector (BTD) in the detection of volcanic lightning during small-scale ash-rich events. Although never tested at volcanoes before, this cost- and data-efficient detector offers good prospects for detecting volcanic lightning locally, as it does not suffer from interference from anthropogenic activity and does not require a direct line-of-sight to the active volcanic vent (Section 1.3.4). Here, the aim was to address the following research question:

- Can the Biral Thunderstorm Detector be used as a volcano monitoring tool even for small-scale ash-rich eruptions?

To test its capability, a long-term (1.5 years) monitoring campaign was carried out at Sakurajima volcano, Japan, allowing the assessment of the BTD as a volcano monitoring instrument for a wide range of eruption magnitudes (plume heights varying from 100 m to 6 km). Additionally, in order to automatically identify the electrical discharges recorded by the BTD during hundreds of explosions at Sakurajima volcano, a volcanic lightning detection algorithm was developed in Python. The performance of the detection algorithm was assessed through a statistical analysis. Besides detecting volcanic lightning, it was investigated whether the BTD can detect ash fall at the sensor by producing signals of opposite polarity at the two antennas. The results of this research are discussed in Chapter 2.

Figure 1.10: Near-vent volcanic lightning at Sakurajima volcano, Japan, in February 2013. Courtesy of Martin Rietze. Reproduced with permission of the copyright holder.

Eruptions vary greatly between different volcanoes, complicating our understanding of the conditions required for the generation of volcanic lightning due to the amount of variables involved. Electrical monitoring at a single volcano reduces the number of variables contributing to the observed differences in electrical activity, including composition, fragmentation mechanism, eruption dynamics and external conditions (e.g. climate, submarine versus subaerial activity and summit height). Sakurajima volcano is an example of a “laboratory volcano”, as it produces self-similar ash-rich explosions, of predominantly Vulcanian style, on an almost daily basis. Therefore, for the second part of this study, we chose Sakurajima volcano to acquire a first-of-its-kind extensive dataset of volcanic lightning (Figure 1.10, Chapter 2) in order to address the following research question:

- In what way is electrical activity, in terms of number of discharges, magnitude and discharge rate, related to the magnitude of the eruption?

Volcanic lightning is less frequently observed during milder explosive eruptions, generally of mafic composition. This raises the question whether plume electrification and volcanic lightning are generated over the whole spectrum of explosive styles and magma compositions. Therefore, the third part of this study focused on the occurrence of volcanic lightning during a variety of eruption styles, magma compositions and magnitudes (<9 km plume height) and was designed to address several research questions:

- Does ice nucleation play a role as a plume electrification mechanism during small-scale ash-rich eruptions?
- Do mafic volcanoes, which generally produce explosions of lower explosivity at magmatic temperatures, generate detectable electrical activity as well?
- How is the electrical activity affected by changes in the eruption style?

Besides Sakurajima volcano, field measurements were carried out using the BTD at Stromboli volcano (Italy) and Cumbre Vieja (La Palma, Spain) to investigate this. Both dacitic and basaltic magma compositions were covered by these three volcanoes, as well as a wide variety of eruption styles and magnitudes, including Strombolian explosive activity, Strombolian paroxysmal events, lava fountaining and Vulcanian activity.

Both Sakurajima and Stromboli volcano are characterised by short-lived explosions of variable magnitudes. However, Sakurajima produces ash-rich explosions, while Stromboli ejects variable proportions of ash, lapilli and incandescent bombs at magmatic temperatures, adding to the complexity of the eruption dynamics. Chapter 3 describes the different electrical signatures obtained during mafic explosions of variable magnitude at Stromboli volcano. In contrast, the sustained 2021 Cumbre Vieja eruption provided the unique opportunity to observe variations in electrical activity with changing eruption style and magnitude throughout the course of the eruption, which is discussed in Chapter 4.

The electrical data was, where available, compared to visible and thermal images, plume heights, seismic and acoustic data, eruption duration and maximum ejection velocity, with the aim to determine relations between electrical activity and eruption parameters, magnitude and style. Moreover, to assess whether ice nucleation could have potentially played a role as a plume electrification mechanism in addition to silicate particle charging, atmospheric weather profiles were compared to measured plume heights.

Aside from the research project on the occurrence of volcanic lightning in nature, my scientific contributions include carrying out rapid decompression experiments at Ludwig-Maximilians-Universität München, Germany, to study the effect of a standing shock (Chapter 5) and the presence of ice (Chapter 6) on the occurrence of electrical discharges in volcanic jets analogues.

Chapter 2

Long-term observation of electrical discharges during persistent Vulcanian activity

2.1 Abstract

Very low frequency and wide-band lightning detection networks can detect major volcanic plumes via their intense electrical and lightning activity. However, the high number of non-detected explosive episodes confirmed by direct observations, reveals the limits of these systems in the detection of the more frequent smaller ash-rich explosive events. Here, we use a data-efficient thunderstorm detector to observe electrical discharges generated from July 2018 to January 2020 by the persistent Vulcanian activity of Minamidake crater at Sakurajima volcano in Japan.

Two thunderstorm detectors recorded the electrical activity produced by explosions at Minamidake crater from a distance of 3 and 4 km from the active vents. The instruments measured the induced current due to the change in electric field with time within the extremely low frequency range (1-45 Hz). Using a volcanic lightning detection algorithm together with the catalogue of volcanic explosions compiled by the Japan Meteorological Agency (JMA) and Tokyo Volcanic Ash Advisory Center (Tokyo VAAC), the number of electrical discharges, the electrical discharge rate and the total amount of measured voltage were determined for each individual explosive event. In addition, the start of the electrical discharges was compared to the explosion onset as provided by the JMA (with a one-minute time resolution).

The sensors detected electrical discharges in 71% of the 724 recorded explosions. Our detection algorithm successfully recognises the presence/absence of electrical discharges with an accuracy of 73%. We find a non-linear positive correlation between the number of discharges and the plume height. Moreover, we find that the maximum electrical discharge rate and the maximum amount of measured voltage by a single discharge also increase with plume height. Fracto- and tribo-electrification appear to be the dominant plume electrification mechanisms. Even for the few explosive events that exceeded the -10 °C isotherm, the timescale of electrical activity seems to be too short for ice nucleation to make a significant contribution to the plume electrification. Finally, for 12% of the electrically-active explosive events, discharges were detected by the sensors more than a minute before the JMA explosion onset.

Our results show the capability of our detectors in pinpointing the inception of electrified explosive episodes in real-time and in providing an indication of the magnitude of each explosion, demonstrating their effectiveness as a cost- and data-efficient instrumentation for the monitoring of explosive ash emissions at active volcanoes.

2.2 Introduction

The monitoring of volcanoes is improving rapidly (Sparks et al., 2012). Lagging somewhat behind however is the detection and monitoring of volcanic ash plumes, especially in remote areas. Air traffic is particularly at risk (Song et al., 2016), and demands for improved early warning systems of volcanic ash emissions.

Intense electrical activity and lightning in volcanic plumes suggest that electrical monitoring of volcanoes can aid ash emission detection. Volcanic lightning can be detected both instantaneously and remotely, providing the prospect of real-time monitoring at remote volcanoes.

Volcanic lightning (VL) has been universally observed at volcanoes around the world, with 2010 Eyjafjallajökull (Bennett et al., 2010), 2015-2016 Sakurajima (Aizawa et al., 2016; Cimarelli et al., 2016), 2015 Calbuco (Van Eaton et al., 2016), 2017 Bogoslof (Van Eaton et al., 2020) and 2018 Krakatau (Prata et al., 2020) eruptions being the most recently studied. Using laboratory experiments, numerical modelling, field observations and knowledge of thundercloud electrification, researchers have studied the source of VL and its relationship with eruption parameters, such as mass eruption rate (Hargie et al., 2019), plume height (Bennett et al., 2010; Behnke et al., 2013, 2014) and grain size distributions of the eruption products (Gaudin and Cimarelli, 2019). Several volcanic plume electrification processes that lead to charge separation have been proposed. These include fracto-electrification (the emission of charged species from freshly fractured surfaces, Dickinson et al. (1988); James et al. (2000)), tribo-electrification (electron transfer through the collision of ash particles, Lacks and Levandovsky (2007); Cimarelli et al. (2014); Gaudin and Cimarelli (2019)), ice nucleation/riming (Arason et al., 2011; Prata et al., 2020; Van Eaton et al., 2020), interaction with (sea)water (Björnsson et al., 1967; Büttner et al., 1997; James et al., 2008) and, to a lesser extent, natural radioactivity (Clement and Harrison, 1992; Aplin et al., 2014; Nicoll et al., 2019).

Thomas et al. (2010) have distinguished three types of VL based on when and where it occurs in the plume: 1) Vent discharges, also known as Continual Radio Frequency (CRF), are observed in the gas-thrust region at the inception of the explosion (Thomas et al., 2007, 2010). Behnke et al. (2018) found that a single CRF signal has a duration of $\sim$160 ns and a length scale of around 10 metres. 2) Near-vent discharges, in contrast, have a total duration of several ms (Aizawa et al., 2016). They have typical lengths of few tens to hundreds of metres and occur at the transition between the gas-thrust and the convective phases of the plume (Cimarelli et al., 2016). These values are 1-2 orders of magnitude smaller than those of thunderstorm lightning (Aizawa et al., 2016). 3) Plume volcanic lightning is that element of VL which is most similar to thunderstorm lightning, both in length and duration. These flashes can have a length of several kilometres and a duration of 30-650 ms (Thomas et al., 2007; McNutt and Williams, 2010).

Current global thunderstorm networks have demonstrated to be capable of detecting VL during major eruptions. This is especially so for plumes reaching altitudes at which ash becomes an effective catalyst for ice nucleation (Maters et al., 2019, 2020), between the -13 $^\circ$C and -23 $^\circ$C isotherms (Durant et al., 2008), although this temperature range can be extended several $^\circ$C depending on the nucleation mode (Durant et al., 2008), chemical composition, crystallinity and mineralogy (Genareau et al., 2018; Maters et al., 2019, 2020). These lightning detection networks commonly work in the very low to high frequency range, as the electromagnetic emission of thunderstorm lightning is strongest in the radio spectrum (Bennett, 2017). Examples include the Earth Networks Total Lightning Network (ENTLN) (Lapierre et al., 2018; Prata et al., 2020), the Global Volcanic Lightning Monitor of the World Wide Lightning Location Network (WWLLN) (Behnke and McNutt, 2014; Van Eaton et al., 2016; Haney et al., 2018; Hargie et al., 2019), Vaisala GLD360 Global Lightning Detection (Pattantyus and Businger, 2014; Haney et al., 2018; Van Eaton et al., 2020) and the Arrival Time Difference Network (ATDnet) operated by the UK Met Office (Bennett et al., 2010; Arason et al., 2011, 2013). The scattered geographical distribution of the sensors however, leads to reduced sensitivity and therefore to delayed or no detection for a relatively high number of explosive episodes, which do not produce sufficient high-current discharges. Thus, the applicability of these systems to the detection of smaller (and often more frequent) ash-rich explosive events is limited. In contrast, Lightning Mapping Array (LMA) sensors installed on-site have detected electrical discharges in relatively small explosive eruptions with high precision (Behnke et al., 2018). However, these sensors currently have the drawback that they are expensive and data-intensive. Here, we present a novel, long-term and data-efficient method to monitor continuously active volcanoes using a different type of thunderstorm detector, which we have tested in situ at Sakurajima volcano, Japan.

2.3 Material and methods

2.3.1 Study area

Sakurajima is a dacitic stratovolcano in southern Japan. The Minamidake summit-nested crater comprises vents A and B, which are situated approximately 600 m below the crater rim (Figure 2.1a). Sakurajima has been erupting continuously since 1955, with near 500 individual events reported by the Japan Meteorological Agency (JMA) and Tokyo Volcanic Ash Advisory Center (Tokyo VAAC) during 2019. The frequent Vulcanian events are in general relatively small (VEI 2-3 and plume heights of less than 4 km above the crater rim) and are well-known for producing spectacular lightning displays. Here, we use the terms "explosions" and "explosive events" interchangeably to refer to any ash-plume-producing event at Minamidake crater, including ash venting (i.e. a relatively continuous emission of tephra) lasting from a few minutes up to several hours (Cole et al., 2014). The JMA reports explosions at Sakurajima volcano with a one-minute time resolution. However, it is unclear how the JMA assigns the explosion onset (from now on "JMA explosion onset"), therefore in this study we assign to it an error margin of ±1 min. Additionally, plume height above the crater rim (a.c.r.) is reported with a resolution of 100 m, provided the plume is not obscured by clouds. Finally, details on seismicity, infrasound, ash cloud dispersal and ballistic trajectories, are provided when applicable. The Tokyo VAAC combines these reports with satellite data defining flight levels affected by the ash.

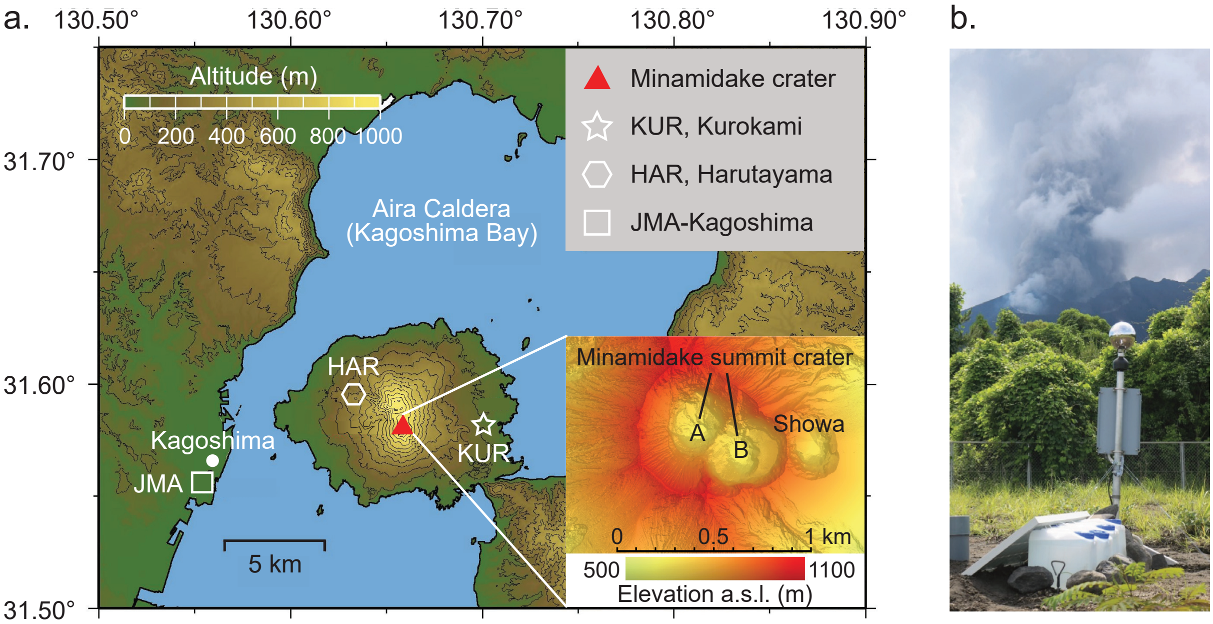

*Figure 2.1: **a)** Map showing Minamidake crater on Sakurajima volcano, the two thunderstorm detectors, KUR and HAR, and the Japan Meteorological Agency (JMA) branch office in Kagoshima city. In the inset: Digital elevation model of vents A and B of Minamidake summit crater and Showa crater obtained by SVO. **b)** Sensor KUR at Kurokami branch observatory with Minamidake crater erupting in the background.*

2.3.2 Instrumentation

In order to detect electrical discharges in situ at Sakurajima, two prototypes of the Biral Thunderstorm Detector BTD-200 were installed (Figure 2.1). The first sensor, hereafter referred to as “KUR”, was deployed 4.0 km east from the centre of Minamidake crater at the Kurokami branch of the Sakurajima Volcano Observatory (SVO). The second sensor, hereafter referred to as “HAR”, was installed 2.8 km northwest of Minamidake crater at the Harutayama branch of the SVO.

The sensor consists of a primary and secondary antenna detecting the slow variation in electrostatic field resulting from charge neutralisation due to an electric discharge (Bennett, 2017). The primary antenna is composed of an aluminium sphere that sits at the top of the sensor (Figure 2.1b), while the secondary antenna consists of a disc plate and is shielded from impact transients (e.g., charged precipitation or ash fall impacting the antenna). In the event of impact transients, the impacted primary antenna will produce a transient change in the electric field whilst the charge flows to the ground. As a result, a current of opposite polarity is simultaneously induced upon the shielded secondary antenna due to its close proximity (Bennett, 2013). While opposite polarity indicates impact transients, electrical discharges produce signals of identical polarity. The sensitivity of the antennas, and thus the ratio between the primary and secondary antenna, depends on both the position and surface area of the antenna (fixed) and the electrostatic “form factor”, the latter of which will depend on the height and proximity of any nearby objects, as well as the slope of the ground at the installation site. In the case of a flat, open installation site and assuming a uniform vertical ambient electric field, the primary antenna is a factor of $\sim$10 times more sensitive than the secondary antenna.

The instrument can reliably and routinely detect thunderstorm lightning up to 35 km distance and for larger lightning events up to 100 km. Although electromagnetic emissions of thunderstorm lightning are strongest in the radio frequency spectrum (Bennett, 2017), their discrimination may be complicated by interference caused by anthropogenic activity. To avoid this, the detector has a frequency response of 1-45 Hz (extremely to super low frequency range), which is unaffected by anthropogenic radio emissions (Bennett, 2017), in contrast to the commonly used very low frequency and wide-band thunderstorms detectors. The only exception to this is the mains power AC signal, which can be filtered out from the raw data.

The sensor is powered by a 12 V 40 Ah DC battery charged by a 100 W solar panel. The original data logger consists of a SD card. In February 2019, the data logger of KUR was replaced by a Banana Pi and GPS to have more storage capacity and an automatic GPS synchronisation. The data of HAR was stored on the SD card and, as this sensor did not have a GPS receiver, was later synchronised with KUR to correct for any time offset.

The detector records at a sample rate of 100 Hz, which is sufficient to detect near-vent and plume VL. On the contrary, the very short-lived CRF signals fall below the sampling period of the sensor.

2.3.3 Data collection

The detectors recorded continuously between 18 July 2018 and 18 January 2020. A detailed database of the explosions at Minamidake crater has been compiled from the reports of the JMA and Tokyo VAAC. During the time of monitoring, 750 explosions were reported at Minamidake, which were assigned chronological numbers (events 1-750). During 20 of those explosions, thunderstorm lightning within a 100-km radius of Minamidake was reported by WWLLN. To focus only on VL, these explosive events were excluded from the analysis. Due to the different locations of KUR and HAR, the sensors were not equally affected by weather and ash fall out, resulting in more data gaps due to low solar power for KUR. Of the remaining 730 explosions, KUR and HAR recorded data for 486 and 577 events, respectively. No data was available from either sensor for only 6 out of 730 explosions.

2.3.4 Data processing

Data processing involved an analog-to-digital converter (ADC) to digitise the raw voltage output from both antennas into a voltage (V) used for calculation by the internal processors. Note that the measured voltage is proportional to the current induced on the antennas by the atmospheric electric field change associated with the discharge. In addition, the covariance between the primary and secondary signals was calculated over a moving window of 16 samples with a step size of 1 sample.

Since thunderstorm lightning differs from VL in length, duration and peak current (Aizawa et al., 2016), a specific volcanic lightning detection algorithm was developed. The explosion database described in Section 2.3.3 was used to single out the 724 explosive events. The algorithm selected the electrical data starting 5 min prior and ending 15 min after the JMA explosion onset in order to include the true explosion onset and to encompass its full duration.

In order for the VL detection algorithm to interpret a signal as an electrical discharge, the signal needs to have the same polarity at both antennas, hence a positive covariance. In addition, a minimum ratio between the primary and secondary antenna and a minimum signal-to-noise ratio (SNR) is required. A detailed description of the algorithm and the discharge criteria is provided in Appendix A.

Using the algorithm, the total number of electrical discharges, the sum of measured voltage (V) and the maximum measured voltage of a single discharge (V) were computed for each explosive event. Summing all explosive events with the same plume height allowed us to calculate the average number of discharges and the average sum of measured voltage for each measured plume height. In addition, discharge rates (discharges/10 s) for each explosive event were calculated in overlapping time windows of 10 s with a step size of 0.01 s. We defined the period of electrical activity as the time between the first discharge and the last discharge prior to cessation of electrical activity for at least two minutes. In this manner, the total duration of electrical discharges was calculated.

2.3.5 Performance of detection algorithm

To determine the performance of the VL detection algorithm, a statistical classification was manually carried out by comparing the raw electrical signal of the sensors to the outcome of the algorithm. A detailed description is provided in Appendix B. To assess the overall performance, 550 time windows (one for each day within the time of monitoring) for which no explosions were reported, were evaluated in addition to the 724 explosion time windows. The analysed time windows were divided into four categories: True Positive (TP), True Negative (TN), False Positive (FP) and False Negative (FN). Consecutively, the overall accuracy, precision and recall of the algorithm were calculated (equations are given in Appendix B). Furthermore, the fraction of explosions that produced electrical discharges (prevalence), was calculated by only including the statistical results of the explosion time windows.

2.3.6 Data comparison

The JMA branch of Kagoshima (Fig. 1a) reports standard atmospheric parameters (T, P, RH%, wind speed and direction) through weather balloon profiles twice a day. Plume altitudes have been compared to the elevation of the isotherms 0 °C, -10 °C and -20 °C to account for potential ice nucleation in the plume. To ease reading, the isotherms were smoothed using a one-dimensional Gaussian filter with a standard deviation of 1σ.

We compared our lightning data to data from WWLLN and ENTLN. In two cases, electrical discharges were reported by WWLLN within a 20-km radius from Sakurajima at the time of an explosive event, in the absence of any meteorological thunderstorm. These discharges are denoted as VL. One VL flash was reported during event 222 and two more VL flashes during event 548, the explosion with the tallest plume at Minamidake in 2019. Also ENTLN detected one single discharge during event 548. The JMA reported sighting of VL for events 548 and 558.

2.4 Results

2.4.1 Detection algorithm

The outcome of the statistical classification is listed in Table B.2 of Appendix B. An accuracy of $\sim$73% indicates that the algorithm correctly identified the presence/absence of electrical discharges for a great portion of the analysed time windows. A few of the explosion time windows contained signals from meteorological lightning, which likely occurred outside the 100-km radius of Sakurajima as it was not reported by WWLLN. The discharges detected during the time windows without reported explosions, could be correlated to meteorological thunderstorms in most cases as well. False Positives were mainly the result of false signals deriving from the electronics powering both instruments, which in rare cases would meet the discharge criteria set by the algorithm. False Negatives were typically discharge-like signals with a very low SNR that were recorded simultaneously at both sensors, but remained undetected by the algorithm.

The precision of the algorithm is high ($\sim$90%) for both sensors, which shows that most of the signals detected by the algorithm are indeed electrical discharges. The probability of the algorithm to identify the discharges when present in the electrical signal, also called the "recall", is 56% and 67% for KUR and HAR, respectively.

The prevalence calculated for the explosion time windows alone, shows that KUR and HAR detected electrical discharges in 65% of the 486 and 69% of the 577 recorded explosions, respectively. Combining the two sensors, 511 out of the 724 recorded explosions (71%) produced electrical discharges. We will refer to these explosions as "electrically-active explosions". Note that electrified ash clouds passing over one of the sensors minutes after the explosion, resulted in a slow varying electrical signal at the antennas. The criteria of the algorithm allowed for the detection of VL that occurred within the charged ash cloud, while generally disregarding the slower oscillations of the charged ash cloud. For unknown reasons, however, in several charged plumes every individual oscillation was identified as a discharge by the algorithm, resulting in false detections. Therefore, only the TP detected explosions that showed no signal from ash passing over the sensors, giving the most accurate detection of electrical discharges, will be discussed in more detail. Explosions with unknown plume height were also disregarded.

2.4.2 Electrically-active explosions

Figure 2.2a shows the total number of electrical discharges detected by the algorithm for both KUR and HAR as a function of plume height. Overall, HAR detected more discharges than KUR. It is evident that HAR has a better response due to its closer position to Minamidake crater, which facilitated the identification of electrical discharges by the algorithm. For this reason, we focus only on the data of HAR in our efforts to discover interrelations between electrical activity and plume height. There appears to be an overall increase in the number of discharges with increasing plume height, but the correlation is weak. However, taking the average number of discharges for all explosive events with the same plume height, reveals a strong non-linear positive correlation between these two parameters (Figure 2.2b). This correlation has a Spearman's rank order correlation coefficient (in short: Spearman correlation) of rs = .74, p < .001 and N = 37, indicating that the correlation is strong and not due to chance.

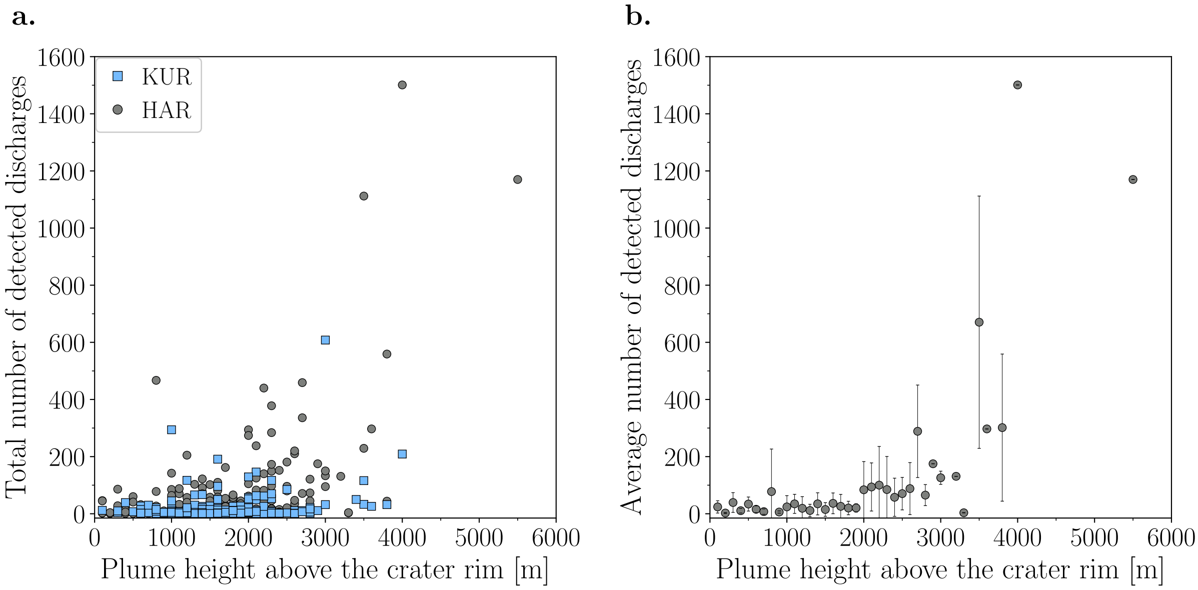

*Figure 2.2: **a)** The total number of discharges detected by the VL detection algorithm as a function of plume height [m a.c.r.] for both sensors. **b)** The average number of discharges calculated over all explosive events with the same plume height for HAR. The error bars indicate the standard deviation.*

A wide range of measured voltages could be observed in the electrically-active explosions, varying from 0.0001 to 0.5V per individual discharge. The average sum of measured voltage for all events with the same plume height shows a very strong non-linear positive correlation (Spearman correlation of rs = .95, p < .001, N = 37) with the average number of discharges for HAR (Figure 2.3a). Moreover, the total amount of measured voltage increases with increasing plume height. For explosions with a plume height <2000 m a.c.r., the amount of measured voltage per discharge is small, typically adding up to less than 0.075V. With increasing plume height (>2000 m a.c.r.), there is a gradual increase in both the total number of discharges (Figure 2.2) and the maximum measured voltage of a single discharge (Figure 2.3b).

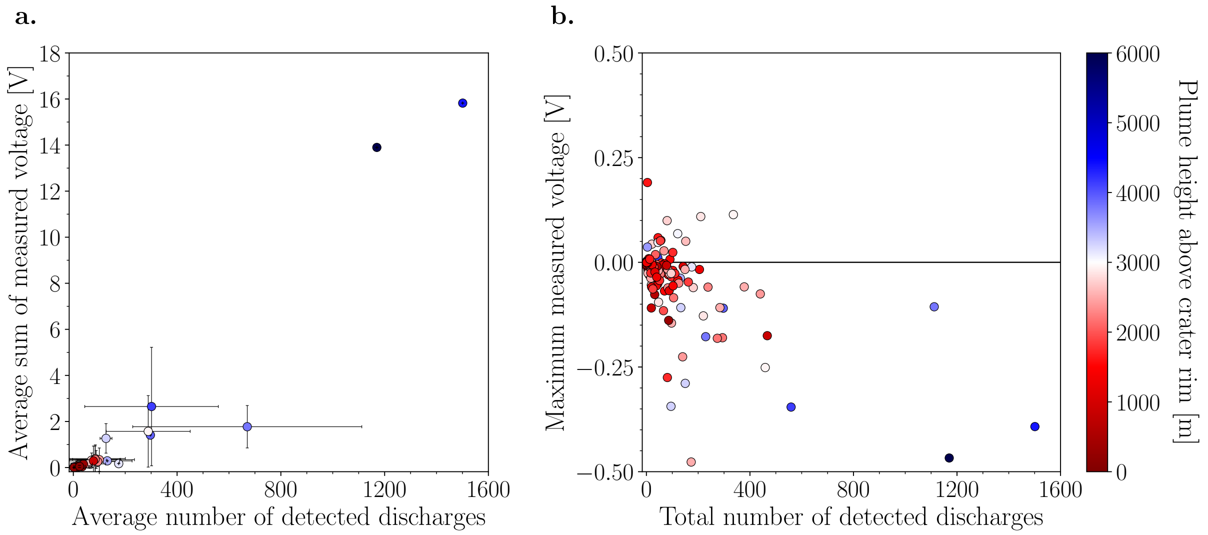

*Figure 2.3: **a)** Average sum of measured voltage (V) as a function of the average number of discharges for HAR. **b)** The maximum amount of measured voltage (V) produced by a single discharge as a function of the total number of discharges for HAR. The colours of the data points correspond to the plume height [m a.c.r.].*

The total duration of discharges varies from milliseconds up to several minutes. There is no apparent correlation with plume height. On the contrary, there is a moderate linear positive correlation between the maximum discharge rate (discharges/10 s) and the plume height (Figure 2.4), indicated by Pearson's correlation of r(279) = .48, p < .001. The discharge rate is generally highest shortly after the start of the explosion, but the observation of several maxima within a single explosion is not uncommon.

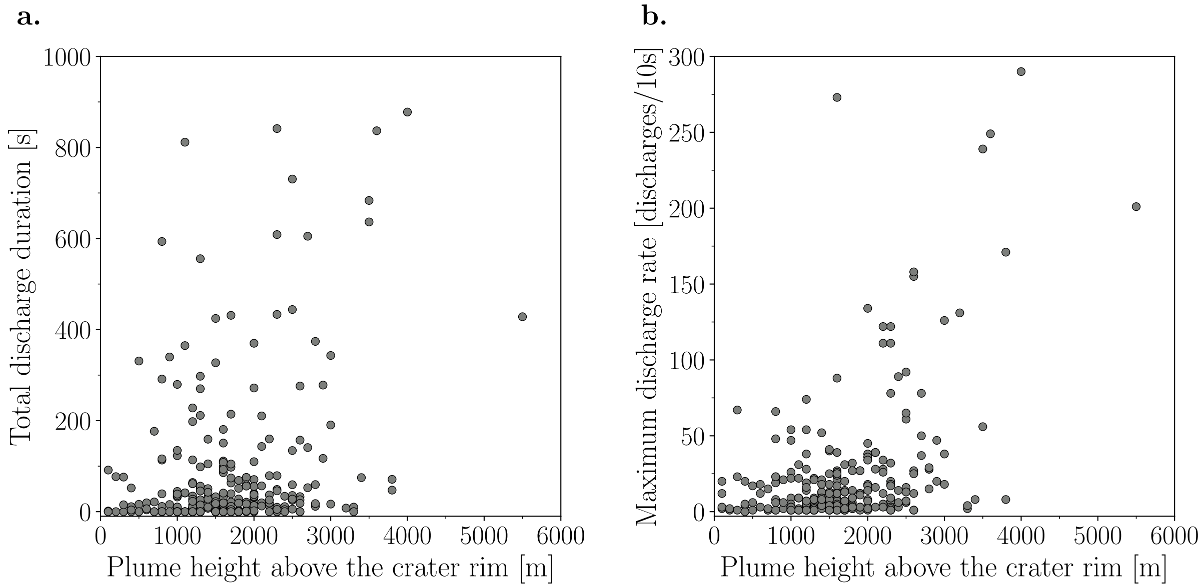

*Figure 2.4: **a)** The total discharge duration [s] and **b)** the maximum discharge rate [discharges/10 s] as a function of plume height [m a.c.r.] for HAR.*

In order to determine whether ice nucleation played an important role in plume electrification, the plume height of each explosion is correlated with different temperature regions (Figure 2.5). Most electrically-active plumes did not ascend above freezing level. Only 18% of the 724 recorded explosions ascended above the freezing level, of which 79% produced electrical discharges. Six explosions exceeded the -10 °C isotherm, with event 548 being the only one to ascend above the -20 °C isotherm. Table 2.1 gives approximate atmospheric T and RH% at the top of the ash plume, obtained from the JMA radiosondes, together with the total duration of discharges and maximum discharge rate for those six explosions. Each of these explosive events was electrically active, although the algorithm failed to detect discharges for event 713 presumably due to its extremely low amplitude signal.

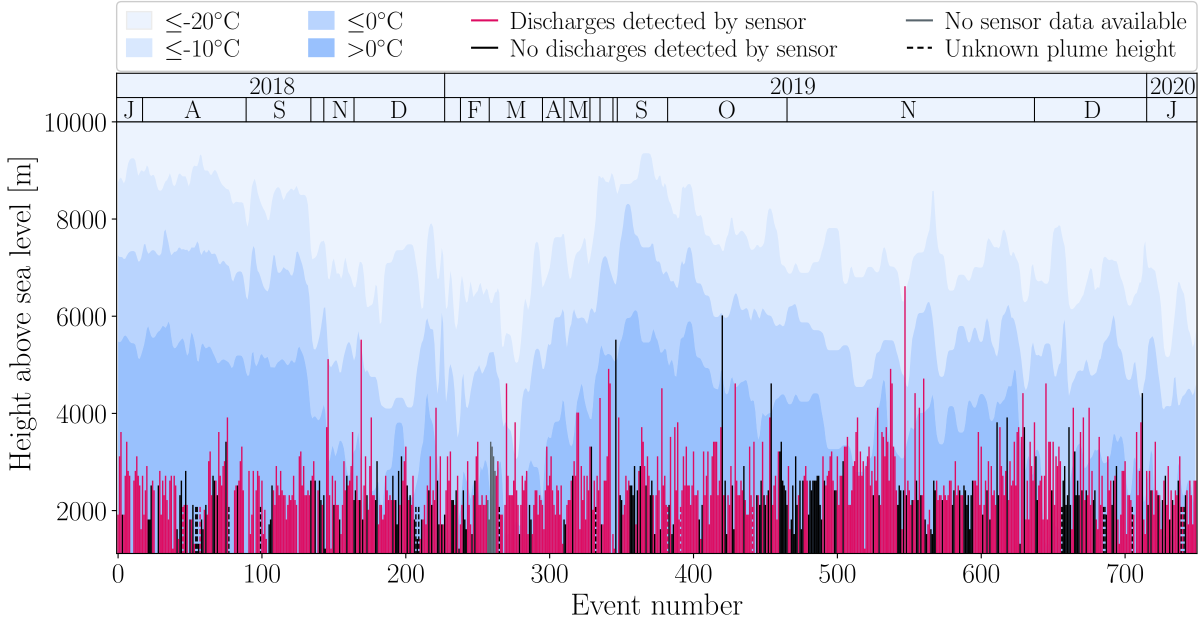

Figure 2.5: Different temperature regions (shades of blue) as a function of height above sea level. The temperature data has been smoothed using a one-dimensional Gaussian filter with a standard deviation of 1σ. The corresponding calendar months are denoted at the top of the figure with a single letter. Vertical lines indicate plume height for explosions at Minamidake during the observation period. Note that the plume heights are reported as metres a.c.r. (i.e. 1117 m a.s.l. for Minamidake). Red lines indicate electrically-active explosions recorded by at least one sensor. Black and grey lines indicate explosions that did not produce any electrical discharges and explosions with no associated sensor data, respectively. Dashed lines indicate explosions with unknown plume height to which an arbitrary value of 1000 m a.c.r. has been assigned. Gaps correspond to explosions that coincided with meteorological thunderstorms.

Table 2.1: Approximate atmospheric temperature [°C] and relative humidity [%] at the top of the ash plume, the total duration of discharges [s] and the maximum discharge rate [discharges/10s] for explosions exceeding the -10 °C isotherm.

Event Number	Plume height (m a.c.r.)	Atmospheric temperature, T (°C)	Atmospheric relative humidity, RH (%)	Total duration of discharges (s)	Maximum discharge rate (discharges/10 s)
237	1600	-12.2	94	88.70	91
277	2700	-11.8	100	26.27	6
713	3300	-10.3	2	N/A	N/A
271	3500	-15.2	94	27.33	19
147	4000	-17.5	11	877.85	290
548	5500	-21.4	8	428.22	201

N/A = Not available; discharges remained undetected by VL detection algorithm.

To further document the above findings, four case studies comprising 10 electrically-active explosions in total, will be discussed in more detail.

2.4.3 Case study 1: KUR versus HAR

This case study will describe the differences in electrical signal recorded by the two detectors. Figure 2.6 shows the electrical signal of event 324 detected by the primary and secondary antenna of KUR and HAR. In addition, the covariance between the primary and secondary signal for HAR is shown. Electrical discharges started 55 s after the JMA explosion onset, hence within the one-minute error margin, and lasted approximately 40 s. Each detected discharge has a positive covariance, as is required by the VL detection algorithm. The discharges recorded at HAR show measured voltages one order of magnitude higher than at KUR. Although throughout all the explosions the measured voltage is always higher at HAR, the ratio in measured voltage between HAR and KUR varies from zero to two orders of magnitude.

A second electrical signal is visible in the data of HAR approximately 8 min after the initial electrical discharges, while absent in the data of KUR (Figure 2.6). A large portion of this signal has a negative covariance, which is an indication of impact transients. The ash plume reached a maximum plume height of 1100 m a.c.r. The JMA weather balloons measured a southeast (161°) wind with a speed of 8 m/s at this altitude, less than half an hour after the explosion. Since the wind direction is typically constant over Sakurajima volcano, due to the orography of the peninsula and its surroundings, it is reasonable to believe the wind direction had not changed significantly within that time frame. This suggests that the ash plume was blown to the northwest, directly over sensor HAR. At this speed, it would take approximately 6 min for the ash to reach HAR at 2.8 km distance from Minamidake crater. Assuming the ash plume rose vertically before being dispersed by the wind, it is very plausible that this second signal is due to ash impacting sensor HAR. As KUR was installed on the east side of Minamidake crater, this signal is absent in the data of KUR (except for the single discharge that occurred within the charged ash cloud at 11:45:43 UTC). With reasonable certainty, based on wind direction and speed, similar observations could be made for 14 additional explosions at sensor HAR and for 8 explosions at sensor KUR.

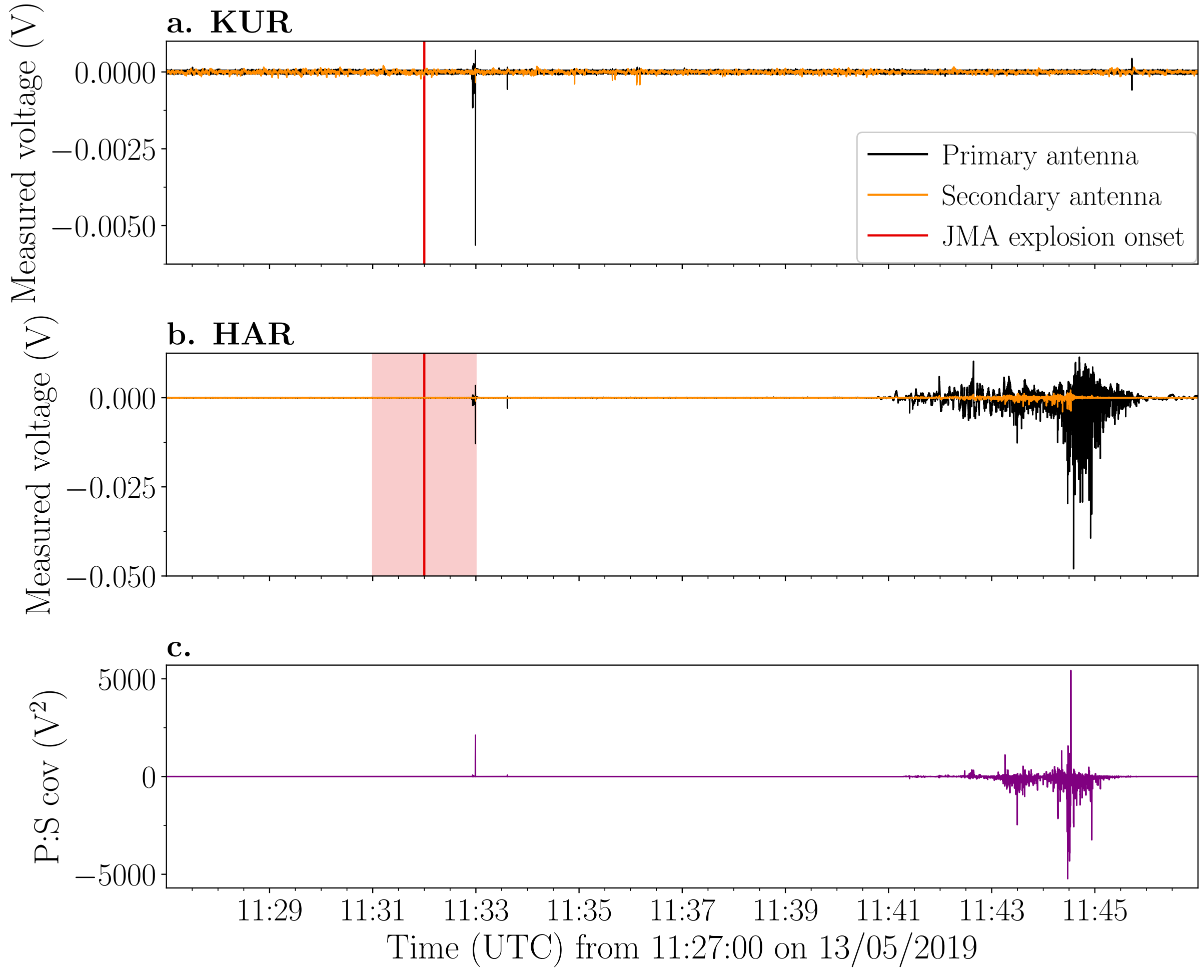

*Figure 2.6: Event 324 on 13 May 2019. The ash plume reached an altitude of 1100 m a.c.r. before it was blown in a northwest direction, passing over sensor HAR. Electrical discharges detected at **a)** KUR and **b)** HAR (note the different scale on the y-axes). The red vertical line indicates the JMA explosion onset with its associated error (±1 min; shaded area). **c)** The covariance (V^2) between the primary and secondary signal for HAR.*

2.4.4 Case study 2: small explosive events

Here, we demonstrate that our sensors were able to detect electrical signals even during some of the smallest explosive events at Minamidake crater. Event 520 had a plume height of 100 m a.c.r., whereas event 246 and event 412 both had a plume height of 600 m a.c.r. (Figure 2.7). Note that due to the extremely low SNR of event 412, the algorithm detected only 2 discharges. For events 246 and 520, the measured voltage is of the same order of magnitude for individual discharges, regardless of the difference in plume height. On the contrary, the electrical signal of event 412 is two orders of magnitude smaller than for event 246, even though the plume height is the same.

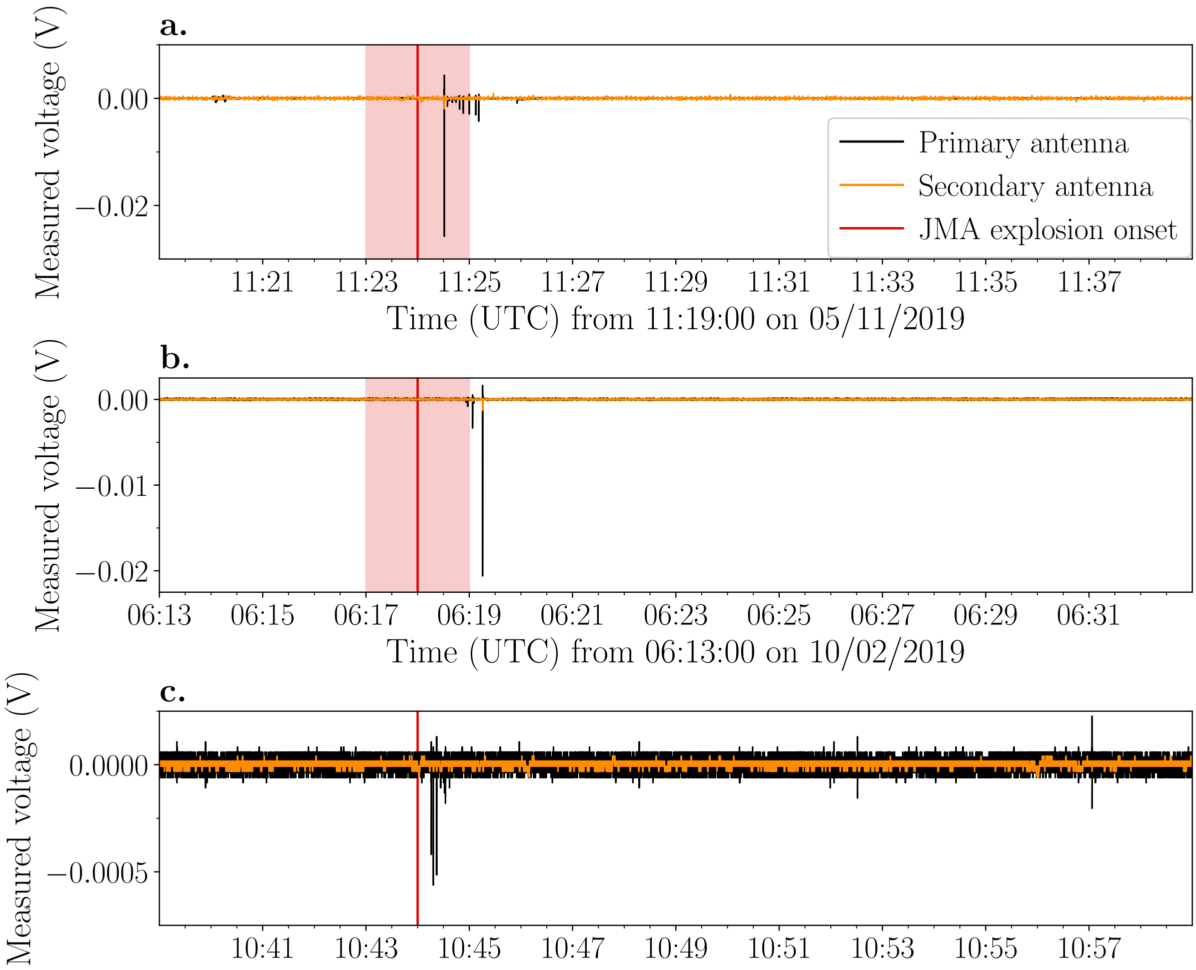

Figure 2.7: The measured voltage (V) of the primary and secondary antenna of KUR for ***a)*** *event 520, plume height of 100 m a.c.r.;* ***b)*** *event 246, plume height of 600 m a.c.r. and* ***c)*** *event 412, plume height of 600 m a.c.r. The red vertical line indicates the JMA explosion onset with its associated error (±1 min; shaded area).*

2.4.5 Case study 3: large explosive events

This case study focuses on the wide variation in electrical signals produced by relatively large explosive events at Minamidake. Events 128 and 561 had above average plume heights, 2100 and 3600 m a.c.r., respectively (Figures 2.8a and 2.8b). Event 548 was the largest explosive event at Minamidake in 2019 as well as in our dataset, reaching an altitude of 5500 m a.c.r. (Figure 2.8c).

In general, these larger explosive events show a significant higher number of discharges (Figure 2.2) as well as higher total measured voltage (Figure 2.3) and maximum discharge rate (Figure 2.4), although showing a certain variability among events. For instance, event 128 produced many discharges extended over a period of approximately 3.5 min (Figure 2.8a), but the measured voltage of each individual discharge had a similar order of magnitude as for the smaller events 246 and 520 of case study 2. On the contrary, event 561 had an initial phase of 11 s with a high discharge rate and a maximum measured voltage of twice the magnitude as event 128, followed by smaller individual discharges (Figure 2.8b). Event 548 has all three characteristics of a big explosion, producing many electrical discharges over a relatively long time period and measured voltages comparable to meteorological lightning detected by our sensors directly above Sakurajima volcano (located by WWLLN) (Figure 2.8c). At the start the discharge rate is high, but minutes after the explosion onset the discharges become less frequent while still producing a high measured voltage.

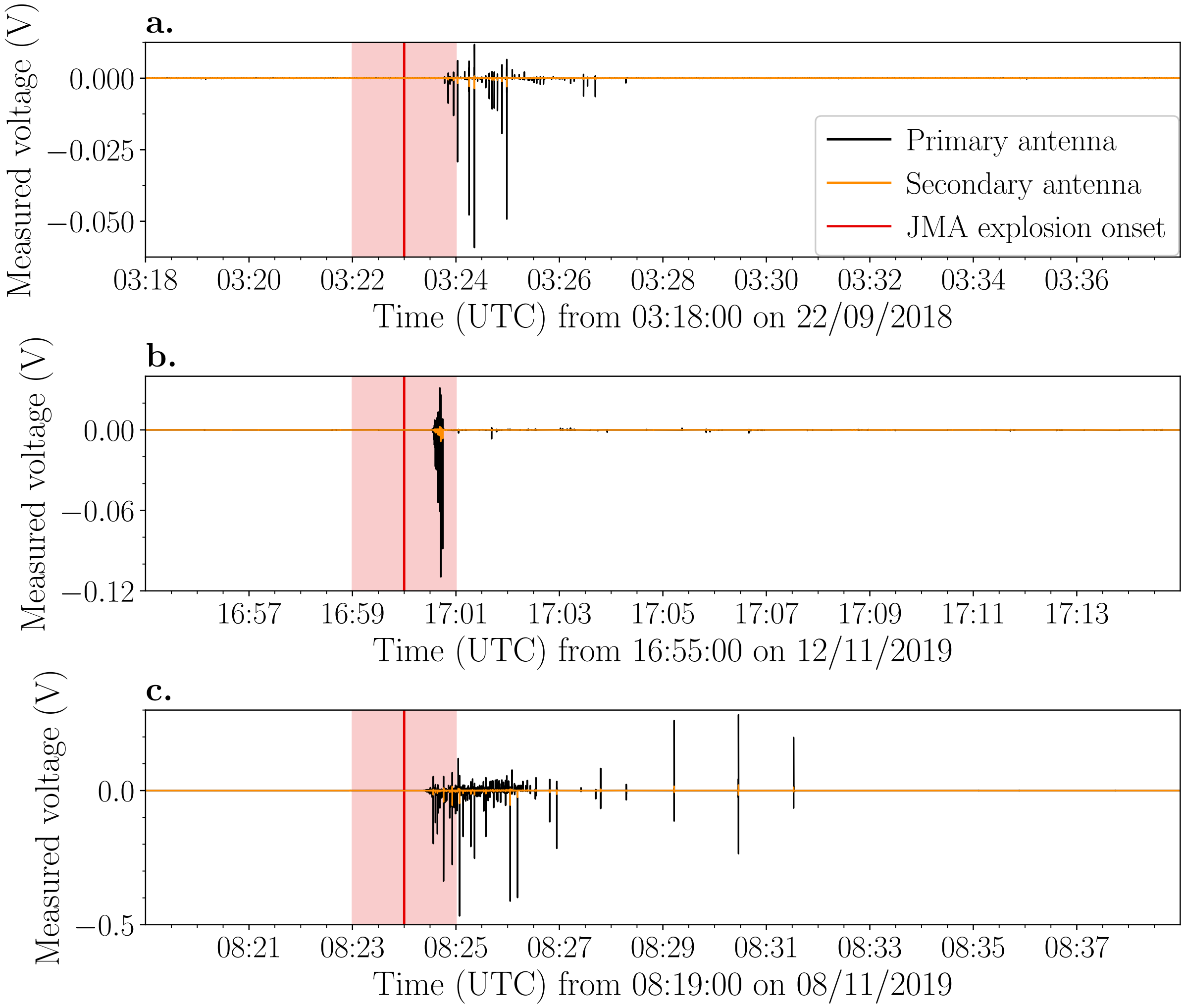

Figure 2.8: The measured voltage (V) of the primary and secondary antenna of HAR for ***a)*** *event 128, plume height of 2100 m a.c.r.;* ***b)*** *event 561, plume height of 3600 m a.c.r. and* ***c)*** *event 548, the biggest explosion of 2019 with a plume height of 5500 m a.c.r. The red vertical line indicates the JMA explosion onset with its associated error (±1 min; shaded area).*

2.4.6 Case study 4: timing of discharges

This case study discusses the timing of discharges with respect to the JMA explosion onset. In the previous case studies, discharges started within the error margin of the JMA explosion onset. This is also the case for event 397, where electrical discharges started 58 s after the JMA explosion onset (Figure 2.9a). However, two other phases of electrical activity can be observed, 3.5 min before and 10 min after the JMA explosion onset. These phases of electrical activity were likely caused by consecutive pulses of the same explosive event, since they occur within minutes of one another, yet only the pulse at 08:16:58 a.m. UTC was reported by the JMA.

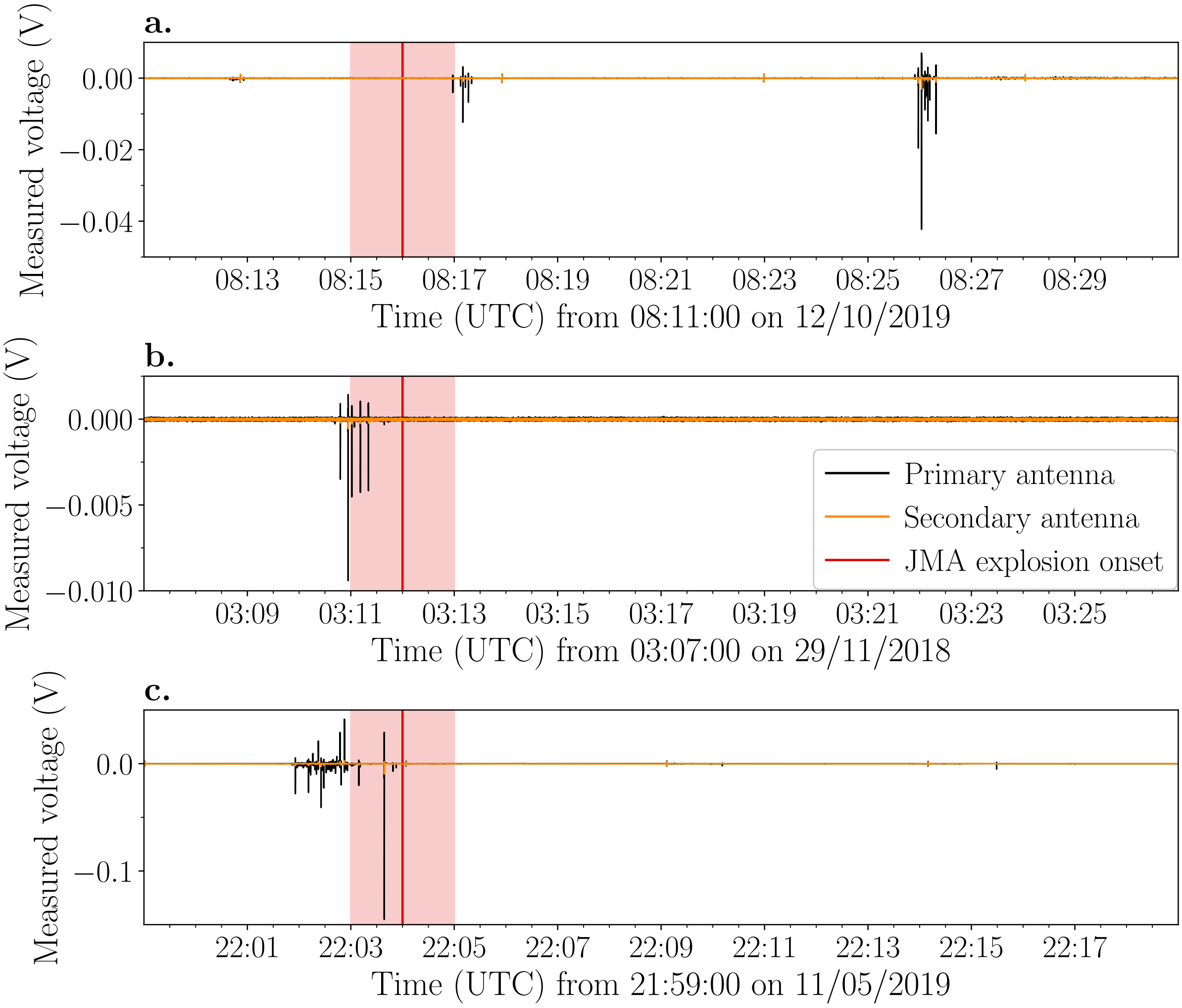

*Figure 2.9: The measured voltage (V) of the primary and secondary antenna of HAR for **a)** event 397, plume height of 1400 m a.c.r., showing three phases of electrical activity; **b)** event 162, plume height of 1500 m a.c.r., producing discharges 73 s before the JMA explosion onset; **c)** event 321, plume height of 2900 m a.c.r., producing discharges 125 s before the JMA explosion onset. The red vertical line indicates the JMA explosion onset and associated error (±1 min; shaded area).*

Importantly, for 12% of all electrically-active explosions the electrical discharges started more than a minute before the JMA explosion onset. The offset of the JMA explosion onset could be the result of a delayed observation of ash due to the Minamidake vents being nested approximately 600 m below the crater rim (Figure 2.1a). Since the electric field lines bend around the conductor, in this case the earth, our electrostatic sensors can detect discharges below the crater rim, without needing a direct line of sight (Tzur et al., 1985). This enables pinpointing the inception of the explosion with a higher precision. This likely was the case for event 162, where discharges started 73 s before the JMA explosion onset (Figure 2.9b). Another explanation for the offset could be that the initial pulse was not reported, as was the case for event 397 (Figure 2.9a). For event 320, discharges were detected 125 s before the JMA explosion onset (Figure 2.9c). Note that there is a small break in electrical activity of approximately 18 s. This pause of activity might indicate two closely followed pulses, of which only the second (possibly larger) pulse was reported by the JMA.

2.5 Discussion

2.5.1 Thunderstorm detector

The electrostatic thunderstorm detectors presented here, have proven effective in detecting discharges at Minamidake, regardless of plume height (Figures 2.5 and 2.7). Not only was the fraction of electrically-active explosions significantly higher than reported by ENTLN and WWLLN, the sensors also detected a higher total number of discharges for events 222 and 548 compared to these networks. These results show that global thunderstorm networks may be inadequate in detecting smaller ash-rich eruptions due to the scattered geographical distribution of their sensors.

The time delay between the onset of the explosion and the first visual detection of volcanic ash calls for a monitoring method that can immediately identify ash emission without requiring visibility on the crater. It has been demonstrated here that electrostatic monitoring at active volcanoes can be used as an ash early warning system. Assuming that discharges coincided with the start of the explosions, the sample rate of the sensors enabled the timing of the inception of the explosion with a higher precision than the JMA one-minute time resolution observation (Figures 2.6-2.9). Early detection, as demonstrated in Figures 2.9b and 2.9c, might be crucial in the event of a large explosion threatening the local population or air traffic. Moreover, the electrical signal recorded by the sensors can give additional information on the course of the explosion. Consecutive pulses within a single explosion, while commonly not reported by the JMA, could be distinguished based on fluctuations in the discharge rate and renewed electrical activity (Figures 2.9a and 2.9c). Further, charged ash clouds and ash fall were clearly visible in the data (Figure 2.6), which might yield important information for ash nowcasting. These results show the capability of our detectors for the long-term electrical monitoring of active volcanoes. Combining current detection systems, such as seismic measurements, with our observations could be decisive in future in interpreting the signal as an ash-rich explosion.

2.5.2 Detection algorithm

The high accuracy and precision of the algorithm indicate its adequacy for identifying the presence/absence of discharges (Table B.2 of Appendix B). Although the thresholds used to detect discharges depend on the distance from the active vent, the local noise level and the magnitude of the explosions, this algorithm can be fine-tuned easily and is thus almost certainly suitable for other active volcanoes as well.

KUR was situated in a less remote area and 1 km further away from the active vent than HAR. At frequencies $<$100 Hz, Pierce (1955) showed that the electrostatic field magnitude dominates over the induction and electromagnetic components for distances $<$100 km. In this case, the electric field decreases proportional to the distance cubed from the discharge location, since an elevated point charge forms a vertical charged dipole due to the image effect of the conducting ground (Wilson, 1921; Bennett and Harrison, 2013). This effect resulted in an overall lower measured voltage at KUR compared to HAR (Figure 2.6). In addition, the location of KUR amounted to a lower SNR, complicating the discrimination of discharges from noise. This led to a higher number of False Negatives and thus a lower recall than for sensor HAR (Table B.2 of Appendix B). Hence, both a close proximity to the vent and a remote location are preferred to optimise the detection of discharges.

2.5.3 Type of volcanic lightning

Most explosions with a plume height $<$2000 m a.c.r. only produced discharges with individual measured voltages of 0.0001-0.1V. In comparison to the measured voltages of $>$0.1V produced by meteorological lightning that occurred directly above Sakurajima volcano (located by WWLLN), these VL flashes are 1-3 orders of magnitude smaller. In contrast, explosions with a plume height $>$2000 m a.c.r. showed an increase in the maximum measured voltage of individual discharges. The largest discharges produced measured voltages between 0.1-0.5V, similar to thunderstorm lightning detected above Sakurajima. The differences in measured voltage suggest that larger explosive events tend to produce discharges that neutralise more charge, and are possibly longer in length, compared to smaller explosions. During these larger explosions, the increase in the amount of material being ejected enhances the amount of plume electrification. For fully developed ash plumes, more extensive charge regions are expected to exist, which produce correspondingly larger but often less frequent flashes owing to the greater amount of charge neutralised by each flash. This electrical behaviour was observed during several large explosive events (Figure 2.8c).

Additional information on where the VL occurred in the plume (Thomas et al., 2010), together with the duration and the length of the flashes, would be needed to identify the type of VL. Nevertheless, we speculate that the detected discharges are most likely near-vent VL, considering the timing of the discharges relative to the explosion onset and the short-lived and impulsive eruptive dynamic of the volcanic explosions that generated them.

2.5.4 Electrification mechanisms

Although previous studies have generated much knowledge about plume electrification processes (e.g. James et al., 2000; Gaudin and Cimarelli, 2019; Prata et al., 2020), it remains difficult to determine the relative contributions of each process. McNutt and Williams (2010) found no latitudinal dependence in VL, indicating that the water content of the erupting magma is more important in the generation of VL than the entrainment of meteorological water. Sekine et al. (1979) estimated the initial magma water content of Sakurajima volcano to be 3–6 wt.%. This is likely greater than the water concentrations of typical meteorological thunderstorms (Williams and McNutt, 2005), suggesting that there is abundant water in the ash plume for ice to nucleate if sufficient altitudes are reached. All six explosions that exceeded the -10 °C isotherm (Figure 2.5) produced electrical discharges, although for event 713 the measured voltage was too low to be detected by the algorithm (Table 2.1). The temperature at the top of this particular ash plume only reached approximately -10.3 °C, suggesting that this temperature is too low to make ice nucleation a determinant factor of plume electrification, which is consistent with the findings of Durant et al. (2008). Explosions without any electrical activity, even after reaching sufficient altitudes for ice nucleation to occur, might also be the result of too short-lived ash emissions (Van Eaton et al., 2020) or weak updrafts, for example during ash venting (Cole et al., 2014), resulting in insufficient formation of charged clusters (Behnke et al., 2013).

Minutes-long electrical activity was detected for events 147 and 548 (Table 2.1). The initial phase of high discharge rate is likely the result of intense fracto- and tribo-electrification in the gas-thrust and convective regions of the plume. Discharges that occurred minutes after the explosion onset when the plume had reached its maximum height, might be a result of both tribo-electrification and ice nucleation, especially for event 548 which exceeded the -20 °C isotherm (Figures 2.5 and 2.8c). The atmospheric RH% at the top of these ash plumes was very low according to JMA atmospheric profiles (Table 2.1). If ice nucleation indeed played a role here, it would be consistent with the findings of McNutt and Williams (2010) that the water content of the erupting magma is more important than the entrainment of meteorological water in the generation of VL. The timescale of electrical activity, however, makes the extent of ice nucleation as a contributing factor questionable. Although it is feasible that volcanic ice nuclei became activated several minutes after the start of the explosion, Van Eaton et al. (2020) found that sufficient charge build up through ice-ash particle collisions and gravitational settling required sustained plumes on a time scale of tens of minutes or hours rather than the minutes of electrical activity detected for these explosions. This is leading us to infer that although ice nucleation likely occurred, it did not play a major role.

The remaining three explosions had electrical activity comparable to explosions that did not reach these altitudes, both in total duration of discharges and maximum discharge rate (Table 2.1). Since the total duration of discharges lasted less than two minutes after the explosion onset, it is improbable that ice nucleation was one of the main drivers for plume electrification. For the other explosions that did exceed the atmospheric freezing level but not the -10 °C isotherm, it is unlikely that ice nucleation was involved. At those temperatures, only a small amount of volcanic ice nuclei might have become activated (Durant et al., 2008), but not enough to make a significant contribution to the plume electrification. These findings suggest that fracto- and triboelectrification are the prime mechanisms of plume electrification for moderate Vulcanian explosions as those observed at Sakurajima.

2.5.5 Correlations between plume height and electrical activity

Plume height can be a representation of the magnitude of the eruption. However, since the JMA provides plume height measurements at 100 m resolution and no wind correction has been applied, there is some uncertainty in the plume heights presented here. This should be considered when correlating it with electrical activity. Besides the atmospheric wind regime, the maximum plume height is dependent on several conditions at the vent, of which the mass eruption rate (MER) is the most important (Settle, 1978; Wilson et al., 1978). Plume height is positively correlated to MER (Settle, 1978). A higher MER also means more triboelectrification (Cimarelli et al., 2014; Méndez Harper and Dufek, 2016). This could explain the non-linear positive correlation that we observed for both the total number of electrical discharges and the sum of measured voltage with increasing plume height (Figures 2.2 and 2.3). Behnke et al. (2013) found a similar correlation for explosive events with higher plume heights (>5 km a.c.r.). Albeit the evident correlation, the electrical activity detected during this study can only give an estimate of the plume height so far. Correcting the plume heights for wind, increasing the number of sensors at different distances from Minamidake crater and deploying our sensors at other active volcanoes, are measures planned for improving this estimate in future.

Similar to Bennett et al. (2010) and Behnke et al. (2014), we found an increase in the maximum discharge rate with increasing plume height (Figure 2.4b), which additionally could be the result of an increase in MER. However, Hargie et al. (2019) found that changes in discharge rate throughout a single explosion cannot be explained by MER itself. Behnke et al. (2014) suggested that increases in discharge rate during a single explosion could be the result of either intensified vent charging due to an increase in source flux or enhanced plume electrification due to ice nucleation after reaching sufficient altitudes. Since ice nucleation does not play a role during most explosions at Minamidake crater, the changes in discharge rate must be controlled by the fluctuations in the acceleration/deceleration of the particles (Cimarelli et al., 2014; Hargie et al., 2019). A period of no or decreased electrical activity is observed in between consecutive pulses (Figure 2.9). A new pulse would create a relative increase in MER (Scharff et al., 2008), producing renewed electrical activity. The total duration of discharges would then depend on how long the acceleration of the particles lasts. This predominantly influences the generation of near-vent VL, which could explain the lack of correlation between the total duration of electrical discharges and plume height (Figure 2.4a).

2.6 Conclusion

We present a novel, long-term and data-efficient method to monitor relatively small ash-rich eruptions at active volcanoes using extremely low frequency thunderstorm detectors. To test this approach, we continuously monitored the persistent Vulcanian activity at Minamidake crater of Sakurajima volcano in Japan for 1.5 yr. The sensors successfully detected in situ electrical discharges during 511 out of 724 events, independent of plume height, compared to only 1 and 2 events detected by ENTLN and WWLLN, respectively.

Monitoring of the electrical activity enables the recording of the start of the explosion with a higher precision than the one-minute time resolution provided by the JMA. For 12% of the electrically-active explosions this implied that the inception occurred more than a minute before the JMA explosion onset, which can be explained by a delayed visual observation of ash by the JMA or an unreported first pulse. In addition, the electrical signal can yield information on the number of consecutive pulses, ash cloud directions and ash fall.

A volcanic lightning detection algorithm was developed to identify discharges. The total number of electrical discharges, the sum of measured voltage and the maximum electrical discharge rate increase overall with increasing plume height, likely due to an increase in MER. Fluctuations in the electrical discharge rate within a single explosive event might be controlled by particle accelerations/decelerations. Fracto- and tribo-electrification appear to be the dominant plume electrification mechanisms. Even for the explosive events that reached sufficient altitudes, the timescale of electrical activity (minutes) is most likely too short for ice nucleation to play a role as an electrification mechanism.

Our results show the capability of our detectors in pinpointing the inception of electrified explosive episodes in near real-time and in providing indications on the magnitude of the explosions, thus making them a cost- and data-efficient instrumentation for the long-term monitoring of explosive ash emissions at active volcanoes.

Chapter 3

The electrical signature of mafic explosive eruptions at Stromboli volcano, Italy

3.1 Abstract

Volcanic lightning is commonly observed in explosive volcanic eruptions of Volcanic Explosivity Index (VEI) > 2 and can be detected remotely providing real-time volcano monitoring information. However, little is known about the electrical activity accompanying the lower-magnitude spectrum of explosive eruptions, often involving mafic magmas. We narrow this gap in knowledge by presenting the electrical signature of the explosive activity (VEI ≤ 1) of Stromboli volcano (Italy) recorded by an electrostatic thunderstorm detector. The persistent eruptive activity of mild Strombolian explosions is occasionally interrupted by larger-scale major explosions and paroxysmal events.

Here, we present electrical observations of three major explosions and unprecedented measurements of the 3 July 2019 paroxysm. The electrical signals of the major explosions show apparent similarities, with movements of charge and tens of electrical discharges, arising the question of whether these observations could be used to supplement the classification scheme of explosions on Stromboli. The electrical signals from the 3 July 2019 paroxysm exceed those from the major explosions in amplitude, discharge rate, and complexity, showing characteristic variations during different phases of the eruption.

These results show that also impulsive lower-magnitude explosions generate detectable electrical activity, which holds promise for monitoring low VEI activity at mafic volcanoes.

3.2 Introduction

3.2.1 Electrical activity and lightning in volcanic plumes

Explosive volcanic eruptions generate changes in the electric field and volcanic lightning (Cimarelli and Genareau, 2021). An important component of plume electrification is the presence of silicate particles, which are considered the main carrier of electrical charge in volcanic jets and plumes. Upon explosion, the fragmentation of magma into pyroclasts (Dickinson et al., 1988; James et al., 2000) (fragments of silicate melts) and their subsequent collisions (Lacks and Levandovsky, 2007; Cimarelli et al., 2014; Gaudin and Cimarelli, 2019) generate high electrical charge in the expanding volcanic jets. Under specific conditions, also ice nucleation/riming (Arason et al., 2011; Van Eaton et al., 2020), interaction with (sea)water (Björnsson et al., 1967; Büttner et al., 1997; James et al., 2008) and, to a lesser extent, natural radioactivity (Clement and Harrison, 1992; Nicoll et al., 2019) may contribute to plume electrification. Besides these external effects, the distribution of charges in the evolving plume creates the conditions for electrical discharges to occur (Cimarelli and Genareau, 2021).

Volcanic plume electrification and lightning is commonly observed at volcanoes characterized by a Volcanic Explosivity Index (VEI) > 2, therefore being generally associated with intermediate to high-silica magma compositions (McNutt and Williams, 2010; Cimarelli and Genareau, 2021). The occurrence of volcanic lightning during explosive eruptions of basaltic composition was reported for a wide range of plume heights (1-21 km), although considerably fewer reports were found for eruptions of VEI ≤ 1 (Houghton et al., 2013), such as Strombolian explosions (McNutt and Williams, 2010). Albeit experiencing brittle fragmentation (Taddeucci et al., 2021), the reduced ability of such magmas to produce lightning activity is generally attributed to the low viscosity and high temperature of low-silica magmas which promotes outgassing and gas-magma decoupling, often resulting in effusive eruptions or mild explosions (Colombier et al., 2021). However, specific processes, such as molten fuel-coolant interaction (MFCI) (Büttner et al., 1997; Büttner and Zimanowski, 1998), the combination of strong magma foaming and geometrical obstructions (Papale, 1999), the obstruction of the conduit through talus accumulation (Calvari et al., 2006) or the presence of a magma plug, can result in enhanced explosivity and consequently generate more volcanic lightning.

High-temperature experiments have investigated the production of electrical signals of basaltic magma upon fragmentation (Büttner et al., 1997, 2000). The experiments indicate that formation of new surface area and subsequent particle cloud expansion generate charge separation, which can be detected on a short timescale as an electrostatic field gradient. Electrostatic field gradients comparable to those measured in the experiments were detected during mild Strombolian explosions (Büttner et al., 2000; Calvari et al., 2012). Additionally, an electric potential gradient accompanied by electrical discharges was recorded during an ash-rich major explosion on 7 September 2008 (Calvari et al., 2012).

To further increase our knowledge of electrical activity accompanying basaltic eruptions, we carried out long-term electrostatic field measurements on Stromboli volcano, Italy.

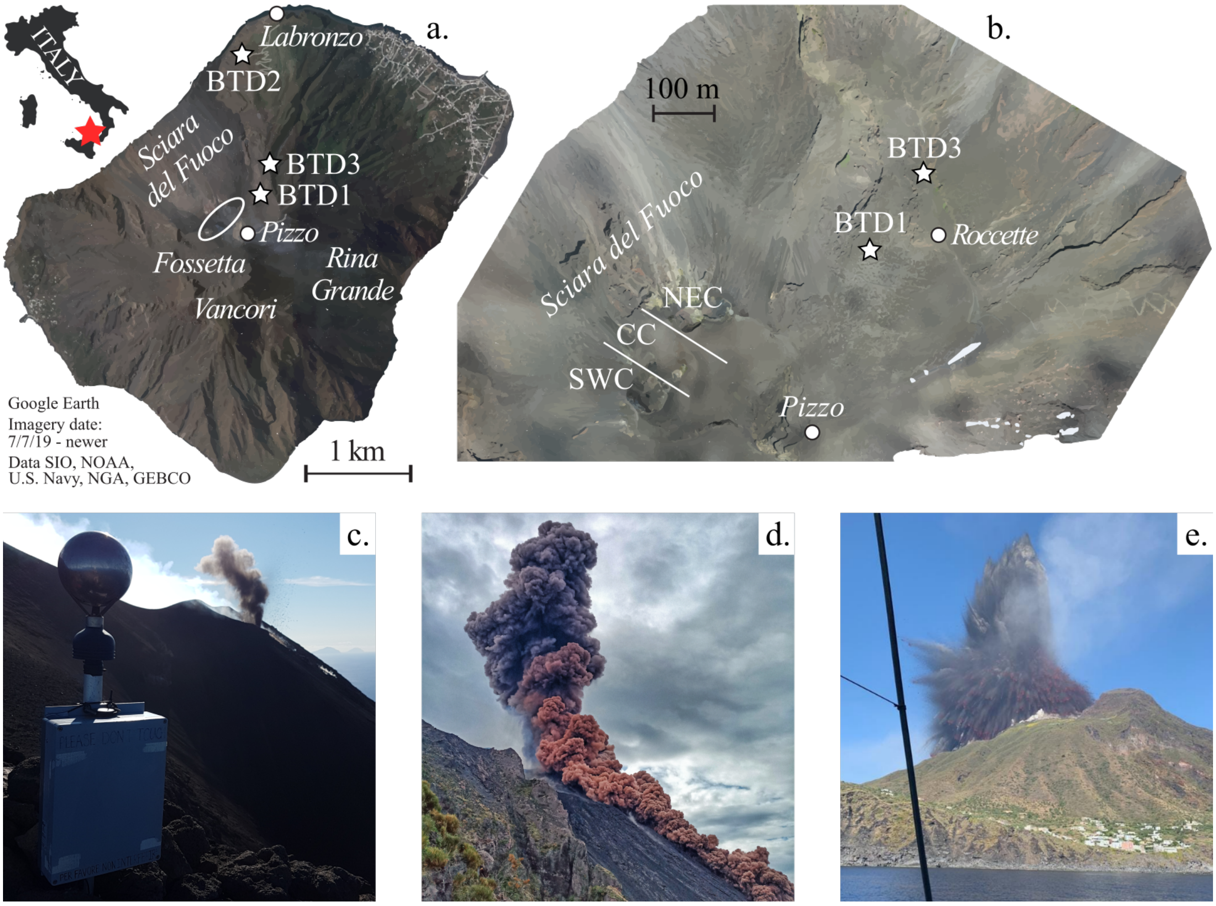

*Figure 3.1: **a)** Map of Italy (Inset), showing the location of Stromboli island (red star), together with a satellite image from Google Earth (Imagery date: 7/7/2019 – newer. Data SIO, NOAA, U.S. Navy, NGA, GEBCO. http://www.earth.google.com [2 June 2021]). The location of the crater terrace (780 m a.s.l., encircled in white), the three succeeding locations of the sensor (BTD1, BTD2 and BTD3, star symbols), and important localities (Pizzo (918 m a.s.l.), Vancori (924 m a.s.l.), Punta Labronzo, Sciara del Fuoco, Rina Grande and Fossetta) are indicated. **b)** Drone image of the crater terrace, showing the Northeast Crater (NEC), Central Crater (CC) and Southwest Crater (SWC) zones, and the locations of BTD1 and BTD3 close to Roccette. The drone flight was carried out in June 2019 (Schmid et al., 2021). **c)** BTD3 installed close to Roccette on 9 October 2020. A Strombolian explosion (type 2b; Gaudin et al., 2017a) from the NEC zone is visible in the background. **d)** Photograph of the 16 November 2020 major explosion. Courtesy of Adriano Di Pietro. **e)** Photograph of the 3 July 2019 paroxysm taken from a sailing boat. Courtesy of Francesco Rinauro.*

3.2.2 Study area

Stromboli volcano is well known for its persistent mild explosive activity since historic times (Rosi et al., 2000) for which it is also referred to as “the lighthouse of the Mediterranean” (Figure 3.1a). Although the number of active vents changes frequently, the crater terrace of Stromboli consists of three main crater zones, the Northeast (NE), Central (C) and Southwest (SW) crater zones (Figure 3.1a-b) (Rosi et al., 2013). Due to its constant explosive conditions, Stromboli is closely monitored by permanent geophysical networks of the Laboratorio di Geofisica Sperimentale (LGS) of the University of Florence and the Istituto Nazionale di Geofisica e Vulcanologia (INGV) including seismometers, an infrasonic array, tiltmeters, dilatometers and visible and thermal cameras.

3.2.3 Volcanic activity at Stromboli

Stromboli is characterized by continuous active degassing (puffing) alternated with mild explosions (VEI ranging from -6 to -3, Houghton et al., 2013, 2016) that episodically eject variable proportions of volcanic ash and incandescent ballistic particles to heights of tens to hundreds of metres every few minutes (Mercalli, 1907; Taddeucci et al., 2013). This Strombolian activity, also referred to as “normal activity”, is fed by a degassed, highly crystallised, high porphyritic (HP) magma of basaltic composition stored in the shallow ($<$ 2 km depth) plumbing system (Métrich et al., 2001, 2005; Francalanci et al., 2008; Bertagnini et al., 2011). The normal activity is occasionally interrupted by lavas flowing down the Sciara del Fuoco as well as major explosions (VEI ranging from -3 to 0, Houghton et al., 2016) and paroxysmal events (VEI = 0-1, Houghton et al., 2013, 2016).

Major explosions occur on average twice per year (Barberi, 1993; Rosi et al., 2013) (Figure 3.1d). During these eruptions, multiple vents of one or more craters simultaneously eject decimetre-sized ballistic blocks and bombs within a distance of hundreds of metres from the crater terrace (Bertagnini et al., 2008; Gurioli et al., 2013). The plumes are short-lived and can reach up to one kilometre height above the crater rim (Bertagnini et al., 2008). The subsequent fallout of ash and light-lapilli is typically restricted to the slopes of the volcano. The deposits commonly consist only of HP magma.

Paroxysms occur on average once every 5-15 years (Barberi, 1993; Rosi et al., 2013) (Figure 3.1e). They are similar to major explosions, but larger in magnitude, more violent and often accompanied by pyroclastic flows (Rosi et al., 2013; Giudicepietro et al., 2020). Paroxysms occur when deep (7-10 km depth) volatile-rich, crystal-poor, low porphyritic (LP) magma of basaltic composition rapidly ascends to the surface, increasing the pressure either due to bubble growth upon decompression or the accompanying rise of a gas slug (Métrich et al., 2001, 2005; Francalanci et al., 2008; Bertagnini et al., 2011). Deposits from the 1930, 2003 and 2007 paroxysms consist of golden-coloured pumices, products of the LP magma, mixed with black scoriae, products of the HP magma, indicating that the two magmas mingled shortly before and during the eruption (Métrich et al., 2001, 2005; Francalanci et al., 2008; Bertagnini et al., 2011). Typically all active vents are involved from which metre-sized ballistic scoria bombs and blocks are ejected up to several kilometres from the crater terrace (Bertagnini et al., 2008; Rosi et al., 2013; Andronico et al., 2021). The convective plume rises to several ($>$3-4) kilometres in height, followed by tephra fallout beyond the coastline (Bertagnini et al., 2008; Rosi et al., 2013; Giudicepietro et al., 2020; Andronico et al., 2021).

Here, we present the electrical signals recorded during three selected major explosions within 1.5 years, and the 3 July 2019 paroxysmal event. Although volcanic lightning was reported during the 15 March 2007 paroxysm (Pistolesi et al., 2011), it has never been measured during one of the paroxysmal events at Stromboli until now.

3.3 Methods

3.3.1 Instrumentation

To detect electrical discharges in situ, a prototype of the Biral Thunderstorm Detector BTD-200 was used. The detector consists of two antennas, which detect slow variations in the electrostatic field resulting from charge neutralisation due to electrical discharges (Bennett, 2017; Von der Linden et al., 2021). The primary antenna has the highest sensitivity, while correlation and decorrelation with the secondary antenna allow for the discrimination between electrical discharges and impact transients (ash falling or charged precipitation) on the antenna (Bennett, 2017; Von der Linden et al., 2021), respectively. The sensor measures within the extremely to super low frequency range (1-45 Hz) at a sample rate of 100 Hz and has been modified to allow for GPS time synchronisation and several months of data storage (Vossen et al., 2021).

The first detector, BTD1, was installed on Stromboli on 11 June 2019 and was operational for three weeks. The related data set allows for distinguishing eruptive activity of different intensities and different phases of the paroxysm. The sensor was installed northeast from the crater terrace, at a distance of 292 m from the NE and 469 m from the SW crater zone, respectively, and at an altitude of 774 m (Figure 3.1a-b). Although BTD1 did not get damaged during the 3 July 2019 paroxysm (as well as the 28 August 2019 paroxysm), hot ballistics destroyed the power system, effectively cutting off power and stopping the recording 45 seconds after the onset of the paroxysm.

Due to the apparent volcanic hazard after the 2019 paroxysms, access was restricted to an altitude of 290 m a.s.l. A new detector, BTD2, was installed on 22 September 2019 at an altitude of 190 m a.s.l. at the edge of the Sciara del Fuoco near Punta Labronzo, at a distance ranging between 1.55-1.71 km from the craters (Figure 3.1a-b).

As the intensity of the electric field decreases proportional to the distance cubed (Wilson, 1921; Bennett and Harrison, 2013), a closer location of the instrument to the craters was preferable but unavailable in September 2019 due to access restrictions. On 9 October 2020, BTD2 was relocated close to Roccette at a distance ranging between 425-616 m from each crater zone and at an altitude of 798 m, and was renamed BTD3 (Figure 3.1a-b). At the time of writing, BTD3 is still up and recording continuously (Figure 3.1c).

3.3.2 Data processing

The analogue raw voltage output from the antennas is converted to a digital voltage (V) used for calculation by the internal processors. Note that the resulting voltage is not the actual voltage of the electrical discharge, but rather a signal proportional to the current induced by the atmospheric electric field change associated with an electrical discharge. This depends on the distance of the sensor and the height at which the discharge occurs. In general, charge movement will produce a relatively slow-varying electrical signal, while electrical discharges produce a sharp transient. Electrical discharges were identified using an adjusted version of the volcanic lightning detection algorithm used at Sakurajima volcano, Japan (Vossen et al., 2021). Signals were interpreted as electrical discharges based on the following empirical thresholds: i) The signal needed to have the same polarity at both antennas (positive covariance); ii) The positive covariance is ≥ 0.5; iii) The ratio between the two antenna signals is >3.0; iv) The signal-to-noise ratio (SNR) is >2.0 and >1.1 for the primary and secondary antenna, respectively.

The covariance was calculated over a moving window of 16 samples (step size of 1 sample), while the noise was calculated over a moving window of 128 samples (step size of 1 sample). Albeit the good accuracy of the algorithm (Vossen et al., 2021), the low SNR of the secondary signal led to the omission of electrical discharges at certain times. On the other hand, attenuation of the transient caused by an electrical discharge and oscillations in the electrical signal occasionally met all criteria of the algorithm, resulting in wrongly interpreted discharges. These small inaccuracies were manually corrected.

For each explosion, the total number of discharges and the maximum discharge rate per 5 seconds, with a step size of 1 second, were determined. Also, the total duration of electrical activity was calculated. As it may take time for the remaining charge to dissipate after the explosion, the last discharge is used to mark the end of the electrical activity.

To compare the magnitude of the different explosions, the peak voltage of the charge movement detected by the sensor shortly after the explosion, needed to be corrected for the distance cubed between the sensor and the active crater (Wilson, 1921; Bennett and Harrison, 2013). This provided an estimate of the magnitude of the initial charge moved at the active crater during the each explosion. Similar to the measured voltage of the discharges, this value is proportional to the current induced by the atmospheric electric field change.

These electrical measurements are compared to several eruption parameters, including acoustic pressure, maximum particle ejection velocity, plume height above the crater rim (a.c.r.) and eruption duration.

3.4 Results

More than 40 Strombolian explosions of varying types (1, 2a and 2b according to the classification scheme proposed by Gaudin et al., 2017a) were recorded on 11 and 12 June 2019 by BTD1. An example of each type is shown in Figure C.1 of Appendix C (Vossen and Cimarelli, 2022). During most of these explosions, the primary antenna recorded slow ($\sim$1-3 s) electrostatic variations, which are caused by movements of charge due to the ejection of pyroclasts. Some of the ash-rich explosions additionally showed transient-like signals, which correspond to small discharges following the explosions. Although the results indicate that these explosions produce faint detectable electrical signals, the wide variety of explosions (regarding the size of pyroclasts, ejection velocity and bulk volume) impedes our understanding of the origin of these signals and requires a more thorough analysis. For this reason, the rest of this study will only focus on the electrical activity produced by the larger explosions at Stromboli.

The sensor recorded a major explosion at each location: the 25 June 2019 major explosion (BTD1), the 19 July 2020 major explosion (BTD2) and the 16 November 2020 major explosion (BTD3) (Vossen and Cimarelli, 2022). Additionally, BTD1 recorded the 3 July 2019 paroxysm (Figure 3.1e) (Vossen and Cimarelli, 2022). Detailed information on each explosion was gathered, inter alia, from the weekly monitoring bulletins provided by INGV on www.ct.ingv.it and LGS on http://lgs.geo.unifi.it/ (Table 3.1).

Table 3.1: Eruption parameters and electrical measurements for the 25 June 2019, 19 July 2020 and 16 November 2020 major explosions and the 3 July 2019 paroxysm

	Major explosion 25 June 2019	Major explosion 19 July 2020	Major explosion 16 November 2020	Paroxysm 3 July 2019
Onset time (UTC)	23:03:08 [3]	03:00:42 03:01:11 03:01:28 [4]	09:17:45 [5]	14:45:43 14:45:53 [7]
Active crater zone	CC [3]	CC, SWC [4]	NEC, CC, SWC [1]	SWC, NEC [7]
Acoustic pressure (Pa)	170 [6]	>1500 [9]	562 [8]	N/A
Maximum particle ejection velocity (m/s)	54.41 [1]	78.22 [1]	54.51 [1]	101.92 [1]
Plume height a.c.r. (m)	$\sim$500 [1]	>750 [1]	1000 [5]	8400 [2]
Explosion duration (s)	8 [1]	58 [1]	54 [1]	160[1]
Onset of electrical activity (UTC)	23:03:08.08	03:00:42.8	09:17:44.87	14:45:43.63
Time until last discharge (s)	7.32	68.2	13.13	>44.74
Number of discharges	37	80	49	>321
Maximum discharge rate (discharges/5 seconds)	24	20	33	49
Distance between active crater(s) - sensor (m)	403	1556-1649	425-616	292
Peak value of charge movement at sensor (V)	0.0012	0.00065	0.033	0.023
Peak value of charge movement at active crater (V)	$7.85\text{x}10^{4}$	$2.45\text{x}10^{6}$- $2.91\text{x}10^{6}$	$2.53\text{x}10^{6}$- $7.71\text{x}10^{6}$	$5.73\text{x}10^{5}$

N/A = Not available. [1]*Calvari et al. (2021);* [2]*Giordano and De Astis (2021);* [3,4,5]*Istituto Nazionale di Geofisica e Vulcanologia (2019, 2020a,b);* [6,7,8,9]*Laboratorio Geofisica Sperimentale (2019a,b, 2020a,b)*

3.4.1 The 25 June 2019 major explosion

INGV reported a major explosion on 25 June 2019 at 23:03:08 UTC (Istituto Nazionale di Geofisica e Vulcanologia, 2019). At 23:03:08.08 UTC (Table 3.1), BTD1 recorded a positive variation in charge, which changed polarity one second later (Figure 3.2a). This was followed by small electrical discharges shortly after (Figure 3.2a), which is evident by the positive covariance (Figure 3.2b). Approximately 7.3 seconds after the explosion onset, the last discharge was detected, which had a measured voltage an order of magnitude higher than the preceding ones. The electrical signal returned to pre-explosion background levels in about 48 seconds. The entire electrical perturbation caused by the eruption lasted 54 seconds.

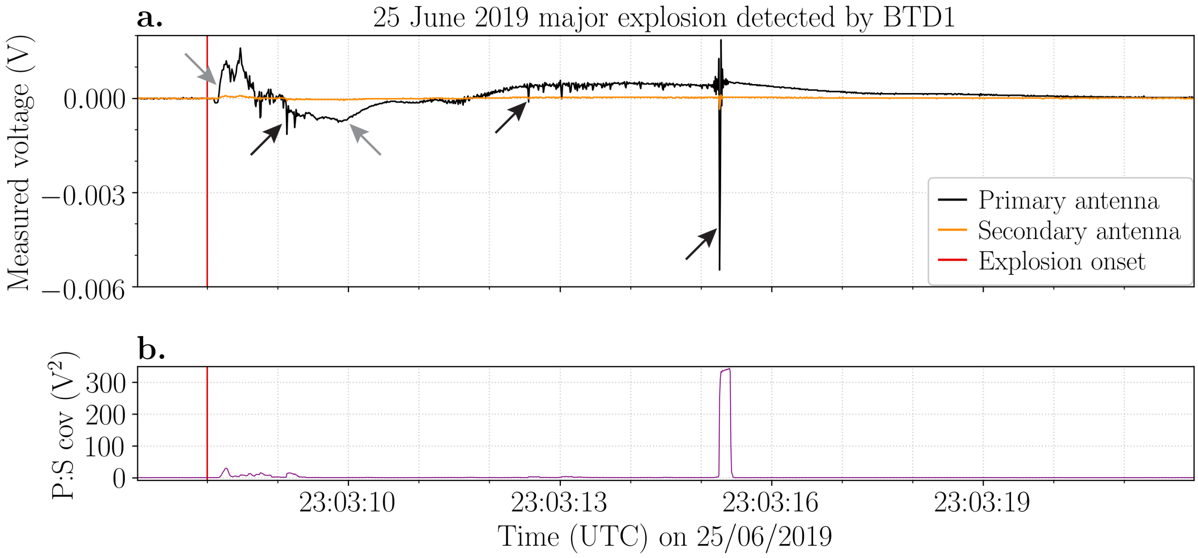

Figure 3.2: Electrical data of the 25 June 2019 major explosion recorded by BTD1. ***a)*** *Voltage (V) measured by the primary (black line) and secondary (orange line) antennas. Examples of movement of charge and electrical discharges are indicated by the grey and black arrows, respectively.* ***b)*** *The covariance (V^2) between the primary and secondary signals. The red vertical line indicates the explosion onset.*

3.4.2 The 19 July 2020 major explosion

Even though BTD2 was installed at a much greater distance from the crater terrace, it successfully detected the electrical activity generated by the 19 July 2020 major explosion. The explosion onset was estimated at 03:00:42 UTC based on images from the INGV monitoring cameras (Istituto Nazionale di Geofisica e Vulcanologia, 2020a). A positive charge variation was detected at 03:00:43.8 UTC (Table 3.1), promptly followed by small electrical discharges (Figure 3.3a-b). Several discharges with higher measured voltages were detected approximately 5 seconds later. At 03:01:11 UTC a second explosion occurred, accompanied by a new movement of charge, although of slightly lower magnitude than the one associated with the first explosion. A third explosion occurred at 03:01:28 UTC, but no clear electrical signal was detected at this point. In total, these three explosions lasted 58 seconds (Calvari et al., 2021).

However, INGV reported that this phase was followed by several smaller explosions (Istituto Nazionale di Geofisica e Vulcanologia, 2020a), which likely explains the three discharges detected at around 03:01:52 UTC. Afterwards, the electrical signal continued to vary for several minutes.

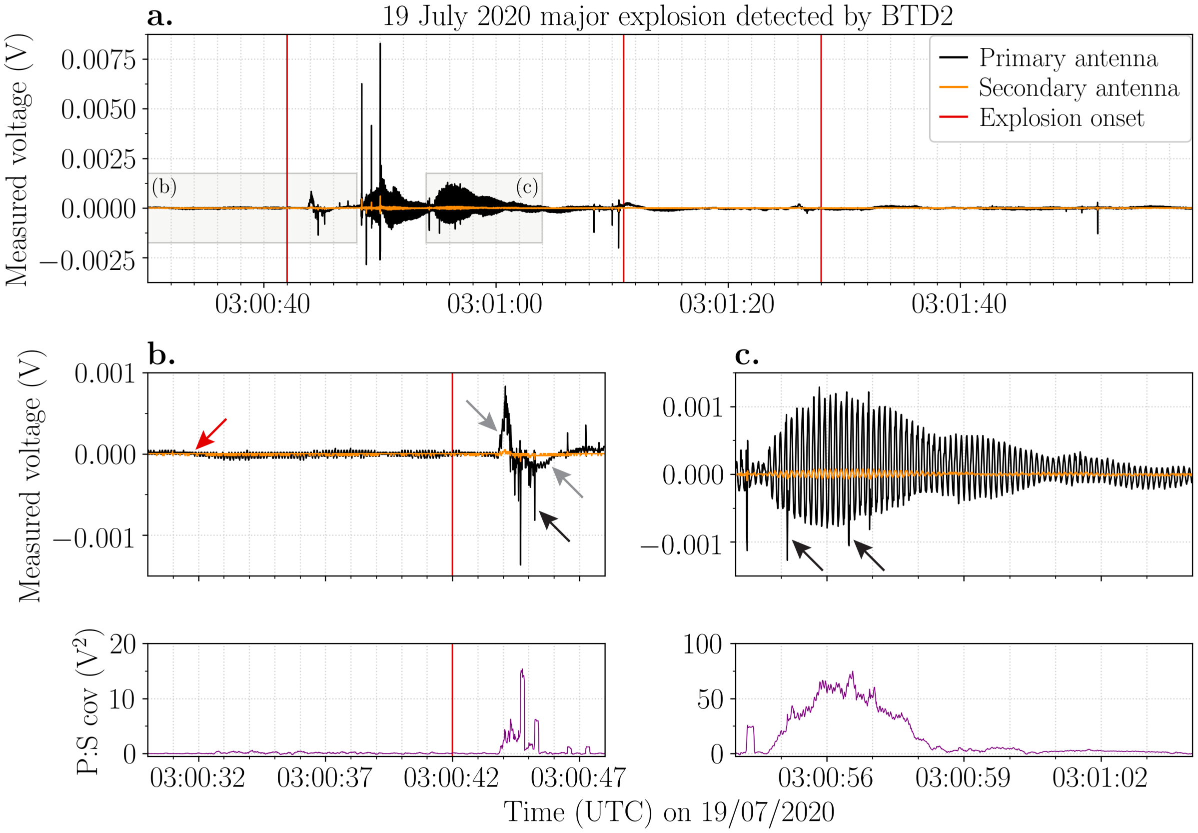

Figure 3.3: Voltage (V) measured by the primary (black line) and secondary (orange line) antennas of BTD2 during the 19 July 2020 major explosion. ***a)*** *Electrical signal detected during three separate explosions (red vertical lines) at 03:00:42 UTC, 03:01:11 UTC and 03:01:28 UTC.* ***b)*** *An oscillating electrostatic signal starts approximately 10 s before the explosion onset (red arrow). Shortly after the onset, movement of charge (grey arrows) and electrical discharges (black arrows) were detected.* ***c)*** *The amplitude of the oscillation is correlated to the magnitude of the charge variation. Electrical discharges are superimposed on the oscillations (black arrows). The corresponding covariance (V^2) between the primary and secondary signals is shown below for panels* ***b*** *and* ***c****.*

In addition to detecting electrical discharges and movement of charge, an oscillating signal with a frequency of 8-9 Hz was observed in both the primary and secondary antenna time-series for the whole eruption (Figure 3.3). This oscillating signal started at 03:00:31.7 UTC (Figure 3.3b), approximately 10 seconds before the explosion onset and shows time correlation with the first peak in seismicity recorded by the LGS seismic network (Figure C.2 of Appendix C). The signal amplitude correlates positively with the magnitude of charge variation (Figure 3.3c), while electrical discharges are superimposed.

3.4.3 The 16 November 2020 major explosion

The 16 November 2020 major explosion produced an electrical signal similar to the 25 June 2019 explosion (Figure 3.4a). Movement of charge was detected at 09:17:44.87 UTC (Figure 3.4b), which corresponds well to the estimated explosion onset at 09:17:45 UTC (Istituto Nazionale di Geofisica e Vulcanologia, 2020b) (Table 3.1). Electrical discharges started to occur almost simultaneously but decreased in frequency and magnitude 2 seconds later (Figure 3.4b). Approximately 13 seconds after the eruption onset, a single electrical discharge occurred, with a measured voltage about one order of magnitude higher than the preceding discharges (Figure 3.4a).

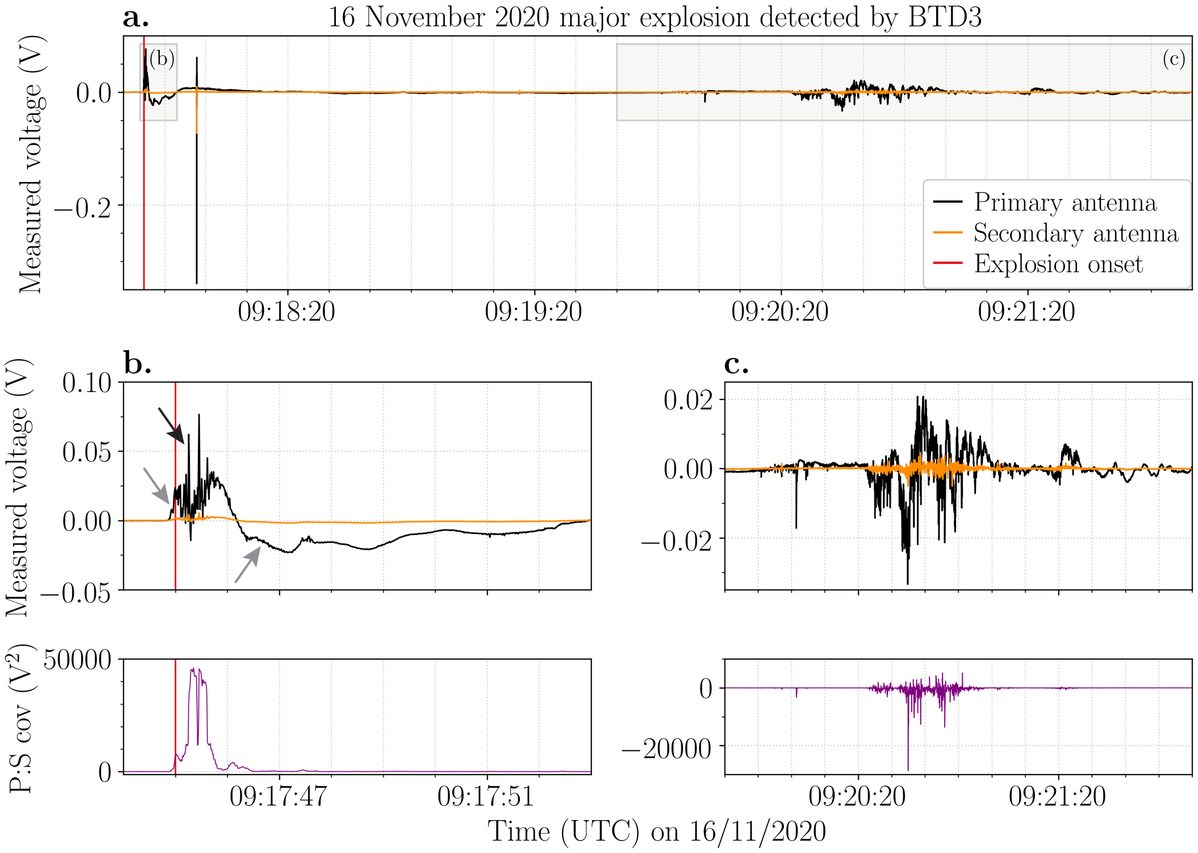

Figure 3.4: ***a)*** *Voltage (V) measured by the primary (black line) and secondary (orange line) antennas of BTD3 during the 16 November 2020 major explosion. The red vertical line indicates the explosion onset.* ***b)*** *Movement of charge (grey arrows) and electrical discharges (black arrow) were detected almost immediately at the start of the explosion. The corresponding covariance (V^2) between the primary and secondary signals is shown below.* ***c)*** *Electrical signal likely caused by ash impact transients as confirmed by the corresponding negative covariance (below).*

At 09:20:00 UTC an electrical signal with dominantly negative covariance values was recorded (Figure 3.4c), indicating impact transients. INGV published images from monitoring cameras showing a pyroclastic density current (PDC) flowing down the Sciara del Fuoco seconds after the onset (Istituto Nazionale di Geofisica e Vulcanologia, 2020b). Subsequently, both the ash plume caused by the explosion and the ash cloud produced by the PDC seem to move in a west-southwest direction. This is confirmed by weather data obtained from station LICT at Trapani Airport (Sicily, Italy) provided by the University of Wyoming, Department of Atmospheric Science (http://weather.uwyo.edu/). At 12:00 UTC the wind direction varied between 220° and 270° at heights ranging from sea level to the maximum height of the ash plume (1000 m a.c.r., Table 3.1). Hence, it is probable that ash fell at BTD3, producing a signal of opposite polarity at the two antennas.

Note that the peak change in charge and the measured voltages of the electrical discharges produced by the 16 November 2020 major explosion are in general 1-2 orders of magnitude higher than those produced by the 25 June 2019 major explosion, even though BTD3 was located further away from the active craters with respect to BTD1.

3.4.4 The 3 July 2019 paroxysm

A paroxysmal event occurred on 3 July 2019 (Figure 3.1e). Although a posteriori analysis indicated heightened CO2 emissions months before the paroxysm (Aiuppa et al., 2021), no clear precursory signals were detected by INGV and LGS at the time of the eruption. Both institutes classified the volcanic activity in the week preceding the paroxysm as “moderate”.

Preceded by lava extruding from all vents, the paroxysm started with a localised explosion at 14:45:43 UTC at the SW crater zone and was followed by a second explosion at 14:45:53 UTC at the NE crater zone (Laboratorio Geofisica Sperimentale, 2019b). Dm-sized ballistics started falling close to Roccette 7 seconds after the start of the explosion, lasting for at least 7 seconds (Giordano and De Astis, 2021). This was based on images taken by the Skyline webcam located at Roccette, approximately 100 m further away from the crater terrace than BTD1. Pictures of the eruption column initially suggested a plume height of 5 km above the summit of the volcano, but it was later estimated that the umbrella cloud reached a height of 9180 m a.s.l. (Giordano and De Astis, 2021). The latter agrees with the observation of the Volcanic Ash Advisory Center (VAAC) Toulouse, which reported the presence of ash at flight level FL300. A flash of volcanic lightning is visible in the top part of the convective plume in a video taken offshore by a witness. Portions of the eruption column and the crater terrace outer rim collapsed, forming at least two PDCs down the Sciara del Fuoco, which reached the sea at 14:46:29 UTC and 14:46:39 UTC, respectively, based on the LGS monitoring camera at Punta Labronzo (Laboratorio Geofisica Sperimentale, 2019b). They continued to travel for approximately 1 km beyond the coastline.

The BTD1 remained visibly unscathed during the eruption, providing us with unprecedented electrical observations of the paroxysm. The paroxysm lasted 160 seconds (Calvari et al., 2021) (Table 3.1), of which BTD1 recorded 45.35 seconds. The electrical activity generated by this event was much more intense compared to the previously discussed major explosions. Four phases of electrical activity can be distinguished (Figure 3.5):

1) A slow varying electrostatic signal started at 14:45:43.63 UTC (Figure 3.5b, Table 3.1), which corresponds to the moment incandescent lava fragments emerged from the SWC zone and expanded radially (Figure 3.1e), based on the images of the INGV thermal cameras at Pizzo

(Behncke, 2019). Within a second, small irregular electrical variations were detected, followed by the first electrical discharge at 14:45:44.85 UTC. Electrical discharges became more frequent after 14:45:50 UTC.

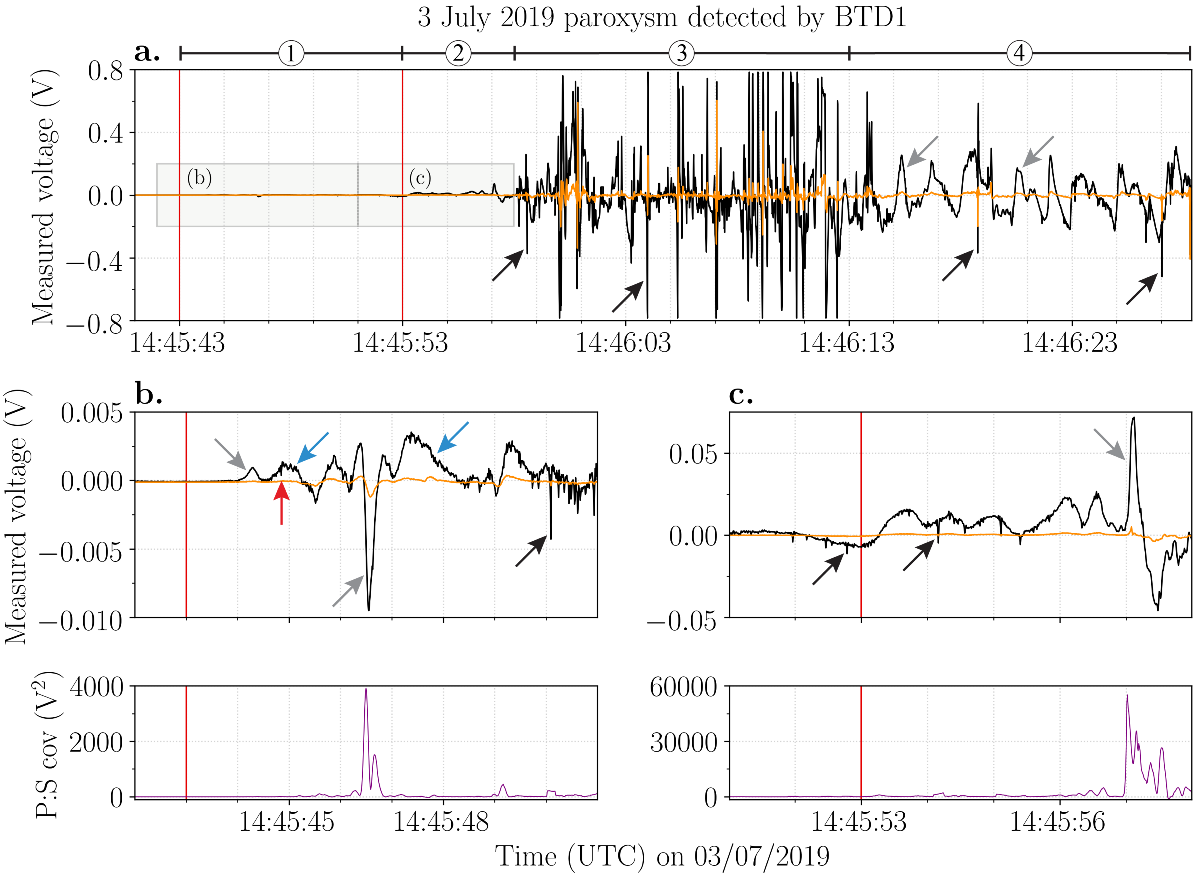

Figure 3.5: Voltage (V) measured by the primary (black line) and secondary (orange line) antennas of BTD1 during the 3 July 2019 paroxysm. The red vertical lines pinpoint two separate explosions at 14:45:43 and 14:45:53 UTC, respectively. Examples of movement of charge and electrical discharges are indicated by the grey and black arrows, respectively. ***a)*** *The entire electrical signal of the paroxysm until the power cut. Four different phases (1-4) of electrical activity can be distinguished.* ***b)*** *The electrical signal recorded during the first explosion. The red arrow marks the first electrical discharge and the blue arrows mark small irregular variations in the electrical signal likely caused by pyroclasts moving towards BTD1.* ***c)*** *The electrical signals recorded during the second explosion with their corresponding covariance (V^2). Note the different scale on the y-axis of each panel.*

2) After the second explosion at 14:45:53 UTC, both the magnitude of charge being moved and of the electrical discharges increased by more than one order (Figure 3.5c). The peak charge change detected directly after the first explosion was approximately 0.0009V, which increased by more than 25 times (0.023V) immediately after the second explosion. We need to consider, however, that the second explosion occurred at the NEC zone, 177 m closer to BTD1 than the first explosion from the SWC zone. The difference in distance accounts for an increase in mag-

nitude of approximately four times, indicating that the change in magnitude is not solely due to the shorter distance. Note that during the two explosions, higher peak values were reached, but to compare it to the major explosions, we took the initial movement of charge caused by the explosion.

3) At 14:45:58 UTC, the electrical activity evolves into a high-intensity phase. Here, the measured voltages of the electrical discharges caused the primary antenna to saturate, meaning their measured voltage exceeded 0.78V (Figure 3.5a).

4) This is followed by an abrupt change in signal around 14:46:13 UTC, with mostly low voltage discharges (occasionally interrupted by a larger discharge) and a relatively slow varying, high magnitude movement of charge (Figure 3.5a). This signal continued until the power was cut off approximately 15 seconds later.

3.5 Discussion

To our knowledge, none of the global thunderstorm networks recorded any volcanic lightning during the three major explosions and paroxysmal event discussed here. On the contrary, our thunderstorm detector was able to detect many electrical discharges and strong movements of charge, regardless of its position on Stromboli. These results show that sufficient charging occurs during the fragmentation of hot basaltic magma to result in volcanic lightning.

3.5.1 Major explosions

The similarities between the electrical signals of the three major explosions are evident (Figure 3.2, 3.3 and 3.4), especially for the 25 June 2019 and 16 November 2020 events. The ejection of the gas-particle mixture and consequent expansion of the jet produced a strong movement of charge, which was promptly detected by the sensors at the start of each explosion. This shows that electrical signals could be valuable in pinpointing the start of the explosions. The accompanied plume electrification resulted in many discharges of low measured voltage almost immediately after the onset. Subsequently, the movement of charge reversed polarity due to the rapid movement of charged gases and particles during the initial burst. These signals are comparable to the signal detected during the 7 September 2008 major explosion (Calvari et al., 2021). This could indicate a self-similar dynamic of such explosions where the mechanism of fragmentation, particle ejection velocity and erupted mass are alike.

The single electrical discharge detected seconds after the start of the 25 June 2019 and 16 November 2020 major explosions likely occurred to neutralise most of the remaining charge and therefore had a higher measured voltage than the previous discharges. The 19 July 2020 major explosion produced more of these high voltage discharges. The first two main explosions of the 19 July 2020 paroxysm generated a movement of charge that was detected by BTD2 (Figure 3.3a). Istituto Nazionale di Geofisica e Vulcanologia (2020a) reported that the second and third explosions were less intense than the first. This observation fits with the electrical data. The magnitude of the charge change detected during the second explosion is lower than the first, while no electrical activity was detected at all during the third explosion (Figure 3.3a). A possible explanation for the absence of electrical activity could be that the sensor was not able to detect the weak change in charge generated by the third explosion at such a great distance from the craters. Note, however, that a small movement of charge was detected at 03:01:26 UTC (Figure 3.3a). As images from monitoring cameras sometimes make it difficult to pick the exact explosion onset, it could be possible that this is the true onset of the third explosion.

Although the maximum particle ejection velocities of the 25 June 2019 and 16 November 2020 major explosions were almost equivalent, the explosion duration was longer and the plume height was twice as high for the latter (Calvari et al., 2021) (Table 3.1). This suggests a higher intensity, also evident from the higher acoustic pressure, and a greater erupted mass for the 16 November 2020 explosion, which would result in stronger plume electrification. This scenario agrees with our results, as both the measured voltages of the electrical discharges and the corrected peak charge variation were 1-2 orders of magnitude higher during the 16 November 2020 explosion (Figure 3.2 and 3.3). Also the number of discharges, the maximum discharge rate and the duration of electrical activity were higher (Table 3.1). The number of discharges, as well as the duration of electrical activity, were highest for the 19 July 2020 explosion. This is not surprising, as this eruption consisted of multiple ejection pulses over several minutes instead of a single explosion. Each pulse would generate renewed electrification by ejecting new material. Even though the maximum particle ejection velocity was highest for the 19 July 2020 explosion, the maximum discharge rate was lower than for the other two explosions. These results suggest that the eruptive mass and the total duration of the explosion play a more important role in the generation of electrical activity than the maximum particle ejection velocity.

There is some debate about whether the 19 July 2020 explosion should be classified as a major explosion or a paroxysmal event. Calvari et al. (2021) combined volcanological and geophysical monitoring data with remote sensing techniques to classify explosions of variable intensity. They classified the 19 July 2020 explosion as a paroxysmal event based on two parameters, the Very Long Period (VLP) size (Giudicepietro et al., 2020) and the power of explosive activity (VD parameter Calvari et al., 2021). On the other hand, Istituto Nazionale di Geofisica e Vulcanologia (2020a) and Laboratorio Geofisica Sperimentale (2020b) classified it as a major explosion, based on the magnitude of several geophysical parameters (seismicity, deformation and acoustic pressure) as well as the dispersion of pyroclasts restricted to the slopes of the volcano. Moreover, the contained plume height would rather fit the size of a major explosion (Table 3.1). The electrical signal accompanying this event shows more similarities with the signals recorded during 25 June 2019 and 16 November 2020 major explosions and lacks the many electrical discharges of thunderstorm-like magnitudes characterising the paroxysm (phase 3, Figure 3.5). The maximum ejection velocity, the total explosion duration and the plume height were considerably lower than for the paroxysmal event (Table 3.1). As a consequence, the 19 July 2020 explosion likely had weaker plume electrification and smaller charge regions, resulting in less intense electrical activity. Therefore, based on electrical signals, the 19 July 2020 explosion would fit the rank of a major explosion. Additional electrical data of both major and paroxysmal explosions at Stromboli would supplement or even elaborate further the classification scheme of such events.

Of particular interest is the oscillating signal characterising the 19 July 2020 explosion (Figure 3.3b). Oscillating signals can be caused by strong winds or ground movement. In the latter case, the antennas themselves are rapidly moving in the electric field (due to ground-shaking), thereby producing a displacement current in the antenna. The stronger the electric field, the higher the amplitude of the oscillations, as is evident from the electrical data (Figure 3.3c). Seismic signals recorded by LGS show an increase in peak amplitude about 10-15 seconds before the main peak associated with the explosion (Figure C.2 of Appendix C). This coincides with the start of the oscillations in the data at around 03:00:31.7 UTC. Hence, we conclude that the seismic tremor associated with the 19 July 2020 major explosion was recorded in the electrostatic data as a result of the oscillating antennas in the presence of an increased electric field, creating an important link between these two geophysical parameters. As volcanic lightning can be recorded by seismometers in the form of spikes or simultaneous gain ranging (McNutt and Davis, 2000), we argue that ground-shaking accompanying explosive eruptions may be recorded by electrical sensors coupled to the ground.

3.5.2 The 3 July 2019 paroxysm

Four different phases of electrical activity were distinguished within the 45 s of data recorded during the 3 July 2019 paroxysm (Figure 3.5), which can be tentatively matched to different phases of the eruption.

1) The slowly varying electrostatic signals recorded following the first explosion are caused by the movement of charge due to the growing and rupturing of a metre-sized lava bubble (Figure 3.5b), as shown by thermal images from the INGV monitoring cameras (Behncke, 2019). The small irregular electrostatic variations detected by the primary antenna one second later, are likely caused by weakly charged pyroclasts moving towards and landing in front of the sensor. There is insufficient charge to induce a detectable opposite effect on the secondary antenna. The movement of charge reversing to a negative polarity likely corresponds to the radially expanding, pyroclasts-rich eruption jet passing over the sensor and moving away from it.

2) After the second explosion, the magnitude of the change in charge and discharges increased by an order of magnitude (Figure 3.5c). We showed that the shorter distance to the NEC zone only accounts for a small increase in the magnitude measured by the sensor. Instead, the additionally erupted material, which encountered an already ash-contaminated and charged atmosphere, enhanced the plume electrification and consequently generated discharges of higher magnitude (Cimarelli et al., 2014; Méndez Harper and Dufek, 2016).

3) While the plume continued to rise and grow by convection, the turbulence caused charged clusters to form, further increasing the magnitude of the electric field (Cooray, 2015). As a consequence, electrical discharges became more frequent (reaching the maximum detected discharge rate) and produced higher measured voltages (Figure 3.5a), saturating the primary antenna similar to nearby thunderstorm lightning (Vossen et al., 2021).

4) The abrupt shift in the electrical signal from discharges of high voltages to low voltages at 14:46:13 UTC (Figure 3.5a) seems to coincide with partial collapse of the plume and the

subsequent PDCs flowing down the Sciara del Fuoco, based on visible images taken by the LGS monitoring camera at Labronzo locality (Laboratorio Geofisica Sperimentale, 2019b) (Figure 3.1a). The partial collapse likely resulted in charge removal from the volcanic plume, similar to the dissipating stage of a thunderstorm, where the downdraft cuts off the updraft of a thunderstorm, weakening it and ceasing meteorological lightning (MacGorman and Rust, 1998). The turbulence of the PDCs generated new electrification. The movement of charge caused by the fast-moving PDCs close to the sensor produced the slow varying electrostatic signal of high magnitude. The charge clusters within the PDCs are probably smaller compared to those in the volcanic plume. As these regions are less extensive, electrical discharges of smaller magnitude are expected to occur, which is consistent with the last 15s of the electrical data recorded by BTD1. It is uncertain whether the occasional discharge of higher measured voltage occurred within the volcanic plume or the PDCs.

The electrical activity detected during the 3 July 2019 paroxysm was much more vigorous, in both magnitude and discharge rate, and complex compared to the electrical signals detected during the major explosions. The eruption duration, plume height and maximum ejection velocity were significantly higher for the paroxysmal event (Table 3.1), indicating higher material ejection rates. This would have greatly attributed to the plume electrification, resulting in more electrical discharges with a larger magnitude. Despite this, the first electrical discharge occurred at a later time with respect to the explosion onset when compared to the three major explosions. Thermal images from the INGV monitoring cameras (Behncke, 2019) showed lava overflows from all eruptive vents in the seconds before the explosion onset, pushed out by a substantial gas pocket rising from depth. Due to magma properties, the explosion occurred at shallow depths inside the conduit and manifested as a metre-sized exploding gas bubble (Métrich et al., 2021), delaying the electrification processes. We speculate that this was further attenuated and delayed by the magmatic temperature (Stern et al., 2019) of the erupted mass of the 3 July 2019 paroxysm, evident by the incandescence even during daylight (Figure 3.1e). Additionally, the greater magnitude of the explosion would have created a well-mixed, chaotic flow with relatively small eddies, hindering the organisation of charge and the formation of clusters. On the other hand, during the major explosions fragmentation occurred at a deeper level in the conduit, resulting in readily fragmented and charged material emerging from the crater.

3.6 Conclusion

The electrical activity of three major explosions and the 3 July 2019 paroxysm at Stromboli was detected using a thunderstorm detector. Similarities in the electrostatic signal of major explosions were found: the emergence and expansion of the plume produced a movement of charge at the onset, shortly followed by a few tens of electrical discharges, with one or more discharges of higher magnitude towards the end of the explosion. We propose that these recurrent observations could supplement the classification scheme used for the explosions on Stromboli in future. In addition to these characteristics, an oscillating electrostatic signal was detected during the 19 July 2020 major explosion, which was most likely caused by shaking of the antenna due to seismicity.

The electrical measurements obtained during the 3 July 2019 paroxysm are unprecedented. The electrical activity was much more intense and complex compared to the major explosions. Four phases of electrical activity could be distinguished and were tentatively matched to different phases of the eruption. Particularly interesting is the shift in electrical activity concomitant to the partial collapse of the plume and the subsequent onset of pyroclastic density currents down the Sciara del Fuoco.

Although not further discussed in this study, normal Strombolian explosions also produced detectable electrical signals. These results show that basaltic explosions at magmatic temperatures produce detectable movements of charge and electrical discharges, which holds promise for monitoring low VEI activity at basaltic volcanoes using robust electrostatic sensors.

Chapter 4

Linking electrical activity to explosive eruption styles during the 2021 Cumbre Vieja eruption

4.1 Abstract

The 2021 Cumbre Vieja eruption on the island of La Palma (Canary Islands, Spain) started on 19 September 2021, continuously producing lava flows and tephra of average basanite to tephrite composition during 86 consecutive days, eventually generating a 180 m tall scoria cone (about 1220 m a.s.l.) and a vast compound lava flow field. Lightning was frequently observed in the plume during different phases of the explosive activity. This eruption provided the rare opportunity to monitor variations in the electrical activity on various time scales continuously over several weeks. We measured such electrical activity using a lightning detector operating in the extremely low frequency range with a sample rate of 100 Hz, installed 1.8 and 2.7 km away from the active vents. The detector was deployed on 11 October 2021 and recorded continuously until the end of the eruption on 13 December 2021, thus providing a unique dataset of its kind.

Throughout the eruption, an abundance of volcanic lightning was detected with highest electrical discharge rate exceeding 5,000 discharges/hour. Fluctuations in the electrical discharge rates were likely controlled by variations in the mass eruption rate and/or changes in the type of electrical activity as a result of changes in the explosive eruption style. Comparing the ash-affected flight levels reported by the Toulouse Volcanic Ash Advisory Centre to atmospheric temperature data, it can be concluded that silicate particle charging was the main plume electrification mechanism during the 2021 Cumbre Vieja eruption.

In addition to movement of charge and ash fall at the sensor, four types of electrical activity were observed, which can be linked to different explosive eruption styles as determined from thermal and visual images. The different electrical signatures are caused by differences in the fragmentation mechanism, eruption dynamics and source parameters. Strong ash emissions, producing high volcanic ash plumes, generated hours-long periods of high intensity volcanic lightning, while weak ash emissions only produced faint electrical discharges. Bursts of low intensity continuous electrical discharges were detected during phases of gas jetting, Strombolian activity and lava fountaining, which only ejected relatively small amounts of ash. The duration of these bursts increase with increasing kinetic energy, height and duration of the explosion and temperature of the erupted mass.

This study is the first to show that different electrical signatures can be generated by different explosive eruption styles throughout a single eruption, which holds promise for obtaining near real-time information on the evolution of explosive volcanic activity through electrostatic monitoring in the future.

4.2 Introduction

On 19 September 2021 at 14:10 UTC, Cumbre Vieja volcano on La Palma island (Spain) erupted, 50 years after its last eruption in 1971 (Longpré and Felpeto, 2021). The eruption was preceded by seismic activity, which had gradually increased in both frequency and intensity, together with signs of inflation. For almost three months, several vents along a NW-SE aligned fissure (Figure 4.1b) produced large amounts of lava and tephra of dominantly basanite to tephrite composition (Pankhurst et al., 2022). It resulted in a vast compound Aa lava flow field, which destroyed a large area containing infrastructure and plantations, and a 180 m tall scoria cone. The eruption ended on 13 December 2021. Romero et al. (2022) estimated total tephra and lava volumes of 45x10^6 m^3 and 170x10^6 m^3, respectively. Throughout the eruption, the explosive activity varied between mild to strong ash emissions, gas jetting, Strombolian activity and lava fountaining. On many occasions, flashes of volcanic lightning were observed. The eruption column had an average height of 2.9 km, reaching up to 5.6 km above the active vents (Romero et al., 2022).

Volcanic lightning is frequently observed during ash-rich explosive eruptions, as a result of electrification and charge separation in the eruption column (Cimarelli and Genareau, 2021). For plumes that do not reach atmospheric freezing levels, silicate particle charging, through fracturing into smaller particles (Dickinson et al., 1988; James et al., 2000) and colliding with one another (e.g. Lacks and Levandovsky, 2007; Cimarelli et al., 2014; Gaudin and Cimarelli, 2019; Méndez Harper et al., 2021), is the dominant charging mechanism. For large explosive events, ice nucleation can further enhance the plume electrification at later stages of the eruption (Prata et al., 2020; Van Eaton et al., 2020). Generally, ash becomes an effective catalyst for ice nucleation between temperatures of -13 °C and -23 °C (Durant et al., 2008), although the exact temperature is controlled by, i.e., the nucleation mode (Durant et al., 2008), chemical composition, crystallinity and mineralogy (Genareau et al., 2018; Maters et al., 2019, 2020). The occurrence of volcanic lightning has been investigated for a wide range of explosion magnitudes (e.g. McNutt and Williams, 2010; Van Eaton et al., 2020; Vossen et al., 2021), but little is known about how the electrical activity changes with eruption style throughout the course of a single eruption. The 2021 Cumbre Vieja eruption provided the unique opportunity to continuously detect the electrical activity throughout a mix of eruption styles and intensities, which would vary on the order of hours to days. With the aim to link different electrical signatures to varying explosive activity, electrostatic data was combined with thermal videography, visual imaging and standard atmospheric measurements.

4.3 Methods

4.3.1 Electrical measurements

The electrical activity generated by the explosive activity of the 2021 Cumbre Vieja eruption was recorded by a Biral Thunderstorm Detector BTD-200, hereafter referred to as ”BTD”. The BTD was initially installed NNW from the active craters at a distance of 2.65 km (28.63508°N, 17.87644°W), on 11 October 2021. For logistical reasons, the BTD was removed on 26 October and reinstalled SW from the eruptive vents, at a distance of 1.77 km (28.60236°N, 17.88046°W) (Figure 4.1). We refer to the first and second locations as BTD1 and BTD2, respectively. Both installations were located within the exclusion zone of the eruption, this helped reducing the background noise nearby the instrument.

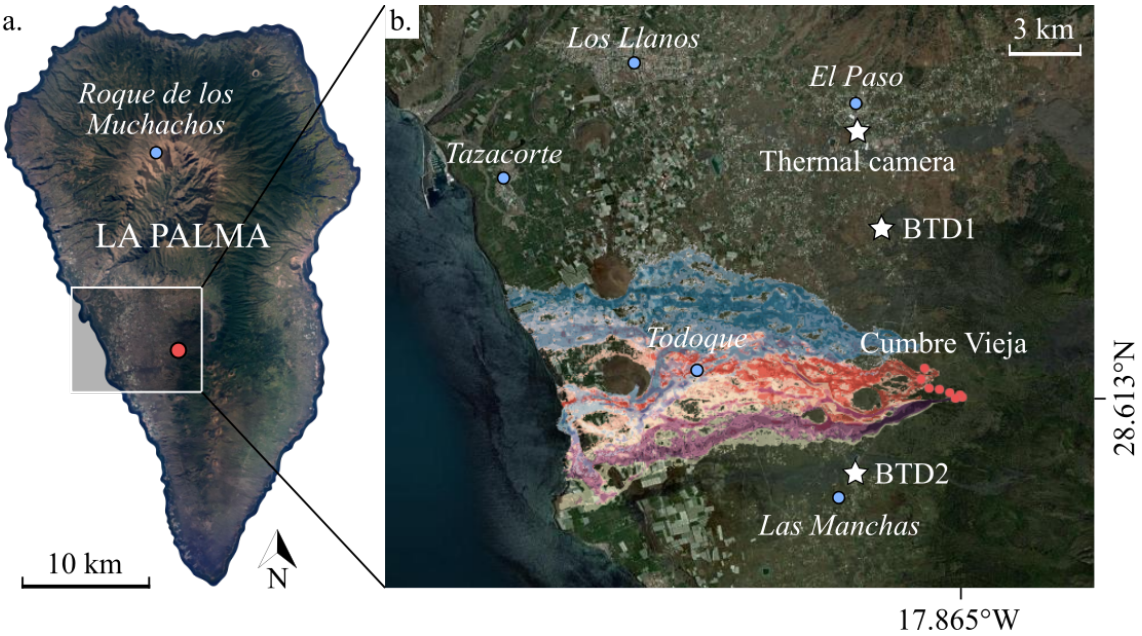

*Figure 4.1: **a)** Satellite image of La Palma island, Canary Islands (Spain) from Google Earth, version 9.141.0.0 (7/7/2019), European Space Imaging 2020. http://www.earth.google.com [11 February 2022]). The location of the eruptive craters is indicated with a red circle. The white box corresponds to the area of panel **b**. **b)** Image from Cabildo Insular de La Palma (https://volcan.lapalma.es, last updated 10/01/2022) showing simulations of the 2021 Cumbre Vieja lava flows (varying colours), in addition to the active vents (red circles) [4 March 2022]. The locations of BTD1, BTD2 and the thermal camera (white stars) are indicated, together with a few localities (blue circles).*

This sensor measures the slow variation in the electrostatic field with time within a frequency range of 1-45 Hz (Bennett, 2017). It consists of a primary antenna, which has the highest sensitivity, and a shielded secondary antenna. These antennas allow the detection of electrical discharges, movements of charge and impact transients, such as charged precipitation or ash falling on the sensor (Bennett, 2017; Vossen et al., 2021). While lightning produces a transient of the same polarity at both antennas, charged particles impacting the primary antenna will induce a signal of opposite polarity at the secondary antenna. A modified version of the volcanic lightning detection algorithm described in Chapter 2 (Vossen et al., 2021) used several empirical thresholds to identify electrical signals as electrical discharges. First of all, the electrical signals needed to have the same polarity at both antennas and a positive covariance of $\geq$1.0. Additionally, the ratio between the two antenna signals needed to be $>$3.0, while the signal-to-noise ratio (SNR) of the primary and secondary antenna signals needed to be above 2.3 and 1.5, respectively. The covariance and noise were calculated over a moving window of 16 and 128 samples, respectively, with a step size of 1 sample.

From the number of electrical discharges identified by the algorithm, the electrical discharge rate (discharges/6 hours) was calculated. In addition, these electrical measurements were compared to the varying plume heights and explosive eruption styles using thermal and visual imaging.

4.3.2 Thermal imaging

To gain more insight into the frequently changing explosive activity of Cumbre Vieja, the continuously recorded electrical data was complemented with thermal videography through the temporary installation of an Infratech HD thermal infra-red (TIR) video camera. The TIR camera was installed NNW from the active craters at a distance of 4.3 km. The camera was focused on the explosive activity at the eruptive vents. It recorded almost continuously between 3-8 November with a maximum definition of 640x480 pixels at 15 frames per second (fps). A Jenoptik IR 1.0/30 LW objective was used, resulting in a pixel resolution of $\sim$3.68 m at the active vents. The camera software corrected the effects of atmospheric absorption *in situ*, based on the temperature and humidity, which were updated several times throughout the week, and the distance between the camera and the active craters.

Rather than using the TIR information to determine the temperature of the eruption column, We use single frames of the thermal recording to determine the eruption style and time/height diagrams to distinguish individual ejection pulses. Time/height diagrams show the evolution of the maximum temperature as a function of time and height (Gaudin et al., 2017a,b). To obtain these diagrams, the algorithm developed by Gaudin et al. (2017a,b) was used, which retains the maximum temperature of each row of a single frame after removing the background brightness by subtracting the previous frame. This analysis was carried out for every 30th thermal frame (i.e. every 2 seconds of recording). These time/height diagrams provide information on the timing of individual ejection pulses, the erupted products (ash- or bomb-dominated) and the rise velocity (based on the slope of the traces) Gaudin et al. (2017a,b).

4.3.3 Standard atmospheric conditions

To determine whether ice charging played a role as a plume electrification mechanism in addition to near-vent silicate particle charging, plume heights were compared to the elevation of the 0 °C, -10 °C and -20 °C isotherms.

The Toulouse Volcanic Ash Advisory Centre (VAAC) reports the flight levels affected by volcanic ash based on satellite data. These flight levels were converted to plume heights above sea level (a.s.l.), providing a general trend throughout the course of the eruption. Note, however, that these values provide an upper limit, as detached ash clouds can remain at high altitudes for a long period of time, while the explosive activity at the vents has diminished or even stopped. In addition, there is often a delay between the plume height and the time it is reported by the

Toulouse VAAC.

Standard atmospheric parameters, such as temperature, pressure, relative humidity, wind speed and direction, were obtained from weather balloon profiles twice a day (at 00:00 and 12:00 UTC), which were provided by the University of Wyoming, Department of Atmospheric Science (http://weather.uwyo.edu/). However, these weather balloons were released about 150 km east at Güímar (station 60018) on Tenerife, Canary Islands (Spain). To ascertain that the temperature measurements are representative for the conditions on La Palma as well, the data was compared to temperature measurements from two fixed weather stations on La Palma, at El Paso (altitude of 844 m) and Roque de los Muchachos (altitude of 2223 m) (Figure 4.1), carried out by the State Meteorological Agency (AEMET) of Spain. Although the temperature variation between night and day is greater for the AEMET stations, the overall trend is very similar between the two data sets (Figures D.1 and D.2 of Appendix D). Therefore, we concluded that the Güímar data is sufficiently accurate to construct the different isotherms over La Palma island and are representative of the atmospheric conditions encountered by the Cumbre Vieja ash plume.

Stable fair-weather conditions over La Palma recorded by meteorological stations during the whole eruption (exception made for a thunderstorm episode on 25 and 26 November 2021), allow a confident attribution of the changeable lightning activity to the explosive activity of Cumbre Vieja volcano. The Volcanic Lightning Monitor of the World Wide Lightning Location Network (WWLLN) reported 21 lightning flashes within 20 km radius of La Palma and 886 flashes within 100 km radius between 25-26 November. The first flash was detected on 25 November at 16:43:47 UTC and the last flash on 26 November at 10:48:51 UTC. During this time, it is unknown whether the electrical discharges detected by the BTD are to be related to volcanic or meteorological lightning. In addition to a single flash at 85 km distance from the active craters on 22 November 2021, WWLLN did not detect any lightning during the Cumbre Vieja eruption.

4.4 Results

4.4.1 Electrical activity versus plume height

To determine whether ice nucleation could potentially have played a role as an electrification mechanism, the plume heights obtained from the Toulouse VAAC reports are compared to the elevation of the 0 °C, -10 °C and -20 °C isotherms (Figure 4.2). Furthermore, the electrical discharge rate (discharges/6 hours) as detected by the BTD and identified by the volcanic lightning detection algorithm is shown for the monitoring period of the BTD.

The results show that throughout the eruption volcanic ash rarely exceeded atmospheric freezing levels (Figure 4.2). On 28 September 2021, Toulouse VAAC did report the presence of volcanic ash at altitudes above the -10 °C isotherm. At this time, the BTD had not been implemented yet, hence information on the electrical activity is not available. Between 18:00 and 03:00 UTC in the night of 13-14 December 2021, volcanic ash was observed at its highest level, exceeding the -20 °C isotherm, as a result of very strong ash emissions and lava fountaining. This explosive phase stopped around 21:30 UTC on 13 December 2021 marking the end of the Cumbre Vieja eruption, which was announced by the Instituto Volcanológico de Canarias (INVOLCAN), the institute responsible for monitoring the volcanic activity of Cumbre Vieja. Nonetheless, the ash remained suspended at high altitudes for several hours longer. Toulouse VAAC did not detect any volcanic ash after 15:00 UTC on 15 December 2021.

Changes in the electrical discharge rate appear to be positively correlated to fluctuations in plume height (Figure 4.2). There are also periods, e.g. between 5-18 November 2021, where no variations in plume height were reported by Toulouse VAAC, while the electrical activity strongly varied. During these days the wind was very strong, frequently resulting in a strongly bent ash plume. In addition, the explosive activity varied greatly in eruption style during these days.

The highest electrical discharge rate (>5,000 discharges/hour) was detected during Strombolian activity on 6 November 2021. Toward the end of the eruption, a small increase in electrical discharge rate is recorded, corresponding to the strong increase in plume height as reported by the Toulouse VAAC.

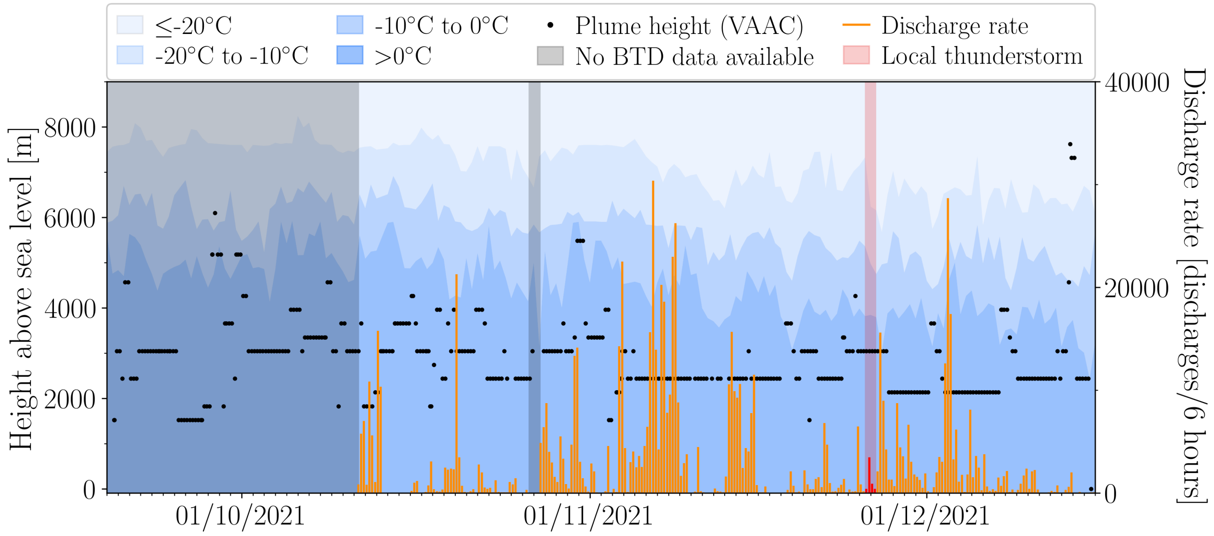

Figure 4.2: Different temperature regions (shades of blue) as a function of height [m] above sea level, together with volcanic plume heights (black dots) as reported by Toulouse VAAC for the entire eruption. The orange vertical lines indicate electrical discharge rates [discharges/6 hours] detected by the BTD and identified by the volcanic lightning detection algorithm between 11 October and 13 December 2021. The red vertical lines and shaded area mark a local thunderstorm on 25 and 26 November 2021. The grey shaded area denotes the periods for which no BTD data is available.

4.4.2 Types of electrical activity

A variety of electrical signals was detected throughout the course of the eruption, which would change frequently on the order of minutes to hours. In general, six types of electrical signatures were observed, hereafter referred to as type 1-6, and are shown in Figure 4.3:

1. Individual high-voltage (typically >0.01V) electrical discharges (Figure 4.3a).
2. Minutes-long ”bursts” of continuous low-voltage electrical activity, with a measured voltage generally ranging between 0.001-0.01V (Figure 4.3b).
3. Seconds-long (∼2-20 s) ”bursts” of continuous low-voltage electrical activity, with a measured voltage commonly below 0.005V (Figure 4.3c).
4. Faint electrical discharges with a very low measured voltage (<0.002V) recorded by the primary antenna. The sensitivity of the secondary antenna is too low to detect any electrical activity. For this reason, these discharges remain mostly undetected by the volcanic lightning detection algorithm.
5. Movement of charge, visible as slow variations (∼1-10 s) in the electrical signal. Simultaneous electrical discharges are superimposed and can still be detected by the volcanic lightning detection algorithm (Figure 4.3e).
6. Ash fall at the sensor can be discriminated from electrical discharges as these impact transients produce electrical signals of opposite polarities at the two antennas, resulting in a negative covariance (Figure 4.3f). Electrical discharges can still be detected during ash fall, as is shown by the positive covariance at 10:27:56.6 UTC in Figure 4.3f.

Combinations of different types were frequently observed. In particular, the individual high-voltage discharges were often accompanied by movements of charge. Also short periods of ash fall were regularly detected during the varying types of electrical activity.

4.4.3 Linking electrical activity to explosive eruption styles

During a field campaign in early November 2021, changes in the explosive activity were observed every few hours. Here, the explosive activity on the evening of 3 November and the entire day of 4 November is used as a study case in order to understand whether variations in the electrical activity can be linked to changes in the explosive eruption style. To do so, the electrical signals are compared to visual (Figure 4.4) and thermal images.

Between 21:00 UTC on 3 November and 00:03 UTC on 4 November, BTD2 recorded individual high-voltage electrical discharges (type 1), which frequently exceeded a measured voltage of 0.1V (Figure D.3a of Appendix D). This electrical activity was recorded during lava fountaining (Figure 4.4a), which produced an ash plume that reached a height of approximately 3 km a.s.l. according to Toulouse VAAC (Figure 4.2). At this time, many flashes of volcanic lightning were observed (Figure 4.4a).

After 00:03 UTC, the electrical discharges initially decreased in magnitude (<0.1V) and subsequently also occurred less frequently (Figure D.3b of Appendix D). This gradual decline in the electrical activity corresponds to a decrease in plume height as reported by Toulouse VAAC (Figure 4.2), which indicates a waning of the explosive activity. Due to the lower magnitude of the electrical discharges, the movement of charge (type 5) produced by the moving electrified ash plume, becomes clearly visible in the electrical data (Figure D.3b of Appendix D).

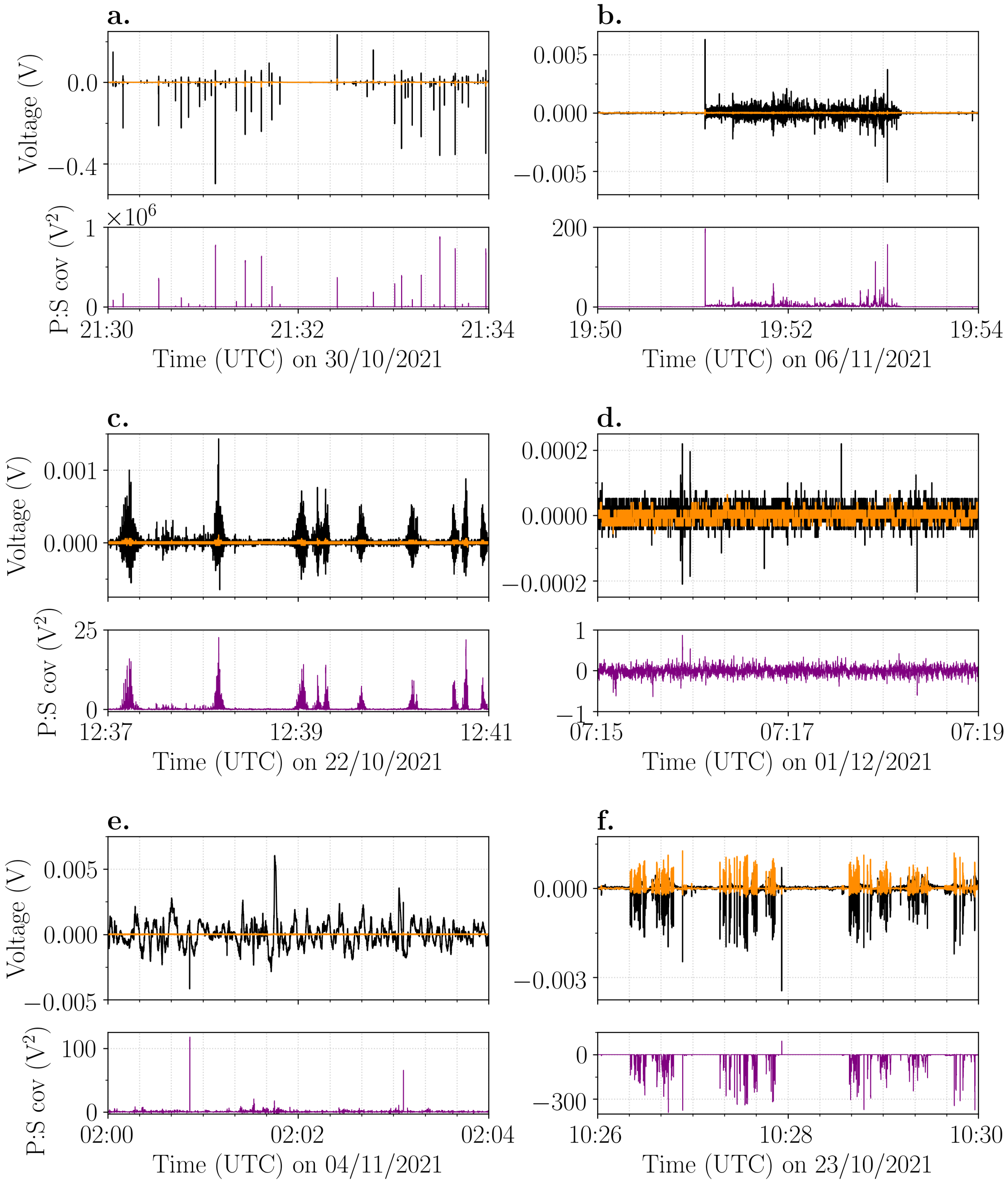

Figure 4.3: Electrical signatures (primary antenna in black, secondary antenna in orange) observed during the 2021 Cumbre Vieja eruption, with the corresponding covariance (V^2) between the primary and secondary signals shown below. Note the different scale on the y-axis for each panel. ***a)*** *Individual high-voltage electrical discharges;* ***b)*** *Minutes-long bursts of continuous low-voltage electrical activity;* ***c)*** *Seconds-long bursts of continuous low-voltage electrical activity;* ***d)*** *Faint electrical discharges that remain unidentified by the detection algorithm;* ***e)*** *Movement of charge, indicated by the slow-varying electrical signal.* ***f)*** *Ash fall at the sensor, indicated by the negative covariance. A single electrical discharge was detected at 10:27:56.6 UTC.*

Hereafter, the lava fountaining stopped and the activity continued with weak ash emissions, which produced a small ash plume with an initial diameter of <100 metres (Figure 4.4b). This was accompanied by very faint electrical discharges (Figure D.3c of Appendix D) that predominantly remained undetected by the volcanic lightning detection algorithm (type 4).

The explosive activity subsequently changed into jetting of gas with minor amounts of particles (Figure 4.4c), which were sometimes accompanied by visible shock waves. BTD2 detected bursts of continuous electrical activity lasting ∼3-10 seconds (type 3) between 13:09-14:16 UTC (Figure D.3d of Appendix D). Between 15:10-15:34 UTC, similar bursts of continuous electrical activity were detected, but of slightly longer duration (up to ∼ 30 seconds) (Figure D.3e of Appendix D). The thermal images showed an increase in both intensity of the gas jetting and magmatic temperature of the erupted material during this time.

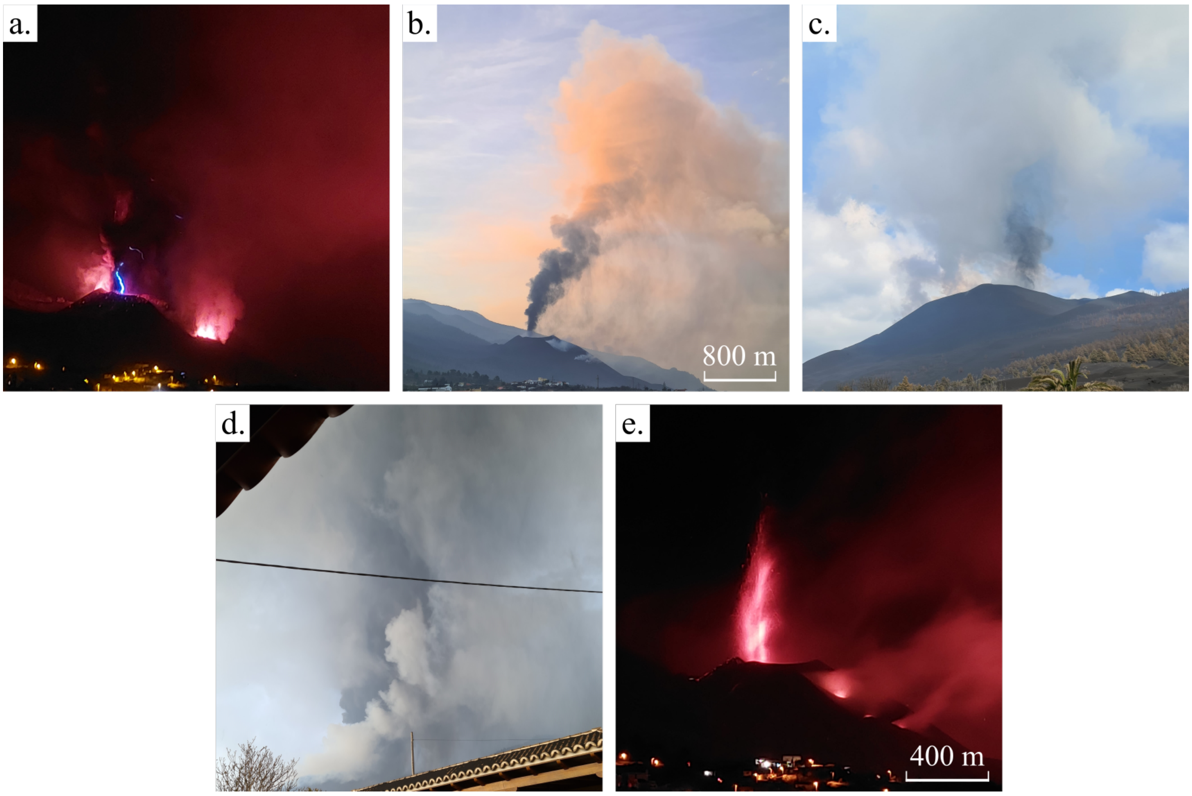

*Figure 4.4: Pictures of different explosive eruption styles on 3 and 4 November 2021, in chronological order, taken from El Paso (panels **a**, **b** and **e**) and Las Manchas (panels **c** and **d**). **a)** Lava fountaining, producing a volcanic ash plume that reached a height of approximately 3 km a.s.l. The picture shows a flash of volcanic lightning at 23:30:53 UTC on 3 November. Courtesy of Francisco Cáceres Acevedo. Reproduced with permission of the copyright holder. **b)** Weak ash emissions at 07:44 UTC on 4 November, producing a small ash plume with an initial diameter of <100 m. **c)** Gas jetting with a minor amount of particles, sometimes accompanied by shock waves. Picture was taken at 13:11 UTC on 4 November. **d)** Strong ash emissions at 17:08 UTC on 4 November, producing a plume of approximately 3 km a.s.l. **e)** Lava fountaining (∼750 m high), producing a small ash plume. Picture was taken at 21:51 UTC on 4 November. Courtesy of Francisco Cáceres Acevedo. Reproduced with permission of the copyright holder.*

From 15:46 UTC onward, ash fall was detected at the BTD (type 6), based on electrical signals of opposite polarity at the two antennas (Figure D.3f of Appendix D) as well as direct observations. The explosive activity changed rapidly from weak to very strong ash emissions around 16:57:43 UTC (Figure 4.4d), which can be distinguished in the height/rise diagram shown in Figure 4.5. Shortly after, individual high-voltage electrical discharges (type 1) were detected (Figure D.3g of Appendix D), which started at 16:57:50 UTC and lasted for about two hours. The ash plume reached a height of approximately 3 km a.s.l. according to Toulouse VAAC (Figure 4.2).

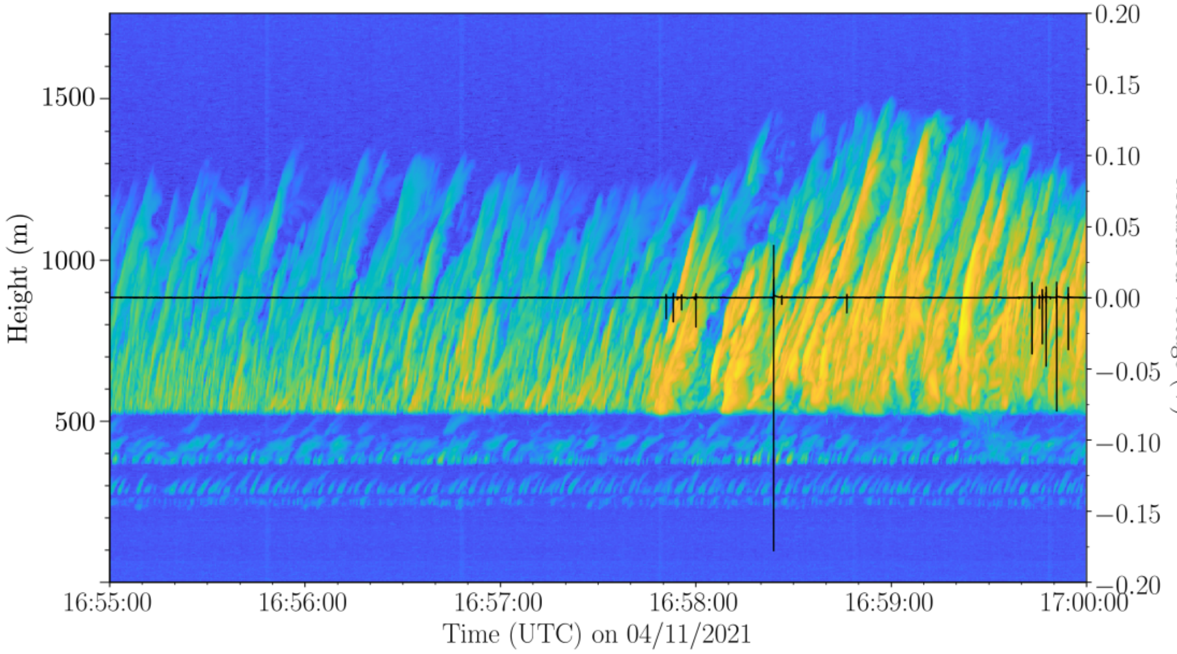

Figure 4.5: Time/height thermal infrared diagram showing the evolution of the maximum temperature (blue is cold and yellow is hot) as a function of time and height. The increase in magnitude of the explosive activity around 16:57:43 UTC coincides with the onset of individual high-voltage electrical discharges (type 1 activity) as recorded by the primary antenna (black line) of BTD2.

Finally, the explosive activity changed to lava fountaining again (Figure 4.4e), dominated by the ejection of incandescent bombs. In general, the lava fountains reached heights of 500-1000 metres above the crater rim, although individual bombs were occasionally ejected to greater heights. In contrast to the lava fountaining on the evening of 3 November, only a small ash plume was produced. This change in explosive activity coincided with a change in electrical activity from type 1 to minutes-long bursts of continuous electrical discharges (type 2, Figure D.3h of Appendix D). However, contrary to the signal shown in Figure 4.3b-c, these signals did not only have positive covariance values, which is one of the criteria of the volcanic lightning detection algorithm. The negative covariance could be the result of the low sensitivity of the secondary antenna or it could be caused by an ash-induced change/lag in the capacitance of one of the antennas due to previous ash fall deposited on the sensor. Hence, not all electrical discharges were identified by the detection algorithm, resulting in an underestimate of the electrical discharge rate.

Strombolian activity was the only explosive eruption style that was not observed on 3 and 4 November, but was observed for several hours on the evening of 6 November (Figure 4.6). Compared to the lava fountains, the incandescent bombs were ejected to much lower heights, generally up to 500 metres above the crater rim. In addition, a semi-opaque ash plume was produced. This type of activity produced a mixture of seconds-long and minutes-long bursts of continuous electrical activity (type 2 and 3).

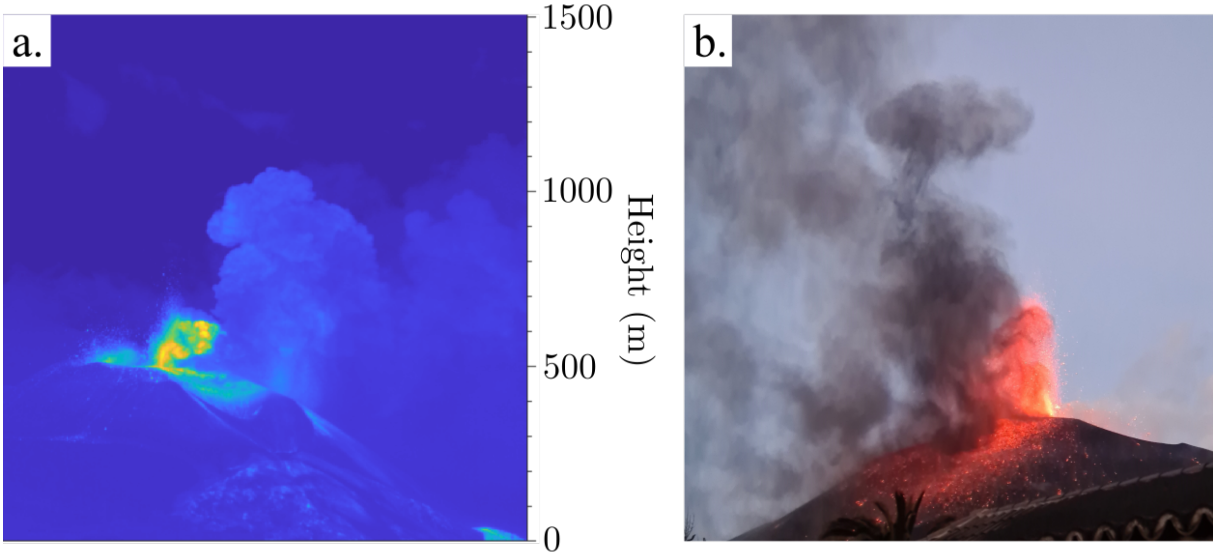

Figure 4.6: Strombolian activity producing incandescent bombs and a small semi-opaque ash plume on 6 November 2021: ***a)*** *Single frame (at 18:16:36 UTC) of thermal video taken at 15 fps from El Paso.* ***b)*** *Picture taken at 18:39 UTC from Las Manchas.*

4.5 Discussion

4.5.1 Plume electrification mechanism

Except during the final explosive phase of the 2021 Cumbre Vieja eruption on the evening of 13 December, volcanic ash did not exceed the -10 °C isotherm within the monitoring period of the BTD (Figure 4.2). As volcanic ash becomes an effective catalyst for ice nucleation at temperatures between -13 °C and -23 °C (Durant et al., 2008), it can be concluded that ice nucleation did not play a key role as a plume electrification mechanism. Vossen et al. (2021) (Chapter 2) reported similar findings for hundreds of relatively small-scale ash-rich explosive events (<6 km plume height) at Sakurajima volcano, Japan. Nonetheless, an abundance of volcanic lightning was detected at both volcanoes, demonstrating the importance of silicate particle charging in the generation of volcanic lightning.

The final explosive activity of the Cumbre Vieja eruption lasted a few hours and produced a plume that reached a height of ∼7600 m a.s.l., exceeding the -20 °C isotherm. At this stage, ice nucleation could have occurred, which would have enhanced the plume electrification. Nonetheless, the electrical discharge rate remained low compared to previous phases of the eruption, even though it did increase after the onset of this particular phase (Figure 4.2). The BTD recorded many individual high-voltage electrical discharges (type 1) during this time, but some of these transients had a negative covariance. We speculate that this is caused by an ash-induced change/lag in the capacitance of one of the antennas due to previous ash fall deposited on the sensor. As a consequence, the detection algorithm disregarded those electrical discharges, resulting in an underestimate of the electrical discharge rate. Hence, it is possible that ice nucleation aided the generation of volcanic lightning at the end of the eruption, but near-vent charging of silicate particles remains the dominant charging mechanism during the 2021 Cumbre Vieja eruption, regardless of plume height and eruption style.

4.5.2 Electrical discharge rate versus plume height

As discussed in Section 2.5.5 of Chapter 2, Behnke et al. (2014) suggested that fluctuations in the electrical discharge rate throughout a single eruption can be either caused by intensified vent charging due to an increase in source flux or enhanced plume electrification as a result of ice nucleation. However, we observed also variations in the electrical activity, and thus the electrical discharge rate, with changing explosive eruption style. For example, while the high-voltage discharges of type 1 are an indication of intense electrical activity in the plume, these discharges were generated at a different frequency compared to the low-voltage bursts of continuous lightning of type 2 and 3. Hence, during the Cumbre Vieja eruption the fluctuations in the electrical discharge rate are controlled by changes in the mass eruption rate (Cimarelli et al., 2014; Hargie et al., 2019) as well as changes in eruption style. The former fits with the observation that the fluctuations in the electrical discharge rate often seem to be positively correlated with changes in the plume height, while the latter explains the changes in electrical discharge rate during periods where Toulouse VAAC did not report any change in the affected flight levels.

The highest electrical discharge rate was detected on 6 November 2021 during Strombolian activity (Figure 4.6), which generated electrical activity of type 2 and 3. These bursts of continuous electrical discharges can result in very high discharge rates. Toulouse VAAC reported that ash was still present at 3 km a.s.l. during this time (Figure 4.2). However, as the Strombolian activity only produced a small ash plume, the plume height here does not represent the eruption column but rather the remainder of ash at high altitudes from previous intense explosive activity.

4.5.3 Linking electrical signatures to explosive eruption styles

The 2021 Cumbre Vieja eruption was characterised by a variety of explosive eruption styles: weak and strong ash emissions, gas jetting, Strombolian activity and lava fountaining. Variations in the electrical signals recorded by the BTD can be linked to distinct changes in the explosive activity. However, to understand the electrical signature of each eruption style, several eruption parameters need to be taken into account, including the kinetic energy, mass eruption rate, erupted volume, plume height, grain size distribution, temperature of the erupted mass and the lifetime of the eruption column.

Strong ash emissions producing ash plumes of several kilometres in height (Figure 4.4d), sometimes accompanied by lava fountaining (Figure 4.4a), generated individual high-voltage (>0.01V) electrical discharges (type 1, Figure 4.3a, Figure 4.5 and Figure D.3a,g of Appendix D). This type of eruption style is characterised by a high kinetic energy and mass eruption rate, which will generate a lot of charge in the plume through collisions and secondary fragmentation of silicate lapilli and ash particles. The development of a tall volcanic ash plume, especially one that is sustained for several hours, allows the build-up of a strong electric field through charge separation and the formation of charge clusters (Mather and Harrison, 2006; Cimarelli et al., 2014, 2016), generating volcanic lightning of high measured voltage. Similar electrical activity was detected during the Vulcanian explosions at Sakurajima volcano, Japan (Chapter 2, Vossen et al. (2021)) and the major explosions and paroxysmal event at Stromboli volcano, Italy (Chapter 3, Vossen et al., 2022 *under review*). This suggests that the electrical signals detected during type 1 activity are produced by the commonly observed volcanic lightning, known as near-vent and plume volcanic lightning (Thomas et al., 2010). This is confirmed by direct observations made during this type of explosive activity on the evening of 3 November 2021, as is shown in Figure 4.4a. The movement of the strongly electrified ash plume resulted in a slow-varying (∼1-10 seconds) electrical signal at the antennas (Figure 4.3e and Figure D.3b of Appendix D).

In contrast, weak ash emissions producing small ash plumes with an initial diameter of <100 metres (Figure 4.4b) generated only faint (<0.002V) electrical discharges (type 2, Figure 4.3d and Figure D.3c of Appendix D, which predominantly remained undetected by the detection algorithm due to the low SNR of both antennas. This type of explosive activity is driven by much lower kinetic energy and a low mass eruption rate. As a consequence, little plume electrification occurs and therefore few electrical discharges are generated. Similar findings were reported during the mild ash-rich Strombolian explosions at Stromboli volcano (Chapter 3, Vossen et al., 2022 *under review*), although the greater distance between the sensor and active craters on La Palma needs to be taken into account, as the electric field decreases with the distance cubed (Wilson, 1921; Bennett and Harrison, 2013). During the few occasions that movement of charge was detected, the slow-varying electrical signals had a much lower magnitude compared to those detected during larger-scale ash plumes produced by Cumbre Vieja volcano, further demonstrating the presence of a weakly charged plume.

Bursts of continuous electrical discharges of low to intermediate measured voltages (< 0.01V, type 2 and 3) were detected during gas jetting (Figure 4.4c), Strombolian activity (Figure 4.6) and lava fountaining (Figure 4.4e), during which the production of ash was reduced. This type of electrical activity has not been detected before using the BTD. It is distinctly different from the individual high-voltage electrical discharges detected during strong ash emissions, and is likely the result of differences in the fragmentation mechanism, eruption dynamics and source parameters of these explosions. Gas jetting, Strombolian activity and lava fountaining have in common that they are driven by large volumes of gas, which fragment the melt into variable amounts of ash, lapilli and (incandescent) bombs (Taddeucci et al., 2015). Hence, the grain size distribution typically extends a wider range compared to the ash-rich explosions (Cashman and Scheu, 2015). Due to decoupling of the gas and melt, the kinetic energy and erupted volume of these explosions is much lower (Taddeucci et al., 2015). As a result, the eruption column reaches only a few hundreds of metres in height and are short-lived due to their pulsing behaviour (Taddeucci et al., 2015). The sustained ash-rich explosions at Cumbre Vieja volcano constantly ejected new material into an existing electrified ash plume, adding to the electrification, a process that was lacking during these gas-rich explosions. Hence, gas jetting, Strombolian activity and lava fountaining do not build up strongly electrified plume with large charge clusters, and consequently do not generate the conventional volcanic lightning. Rather, the large volumes of gas likely resulted in faster charging and more efficient discharging due to increased turbulence, explaining these bursts of low-voltage electrical discharges.

The duration of these bursts increased from gas jetting (<30 seconds) (Figure D.3d-e) to pulsating Strombolian activity (seconds to minutes) to continuous lava fountaining (minutes) (Figure D.3h), which is positively correlated to the relative kinetic energy, the height of the eruption column and duration of each individual explosion phase. The lava fountains were driven by the highest kinetic energy, evident by their higher eruption columns (Wilson et al., 1978; Parfitt and Wilson, 1995). Moreover, the thermal images showed that the temperature of the erupted mass produced by the Strombolian activity and lava fountaining was higher compared to the material ejected during gas jetting. Stern et al. (2019) carried out rapid decompression experiments at temperatures up to 320 °C. Although the effect of temperature in the rapid decompression experiments is of difficult interpretation, the results showed that experiments at higher temperature promoted the increase in the number of small electrical discharges in the gas-particle mixture as well as the total duration of electrical discharges. Furthermore, the experiments at higher temperature produced the highest charging rates early on in the experiment (Stern et al., 2019), this effect being correlated with the increased expansivity and turbulence in the particle-laden jets, possibly driving the charge clusters constantly back together. This could explain the increased electrical activity during Strombolian activity and lava fountaining as well. Similarly, a short period of increased explosive intensity and temperature of the erupted mass during gas jetting resulted in longer bursts (comparing Figure D.3d to D.3e of Appendix D). This suggests that the temperature plays an important role in generating the conditions for the occurrence of these bursts of electrical activity.

4.6 Conclusion

The 2021 Cumbre Vieja eruption provided the opportunity to monitor the variations in electrical activity in response to the changing magnitude and style of the explosive activity. Silicate particle charging of the ejected silicate particles was recognised as the main plume electrification mechanism during the entire eruption, regardless of eruption style or magnitude, as revealed by the comparison of maximum altitude of the plume and the ice nucleation temperature altitudes determined by the 0 °C, -10 °C and -20 °C isotherms. The fluctuations in electrical discharge rate appear to be positively correlated to the changes in the plume height. This is either caused by variations in the mass eruption rate, resulting in intensified or reduced vent charging, or due to a transition in explosive eruption style, resulting in a different type of electrical activity.

Movement of charge resulted in slow-varying electrical signals, while ash fall at the sensor produced signals of opposite polarity at the two antennas. Four additional types of electrical activity were detected throughout the time of monitoring, which could be linked to different types of explosive eruptions styles using visual and thermal images. Strong ash emissions, sometimes accompanied by lava fountaining, generated individual high-voltage electrical discharges, while weak ash emissions produced faint electrical discharges that generally remained undetected by the volcanic lightning detection algorithm. Gas jetting, Strombolian activity and lava fountaining generated bursts of continuous electrical discharges of low-voltage. The difference in the electrical signatures is caused by a combination of differences in the fragmentation mechanism, eruption dynamics and source parameters. Large ash-rich volcanic plumes allow the build-up of a strong electric field through charge separation and the formation of charge clusters, providing the conditions to generate high-voltage volcanic lightning. On the other hand, the smaller-scale gas-rich explosions generate smaller electrical discharges as result of efficient charging and discharging due to increased turbulence. The duration of these bursts of electrical activity appears to be positively correlated to the kinetic energy, the height and duration of each explosion pulse and the temperature of the erupted mass, resulting in seconds-long bursts during gas jetting, minutes-long bursts during lava fountaining and a combination of those during pulsating Strombolian activity.

The 2021 Cumbre Vieja eruption provided a unique electrical data set, which allowed for the first time to link variations in the electrical activity to changes in the explosive activity during a single eruption. A deeper understanding of these electrical signatures and the underlying charge mechanisms could possibly provide estimates of the relative proportion of ash, the mass eruption rate and plume height in the future, similar to how different seismic signals can be related to different processes within the volcanic plumbing system. Moreover, these results show that local electrical monitoring of active volcanoes can provide valuable near real-time information on changes in the explosive eruption style as well as the magnitude, especially since regional and global lightning detection systems were not able to detect any volcanic lightning.

Chapter 5

Ash versus ice abundance controls lightning polarity in volcanic plumes

5.1 Abstract

To examine the relative roles of ice versus volcanic ash abundance in relation to cloud-to-ground (CG) volcanic lightning polarity, shock tube decompression experiments have been conducted using both materials. For those experiments that involved solely ash ejection, and for those where ash was ejected prior to ice, the majority of discharge events were -CG. For those experiments that involved solely ice, or those where ice was ejected prior to ash, there were far fewer discharges which were dominantly +CG. These results are consistent with 1) previous volcanic lightning studies; and 2) satellite analyses of several eruptions from 2018-2020, which show a pronounced ice signature coincident with increased proportions of +CG lightning. The proportion of -CG volcanic lightning events may thus permit the quantification of volcanogenic ice nucleation during explosive eruptions.

5.2 Introduction

Volcanic lightning has been recognised as a common phenomenon during explosive volcanic eruptions (McNutt and Davis, 2000; Williams and McNutt, 2004; Mather and Harrison, 2006; James et al., 2008; McNutt and Williams, 2010) and has been used to monitor hazardous activity and track ash plume dispersion (Behnke et al., 2013, 2014; Behnke and McNutt, 2014; Woodhouse and Behnke, 2014; Behnke and Bruning, 2015; Van Eaton et al., 2016, 2020; Coombs et al., 2018; Hargie et al., 2019; Schneider et al., 2020). Despite some similarities to lightning produced during thunderstorms, volcanic lightning exhibits key differences depending upon the stage of eruption. At the onset of an explosion, the process leading to such sudden fluxes of solid particles (i.e. tephra) into the atmosphere results in both fracto-electrification during magma fragmentation (Lane and Gilbert, 1992; James et al., 2000; Méndez Harper et al., 2015; Aplin et al., 2016) and tribo-electrification due to collisions between particles (Harrison et al., 2010; Cimarelli et al., 2014; Aplin et al., 2016; Méndez Harper and Dufek, 2016). Both the size distribution and altitude reached by volcanic ash particles (tephra <2 mm in diameter) will be controlled by the explosive intensity of the eruption (Sparks et al., 1997).

For certain eruptions, ash grains may ascend to appropriate atmospheric isotherms (ca. -20 °C) where ice nucleation is favoured (Lane and Gilbert, 1992; Durant et al., 2008; Arason et al., 2011; Van Eaton et al., 2012, 2020), causing the transformation of silicate particles into hydrometeors, or volcanogenic ice particles (Genareau et al., 2018; Maters et al., 2019; Prata and Lynch, 2019). Tribo-electrification can occur whether the colliding particles are ash grains, hydrometeors, or a combination of both. In thunderstorms, charging and subsequent separation of hydrometeors (e.g. hail, graupel, ice, supercooled water droplets) generate an electric potential (Takahashi, 1978; Jayaratne et al., 1983; Black and Hallett, 1999; Saunders et al., 2006). This potential is equilibrated by lightning discharges, which includes both intra-cloud (IC) and cloud-to-ground (CG) events. During explosive volcanic eruptions, both IC and CG discharges are typically observed (Aizawa et al., 2016).

The properties of volcanic lightning have been measured using a variety of instrumental and remote sensing techniques. Few of these studies, however, have been able to constrain the polarity of the lightning discharges. During eruptions at Sakurajima volcano in Japan, magnetotelluric measurements of CG discharges revealed dominantly negative, but also positive polarities (Aizawa et al., 2016). Positive discharges (+CG) ranged from 26% to 34%, while negative discharges (-CG) ranged from 66% to 74%, for measurements conducted in 2013 and 2015, respectively (Aizawa et al., 2016). This duality in charge polarity is due to the variable grain size distributions of erupted tephras in the near-vent and convective regions of the column. As shown in studies of tribo-electrification (Shaw, 1926; Henry, 1953; Lowell and Truscott, 1986a,b; Lacks and Levandovsky, 2007; Shinbrot et al., 2008; Kok and Lacks, 2009), the charge generated on particles will depend on particle size, with positively charged larger particles and negatively charged smaller particles, even if those particles are composed of the same electrically insulating material. This holds for both ash and ice and has now been documented both during explosive eruptions (Miura et al., 2002) and controlled shock tube experiments simulating such eruptions (Cimarelli et al., 2014). As documented for the case of Sakurajima volcano, where Vulcanian explosions characterise the persistent explosive activity, the eruption column may not necessarily achieve an altitude sufficient for ice nucleation (Cimarelli et al., 2016; Vossen et al., 2021), such that ash electrification may dominate over the role of ice charging. In contrast, volcanogenic thunderstorms can also be generated by sustained explosive activity with ash-depleted eruptive columns, as in the case of the recent 2018 phreatomagmatic eruption of Anak Krakatau volcano in Indonesia (Prata et al., 2020). In this latter case, deep convection was generated by the sustained underwater volcanic activity producing a water vapour-dominated column reaching 16-18 km and minimum cloud-top temperatures of -80 °C, inducing prodigious nucleation of ice particles. Strong updrafts (>50 m/s) in the ice-rich column substantially contributed to the record production of lightning (>100,000 events) over the six-day duration of the eruption (Prata et al., 2020).

Volcanic lightning polarity was also measured using the World Wide Lightning Location Network's Global Volcanic Lightning Monitor (WWLLN) and Vaisala's Global Lightning Dataset (GLD360) during the 2016-2017 phreatomagmatic eruption of Bogoslof (Alaska, U.S.A.) (Haney et al., 2018; Van Eaton et al., 2020). This eruption produced plumes typically exceeding the level of ice nucleation (∼5 km) and was able to generate >4550 lightning events over the course of 70 explosions, although not all of the explosions produced lightning (Van Eaton et al., 2020). IC and CG lightning events were differentiated based upon the peak current, with discharges exceeding (±) 15 kA classified as CG events following the threshold of Biagi et al. (2007). However, as shown at Sakurajima, CG discharges can have peak currents of <5 kA (Aizawa et al., 2016). Several different explosions during the Bogoslof eruption were closely examined, with numerous lightning discharges of both positive and negative polarity. Although most of the lightning during these explosions was IC, based upon the Biagi et al. (2007) classification, the majority of CG discharges were negative in polarity for five out of eight of the studied electrically active events (Van Eaton et al., 2020). Analyses of lightning occurrence during the Bogoslof eruption revealed that: (1) Tribo-electrification of ash particles dominated in the near-vent region while tribo-electrification of ice dominated above the -20 °C isotherm; and (2) lightning occurrence was detected by global networks only for sustained plumes that rose above the -20 °C isotherm, as discharge events were larger, in both size and magnitude, and thus, more similar to thunderstorm lightning.

The experiments in the study presented here are the first of their kind to examine the interactive roles of ash and ice in charge transfer and their control on volcanic lightning polarity during CG discharges. The results, coupled with satellite analyses, enable an experimentally supported interpretation of the characteristics of volcanic lightning observed during several recent explosive eruptions where ice nucleation has been hypothesised to be an important factor.

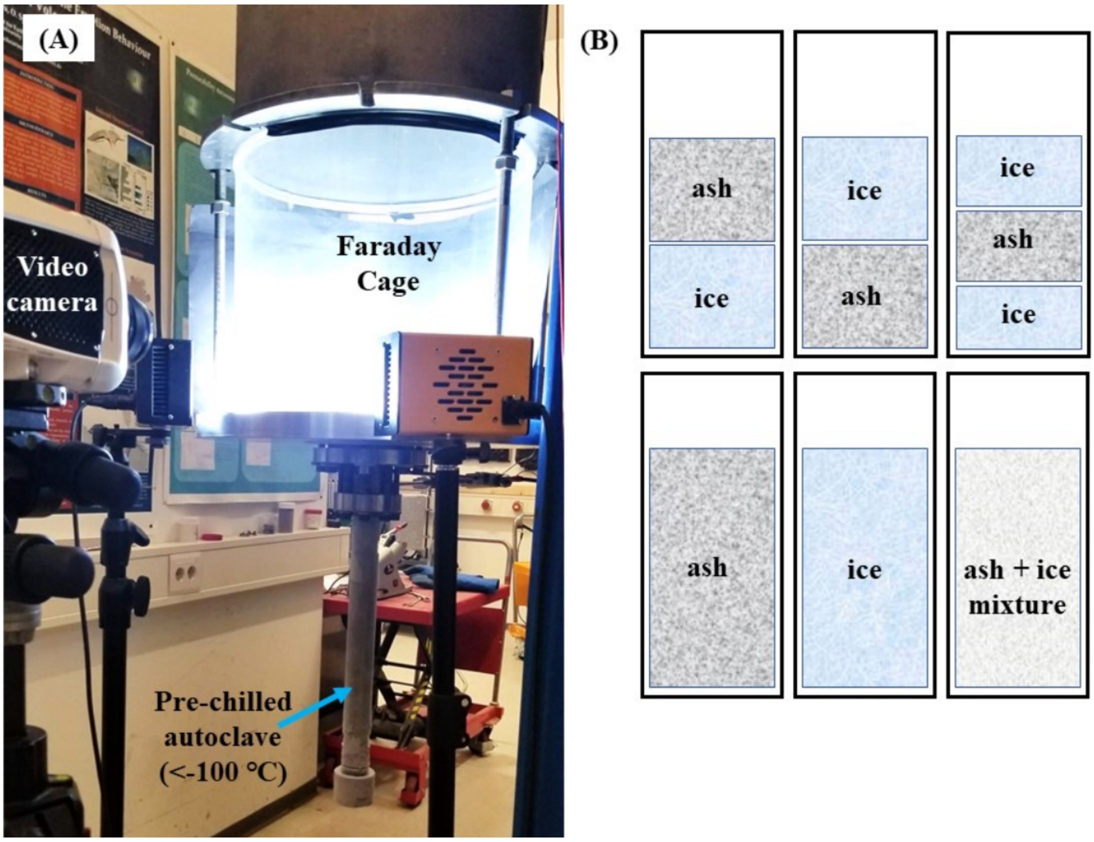

*Figure 5.1: **a)** Experimental apparatus showing the suspended collector tank (Faraday Cage) and mounted 26 mm-diameter, 43 cm-long autoclave, which has been submerged in liquid nitrogen before insertion of the sample; **b)** different sample arrangements (not to scale) used for the experiments, with a combination of ash and ice, ice only, or ash only. The autoclave was not completely filled with sample for any of the 32 separate experiments.*

5.3 Materials and Methods

5.3.1 Experimental methods

Natural samples of ash from the 13-ka Laacher See eruption at a grain size of 40-90 μm (provided by ROTEC GmbH in Mülheim-Kärlich) were used, in addition to shaved ice ground from blocks of frozen tap water using the Smash Ice Device©. Unlike the ash utilised for the experiments, which has been extensively characterised and is of a specific grain size (40-90 μm), the ice used was produced using an instrument that does not provide users with the ability to control the resulting size or size distribution of the shaved ice particles. Consequently, fragmentation of the ice upon decompression and collision events between ice particles will be unique for each experiment. However, the image analysis (using the free software Fiji on images taken with a Keyence optical microscope) of more than 3000 ice particles generated with this technique reveals a positively skewed size distribution (Figure E.1 of Appendix E) with a mode of particle sizes between 3 and 4 phi (62.5-120 μm), which is comparable to the size distribution of the ash particles used. Different combinations of ash and/or ice were loaded into a 26-mm diameter autoclave that was pre-chilled by submersion in a dewar of liquid nitrogen at a temperature of -196 °C. Following submersion, a thermocouple was used to measure the internal temperature of the autoclave, which was consistently less than -100 °C. The experimental methods used here follow those of Stern et al. (2019), who modified the set-up of yet earlier volcanic lightning laboratory studies (Cimarelli et al., 2014; Gaudin and Cimarelli, 2019) using a shock tube apparatus (Figure 5.1a). Thirty-two separate decompression experiments were performed; thirteen in an 18-cm long autoclave and nineteen in a 43-cm long autoclave. The longer autoclave was used to increase the amount of sample exposed to the necessary overpressure needed to cause lightning discharges (Méndez Harper et al., 2018; Stern et al., 2019). Argon gas was added to pressurise the autoclave to 9 MPa, and upon decompression and rupturing of the two diaphragms, the sample expands into the electrically insulated collector tank that functions as a Faraday Cage (FC) and is exposed to constant room temperature (22 °C) and relative humidity (36%), as measured by a probe inserted into the tank and sampling at 1 second intervals. Pressures within the autoclave and at the nozzle were recorded with two separate pressure sensors. The mass of ash and/or ice inserted into the pre-chilled autoclave varied from 30 g to 70 g. For those experiments using a homogeneous mixture of ash and ice, the sample mass was always 40 g. The sample characteristics for all experiments can be found in Table 5.1 and examples are displayed in Figure 5.1b. The experiments were recorded with a V711-Phantom high-speed video camera operating at a frame rate of 50,000 fps.

5.3.2 Satellite data analysis methods

To investigate the relationship between plume phase composition (ice versus ash) and volcanic lightning polarities during explosive eruptions, we compare lightning measurements from the Earth Networks Total Lightning Network (ENTLN) to satellite-measured brightness temperatures from geostationary data collected from the Himawari-8 and GOES-16 satellites. Previous studies have used brightness temperature difference analysis to investigate the composition of volcanic clouds (Wen and Rose, 1994; Rose et al., 1995; Prata and Grant, 2001; Corradini et al., 2008; Prata et al., 2020). In general, brightness temperature difference analysis is most reliable when a volcanic cloud is semi-transparent and there is a large thermal contrast between the temperature at the surface and within the cloud. For a semi-transparent ash cloud, radiative transfer theory predicts that when the brightness temperature measured near the 11 micrometer (μm) wavelength is plotted against the brightness temperature difference between the 11 μm and 12 μm channels, the data will conform to a negative concave upward shape (e.g. Prata, 1989a,b; Prata and Grant, 2001). In contrast, for a cloud composed of hydrometeors (ice particles or water droplets), the data will conform to a positive concave downward shape (e.g. Inoue, 1985; Yamanouchi et al., 1987; Wang et al., 2011). Similar shapes are predicted and observed using brightness temperature differences between channels centred near the 8.6 μm and 11 μm wavelengths with increased sensitivity for ice particles when compared to brightness temperature differences between the 11 μm and 12 μm channels (Wang et al., 2011; Prata et al., 2020). As we are interested in the role of ice in volcanic lightning generation, we use the brightness temperature difference between the 8.6 μm (8.5 μm for GOES-16) and 11 μm channels in our multispectral analysis of explosive eruption plumes. We grouped lightning flash events into 10-minute and 15-minute intervals for Himawari-8 and GOES-16 satellite observations, respectively, as data are nominally collected at these time intervals. We also collocated each lightning flash in space by finding the nearest satellite pixel to each flash detected for each time interval.

5.4 Results

5.4.1 Shock tube experiments

In these shock tube experiments, discharges which occur from the expanding jet mixture, above the vent (a.k.a. nozzle) and prior to any stratification of charged particle layers, are considered analogous to near-vent CG discharges (Gaudin and Cimarelli, 2019; Stern et al., 2019). Our detection method requires charges to leave the electrically floating Faraday Cage (FC) in order to reach the grounded sensor (i.e. cloud-to-ground), hence any IC events occurring within the FC will remain undetected. Samples used in our experiments include both volcanic ash and ice particles deployed in several sample arrangements (Figure 5.1b). Using a combination of both materials, discharges of both positive and negative polarity are generated (Figure 5.2a-b), with their occurrence controlled by the relative position of ash and ice within the autoclave. Discharge polarity is dictated by the nature of the material used in the experiments, as ash and ice particles ejected from the autoclave were shown to produce discharges of predominantly opposite polarity (Figure 5.2c-f). There were typically less discharges if ice was present in the sample, with some experiments producing very few discharges. For those experiments that involved solely ash (Figure 5.2c-d), as well as those where ash preceded the ice into the FC, 1106 discharges occurred: 75% with negative polarity and 25% with positive polarity. The prevalence of negative discharges is controlled by the surplus of negative charge introduced by the ash in the FC. Negative charges in the jet are then neutralised to the ground therefore producing negative discharges (-CG). Note, however, that the data logger records the relative change inside the FC, meaning that negative discharges are recorded as positive transients and visa versa. Oppositely, for those experiments that involved solely ice (Figure 5.2e-f), or those where ice preceded ash into the FC, the number of discharges decreased to 429: 33% with negative polarity and 67% with positive polarity. In cases with only or prevailing ice particles, the prevalence of positive discharges from the jet to the grounded portion of the setup is caused by the surplus of positive charge introduced in the FC by the ice particles. In the six experiments conducted using a homogeneous mixture of ash and ice, those samples with $\geq$50 wt.% ice produced positive polarity discharges 78% of the time. However, for those homogeneous mixtures that had $<$50 wt.% ice, 82% of the discharges were negative. Two sample arrangements were composed of frozen ash accretions and were not included in the previously described results. Table 5.1 provides the sample characteristics for each experiment, together with the numbers/percentages of positive and negative discharges.

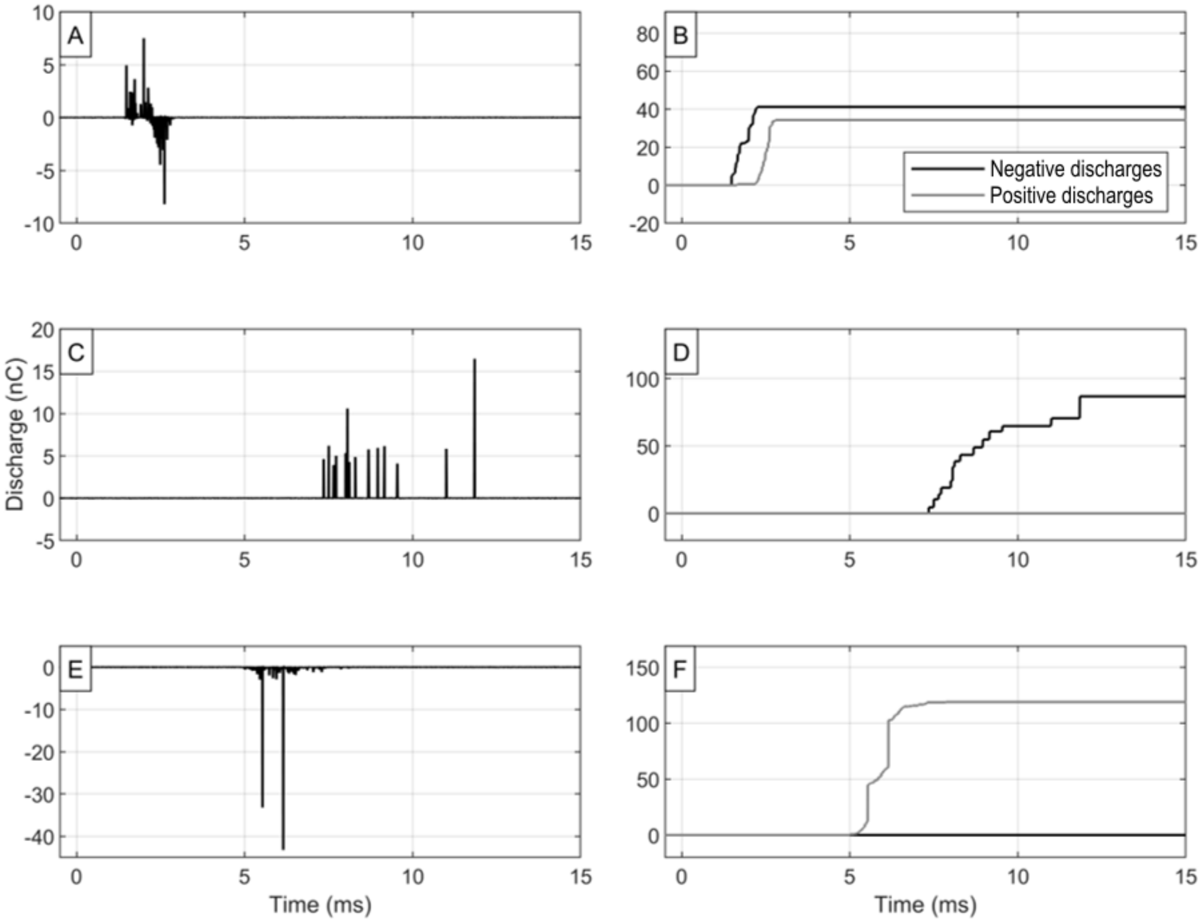

Figure 5.2: Panels on the left show discharge events. Note that positive transients are caused by negative cloud-to-ground discharges, while negative transients are caused by positive cloud-to-ground discharges, as the data logger records the relative change in charge inside the Faraday Cage. Panels on the right show the cumulative magnitude of discharges occurring, where darker lines represent the cumulative negative discharge and lighter lines represent the cumulative positive discharge. ***a, b)*** *experiment number 7, with a combination of ash and ice, during which ash entered the Faraday Cage first;* ***c, d)*** *experiment number 26, which used ash only; and* ***e, f)*** *experiment number 18, which used ice only.*

5.4.2 Satellite analyses

Five recent explosive eruptions that exhibited volcanic lightning observed by the Earth Networks Total Lightning Network (ENTLN) were selected for our analysis (Ambae, Vanuatu, 2018; Anak Krakatau, Indonesia, 2018; Fuego, Guatemala, 2018; Ulawun, Papua New Guinea, 2019; and Taal, Philippines, 2020). These eruptions were selected because they all produced variable amounts of lightning and occurred within a time period of two years, making the efficiency of lightning detection equipment and satellite retrievals uniform between all cases, allowing direct comparisons. In each case we used a 100 km radius centred on the volcano of interest and performed the brightness temperature difference analysis. The lightning data recorded by the ENTLN are displayed over the Himawari-8 (and GOES-16 for Fuego volcano)

Table 5.1: Experiment and sample characteristics.

Experiment Number	Sample mass (g)	wt.% ash	wt.% ice	Sample characteristics	Number of discharges		Percentage of discharges	
					-	+	-	+
18	55	0	100	ice only	0	21	0	100
24	40	0	100	ice only	0	1	0	100
17	65	0	100	ice only (residual ash contamination)	55	15	78.5	21.5
1	30 (ash) + 28 (ice)	52	48	ice above ash	0	7	0	100
3	30 (ash) + 14 (ice)	68	32	ice above ash	6	1	86	14
21	20 (ash) + 30 (ice)	40	60	ice above ash	5	20	20	80
22	30 (ash) + 20 (ice)	60	40	ice above ash	12	26	32	68
23	30 (ash) + 10 (ice)	75	25	ice above ash	0	10	0	100
6	5 (ash) + 38 (ice)	12	88	ice, ash, ice	0	13	0	100
19	10 (ash) + 60 (ice)	14	86	ice, ash, ice	40	144	22	78
20	15 (ash) + 30 (ice)	33	67	ice, ash, ice	23	30	43	57
26	40	100	0	ash only	14	0	100	0
27	40	100	0	ash only	4	0	100	0
2	12 (ash) + 33 (ice)	27	73	ash above ice	79	14	85	15
4	5 (ash) + 33 (ice)	13	87	ash above ice	13	6	68	32
5	5 (ash) + 33 (ice)	13	87	ash above ice	28	36	44	56
7	5 (ash) + 33 (ice)	13	87	ash above ice	26	23	53	47
8	5 (ash) + 33 (ice)	13	87	ash above ice	2	1	67	33
9	5 (ash) + 33 (ice)	13	87	ash above ice	7	0	100	0
10	5 (ash) + 33 (ice)	13	87	ash above ice	5	6	45	55
11	5 (ash) + 33 (ice)	13	87	ash above ice	8	0	100	0
14	30 (ash) + 51 (ice)	37	63	ash above ice	154	86	64	36
15	30 (ash) + 50 (ice)	37.5	62.5	ash above ice	322	68	82.5	17.5
16	30 (ash) + 50 (ice)	37.5	62.5	ash above ice	164	40	80	20
25	7 (ash) + 33 (ice)	17.5	82.5	homogeneous mixture	56	113	33	67
28	20 (ash) + 20 (ice)	50	50	homogeneous mixture	0	55	0	100
29	20 (ash) + 20 (ice)	50	50	homogeneous mixture	0	36	0	100
30	33 (ash) + 7 (ice)	82.5	17.5	homogeneous mixture	0	3	0	100
31	33 (ash) + 7 (ice)	82.5	17.5	homogeneous mixture	4	0	100	0
32	37 (ash) + 3 (ice)	92.5	7.5	homogeneous mixture	10	0	100	0
12	3 (ash) + 30 (ice)	9	91	frozen accretionary lapilli above ice	0	0	0	0
13	30	100	0	frozen accretionary lapilli in ash matrix	1	68	1	99

Experiments 1-13 were conducted using the 18 cm-long autoclave, while experiments 14-32 were conducted using the 43 cm-long autoclave. The experiments are organised based upon similar sample arrangements. The mass (error is ± 1 g), weight percentage (wt.%) of ash versus ice, and characteristics of each sample arrangement are provided, in addition to the number of discharge events of positive (+) and negative (-) polarity and the percentage of these *relative to the total. For comparison with natural systems, all discharges can be considered cloud-to-ground (CG) lightning. Error in the number of discharges is ± 1.*

satellite imagery for each case study (Figure 5.3). The brightness temperature difference analysis reveals a characteristic ice signature (positive concave downward shape) and the comparison of the brightness temperature difference curves with lightning locations reveals that most lightning is detected in the opaque part of the volcanic plume. In some cases, particularly during the Taal eruption, volcanic lightning is collocated with semi-transparent pixels, suggesting the presence of ice particles. For comparison, the lightning data recorded by the Earth Networks Global Lightning Network (ENGLN) were also employed. Unlike the ENTLN, the ENGLN includes lightning detected by the WWLLN. As noted above, the WWLLN is often utilised in studies of volcanic lightning (Van Eaton et al., 2016, 2020; Hargie et al., 2019; Prata et al., 2020; Schultz et al., 2020). As this study focuses on the polarity of CG events, we include the WWLLN data but also provide lightning flash counts without these data, as WWLLN preferentially detects a higher proportion of CG lightning compared to IC lightning (Abarca et al., 2010; Hargie et al., 2019). Table 5.2 presents the detected lightning both with (Table 5.2a) and without (Table 5.2b) WWLLN data.

The characteristics of the volcanic lightning (i.e. flash rate, polarity, proportion of IC to CG) are complex and evolve with time. Upon closer investigation of the ENTLN results (Table 5.2b), we observe that the number of IC flashes detected is greater than the number of CG flashes detected and the proportion of +IC lightning was generally higher than -IC lightning for most cases. Anak Krakatau, during some of the observed intervals, was the only exception. Note that in the case of IC lightning, +IC and -IC refers to upward and downward propagation, respectively, between regions of positive and negative charge within an electrified cloud (Schultz et al., 2020). The proportion of +CG lightning was as high as 75% of the total CG lightning detected during some of the observed time intervals at Taal, but -CG lightning dominates over +CG lightning for all five eruptions. Figure 5.3 presents a snapshot during each eruption sequence where the brightness temperature difference curves conform to an ice-particle signature and coincide with peak lightning occurrence detected by the ENTLN network. At the time intervals of peak lightning discharge, the total number of flashes ranges from a minimum of 11 for the Fuego eruption (Figure 5.3a) to a maximum of 649 for the Taal eruption (Figure 5.3e). The number of CG discharges during this same time interval ranges from a minimum of 5 for the Fuego eruption (Figure 5.3a) to a maximum of 123 for the Anak Krakatau eruption (Figure 5.3c). The proportion of -CG is 100% of this total number in all cases, except for Taal, for which it was 93.6% (Figure 5.3e). Consequently, when CG lightning activity is at its peak during these five explosive eruptions, it is almost exclusively -CG.

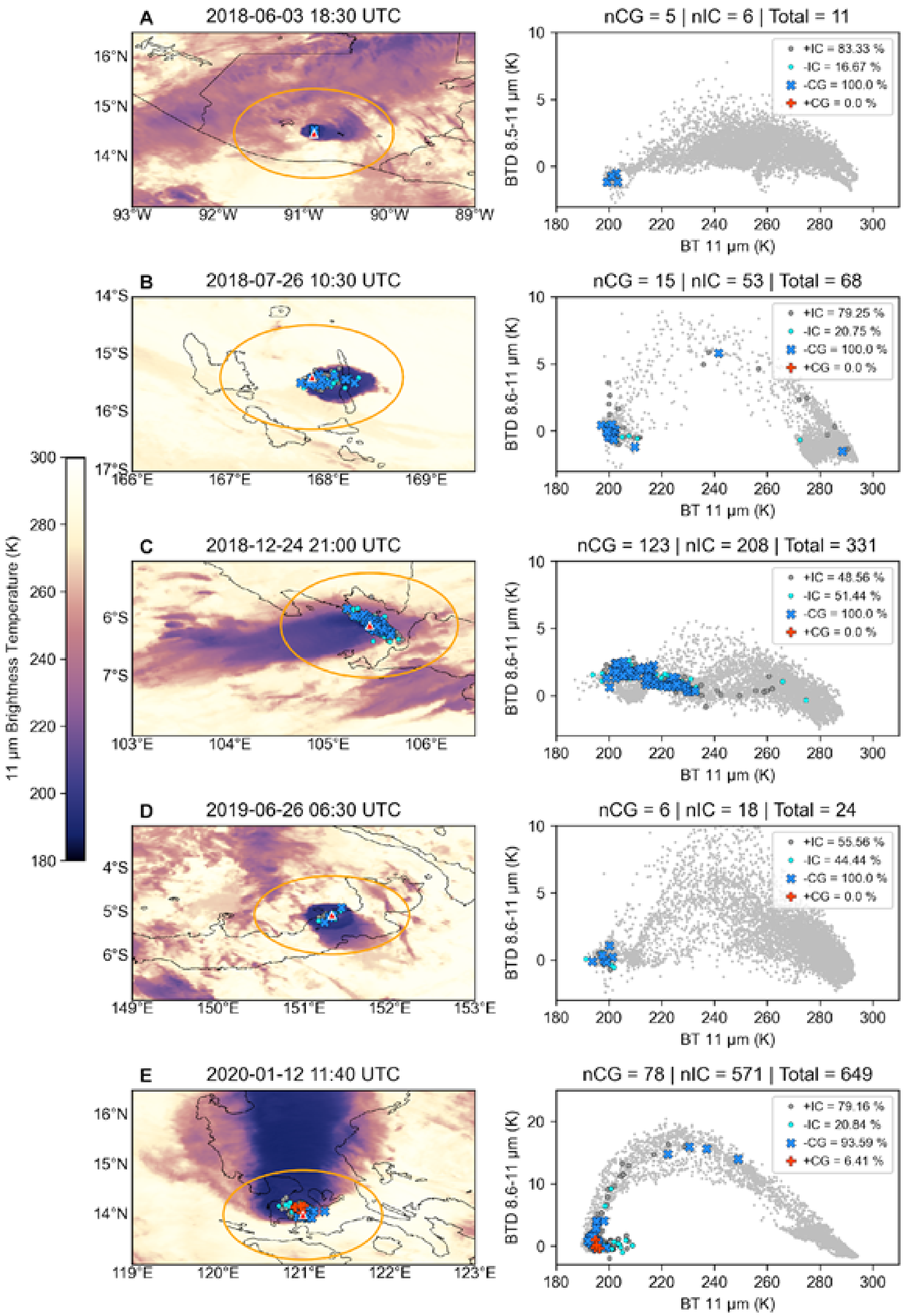

*Figure 5.3: Left panels: Panel **a** is GOES-16 11 μm brightness temperatures (BTs). (Continued)*

Figure 5.3: (Continued) The remainder are Himawari-8 11 μm BTs, with -CG (blue crosses), +CG (red pluses), -IC (blue circles) and +IC (grey circles) lightning flashes detected by the ENTLN network. Right panels: 11 μm BTs plotted against the 8.6 μm (8.5 μm for GOES-16) and 11 μm brightness temperature differences (BTD). Only data points within a 100 km radius (orange oval in left panels) are shown. The total number of discharges is given for these time intervals (Total = n), in addition to the number of cloud-to-ground (nCG) and in-cloud (nIC) discharges. ***a)*** *2018 Fuego eruption;* ***b)*** *2018 Ambae eruption;* ***c)*** *2018 Anak Krakatau eruption;* ***d)*** *2019 Ulawun eruption; and* ***e)*** *2020 Taal eruption.*

Table 5.2: ***a)*** *Lightning recorded by the Earth Networks Global Lightning Network (ENGLN) for each examined eruption, which includes data from the World Wide Lightning Location Network (WWLLN). Only lightning within a 100 km radius of the volcano that occurred between the start and end times of the eruption were considered. All WWLLN flashes are classified as CG.* ***b)*** *Earth Networks Total Lightning Network (ENTLN) data, which does not contain flashes detected by the WWLLN.*

a) ENGLN including WWLLN data

Volcano	Start time (UTC)	End time (UTC)	Cloud-to-ground (CG)			Intracloud (IC)			Total lightning
			+CG	-CG	Total CG	+IC	-IC	Total IC	
Fuego	16:00 03/06/2018	18:45 03/06/2018	6	26	32	21	12	33	65
Ambae	09:00 26/07/2018	12:00 27/07/2018	0	118	118	123	45	168	286
Anak Krakatau	12:00 22/12/2018	12:00 28/12/2018	44,734	32,203	76,937	12,537	12,901	25,438	102,375
Ulawun	04:00 26/06/2019	11:00 26/06/2019	18	140	158	42	41	83	241
Taal	06:00 12/01/2020	21:00 12/01/2020	396	3,209	3,605	10,073	4,410	14,483	18,088

b) ENTLN without WWLLN data

Volcano	Start time (UTC)	End time (UTC)	Cloud-to-ground (CG)			Intracloud (IC)			Total lightning
			+CG	-CG	Total CG	+IC	-IC	Total IC	
Fuego	16:00 03/06/2018	18:45 03/06/2018	0	18	18	21	12	33	51
Ambae	09:00 26/07/2018	12:00 27/07/2018	0	57	57	123	45	168	225
Anak Krakatau	12:00 22/12/2018	12:00 28/12/2018	0	23,465	23,465	12,537	12,901	25,438	48,903
Ulawun	04:00 26/06/2019	11:00 26/06/2019	0	32	32	42	41	83	115
Taal	06:00 12/01/2020	21:00 12/01/2020	213	1,063	1,276	10,073	4,410	14,483	15,759

5.5 Discussion

5.5.1 Implications of experimental results

As shown in Table 5.1, there is wide variability in the number of discharges that consequently occur, even between experiments with identical sample arrangements. These variations in the results are due to variability in the materials used; mainly the inability to produce ice with consistent grain size distributions and changing ice size throughout the experiments due to collision events. It is likely that during the expansion of the gas-particle mixture upon decompression in the shock tube, the ice particles would progressively decrease in size due to mechanical interactions between them and with the autoclave. The mass of both ice and ash inserted into the autoclave was carefully measured for all experiments. Nonetheless, further experiments using controlled ice particle sizes and size distributions will likely enable improved repeatability, allow quantification of the charging mechanisms, and also permit examination of how ice charging varies with particle size. A primary motivation for these experiments was to determine if ash and ice produced comparable discharge behaviour in the shock tube despite being very different materials. Thus, testing a wide variety of sample arrangements was paramount during limited facility availability. Further experiments can confirm or refute the repeatability of these results.

Previous shock tube studies (Cimarelli et al., 2014; Stern et al., 2019) have shown that introduction of ash into the FC generates discharges of negative polarity. The presence of water was also shown to affect the tribo-electrification of ash particles during experiments, as it decreases the transfer of charge by adhering to the surfaces of insulating particles (Stern et al., 2019; Méndez Harper et al., 2020). The charge introduced to the FC by both the ash and ice in our experiments may originate from the friction of these particles with the interior walls of the autoclave, particle-particle collisions before and during ejection, and fracto-charging upon decompression. The sample expands into the collection tank held at room temperature (∼22 °C), well above the freezing point of water (0 °C). As the ice exits the nozzle, travelling at a velocity of $>$100 m/s, it will impact both the interior of the autoclave, the ash grains (if present), and other ice particles. Although water is not inserted into the autoclave, small amounts are likely generated on ice crystal surfaces as the sample enters the higher-temperature FC and also upon impact due to collisional melting (Dash et al., 2001); a process enhanced by surface irregularities and compositional impurities (Pengra et al., 1991; Beaglehole and Wilson, 1994; Netz and Andelman, 1997; Wettlaufer, 1999; Dash et al., 2001). Such melting may, in some cases, result in the ice crystals acquiring a negative charge, similar to the phenomenon exhibited by ice and graupel particles falling below the freezing level in thunderstorms (Dinger and Gunn, 1946; Kikuchi, 1965; Drake, 1968; Takahashi, 1969; Jayaratne and Saunders, 2014). The presence of this impact-generated water will also decrease the efficacy of tribo-electrification (Stern et al., 2019; Méndez Harper et al., 2020), providing an explanation for why samples containing ice generally show fewer discharge events. The charging mechanisms in these experiments are potentially different to those proposed in volcanic plumes, where several different mechanisms may simultaneously be at play, but the result is consistent: more ice leads to more lightning discharges of positive polarity.

Charging of ice particles in the mixed-phase region of thunderstorms has been a topic of extensive study. When two ice particles collide above the atmospheric freezing level, positive charge is acquired by the faster-growing particle, provided there is available water vapour (Baker et al., 1987; Saunders, 1994; Avila et al., 1996; Jayaratne, 1998; Saunders and Peck, 1998; Dash et al., 2001). The experiments presented here do not permit us to specify charging mechanisms at play in either the experimental apparatus or in volcanic plumes. However, if we consider that during eruptions, volcanogenic ice particles continue to grow once nucleated above the freezing level (due to abundant water vapour supplied by the explosion; i.e. high cloud water contents), then these particles may develop a positive charge as smaller, ice-free ash particles develop a negative charge before they eventually become sites of ice nucleation. As shown in the experiments here, whatever charging mechanisms are at play result in predominantly discharge events of positive polarity to ground (+CG) from the ice and discharge events of negative polarity (-CG) from the ash. Consequently, nucleation of volcanogenic ice in the plume may change the dominant sign of charge. This key finding suggests that volcanic ash and ice, regardless of charging mechanism and charge acquired by individual particles, will produce lightning discharges of *opposite* polarity.

The shock tube experiments presented here cannot re-create the complex, multiphase environment within explosive eruption plumes in its entirety, as ice crystals are not emitted from the vent with fragmented ash particles during the explosion. Thus, the charge structure of actual volcanic columns and plumes must differ in detail from that of our experiments. In near-vent regions, fragmented tephra will span a range of sizes from very fine ash particles (<32 μm) to large blocks and bombs up to several metres in diameter. Charged particles emitted from the vent during the jet phase of an eruption will enter a region of strong turbulence once entrainment of the ambient atmosphere occurs in the convective phase, and this will enhance particle collisions and tribo-electrification. These dynamics will produce clusters of charge in the near-vent regions of the column where coarser particles tend to develop a positive charge and finer particles develop a negative charge (Miura et al., 2002; Cimarelli et al., 2014). The turbulent nature of the convective column will inhibit stratification of charge (Behnke et al., 2013), and thus, charge clusters of opposite polarity may result in lightning discharges of smaller length scales (10s of metres). Over time, as turbulence decreases and ash plumes reach a height (and hence a temperature) sufficient for both ice nucleation and charge stratification, lightning discharges will be larger (several km) and more similar to those in thunderstorms (McNutt and Williams, 2010; Thomas et al., 2010; Arason et al., 2011; Behnke et al., 2013; Behnke and Bruning, 2015). In the case of eruptions dominated by magma-water interaction (as in the case of the phreatomagmatic eruptions of Anak Krakatau and Taal reported in this study), flash-steaming of ocean or lake water heated by the magma produces water vapour in excess compared to what generally is produced by magmatic degassing, inducing vigorous updrafts (20-40 m/s) exceeding those measured in deep convective systems. The ejection velocity of ice particles reproduced in our experiments double those estimated for phreatomagmatic plumes and very likely also the size distribution of particles exceeds that of ice particles generated in those eruptions. In this respect our experiments do not fully replicate the kinetic energy of collisions acting in nature but they rather set an upper limit and may be particularly valid for those eruptive phases where water-dominated strong convective plumes may generate ice in excess through fast nucleation of undercooled vapour.

5.5.2 Implications of satellite analyses

It is important to note that an explosive eruption is a continually changing system that varies over time, i.e. a system operating with a substantial degree of unsteadiness. Thus, with altitude and time, the proportion/size distribution of both volcanic ash and volcanogenic ice will vary, as will the optical properties of the plume and the number/characteristics of lightning discharges. There are also sources of uncertainty produced by the variable efficiencies of lightning detection networks. As stated previously, the WWLLN will detect more CG flashes, which have higher energy and higher peak currents compared to IC flashes. No system is able to detect 100% of lightning, but ground-based detection efficiency improves based upon location and density of sensor coverage (Hutchins et al., 2012). Discharges generated in the near-vent region by ash tribo-electrification may be missed by sensor networks due to lower peak current ($<$15 kA). This may bias volcanic lightning detection toward those flashes with greater current magnitudes (i.e. CG flashes).

In recent studies (Prata et al., 2020; Van Eaton et al., 2020), the nucleation of volcanogenic ice has been hypothesised to contribute to both the frequency and characteristics of the discharge events during explosive eruptions. As the majority of CG lightning strikes from thunderstorms are of negative polarity (e.g. Anderson and Eriksson, 1980; Rakov and Uman, 2003; Visacro et al., 2004), this analysis shows that so too are the majority of CG strikes from volcanic lightning. This is because the transition from ash particles to volcanogenic ice particles results in similar charging mechanisms (i.e. hydrometeor tribo-electrification) in both environments. For the five explosive eruptions examined here, the lightning detection and satellite retrievals indicate that the majority of CG volcanic lightning will be -CG, similar to the majority of thunderstorm lightning. As revealed in the satellite analyses, external water plays an important role in the amount of CG volcanic lightning. The Fuego eruption produced only 5 CG flashes during the time interval of peak lightning occurrence, while the Anak Krakatau and Taal eruptions produced 123 and 78, respectively. The latter two volcanoes exist in more water-rich environments compared to Fuego, increasing the amount of water vapour lofted to altitudes sufficient for ice nucleation.

Importantly, our shock tube experiments corroborate the satellite analyses, indicating that ash will cause dominantly -CG lightning while ice causes dominantly +CG lightning. It is very likely that the mixed-phase environment of a volcanic plume may favour the production of -CG, while prevalent +CG may be dominating vigorous advection of vapour-derived ice particles during intense phreatomagmatic phases of an eruption. However, amongst other variables it can be expected that the relative proportions of magmatic volatiles versus external water will also play a significant role. Thus, in future analyses of volcanic lightning using local and regional lightning detection networks, it is plausible that the percentage of +CG events may provide a means to quantify the relative amount of volcanogenic ice nucleation in the eruption plume.

5.6 Conclusions

Shock tube decompression experiments were conducted to examine the interaction of volcanic ash and ice particles and the resulting polarity of lightning discharge. Near-vent, cloud-to-ground (CG) discharges were simulated using a sample composed 1) solely of volcanic ash grains, 2) solely of ice, or 3) a combination of ice and ash. Experiments show that volcanic ash will produce discharge events with dominantly negative polarity (-CG), while the presence of ice results in discharge events with dominantly positive polarity (+CG). Experiments using ice generally had fewer discharge events than those using only ash, potentially due to the generation of water on ice grain surfaces upon collisional melting, which inhibits triboelectrification. These experimental findings are consistent with volcanic lightning detection and satellite analyses of explosive plume properties during five eruptions in 2018-2020. -CG events dominate over +CG events in the optically opaque portions of the plume at levels where ash is dominating. Findings suggest that, during explosive eruptions, as the proportion of volcanogenic ice increases with altitude above the appropriate isotherm (-20 °C), the proportion of lightning discharges with positive polarity will also increase and lightning properties may provide a means to quantify the amount of volcanogenic ice nucleated on ash grains.

Chapter 6

Standing shock prevents propagation of sparks in supersonic explosive flows

6.1 Abstract

Volcanic jet flows in explosive eruptions emit radio frequency signatures, indicative of their fluid dynamic and electrostatic conditions. The emissions originate from sparks supported by an electric field built up by the ejected charged volcanic particles. When shock-defined, low-pressure regions confine the sparks, the signatures may be limited to high-frequency content corresponding to the early components of the avalanche-streamer-leader hierarchy. Here, we image sparks and a standing shock together in a transient supersonic jet of micro-diamonds entrained in argon. Fluid dynamic and kinetic simulations of the experiment demonstrate that the observed sparks originate upstream of the standing shock. The sparks are initiated in the rarefaction region, and cut off at the shock, which would limit their radio frequency emissions to a tell-tale high-frequency regime. We show that sparks transmit an impression of the explosive flow, and open the way for novel instrumentation to diagnose currently inaccessible explosive phenomena.

6.2 Introduction

In nature, electrical discharges are frequently observed in widely diverse environments that, beside the common occurrence in thunderclouds (Rakov, 2013), include also volcanic plumes (McNutt and Williams, 2010) and other turbulent particle-laden flows such as dust devils (Lorenz et al., 2016), on Earth and other planets. The underlying processes are regulated by the mechanism of induction and separation of electrical charges. Upon electrical discharge, radio frequency (RF) emissions can be recorded, thus providing a means to track the progressive evolution in space and time of the discharge source. Analogous to the detection of thunderclouds and storms, RF detection is now also being used to detect, and inform on the hazards associated with ash-laden volcanic plumes and ash-clouds. In particular the occurrence of electrical discharges at active volcanoes under unrest can be regarded as an indication of the onset of hazardous explosive activity and the production of ash plumes (Behnke and McNutt, 2014; Coombs et al., 2018; Baissac et al., 2021). In addition, both observable discharges and RF emissions can reveal the mechanisms that initiate the discharges (Rison et al., 2016). The broad RF spectrum associated with lightning discharges results from cascading processes on a hierarchy of time and spatial scales (Bazelyan and Raizer, 2000, 2017). Electric fields accelerate electrons, creating ionisation avalanches (Nijdam et al., 2020). A single, or several merging avalanches can collect enough space charge to form a streamer, and such streamers may merge to form a hot self-sustaining plasma channel: a leader. Avalanches and streamers emit very high frequencies (VHF) and leaders emit bright flashes of light together with lower frequencies (Rakov, 2013; Behnke et al., 2014; Liu et al., 2019).

Nature points us to examples where supersonic flows and shocks from explosive events may suppress parts of the hierarchy of the discharge phenomena, such as leaders (Behnke et al., 2018). In particular, explosive volcanic eruptions produce supersonic flows through the sudden release of overpressured gases contained in the erupting magma, resulting in shock waves. Observation of erupting volcanoes in Alaska (Thomas et al., 2007; Behnke et al., 2013), Iceland (Behnke et al., 2014), and Japan (Behnke et al., 2018) have revealed that in the first few seconds following the onset of an explosive eruption, RF signatures distinct from those produced by leader-forming lightning are recorded in the vicinity (within 10's to 100's of metres) of volcano vents. This early quasi-continuous RF emission is called continual radio frequency (CRF). CRF consists of discrete VHF RF spikes, occurring at rates of tens of thousands per second. Lower frequencies are absent during most of the duration of the CRF although they do occur sporadically, and coincide with prominent visual discharges. These observations suggest that supersonic shock flows may alter the breakdown process hierarchy, so that frequent electrical discharges are occurring with only sporadic leader formation (Behnke et al., 2018). The hot, opaque plume makes it difficult to determine how the discharges are altered.

Rapid decompression shock tube experiments allow us to explore explosive flows in the laboratory (Alatorre-Ibargüengoitia et al., 2011; Chojnicki et al., 2015; Roche and Carazzo, 2019). In such experiments, a shock tube ejects a flow of gas and particles into an expansion chamber. Images of non-illuminated decompression reveal bright sparks that are mostly vertical immediately above the nozzle of the shock tube, but bend horizontally at a certain height (Cimarelli et al., 2014; Gaudin and Cimarelli, 2019; Stern et al., 2019). Méndez Harper et al. (2018) suggests that the barrel shock structure of a high pressure outflow localises sparks. Here, we report simultaneous imaging of the Mach disk and coinciding spark discharges, and we provide results of fluid dynamic and kinetic simulations describing the shock flows and breakdown processes. The spatial and temporal scales of the sparks convey an impression of the shock tube flow and kinetic simulations indicate that conditions for discharge are most favourable just upstream of the Mach disk.

6.3 Methods

6.3.1 Fast decompression experiments

The fast decompression experiments at the Special Technologies Laboratory (STL) described here are designed and operated as described in Alatorre-Ibargüengoitia et al. (2011) and Cimarelli et al. (2014) with two notable exceptions. A 1 l reservoir volume is added to the high-pressure side to ensure the transition to the “infinite” reservoir Mach disk regime. Moreover, for the low particle content shot described here, natural 5 μm diamond powder (Lands Superabrasives, LSNPM 3–7, $\sim$5 μm) was deposited through a previous decompression along the walls of the shock tube and surfaces of the expansion chamber. By comparing the observed particles to shots with mg sample masses in the sample holder we determine the particle mass in the shot described here to be no larger than 100 mg. Argon gas is used to pump the high-pressure side of the shock tube. When the pressure exceeds the pressure at which the diaphragm (Oseco, 6.9 MPa, 2.54 cm diameter STD rupture disc) is rated to burst, the gas and entrained particles are rapidly ejected out of the transparent plastic vent above the baseplate into ambient air in the expansion chamber (with internal diameter 39 cm and height of 137 cm). The compressible fluid dynamics is diagnosed with a pressure transducer at the reservoir, and using camera images of the condensation plume. Camera 1 and 2 are Photron SA4 and SA3 high-speed cameras, respectively. For the shot described here camera 1 imaged a field of view of 11.1 × 11.2 cm, 9.9 cm above the nozzle and camera 2 imaged a field of view of 5.9 × 7.4 cm, 6.4 cm above the nozzle. The electrical activity is diagnosed using camera imaging and self-built inductive (ring) and dipole antennas.

In addition to the shot discussed in this paper, sparks were observed in the condensation during four illuminated argon rapid decompression experiments (6.9 MPa) with only diamond particles, and in one shot with residual 50 μm diamond and 150 μm graphite (15 g) before graphite entrainment was observable. In an illuminated shot with a considerable quantity of 5 μm diamond present (30 g) sparks framed by the condensation were not observed. This may be due to early entrainment of the particles creating an opaque and reflective cloud, which obscured observation of Mach disk framed sparks. In contrast, in two illuminated shots (6.9 MPa) of pure argon, only the sharp condensation boundary was observed without any sparks. With the illuminated blank shot for which RF was recorded, there was no RF activity between 0.3 and 13 ms. In a third pure argon shot with lights off, no sparks were observed at all, and there was no RF activity between 0.28 and 9.7 ms. The sharp boundary in the condensation without sparks was also observed in three gas shots without particles at the Ludwig-Maximilians-Universität (LMU) of Munich rapid decompression facility described in Cimarelli et al. (2014) with a burst pressure of 8.9 MPa. Notably, the LMU shock tube does not have a reservoir volume, resulting in more transient decompression.

6.3.2 Image analysis

A Hough transform (Duda and Hart, 1972) of the image was taken to identify and fit the edge in the image intensity caused by the sharp condensation boundary. The endpoints of the most probable edge were fit with a linear equation. The error was taken to be the difference between the heights at the ends of the fit line. To avoid confusion with intensity edges from stationary components such as the antennas, the image frame was cut to a 200 × 232 pixel frame of the central area immediately above the inductive antennas. The known distance between the three inductive antenna rings and a pixel count between the rings determined the cm per pixel resolution of the camera frames.

6.3.3 Fluid dynamic simulations

Only the shock tube with the reservoir was simulated here. The simulations of the argon flow were conducted by solving compressible Navier-Stokes equations with the HyBurn code based on the AMRex framework (Zhang et al., 2019). HyBurn uses a high-order Godunov algorithm with the HLLCM approximate Riemann solver (Shen et al., 2016) and the seventh-order WENO method (Balsara and Shu, 2000) to reconstruct the primitive variables (pressure, temperature, and velocity). The solution was marched in time using third-order strong-stability preserving Runge-Kutta (Gottlieb, 2005). HyBurn implements the complex geometry of the gas reservoir, shock tube, and expansion chamber using immersed boundary methods (Chaudhuri et al., 2011). First, the geometry was drawn using the SolidWorks computer-aided design package and exported to a stereolithography file. The complex geometry was input into HyBurn by generating a signed-distance function (Min and Gibou, 2007) based on the intersection points of triangles in the stereolithography file with the computational mesh. The boundary conditions on the embedded geometry are enforced using the method of images (Chaudhuri et al., 2011). The uncertainty in the simulation was determined by varying the burst pressure of the diaphragm within the -3% / +6% rating of the manufacturer and by conducting a convergence study. The convergence study revealed that not all features of the flow at the 90° reservoir connection to the shock tube can be resolved; however, the Mach disk evolution is relatively insensitive to the resulting variation in pressure profile due to Mach disk hysteresis (Irie et al., 2005).

6.3.4 Kinetic simulations

The Townsend ionisation coefficient α is calculated with the Boltzmann solver BOLSIG+ (Hagelaar and Pitchford, 2005). To calculate α, BOLSIG+ needs density, temperature, electric field, and molecular cross-sections. The spatial distributions of density n_0 and temperature are obtained from the Hyburn fluid dynamics simulation output. The reduced electric field E/n_0 is modelled as described in the results section. Among neglected effects is the influence of the metallic burst disc fragments pointed out in Figure 6.2. A future campaign with non-fragmenting burst discs could determine if the model needs to be adjusted. The argon reaction cross sections are obtained from the LXCat (Pitchford et al., 2017) Morgan database (retrieved on May 21, 2020). The background ionisation to neutral ratio is approximated from the Saha equation as $\sim 10^{-28}$; the results are very insensitive to this number. BOLSIG+ produces as output the reduced ionisation coefficient α/n_0, which is very strongly dependent on E/n_0. The procedure for finding potential breakdown paths begins with tabulating all local maxima of α to use as initiation points for discharges. Paths are then found by computing forward and backward streamlines along the electric field through these points, terminating when α falls below some chosen threshold. Finally, we integrate α along each path to obtain the total number of ionisation lengths K, allowing direct comparison to Equation 6.2. This model provides a rough estimate of the discharge conditions in the bulk flow.

6.4 Results

6.4.1 Optical observations

To better understand the peculiar localisation of spark discharges in the supersonic jet flow, we imaged the evolution of gas-particle mixtures under rapid decompression. In contrast to previous shock tube experiments designed to investigate the role of grain size distribution (Gaudin and Cimarelli, 2019), mass eruption rate (Gaudin and Cimarelli, 2019), and water content (Stern et al., 2019) in the electrification of volcanic jet analogues, here we focus on the time-space relationship of the discharges and the standing shock, with the objective of informing computer simulations. A series of shock-tube experiments was carried out using mixtures of argon gas and micrometric unimodal diamond powder with nominal average diameters of 5, 50, 250, and 500 μm. Rapid expansion experiments were performed with starting confining pressures of 6.9 and 8.9 MPa depending on the strength of the diaphragms used (Table F.1 of Appendix F). In contrast to previous experiments that used multiple grams of particulate samples to study the dependence of the spark discharges on the standing shock (Méndez Harper et al., 2018), here we use a reduced load of particles to enhance the transparency of the flow and the imaging of the shock barrel evolution over time.

The experimental setup (Figure 6.1a) consists of a shock tube ($\sim$2.5 cm inner diameter) connected through a nozzle to a large expansion chamber where cameras and antennas diagnose the emerging plume. The images in Figure 6.1b–f image a space extending 9.9 cm above the nozzle and show a plume of argon entrained with <100 mg unimodal natural micro diamond powder ($\sim$5 μm diameter) acting as charge carriers released through the nozzle into ambient air (2019-03-08 10:15 in Table F.1 of Appendix F and data appearing in Figures 6.1-6.4 and Table 6.1, Appendix F Note 1). A time sequence displayed in Figure 6.2 shows the fast decompression process with a condensation cloud forming above the nozzle, rising, and then falling, while sparks appear inside the cloud, outlining its sharp upper boundary. Time is referenced to the first pressure increase at the nozzle. In the first 300 μs (blue squares) the condensation appears in the field of view of the camera, rising in height with a sharp top boundary consisting of a flat center and faintly triangular edges, more evident in ensuing images. The condensation boundary then rises above the field of view; but reappears and declines after 1 ms (orange squares). The sparks are localised inside the bounding condensation cloud in the t = 1.19 ms and t = 1.41 ms frames (red squares, and expanded in Figure 6.1b–e). Visible sparks trace the top edge of the condensation boundary including the left edge triangle (t = 1.19 ms) and appear vertically through the volume of condensation (t = 1.41 ms). Another spark is visible in the t = 1.33 ms frame of camera 2 (Figure F.1 of Appendix F). After 1.5 ms the decline of the condensation slows down, and the boundary (including triangular edges) becomes sharper (black squares, and expanded in Figure 6.1f).

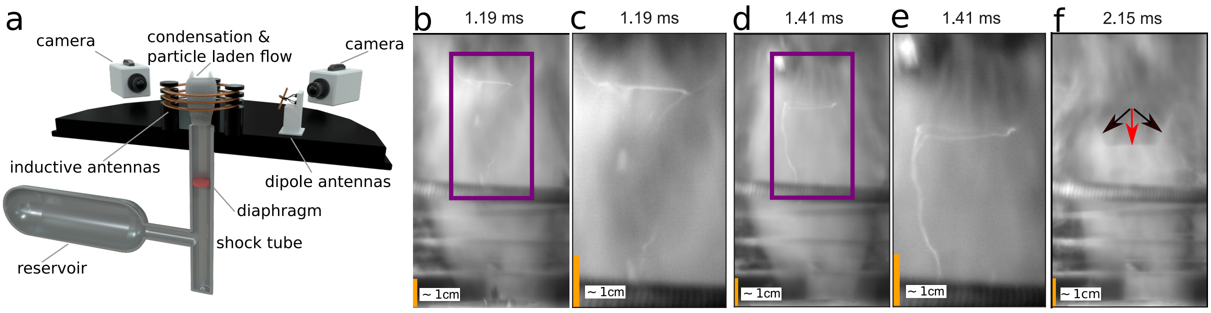

Figure 6.1: Sparks occur below a sharp boundary of the condensation in fast decompression experiments. ***a)*** *Layout of fast decompression experiment. A diaphragm (red) separates a tube into two sides. The bottom side is filled with varying amounts of particles below an inlet connecting to a gas reservoir, and is pumped to high pressure. The top side of the shock tube connects to an expansion chamber held at atmospheric pressure. The diaphragm bursts at a prescribed pressure, letting the particle-laden gas expand along the tube to the nozzle where a plume and electrical sparks are observed by high-speed cameras, and inductive (ring) and dipole antennas. The gas reservoir delays depletion of the high-pressure gas.* ***b, d)*** *Images of condensation and sparks in low particle content, fast decompression.* ***c, e)*** *Enlarged view of the purple-boxed area containing the visible spark.* ***f)*** *Image of the condensation at later time with sharper flat top boundary (marked by red arrow) and triangular edges (marked by black arrows). Both the condensation and the sparks have a ring-like horizontal upper boundary. Triangular edges are visible in the condensation and the sparks shown in panel* ***c****. The time t refers to time since the initial pressure increase at the nozzle.*

6.4.2 Fluid dynamic models

To relate the boundary to fluid dynamics we perform simulations of the argon gas flow in the full geometry, including reservoir, shock tube, and expansion chamber (simulated pressure and temperature). Table 6.1 records the timing of the sequence of events in the experiment in Figure

Table 6.1: Timeline of events, including Mach disk (MD) rise and decline speed, observed in experiment and simulation.

Observation	**Experiment**	**Simulation**
Shock passes nozzle	0 μs	0 μs
CS passes nozzle	-	120 μs
Condensation visible	150 μs	-
MD formation	300 μs	360 μs
MD rise speed	170 ± 70 m s^{-1}	220 ± 10 m s^{-1}
MD exits field of view	440 μs	540 μs
Rarefaction wave passes nozzle	-	540 μs
Reflected rarefaction wave passes nozzle	-	800 μs
MD re-enters field of view	1.0 ms	1.26 ms
Visible spark 1	1.19 ms	-
Visible spark 2	1.33 ms (Figure F.1)	-
Visible spark 3	1.41 ms	-
Initial (0.9-1.5 ms) MD decline speed	-40 ± 20 m s^{-1}	-114 ± 1 m s^{-1}
MD decline speed after 1.5 ms	-14.98 ± 0.03 m s^{-1}	-9.86 ± 0.07 m s^{-1}

Shock, contact surface (CS), and rarefaction passing refer to the shock tube characteristics exiting the nozzle. The rise and decline speeds are the slopes of linear regressions of the Mach disk height identified in the images and simulations. The measurement of the initial MD decline speed from camera images suffers from the more diffuse boundary in this phase.

6.1 and the simulation. The argon gas expands through the shock tube as described by fluid dynamic characteristics with the shock, the contact surface between the expanding argon and the low pressure air, and the rarefaction wave propagating through the tube (Figure 6.3b). When the gas reaches the nozzle, its pressure is higher than that of the ambient air. When the exit pressure P_e of an expanding gas greatly exceeds the background pressure P_∞ ($P_e/P_\infty > 4$) a singular Mach disk forms (Franquet et al., 2015) (Figure 6.3a). In the simulation results this is identifiable as a jump in pressure and temperature (Figure 6.4a). The Mach disk boundary in the simulation agrees in shape with the sharp condensation boundary observed in the camera images including the triangular edges. Upstream of the Mach disk the gas expands supersonically, dropping in pressure by 2 orders of magnitude and temperature to below 50 K. While the simulation does not account for phase changes such as heating due to condensation, this cooling is large enough for the argon to reach temperatures and pressures corresponding to the liquid-vapour phase interface (Bolmatov et al., 2015). In this case the presence of particles should enhance inhomogeneous nucleation, making it reasonable to assume that the condensation visible in the images is due to argon condensing (Liger-Belair et al., 2019). The Mach disk is surrounded by supersonic flows bounded by the shear layer between the expanding gas and the background atmosphere. At the edges of the Mach disk the pressure and temperature isosurfaces are triangular (Khalil and Miller, 2004) as outlined by the condensation and sparks. Downstream of the Mach disk the flow becomes subsonic and the gas piles up, leading to a pressure jump. The condensed argon vaporises through the shock wave because of the increment in the temperature and pressure by decreasing the kinetic energy. The

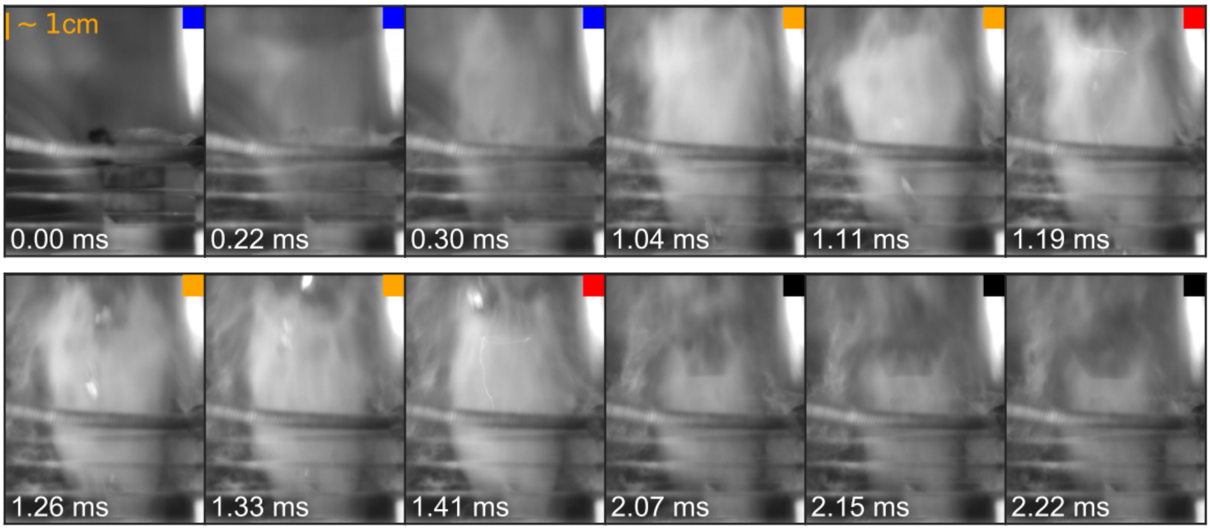

Figure 6.2: Image sequence of sparks and condensation cloud forming a sharp upper boundary, rising, and dropping captured by camera 1. Camera 1, exposing 20 μs frames at a rate of 13, 500 Hz, is triggered by a pressure increase at the nozzle (t = 0), and is viewing the nozzle opening and the region above the nozzle including portions of the inductive antennas (10.3 × 8.3 cm shown here). Coloured squares mark sequential phases of the decompression experiment: rise of condensation and formation of sharp upper boundary (blue), rapid drop of condensation boundary (orange) and electrical sparks (red), slower drop of condensation boundary (black). Sparks are visible in the 1.19 and 1.41 ms frames. Reflective ruptured diaphragm pieces are visible at 1.26, 1.33, and 1.41, and possibly 1.11 ms.

contrast between the condensed argon in the cool rarefaction region and its vaporisation due to heat of the shock, make its perimeter a tracer of the Mach disk. The simulation reveals the coupling of the Mach disk height to the pressure at the vent (Figure 6.4b). As the pressure rapidly increases and the fluid dynamic characteristics of the shock tube flow past the nozzle, the Mach disk forms and rises in both the experiment and simulation by $>$100 m s^{-1}. After 0.5 ms the Mach disk reaches its maximum height in the simulation, rising above the field of view of the camera. During this time, the nozzle pressure reaches its maximum as the reflection of the rarefaction off the bottom of the shock tube reaches the nozzle, after which the nozzle pressure decreases and the Mach disk recedes by $<$-30 m s^{-1}. At about 1.5 ms steadier pressure at the nozzle causes a slow down in the Mach disk decline to $\sim$ -10 m s^{-1}. This change in pressure at the nozzle is caused by a complex corner flow structure that forms at the right angle entrance of the high-pressure reservoir into the shock tube (Figure 6.1a). Initially, the outflow from the tube resembles a standard one-dimensional Sod shock tube flow (Sod, 1978). However, the corner flow creates a standing pressure wave that constricts the outflow from the reservoir and tube below the connection and drives asymmetries in the shock tube flow. In contrast to the outflow from an axisymmetric geometry with equivalent volumes, the corner flow creates observable asymmetries in the pressure profiles, which drive unsteady tilting of the Mach disk. Orescanin and Austin (2010) differentiates between constant pressure outflows, as “infinite” reservoir flows (Ogden et al., 2008; Carcano et al., 2014), and depleting pressure outflows as "finite" reservoir flows and noted that both can be described with a power law relation (Ashkenas and Sherman, 1965) for the Mach disk height h_m

$$h_m = Cd_m(P_n/P_a)^{\beta}, \tag{6.1}$$

where d_n is the nozzle diameter, P_n and P_a are the nozzle and ambient pressure, and C and β are constants. The observed condensation boundary heights are within the bounds of the power law for an "infinite" reservoir with C = 0.85-0.67 and β = 0.6 (Méndez Harper et al., 2018), with excursions in height occurring when there is a reversal in sign of the change in pressure (Figure 6.4b), possibly indicating hysteresis in the Mach disk height with respect to pressure changes (Irie et al., 2005). The agreement between the temporal evolution of the experimentally observed condensation boundary and the simulated Mach disk height are further evidence that the Mach disk regulates the condensation.

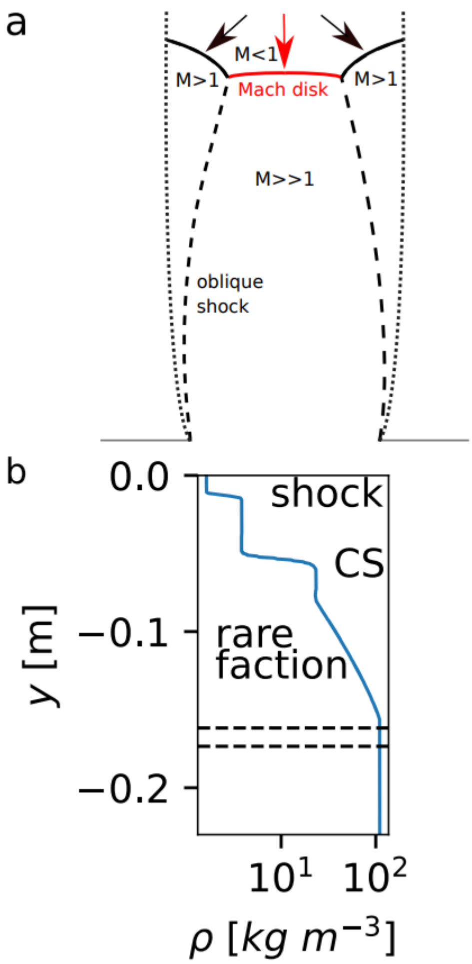

Figure 6.3: Structure of shock flow above and below the nozzle. ***a)*** *Structure of under-expanded jet above nozzle (Franquet et al., 2015) corresponding to t ∼ 1 ms in the experiment and simulation. Oblique shocks launching from the nozzle (long dashed lines) merge to form a flat shock surface, the Mach disk (red line marked with red arrow) separating supersonic rarefaction region from subsonic flow. The reflection of the oblique shocks (solid black line marked with black arrows) form triangular edges with the atmospheric pressure lines (short dashed lines). Discharges are observed in the rarefaction region below the Mach disk enclosed by the oblique shocks.* ***b)*** *Density along the center axis of the shock tube at t = 0.14 ms before the shock characteristics reach the nozzle at y = 0. The shock and contact surface (CS), and foot of the rarefaction region are moving towards the nozzle. The head of the rarefaction region is propagating towards the bottom of the tube and will reflect. Outflow from the reservoir connection (dashed lines) will later modify the Sod shock tube characteristics.*

6.4.3 Radio frequency measurements

Measurements of RF emission suggest that micro-particle charge carriers are necessary to produce sparks during the Mach disk lifetime. With particles present in the flow, both the inductive and dipole antennas respond to intermittent RF pulses throughout the decompression (Figure 6.5). The two sparks visible in camera 1 frames of Figure 6.1 were imaged at 1.19 ms when RF activity was recorded on the dipole and inductive antennas and at 1.41 ms when RF activity was recorded on the inductive antenna. There are also camera frames with no discernible discharge even though their exposure time overlaps with RF activity. This could be because discharges are obscured by condensation or are occurring inside the tube. There is also considerable RF activity during the inter-frame dead time of the cameras. In contrast, we note that fast decompression of an argon filled shock tube without particles produced only two pulses on the inductive antenna (2019-03-06 13:00 in Table F.1 of Appendix F and Figure 6.5 inset, Appendix F Note 1). These appeared within the first 500 μs and were an order of magnitude weaker in amplitude and probably associated with diaphragm rupture. Following that, no additional pulses were observed on either antenna for the ensuing 10 ms.

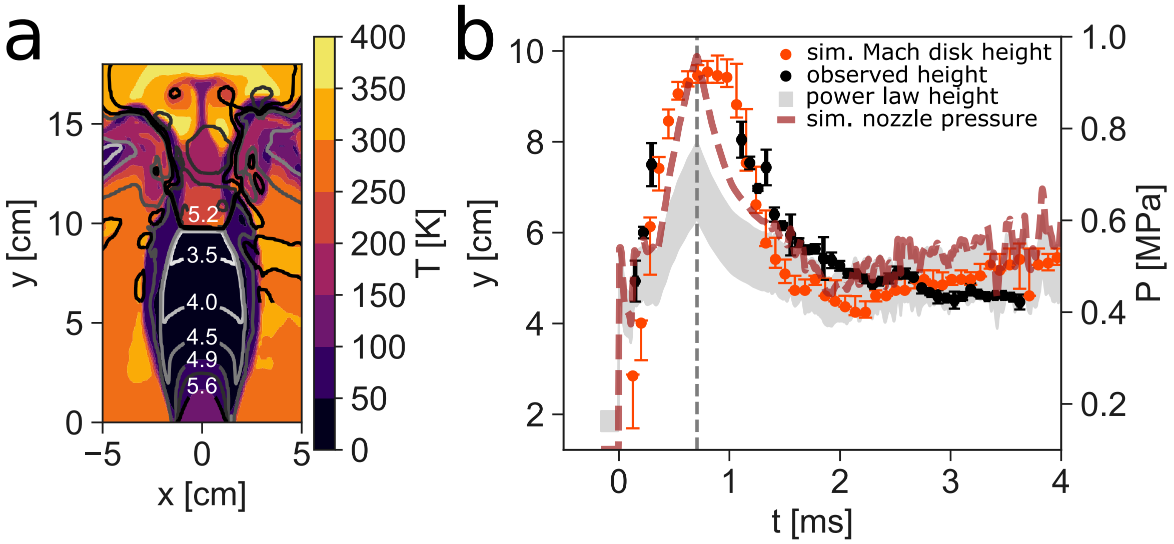

Figure 6.4: Simulation of Mach disk shock agrees with observed evolution of condensation boundary height. ***a)*** *Simulated temperature in K (filled colour contours) and* $\log_{10}$ *of pressure in Pa (grey contour lines) of fully formed Mach disk above nozzle at* $t = 700$ μ*s after the shock passes the nozzle (y = 0 cm).* ***b)*** *Simulation compared with experiment. Height of Mach disk shock in the simulation (red dots) plotted together with nozzle pressure in the simulation (rust dashes). Error bars in the simulated Mach disk height signify uncertainty due to the uncertainty rating of diaphragm burst pressure and under-resolved features in the corner flow at the reservoir connection. For comparison, the sharp boundary in condensation opacity as identified in the images of the low particle, fast decompression is plotted (black dots). Error bars of experimental Mach disk heights signify high and low points of a linear fit to the sharp condensation boundary in the images. The grey shaded region is the Mach disk power law height calculated with Equation 6.1, the simulated nozzle pressure,* $\beta = 0.6$*, and the "infinite" reservoir range of C values 0.85-0.67. Dashed grey line marks time of panel* ***a****.*

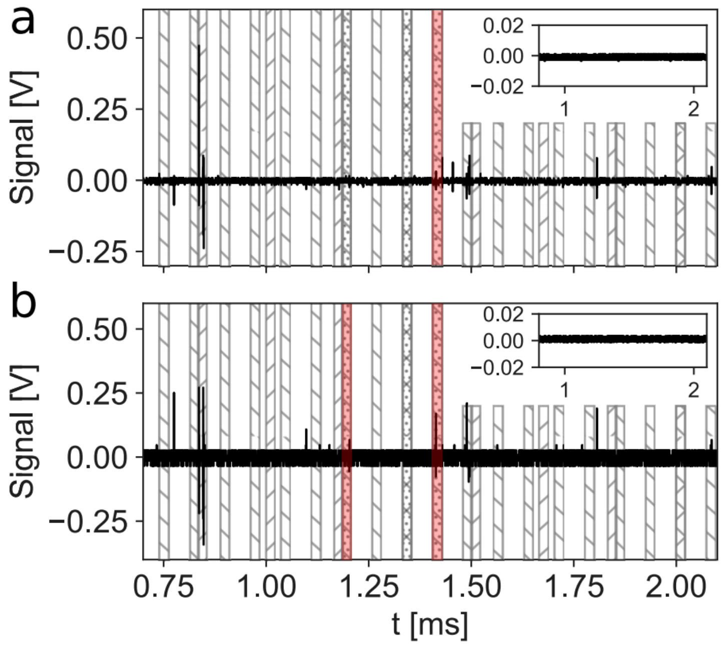

*Figure 6.5: RF measurements during the low particle mass, fast decompression. The exposure times of both high-speed cameras are marked with hatching (camera 1 frames with backward slashes and camera 2 frames with forward slashes). The three frames with visible sparks are marked with dots. The dipole antenna (**a**) records RF coincident with visible sparks at 1.41 ms (red). The inductive antenna (**b**) records RF coincident with visible sparks at 1.19 and 1.41 ms (red). For comparison, the insets show the signal on the respective antennas during a decompression without any particles.*

6.4.4 Electrical breakdown model

We now turn to analysis of the sparks below the Mach disk. Triboelectric and fracture-charging in the gas and particle outflow can result in a charge imbalance dependent on factors such as particle size distribution, with charge separation then occurring based on inertia (Yair, 2008). The resulting electric fields accelerate electrons, producing impact ionisations, which generate more electrons. When the electric field is high enough and the gas density low enough to allow for electron acceleration to energies sufficient for impact ionisation, this process results in electron avalanches (Raizer and Allen, 1991). As charge density increases, the resulting electric field becomes comparable to the external field and a streamer structure arises, with a low electric field in the interior and an enhanced external electric field that drives the advancing ionisation front.

The number of electrons in the avalanche N_e is roughly

$$N_e = e^{\int_0^d \alpha(E/n_0)dl}, \tag{6.2}$$

where α, the Townsend ionisation coefficient, is the net number of ionisations generated by a particle per unit length along a path, and the integral is taken over the discharge path l of length d. More precisely α is the difference between the Townsend ionisation and attachment coefficients; the latter is typically small for conditions of interest here. We have explicitly noted here the strong dependence of α upon the reduced electric field E/n_0, where E is electric field and n_0 is the local neutral gas number density; ionisation is driven by a strong electric field, but will be suppressed if particle mobility is impeded by too high a particle density. Conditions supporting avalanche may be identified via the Raether–Meek criterion (Raether, 1964), which specifies the required number of ionisation events along the path. This condition depends upon the gas; for argon it is roughly (Montijn and Ebert, 2006; Chvyreva et al., 2018)

$$K = \int_0^d \alpha(E/n_0)dl > 10, \tag{6.3}$$

where K is the natural logarithm of N_e. Méndez Harper et al. (2018) examined what effect the pressure drop upstream of the Mach disk has on the Paschen condition for Townsend breakdown (Townsend, 1910) in experimental volcanic jets similar to those presented here. The Paschen condition is valid for stationary discharges for $pd \leq 300$ Pa m, where p is pressure and d is the breakdown distance. Our observed breakdowns are dynamic over distances ranging from 2 to 8 cm in locations with pressure estimated at 0.03–0.05 MPa along the discharge path, making the pressure distance product $pd \sim 500\text{-}4000$ Pa m. In this regime the appropriate breakdown condition is the Raether-Meek criterion.

In our decompression experiments, the gas density is lowest in the uniform rarefaction region immediately upstream of the Mach disk (Figure 6.4a), and this region should therefore be favourable for producing discharges as E/n_0 will be high. Sparks in the presence of a Mach disk have been observed to trace out a flat top (Gaudin and Cimarelli, 2019; Méndez Harper et al., 2018) or a circle or semi-circle around the Mach disk, and extend along the edge of the low-density part of the barrel (Figure 6.1b–e).

While our fluid dynamic simulations capture gas dynamics well, they do not yet contain a charging model and we are therefore unable to compute electric fields or directly identify breakdown conditions. We can, however, try to surmise the E/n_0 required for streamer formation. To get a rough estimate of the required magnitude of E, we have computed α for an artificially generated, spatially varying electric field. We might expect charge separation to occur due to varying particle inertia in the direction of fluid flow in regions where this flow is relatively unidirectional. This would support discharges consistent with sparks such as those that are seen along the edge of the barrel in Figure 6.1e. For a very rough estimate of the electric field required to produce this spark, we analyse a model field aligned with the fluid flow in this region. Figure 6.6a shows the magnitude of an electric field defined to be in the direction of gas velocity with magnitude proportional to the velocity gradient, with an arbitrary magnitude scaling factor.

Using this model we have computed the Townsend ionisation coefficient α in order to surmise the E/n_0 required for streamer formation. Likely breakdown paths are identified by following along the electric field vector through local maxima of α. The integral of α along these integration paths gives the total number of ionisation lengths, K, allowing direct comparison to

Equation 6.2. Figure 6.6b shows the computed breakdown paths with largest K value for the time corresponding to the spark in Figure 6.1e (t = 1.41 ms). The location of the Mach disk just above 5 cm is marked by the pressure (magenta) isosurface. For this electric field, the maximum K was 23 ionisation lengths, with dozens of streamlines having $K > 10$, the rough argon threshold.

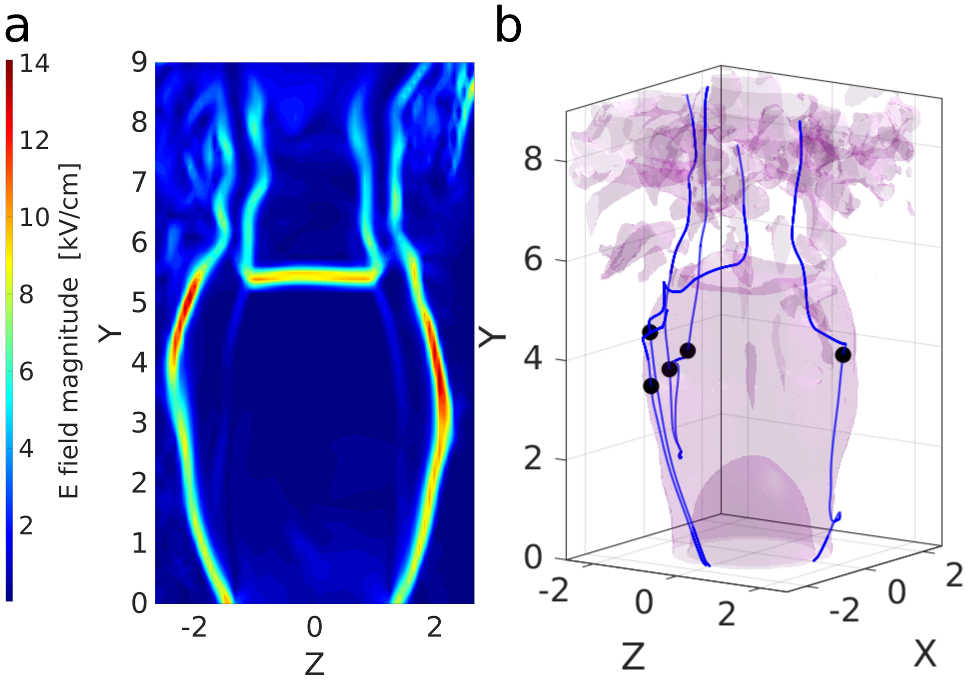

Figure 6.6: Possible discharge paths originating below Mach disk identified by Raether–Meek criterion given in Equation 6.2. ***a)*** *Model electric field generated as a function of gas velocity field. This model electric field and the fluid simulation data are the inputs to the Raether–Meek criterion.* ***b)*** *Isosurfaces of gas pressure 0.09 MPa (magenta), with streamlines marking possible breakdown paths. Black dots mark high-α initiation points for streamlines.*

Since our simple model produces breakdown paths strictly aligned with the velocity field, it cannot predict structures such as the illuminated ring or flat-top seen along the Mach disk in the experiment (Figure 6.1). Recent computational work (Starikovskiy and Aleksandrov, 2019, 2020) has investigated the effect of density discontinuities on streamers, demonstrating their redirection parallel to the discontinuity. This analysis is relevant to our Mach disk geometry and the ring-like horizontal discharges seen along the Mach disk boundary in Figure 6.1c and e. Further analysis of our case awaits implementation of a particle charging model in our simulations.

6.5 Discussion

We observe coincidence between sparks and a sharp boundary in the condensation of a fast decompressing gas loaded with a small quantity of solid particles. The observed sparks result from electrical breakdown and emit RF signals measurable on antennas. Based on the spatial coincidence of rarefaction condensation and electrical sparks, and, based on an analysis of streamer formation criterion upstream and downstream of the Mach disk, we argue that the space occupied by the first shock cell (the distance between the Mach disk and the nozzle exit) regulates the space in which electrical breakdown occurs in the presence of particles.

Explosive granular flows involve multi-phase flows coupled by drag. Solving these coupled multi-phase equations is complicated by non-conserved nozzeling and *pdV* work terms (Houim and Oran, 2016), and the effect of particle pressure (Johnson and Jackson, 1987; Gidaspow, 1994). Rapid decompression presents a validation challenge for granular compressible fluid dynamics models, which must represent the transition from the dense granular regime in the tube to the dilute granular regime in the expansion chamber. Imaging of the condensation, before the particles reach the plume, and sparks, after the particle plume obscures the condensation, may provide measurements of the Mach disk shape and height for comparison with models.

Explosive volcanic eruptions are an example of granular flows that could regulate breakdown processes. Experiments (Orescanin et al., 2010) and simulations (Ogden et al., 2008) have shown that the pressures released in a volcanic eruption could result in under-expanded flows forming standing shock waves with Mach disks (Kieffer, 1981); however, depending on their concentration and Stokes number, particles may perturb or inhibit the Mach disks (Carcano et al., 2014). If Mach disks do form in volcanic outflows, they may regulate electrical discharges between charged ash particles. The continual radio frequency (CRF) signature (Behnke et al., 2018), distinct due to the lack of low radio frequency emission, which is observed with coincident volcanic lightning (Cimarelli et al., 2016) appearing near the volcanic vent, may be regulated by the shock flow. If the sources of near-vent CRF emission are indeed regulated by standing shock waves, then distributed antennas could triangulate their locations, tracking the evolution of the regulating standing shock and providing insight into the pressure and particle content of the explosive flow. Our fast decompression experiments and simulations permit observation and analysis of explosive events producing RF at their onset, and may lead to insights into conditions, which favour streamer/avalanche over leader-forming lightning.

Conclusion and outlook

This study explored the conditions required for volcanic lightning to occur, by carrying out field measurements at three active volcanoes, Sakurajima volcano (Japan), Stromboli volcano (Italy) and Cumbre Vieja volcano (La Palma, Spain), using the electrostatic Biral Thunderstorm Detector (BTD) that had not been tested at volcanoes prior to this study. Additionally, contributions were made to investigate the effect of the presence of ice and a standing shock wave on the occurrence of electrical discharges in volcanic jets analogues by performing rapid decompression experiments inside a Faraday Cage.

The effectiveness of the BTD to detect volcanic lightning within the extremely to super low frequency range was assessed for a wide range of explosion magnitudes and eruption styles. Although the electromagnetic radiation emitted by lightning is strongest in the radio wave spectrum, the BTD demonstrated that it can successfully detect volcanic lightning, even during the smallest explosive events. Moreover, a great advantage of the BTD over the commonly used very low to very high frequency detectors is that it can discriminate impact transients from electrical discharges as well as detect movement of charge from nearby ash plumes (or pyroclastic density currents). Therefore, the BTD can provide additional information on ash cloud directions and the occurrence of ash fall at the sensor. A drawback of the BTD is that the 100 Hz sample rate is too low to accurately locate lightning. The measured voltage can be converted to an estimated distance, assuming the charge moment and an installation site correction, but this has only been done for meteorological lightning so far and thus will require more research. The intensity of the signals might make it possible, however, to distinguish nearby volcanic lightning (at a known source location) from distant thunderstorm lightning. The low sample rate does also not allow the detection of Continual Radio Frequency pulses, which occur in the gas-thrust region at the onset of an explosion, due to their short ($\sim$50 ns) duration. Nonetheless, this study has shown that volcanic lightning detected by the BTD can mark the inception of the explosion with a higher precision than commonly provided by volcano observatories, as it can detect electrical activity instantaneously without needing a direct line-of-sight to the active vent. Regional and global lightning detection networks did not detect any volcanic lightning during the explosions reported in this study, with the exception of 2 out of 511 explosions at Sakurajima. This shows that these lightning detection networks are limited in the detection of ash emissions during relatively small-scale explosive events, due to the scattered geographical distribution of their sensors and possibly additional filtering of the signals. Since visual surveillance is not always available, due to poor visibility, a remote location or limited funds, the cost- and data-efficient BTD would be a valuable addition to the monitoring systems of active volcanoes for the detection of ash emission. Current volcano warning systems rely on precursory signals from geophysical parameters, such as seismicity, acoustic recordings and ground deformation. As these parameters do not confirm the ejection of ash in the atmosphere, the electrical monitoring can complement these systems.

A volcanic lightning detection algorithm was developed in Python to automatically identify electrical discharges. A statistical analysis revealed that the algorithm could identify volcanic lightning during explosions at Sakurajima with an accuracy of $\sim$73% and a precision of $\sim$90%. Only minor modifications of the algorithm were necessary for each sensor location and volcano, as the empirical thresholds, such as the signal-to-noise ratio, depend on the distance between the active crater and the sensor, the magnitude of the explosive events and the local noise level. This suggests that it can be easily fine-tuned for other volcanoes as well. Furthermore, an important future enhancement of the instrument would be the implementation of telemetry for remote data transfer, so that the volcanic lightning detection algorithm may run continuously in order to provide volcanic activity alerts in near real-time.

The electrical monitoring of three different volcanoes provided the opportunity to investigate the electrical activity generated by a wide range of eruption styles (i.e. Vulcanian explosions, mild Strombolian activity, Strombolian major explosions and paroxysmal events, lava fountaining and ash venting), eruption magnitudes (Volcanic Explosivity Index (VEI) of -6 to 3 and plume heights ranging between tens of metres to 8.4 km) and magma compositions (from dacitic to more mafic magmas). In general, the BTD was able to detect electrical discharges and/or movement of charge regardless of eruption style or magnitude, implying that electrical monitoring can be applied to any volcano producing explosive activity. This should be further investigated in the future by expanding the miscellaneous assortment of explosive activity that has been studied so far. Additionally, it would be important to investigate whether eruption styles produce comparable electrical signatures at various volcanoes or if they are volcano-specific.

Although it is well-known that the presence of volcanic ash plays a key role in the generation of volcanic lightning, this study has proven that silicate particle charging is the main driver for plume electrification during smaller-scale explosive events. Based on comparisons made between maximum plume heights and atmospheric temperature profiles, it was concluded that it is improbable that ice nucleation occurred during the explosions studied here, as the ash plumes generally did not reach atmospheric freezing levels or were not sustained long enough for a sufficient amount of volcanogenic ice nuclei to become activated. Nonetheless, these explosions generated an abundance of volcanic lightning as a result of silicate particle charging, further demonstrating the effectiveness of electrically monitoring active volcanoes to detect ash emissions.

More importantly, strong correlations were found between the amount of electrical activity and the explosion magnitude. The extensive data set obtained at Sakurajima, containing hundreds of explosions of prevalent Vulcanian style, revealed that the number of discharges, the maximum measured voltage of a single electrical discharge and the maximum electrical discharge rate increase with increasing plume height, probably due to an increase in the mass eruption rate. Similarly at Stromboli, mild Strombolian explosions generated only faint electrical discharges and movements of charge of low magnitude related to the ejection of pyroclasts, while major explosions and a Strombolian paroxysmal event produced strong movements of charge and tens to hundreds of discharges, respectively. Although the differences in eruption style, magnitude, grain size distribution and composition between the explosions of Sakurajima and Stromboli prevent a direct comparison of the electrical measurements, it is evident from these observations that a greater erupted volume will result in enhanced plume electrification and, as a consequence, it will generate more volcanic lightning.

A variation of electrical signatures was observed during the 2021 Cumbre Vieja eruption, which could be linked to different explosive eruptions styles. Individual high-voltage (>0.01V) electrical discharges were detected during strong ash emissions, which produced plumes of several kilometres in height. Similar electrical signals were detected during the ash-rich Vulcanian explosions at Sakurajima and the major explosions and single paroxysmal event at Stromboli. From these observations we can conclude that the ejection of large volumes of volcanic ash results in strong electric fields within the eruption column as a result of intense silicate particle charging at the vent and subsequent charge separation and formation of charge clusters as the plume rises and grows by convection. The development of a strong electric field results in the generation of high-voltage electrical discharges that can extend hundreds of metres to several kilometres in length, also known as near-vent and plume volcanic lightning.

On the other hand, weak ash emissions, which produced ash plumes up to a few hundred metres high, generated faint electrical discharges (<0.002V) that generally remained undetected by the detection algorithm. Although similar observations were made at Stromboli during mild ash-rich Strombolian explosions, the greater distance between the sensor and the active vents at La Palma needs to be taken into account, as the electric field decreases with the distance cubed. Nonetheless, these results show that the lower erupted volume and likely the lower kinetic energy characterising these weak ash emissions hinders silicate particle charging. Electrically monitoring this type of activity is more complicated due to the low signal-to-noise ratios, in particular for the secondary antenna signal. However, this may be improved by i) installing the BTD at a close distance from the active crater; ii) modifying the detection algorithm to solely use the more sensitive primary antenna signal to identify electrical discharges and ii) complementing the electrical data with other geophysical parameters.

Furthermore, bursts of continuous electrical activity of low to intermediate measured voltages (<0.01V) were detected at Cumbre Vieja during phases of gas jetting, Strombolian activity and lava fountaining during which the production of volcanic ash was reduced. These three eruption styles have in common that they are driven by large volumes of gas, which results in lower kinetic energy, smaller erupted volumes and a wider grain size distribution, in comparison to the ash-rich explosions (e.g. Strombolian major explosions and paroxysmal events, Vulcanian explosions and strong ash emissions). As a consequence, the eruption columns are short-lived and only reach a few hundred metres in height, which hinders the development of a strongly electrified plume with large charge clusters. Instead, the large volume of gas likely intensified the amount of turbulence, resulting in rapid charging and more efficient discharging. Moreover, it is speculated that the explosion magnitude and intensity and possibly the temperature of the erupted mass control the timing and duration of these bursts, as gas jetting and lava fountaining produced seconds- and minutes-long bursts, respectively, while Strombolian activity generated more varied signals. These bursts of electrical activity have not been detected at Sakurajima and Stromboli, as their explosive activity is either much smaller in magnitude, as is the case for the mild Strombolian explosions, or is characterised by ash-rich volcanic plumes. Also, the prolonged continued explosive activity produced during the eruption of Cumbre Vieja is distinct from the typical intermittent activity of Stromboli and Sakurajima volcanoes.

To conclude, this study has shown that the amount of generated electrical activity is directly related to the eruption style and magnitude, which holds promise for estimating certain eruption parameters based on the detection of volcanic lightning in the future. Comparing the electrical measurements to source parameters, such as plume height, erupted volume, mass eruption rate, ejection velocity, grain size distribution and the temperature of the erupted mass, will be essential to obtain a deeper understanding of the underlying causes for the variations in electrical activity between different eruption styles and magnitudes.

In addition to investigating volcanic lightning in nature, the occurrence of electrical discharges can be examined in controlled rapid decompression experiments simulating volcanic jets inside a Faraday Cage.

Previous studies have shown that if volcanic ash plumes reach sufficient altitudes, ice nucleation can enhance the plume electrification and thus the amount of volcanic lightning produced. To study the effect of ice further, experiments involving volcanic ash and ice particles were carried out, which revealed a reversal in the polarity of the electrical discharges between the two components. Volcanic ash introduced negative charge in the Faraday Cage, which resulted in negative cloud-to-ground discharges. In contrast, ice particles introduced a surplus of positive charge, which was neutralised by positive cloud-to-ground discharges. Moreover, less electrical discharges occurred during experiments involving ice, most likely due to a thin layer of water forming on the ice crystal surfaces as a result of collisional melting, decreasing the efficacy of tribo-electrification. Although ice particles are not ejected during explosions in nature, these results are consistent with observations made during volcanic eruptions. Cloud-to-ground discharges during explosive eruptions are predominantly of negative polarity, with a greater proportion of positive discharges detected during eruptions that produced significant amounts of volcanogenic ice.

The sudden release of overpressured gases within the erupting magma can produce shock waves during explosive eruptions. Experiments with minor quantities of solid particles revealed that a standing shock wave can regulate the electrical discharges, as they are favoured upstream in the supersonically expanding flow. Although in nature the particles in the expanding flow most likely perturb or inhibit the formation of a standing shock wave, it is plausible that the occurrence of vent discharges (Continual Radio Frequency) is regulated by the shock flow.

Even though these volcanic jets analogues cannot re-create the complex, multi-phase eruption dynamics in its entirety, they provide the opportunity to study the effects of specific variables on electrical activity in a controlled environment, which might explain certain observations in nature. Moreover, this experimental approach allows the repeatability of self-similar explosions, which is uncommon in nature. Hence, besides exploring the conditions for the occurrence of volcanic lightning in nature, it is fundamental to continue to study electrical discharges in the laboratory as well.

Appendix A

Chapter 2

Long-term observation of electrical discharges during persistent Vulcanian activity

The volcanic lightning detection algorithm filters out the background noise, such as interference from the 60 Hz mains power in Japan, from both the primary and secondary signals. The resulting offset (V/cs) was calculated by taking the cumulative sum of the signal over a specific time window and then dividing it by the number of centiseconds, which is then subtracted from the raw data. The time window used to calculate the offset is determined by looking at the mean value of the signal. In general, the first 15 seconds of the 20-minute time window is only background noise, because the explosion has not started yet. The mean is calculated over these 15 seconds by only including signals with a measured voltage less than ±0.005V, to disregard any possible signals from nearby meteorological thunderstorms that were not detected by WWLLN. In some cases, however, the first 15 seconds contains the electrical signal of a previous pulse or ash passing over or falling on top of the sensor, which will lead to an incorrect offset value. Hence, in order to check if this time window is a good reference, it is compared to the mean value of the whole 20-minute time window (again only for signals smaller than ±0.005V). In case the mean value of the first 15 seconds deviates more than 10% from the overall mean, the overall mean is used as the value for background noise. Otherwise the 15 seconds mean suffices. This determines the time window to calculate the background noise. The mean value is additionally used to calculate the signal-to-noise ratio (SNR) by subtracting it from the raw signal and dividing it by the standard deviation of the signal over the same time window used to calculate the mean.

In order for the volcanic lightning detection algorithm to interpret a signal as an electrical discharge, several criteria needed to be met: 1) The signal needed to have the same polarity at both antennas, as they both detect the current induced on the antennas by a change in the electrostatic field, albeit with a different sensitivity. Opposite polarity indicates impact transients (e.g. charge transfer on contact with the instrument). 2) The ratio between the primary and secondary antenna needed to be above 5.5 for KUR and above 9.0 for HAR. The difference between KUR and HAR is likely due to significant differences in ground slope at the installation sites and/or the presence of nearby objects of sufficient height and proximity that alter the ambient electric field around the sensors. In addition, these values were chosen to discard/minimise potential false signals deriving from the electronics powering both instruments. 3) The SNR needed to be above 2.3 for the primary antenna and above 1.1 for the secondary antenna. The secondary antenna has a lower sensitivity than the primary one, which results in an overall lower SNR. The signal of the secondary antenna is mostly important for the discrimination between electrical discharges and impact transients, and can therefore have such a low SNR limit. On the other hand, the signal of the primary antenna allows the differentiation between electrical discharges and noise and thus requires a higher SNR limit. 4) The covariance needed to be above 2.9. Negative covariance indicates impact transients. In addition, the background noise at KUR and HAR commonly has a covariance below 2.9. These thresholds were obtained through trial and error. Future observations at other active volcanoes will further test the validity of the parameters used for this case study.

Appendix B

Chapter 2

Long-term observation of electrical discharges during persistent Vulcanian activity

The performance of the volcanic lightning detection algorithm was determined by comparing the “true condition” and the “predicted condition”. The true condition indicates whether electrical discharges are present (positive) or absent (negative) in the raw signal recorded by the sensors. On the other hand, the predicted condition gives the outcome of the volcanic lightning detection algorithm, i.e., whether discharges were identified by the algorithm or not. To evaluate the performance of the algorithm also during periods for which no explosions were reported by the JMA, a 20-minute time window was included for each day within the time of monitoring, which was selected on the hour by a random number generator available in Excel. It was assured that these time windows did not overlap with the time windows of the explosions. The analysed time windows were manually divided into four categories: 1) True Positive (TP), electrical discharges were recorded by the sensor and correctly identified by the algorithm; 2) True Negative (TN), no electrical discharges were recorded by the sensor nor identified by the algorithm; 3) False Positive (FP), no electrical discharges were recorded by the sensor, but the algorithm falsely identified signals as electrical discharges; 4) False Negative (FN), electrical discharges were recorded by the sensor, but remained undetected by the algorithm. Note that the focus lies on detecting the overall electrical activity – not on every individual discharge – to determine how effectively explosions can be recognised.

Signals from electrified ash clouds passing over and ash falling on top of the sensors were automatically disregarded by the algorithm, while volcanic lightning that occurred within the charged cloud could still be detected. These explosions were denoted as TP, of which an example is shown in Section 2.4.3. For unknown reasons, however, in several cases the electric field oscillations of the charged ash cloud were incorrectly identified as electrical discharges, resulting in many false detections. These explosions were therefore classified as FP.

The four categories make up the confusion matrix, denoted by the green and red colours in Table B.1. Several derivations can be made from the confusion matrix to quantify the performance of the algorithm, which are listed in a table of confusion (Table B.1). A detailed description of the meaning and equations of all derivations can be found in, e.g. Fawcett (2006); Chicco and Jurman (2020); Powers (2020); Tharwat (2020). In this study, we solely focus on the accuracy, precision and recall of the volcanic lightning detection algorithm. Accuracy gives the proportion of explosions for which the presence or absence of discharges was correctly identified by the algorithm (Equation B.1). Precision is defined as the number of explosions for which discharges were correctly detected divided by the total number of explosions for which the algorithm detected discharges (Equation B.2). Recall gives the probability of the algorithm to detect discharges in the explosions that were electrically active (Equation B.3). The results of the statistical classification for both KUR and HAR can be found in Table B.2.

$$Accuracy = (TP + TN)/(TP + TN + FP + FN) \tag{B.1}$$

$$Precision = TP/(TP + FP) \tag{B.2}$$

$$Recall = TP/(TP + FN) \tag{B.3}$$

In addition, the prevalence, here the fraction of explosions that produced electrical discharges, was calculated for the analysed explosion time windows alone (Equation B.4). Hence, this prevalence is different from the overall prevalence of the algorithm that is listed in Table B.2.

$$Prevalence = (TP^* + FN^*)/(TP^* + TN^* + FP^* + FN^*) \tag{B.4}$$

* *Only including the time windows for which explosions were reported by the JMA.*

Table B.1: Table of confusion.

		True condition				
Predicted condition	Total population	Condition positive	Condition negative	Overall prevalence	Accuracy	
	Predicted condition positive	True positive	False positive	Precision	False discovery rate	
	Predicted condition negative	False negative	True negative	False omission rate	Negative predictive value	
		Recall	Fall-out	Positive likelihood ratio	Diagnostic odds ratio	F$_1$ score
		Miss rate	Specificity	Negative likelihood ratio		

The green and red boxes make up the confusion matrix. The meaning and equations of all derivations are described in detail in, e.g. Fawcett (2006); Chicco and Jurman (2020); Powers (2020); Tharwat (2020).

Table B.2: Table of confusion showing the results for sensor KUR above and sensor HAR below.

		True condition KUR				
Predicted condition KUR	933	506	427	0.54	**0.72**	
	323	**285**	**38**	**0.88**	0.12	
	610	**221**	**389**	0.36	0.64	
		0.56	0.09	6.33	13.20	0.69
		0.44	0.91	0.48		

		True condition HAR				
Predicted condition HAR	1019	693	326	0.68	**0.74**	
	507	**466**	**41**	**0.92**	0.08	
	512	**227**	**285**	0.44	0.56	
		0.67	0.13	5.35	14.27	0.78
		0.33	0.87	0.37		

Box definitions are shown in Table B.1.

Appendix C

Chapter 3

The electrical signature of mafic explosive eruptions at Stromboli volcano, Italy

Figure C.1 shows the electrical signals recorded by BTD1 during three types of Strombolian explosions according to the classification scheme proposed by Gaudin et al. (2017a): Type 1 is bomb-dominated; Type 2a is dominated by both ash and bombs; Type 2b is ash-dominated (Patrick et al., 2007).

For each explosion, there was no variation detected in the secondary signal, indicating that the secondary antenna is not sensitive enough to detect any electrical activity during the Strombolian explosions. On the other hand, the primary antenna does show electric field gradients, visible as slow (~1-3 s) variations in the electrical signal. Additionally, several transients were detected during Type 2a and 2b explosions, which can be interpreted as small electrical discharges.

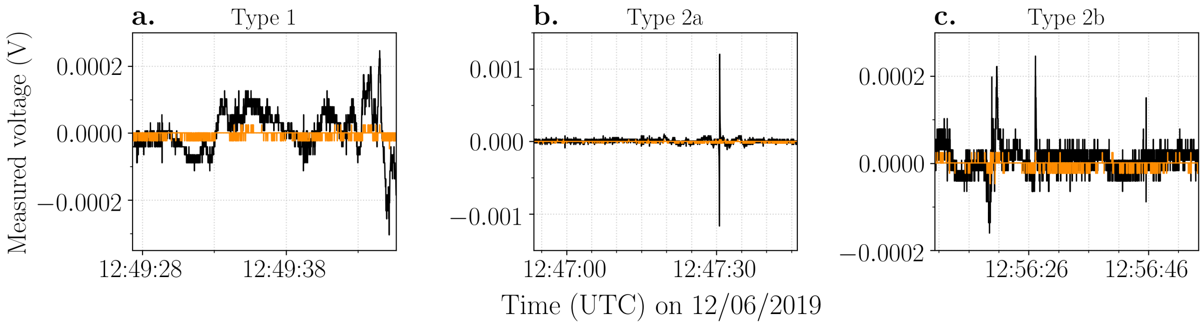

Figure C.1: Voltages (V) measured by the primary (black line) and secondary (orange line) antennas of BTD1 on 12 June 2019. ***a)*** *Strombolian explosion of Type 1.* ***b)*** *Strombolian explosion of Type 2a.* ***c)*** *Strombolian explosion of Type 2b. The time axes correspond to the duration of the explosions, during which pyroclasts were actively ejected.*

Figure C.2 shows the seismic signal recorded by Laboratorio di Geofisica Sperimentale (LGS) of the University of Florence, Italy, during the 19 July 2020 major explosion. The first peak in the seismic amplitude corresponds to the onset of the electrostatic oscillations recorded by BTD2 (Figure 3.3 in main text).

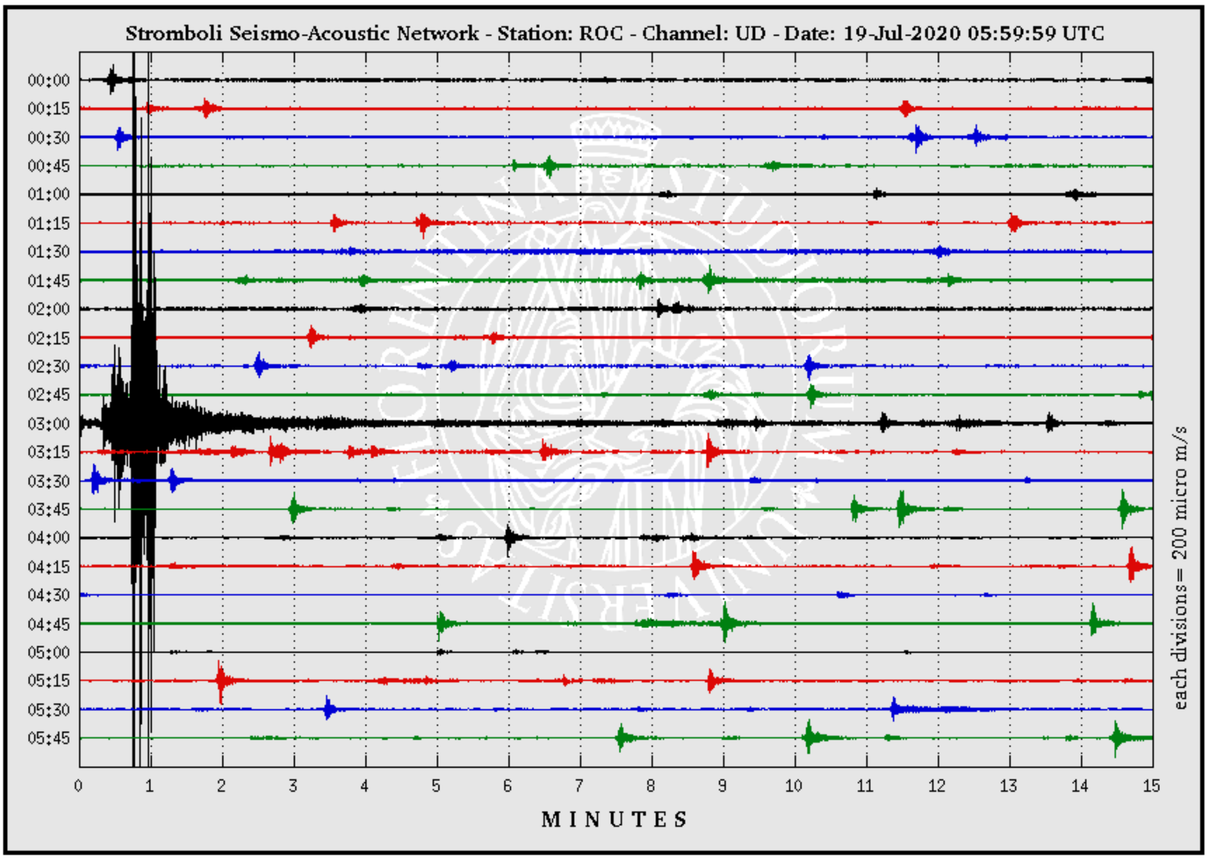

Figure C.2: Seismic signal recorded by LGS station "ROC" during the 19 July 2020 major explosion. Each horizontal line shows 15 min of data and each division on the y-axis corresponds to a seismic velocity of 200 μm/s. Retrieved from: http://lgs.geo.unifi.it/index.php/monitoring/volcanoes/stromboli2 [Accessed 22 December 2021].

Appendix D

Chapter 4

Linking electrical activity to explosive eruption styles during the 2021 Cumbre Vieja eruption

Temperature data from weather balloons released at Güímar (station 60018) on Tenerife, Canary Islands (Spain), is provided by the University of Wyoming, Department of Atmospheric Science (http://weather.uwyo.edu/), which are used to construct the 0 °C, -10 °C and -20 °C isotherms. To ascertain, however, that these measurements represent the conditions on La Palma as well, the data was compared to temperature measurements from two fixed weather stations on La Palma, at El Paso (altitude of 844 m) and Roque de los Muchachos (altitude of 2223 m) (Figure 4.1), carried out by the State Meteorological Agency (AEMET) of Spain. The comparisons are shown in Figures D.1 and D.2. Although the temperature difference between night and day is greater for the local stations on La Palma (AEMET), the overall trend is very similar between the two data sets. Therefore, we concluded that the Güímar data is sufficiently accurate to construct the different isotherms.

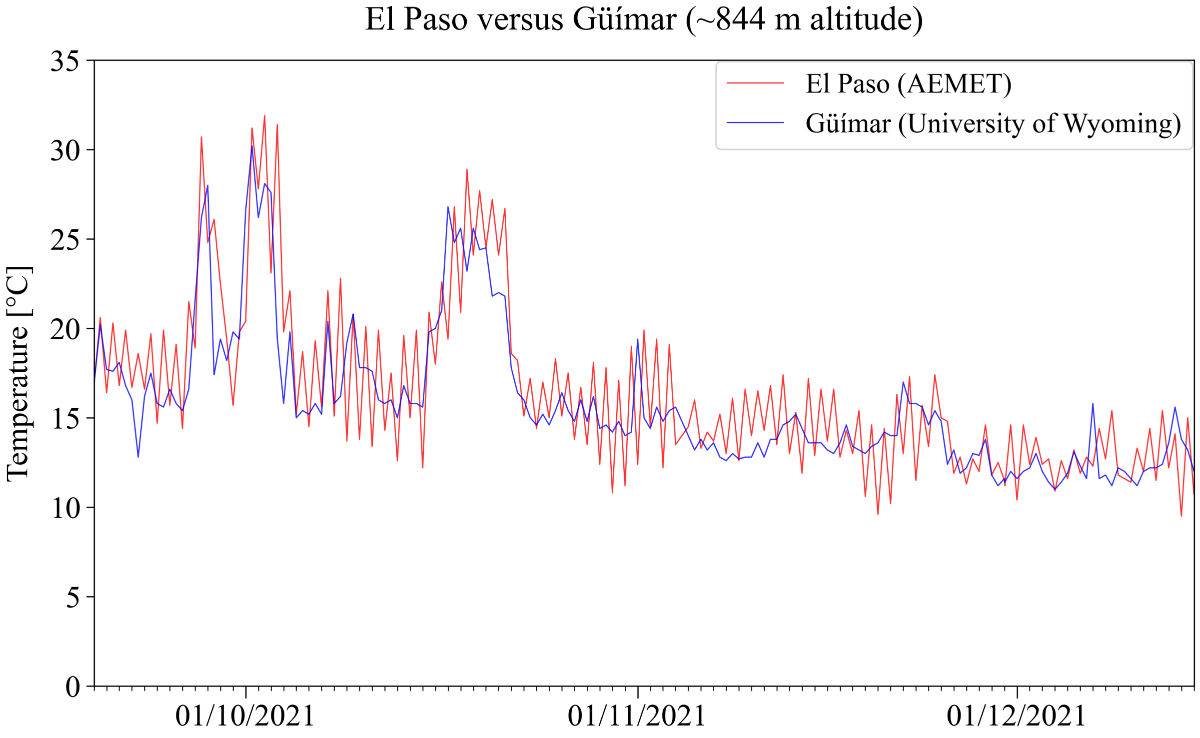

Figure D.1: Comparison of temperature measurements at El Paso, La Palma (red line), and Güímar, Tenerife (blue line), at ∼844 m altitude. The temperature at El Paso is measured each day at 00:00 and 12:00 UTC by a fixed weather station operated by the State Meteorological Agency (AEMET) of Spain. The temperature data of Güímar (station 60018) is obtained from weather balloons that are released twice a day (at 00:00 and 12:00 UTC) and is provided by the University of Wyoming.

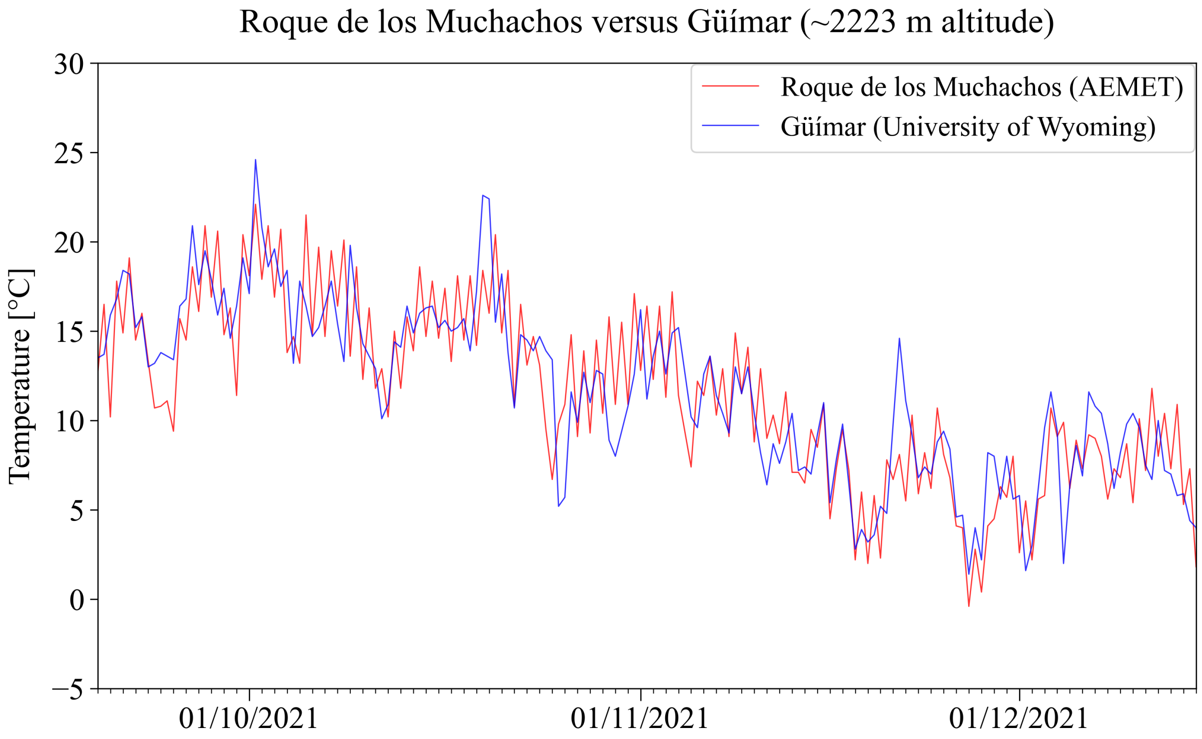

Figure D.2: Comparison of temperature measurements at Roque de los Muchachos, La Palma (red line), and Güímar, Tenerife (blue line), at ∼2223 m altitude. The temperature at Roque de los Muchachos is measured each day at 00:00 and 12:00 UTC by a fixed weather station operated by the State Meteorological Agency (AEMET) of Spain. The temperature data of Güímar (station 60018) is obtained from weather balloons that are released twice a day (at 00:00 and 12:00 UTC) and is provided by the University of Wyoming.

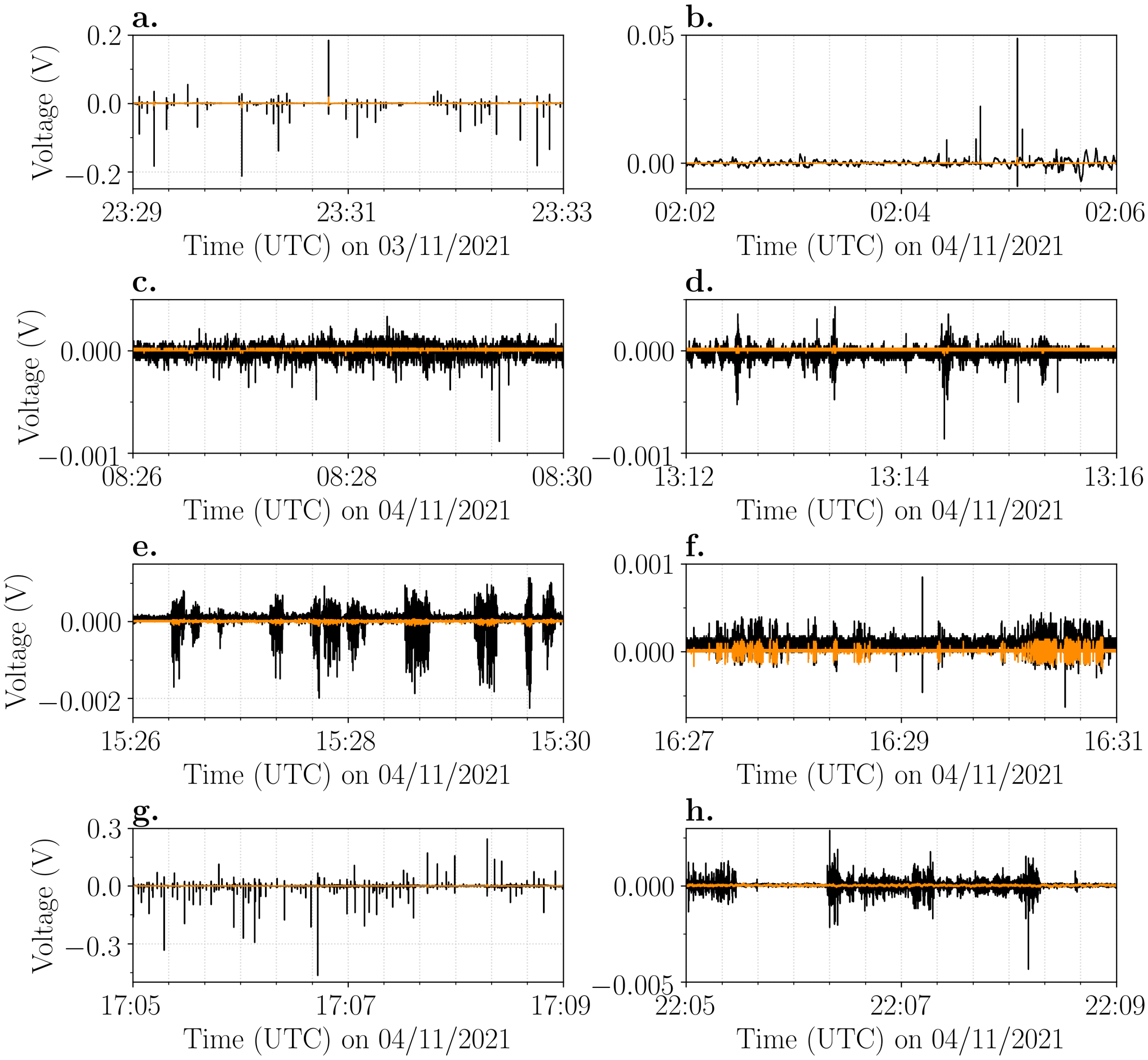

*Figure D.3: Electrical signatures observed on 3 and 4 November 2021 in chronological order: **a)** Individual high-voltage electrical discharges (type 1); **b)** Less frequent electrical discharges (type 1) with measured voltages an order of magnitude lower than in panel **a**. Due to the lower magnitude of the electrical discharges, the movement of charge becomes visible in the electrical signal (type 5); **c)** Faint electrical discharges that remained mostly undetected by the volcanic lightning detection algorithm (type 4); **d)** Bursts of continuous electrical discharges lasting ∼3-10 seconds long (type 3); **e)** Burst of continuous electrical discharges of slightly longer duration (up to ∼30 seconds) than in panel **d** (type 3); **f)** Ash fall at the sensor, producing electrical signals of opposite polarity at the two antennas (type 6); **g)** Individual high-voltage electrical discharges (type 1); **h)** Minutes-long burst of continuous electrical discharges (type 2).*

Appendix E

Chapter 5

Ash versus ice abundance controls lightning polarity in volcanic plumes

Image analysis (using the free software Fiji on images taken with a Keyence optical microscope) of more than 3000 ice particles, generated by shaving blocks of frozen tap water using the Smash Ice Device©, reveals a positively skewed size distribution (Figure E.1) with a mode of particle sizes between 3 and 4 phi (62.5-120 μm). This is comparable to the size distribution of the ash particles used in the rapid decompression experiments.

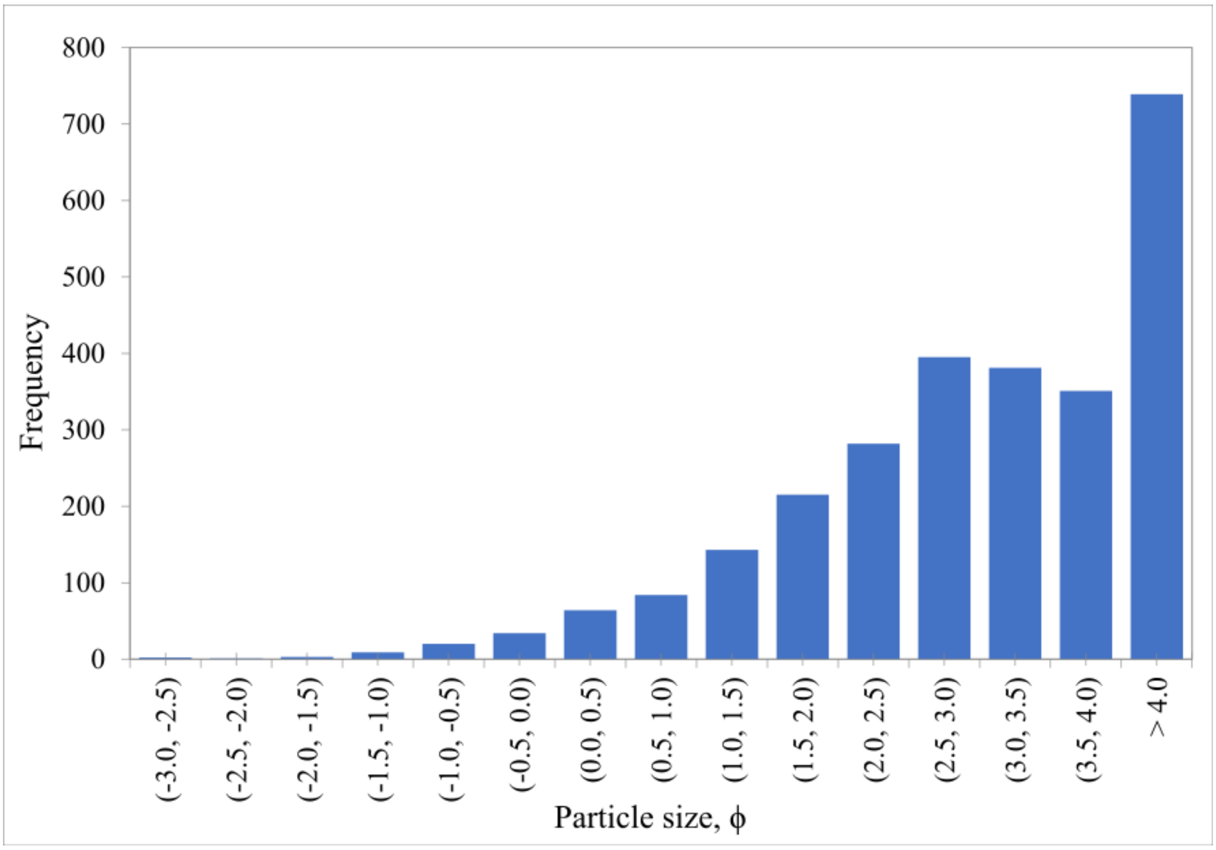

Figure E.1: Grain size distributions of ice particles used in the experiments. Results were obtained on >3000 ice particles using an optical microscope and reveal a positively skewed size distribution with a mode between 3 and 4 ϕ (62.5-120 µm), which is comparable to the size distribution of the ash particles used (40-90 µm). Note that the peak at >4.0 ϕ is an artefact of image resolution as all ice particles smaller than a single pixel are counted in this size range.

Appendix F

Chapter 6

Standing shock prevents propagation of sparks in supersonic explosive flows

Appendix F Note 1 Table F.1 identifies the decompression shots analysed for this study by their date and approximate time. Shot 2019-03-08 10:15 provides the camera images and radio frequency data used in Figures 6.1, 6.2, 6.3 (to determine the condensation boundary height), the main plots of Figure 6.4, Table 6.1 (experiment column) and Figure F.1. The insets in Figure 6.4 show radio frequency data from shot 2019-03-06 13:00 in Table F.1, and described under the section titled radio frequency measurements. Data from all shots in Table F.1 underlies the shot discussion in the methods sections.

Table F.1: Experiment shots used in this study, and observance of sharp condensation boundaries and optical discharges.

Date & approx. local time	Location	Particle fill	Condensation boundary observed?	Optical discharges observed within condensation?
2019-03-06 13:00	STL	None	Yes	No
2019-03-07 16:15	STL	45 g of 500 μm and residual 5 μm diamond	Yes	Yes
2019-03-07 16:50	STL	30 g of 5 μm diamond	Yes	No
2019-03-08 10:15	STL	Residual 5 μm diamond	Yes	Yes
2019-07-26 15:35	STL	None	Yes	No
2019-07-30 16:40	STL	46.7 g of 250 μm diamond	Yes	Yes
2019-08-02 11:14	STL	None	Not illuminated	No
2019-08-02 13:52	STL	46.7 g of 50 μm diamond	Yes	Yes
2019-08-05 14:50	STL	50 g of 50 μm diamond	Yes	Yes
2019-08-05 17:00	STL	15 g of 150 μm graphite powder and residual 50 μm diamond	Yes	Yes
2019-09-16 14:25	LMU	None	Yes	No
2019-09-16 14:40	LMU	None	Yes	No
2019-09-16 17:00	LMU	None	Yes	No

For the shot where 'Condensation boundary observed?' column lists 'Not illuminated' it was not possible to view the condensation due to an illuminating lights being shut off. All shots used argon as gas. All shots at STL used burst discs rated for 6.9 MPa, while the shots at LMU used discs rated for 8.9 MPa. The March 2019 shots at STL measured the pressure at the gas reservoir, while the shots at LMU measured the pressure at the nozzle. All shots were captured with high speed cameras. At STL inductive and dipole antennas were used to record RF signals in the March 2019, and some July/August 2019 shots.

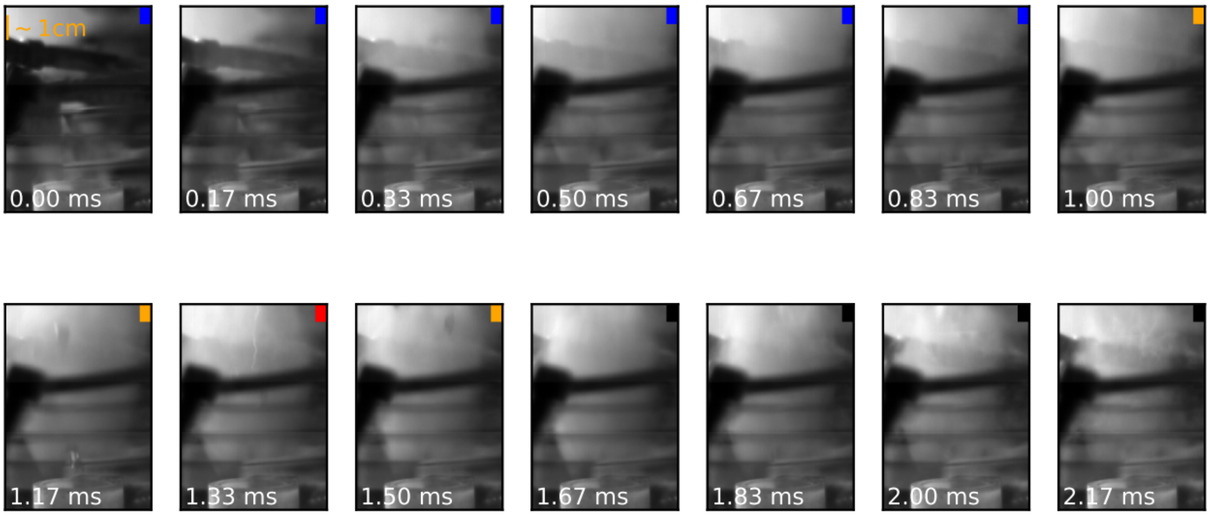

Figure F.1: Image sequence of low particle content, fast decompression captured by camera 2. Camera 2, exposing 20 µs frames at a rate of 6,000 Hz, is triggered by pressure increase at the nozzle t = 0, and is viewing the nozzle opening and the region above the nozzle including portions of the inductive antennas (cut to 9.3 × 6.7 cm). Coloured squares mark sequential phases of the decompression experiment (as in Figure 6.1): rise of condensation and formation of sharp upper boundary (blue), rapid drop of condensation boundary (orange) and sparks (red), slower drop of condensation boundary (black).

Bibliography

Abarca, S. F., Corbosiero, K. L., and Galarneau Jr, T. J. (2010). An evaluation of the worldwide lightning location network (WWLLN) using the national lightning detection network (NLDN) as ground truth. *Journal of Geophysical Research: Atmospheres*, 115(D18).

Agustsson, K., Stefánsson, R., Linde, A., Einarsson, P., Sacks, I., Gudmundsson, G., and Thorbjarnardóttir, B. (2000). Successful prediction and warning of the 2000 eruption of Hekla based on seismicity and strain changes. *Eos Trans. AGU*, 81(48).

Aiuppa, A., Bitetto, M., Delle Donne, D., La Monica, F. P., Tamburello, G., Coppola, D., Della Schiava, M., Innocenti, L., Lacanna, G., Laiolo, M., et al. (2021). Volcanic CO2 tracks the incubation period of basaltic paroxysms. *Science advances*, 7(38):eabh0191.

Aizawa, K., Cimarelli, C., Alatorre-Ibargüengoitia, M. A., Yokoo, A., Dingwell, D. B., and Iguchi, M. (2016). Physical properties of volcanic lightning: Constraints from magnetotelluric and video observations at Sakurajima volcano, Japan. *Earth and Planetary Science Letters*, 444:45–55.

Alatorre-Ibargüengoitia, M. A., Scheu, B., and Dingwell, D. B. (2011). Influence of the fragmentation process on the dynamics of vulcanian eruptions: An experimental approach. *Earth and Planetary Science Letters*, 302(1-2):51–59.

Alidibirov, M. and Dingwell, D. B. (1996). An experimental facility for the investigation of magma fragmentation by rapid decompression. *Bulletin of Volcanology*, 58(5):411–416.

Aloisi, M., Bonaccorso, A., Cannavò, F., Currenti, G., and Gambino, S. (2020). The 24 December 2018 eruptive intrusion at Etna volcano as revealed by multidisciplinary continuous deformation networks (CGPS, borehole strainmeters and tiltmeters). *Journal of Geophysical Research: Solid Earth*, 125(8):e2019JB019117.

Aloisi, M., Bonaccorso, A., Cannavò, F., and Currenti, G. M. (2018). Coupled short-and medium-term geophysical signals at Etna volcano: Using deformation and strain to infer magmatic processes from 2009 to 2017. *Frontiers in Earth Science*, page 109.

Anderson, J., Johnson, J., Steele, A., Ruiz, M., and Brand, B. (2018). Diverse eruptive activity revealed by acoustic and electromagnetic observations of the 14 July 2013 intense vulcanian eruption of Tungurahua Volcano, Ecuador. *Geophysical Research Letters*, 45(7):2976–2985.

Anderson, R. and Eriksson, A. (1980). A summary of lightning parameters for engineering applications. In *Proc. CIGRE*, volume 2, pages 33–0.

Anderson, R., Gathman, S., Hughes, J., Björnsson, S., Jónasson, S., Blanchard, D. C., Moore, C. B., Survilas, H. J., and Vonnegut, B. (1965). Electricity in Volcanic Clouds: Investigations show that lightning can result from charge-separation processes in a volcanic crater. *Science*, 148(3674):1179–1189.

Andronico, D., Del Bello, E., D'Oriano, C., Landi, P., Pardini, F., Scarlato, P., Taddeucci, J., Cristaldi, A., Ciancitto, F., Pennacchia, F., et al. (2021). Uncovering the eruptive patterns of the 2019 double paroxysm eruption crisis of Stromboli volcano. *Nature Communications*, 12(1):1–14.

Aplin, K., Bennett, A., Harrison, R., and Houghton, I. (2016). Electrostatics and in situ sampling of volcanic plumes. In *Volcanic ash*, pages 99–113. Elsevier.

Aplin, K., Houghton, I., Nicoll, K., Humphries, M., and Tong, A. (2014). Electrical charging of volcanic ash. In *Proc. ESA Annual Meeting on Electrostatics*, page 1.

Arason, P., Bennett, A. J., and Burgin, L. E. (2011). Charge mechanism of volcanic lightning revealed during the 2010 eruption of Eyjafjallajökull. *Journal of Geophysical Research: Solid Earth*, 116(B9).

Arason, P., Petersen, G. N., and Björnsson, H. (2013). Estimation of eruption site location using volcanic lightning. *Icelandic Met Office Report VÍ*, 6:2013.

Ashkenas, H. and Sherman, F. S. (1965). Structure and utilization of supersonic free jets in low density wind tunnels. Technical report.

Avila, E. E., Varela, G. G. A., and Caranti, G. M. (1996). Charging in ice-ice collisions as a function of the ambient temperature and the larger particle average temperature. *Journal of Geophysical Research: Atmospheres*, 101(D23):29609–29614.

Baissac, D. M., Nicora, M. G., Bali, L. J., Badi, G. A., and Ávila, E. E. (2021). Volcanic alert system by lightning detection using the WWLLN-ash cloud monitor. *Journal of South American Earth Sciences*, 108:103234.

Baker, B., Baker, M., Jayaratne, E., Latham, J., and Saunders, C. (1987). The influence of diffusional growth rates on the charge transfer accompanying rebounding collisions between ice crystals and soft hailstones. *Quarterly Journal of the Royal Meteorological Society*, 113(478):1193–1215.

Balsara, D. S. and Shu, C.-W. (2000). Monotonicity preserving weighted essentially non-oscillatory schemes with increasingly high order of accuracy. *Journal of Computational Physics*, 160(2):405–452.

Barberi, F. (1993). Volcanic hazard assessment at Stromboli based on review of historical data. *Acta Vulcanologica*, 3:173–187.

Bazelyan, E. M. and Raizer, Y. P. (2000). *Lightning physics and lightning protection*. CRC Press.

Bazelyan, E. M. and Raizer, Y. P. (2017). *Spark discharge*. Routledge.

Beaglehole, D. and Wilson, P. (1994). Extrinsic premelting at the ice-glass interface. *The Journal of Physical Chemistry*, 98(33):8096–8100.

Behncke, B. (2019). The 3 July 2019 paroxysm of Stromboli and its activity during the following days [blog post]. *INGVvulcani.* https://ingvvulcani.com/2019/07/15/the-3-july-2019-paroxysm-of-stromboli-and-its-activity-during-the-following-days/ [Accessed 15 December 2021].

Behnke, S., Thomas, R., Edens, H., Krehbiel, P., and Rison, W. (2014). The 2010 eruption of Eyjafjallajökull: Lightning and plume charge structure. *Journal of Geophysical Research: Atmospheres*, 119(2):833–859.

Behnke, S. A. and Bruning, E. C. (2015). Changes to the turbulent kinematics of a volcanic plume inferred from lightning data. *Geophysical Research Letters*, 42(10):4232–4239.

Behnke, S. A., Edens, H., Senay, S., Iguchi, M., and Miki, D. (2021). Radio Frequency Characteristics of Volcanic Lightning and Vent Discharges. *Journal of Geophysical Research: Atmospheres*, 126(18):e2020JD034495.

Behnke, S. A., Edens, H. E., Thomas, R. J., Smith, C. M., McNutt, S. R., Van Eaton, A. R., Cimarelli, C., and Cigala, V. (2018). Investigating the origin of continual radio frequency impulses during explosive volcanic eruptions. *Journal of Geophysical Research: Atmospheres*, 123(8):4157–4174.

Behnke, S. A. and McNutt, S. R. (2014). Using lightning observations as a volcanic eruption monitoring tool. *Bulletin of Volcanology*, 76(8):1–12.

Behnke, S. A., Thomas, R. J., McNutt, S. R., Schneider, D. J., Krehbiel, P. R., Rison, W., and Edens, H. E. (2013). Observations of volcanic lightning during the 2009 eruption of Redoubt Volcano. *Journal of Volcanology and Geothermal Research*, 259:214–234.

Bennett, A. (2013). Identification and ranging of lightning flashes using co-located antennas of different geometry. *Measurement Science and Technology*, 24(12):125801.

Bennett, A. and Harrison, R. (2013). Lightning-induced extensive charge sheets provide long range electrostatic thunderstorm detection. *Physical review letters*, 111(4):045003.

Bennett, A., Odams, P., Edwards, D., and Arason, P. (2010). Monitoring of lightning from the April–May 2010 Eyjafjallajökull volcanic eruption using a very low frequency lightning location network. *Environmental Research Letters*, 5(4):044013.

Bennett, A. J. (2017). Electrostatic thunderstorm detection. *Weather*, 72(2):51–54.

Bertagnini, A., Di Roberto, A., and Pompilio, M. (2011). Paroxysmal activity at Stromboli: lessons from the past. *Bulletin of Volcanology*, 73(9):1229–1243.

Bertagnini, A., Métrich, N., Francalanci, L., Landi, P., Tommasini, S., Conticelli, S., et al. (2008). Volcanology and magma geochemistry of the present-day activity: constraints on the feeding system. *The Stromboli Volcano, An integrated study of the 2002–2003 eruption, edited by: Calvari, S., Inguaggiato, S., Ripepe, M., Rosi, M., AGU Geophys. Monograph. Series, Washington DC*, 182:19–38.

Biagi, C. J., Cummins, K. L., Kehoe, K. E., and Krider, E. P. (2007). National lightning detection network (NLDN) performance in southern Arizona, Texas, and Oklahoma in 2003–2004. *Journal of Geophysical Research: Atmospheres*, 112(D5).

Björnsson, S., Blanchard, D. C., and Spencer, A. T. (1967). Charge generation due to contact of saline waters with molten lava. *Journal of Geophysical Research*, 72(4):1311–1323.

Black, R. A. and Hallett, J. (1999). Electrification of the hurricane. *Journal of the atmospheric sciences*, 56(12):2004–2028.

Boerner, H. (2019). Thunderstorms and Lightning. In *Ball Lightning*, pages 57–81. Springer.

Bolmatov, D., Zhernenkov, M., Zav'yalov, D., Tkachev, S. N., Cunsolo, A., and Cai, Y. Q. (2015). The Frenkel Line: a direct experimental evidence for the new thermodynamic boundary. *Scientific reports*, 5(1):1–10.

Bonaccorso, A., Carleo, L., Currenti, G., and Sicali, A. (2021). Magma Migration at Shallower Levels and Lava Fountains Sequence as Revealed by Borehole Dilatometers on Etna Volcano. *Frontiers in Earth Science*, page 800.

Büttner, R., Röder, H., and Zimanowski, B. (1997). Electrical effects generated by experimental volcanic explosions. *Applied physics letters*, 70(14):1903–1905.

Büttner, R. and Zimanowski, B. (1998). Physics of thermohydraulic explosions. *Physical Review E*, 57(5):5726.

Büttner, R., Zimanowski, B., and Röder, H. (2000). Short-time electrical effects during volcanic eruption: Experiments and field measurements. *Journal of Geophysical Research: Solid Earth*, 105(B2):2819–2827.

Calvari, S., Buettner, R., Cristaldi, A., Dellino, P., Giudicepietro, F., Orazi, M., Peluso, R., Spampinato, L., Zimanowski, B., and Boschi, E. (2012). The 7 September 2008 Vulcanian explosion at Stromboli volcano: Multiparametric characterization of the event and quantification of the ejecta. *Journal of Geophysical Research: Solid Earth*, 117(B5).

Calvari, S., Giudicepietro, F., Di Traglia, F., Bonaccorso, A., Macedonio, G., and Casagli, N. (2021). Variable magnitude and intensity of Strombolian explosions: Focus on the eruptive processes for a first classification scheme for Stromboli volcano (italy). *Remote Sensing*, 13(5):944.

Calvari, S., Spampinato, L., and Lodato, L. (2006). The 5 April 2003 vulcanian paroxysmal explosion at Stromboli volcano (Italy) from field observations and thermal data. *Journal of Volcanology and Geothermal research*, 149(1-2):160–175.

Carbone, D., Zuccarello, L., Saccorotti, G., and Greco, F. (2006). Analysis of simultaneous gravity and tremor anomalies observed during the 2002–2003 Etna eruption. *Earth and Planetary Science Letters*, 245(3-4):616–629.

Carcano, S., Ongaro, T. E., Bonaventura, L., and Neri, A. (2014). Influence of grain-size distribution on the dynamics of underexpanded volcanic jets. *Journal of volcanology and geothermal research*, 285:60–80.

Carn, S., Fioletov, V., McLinden, C., Li, C., and Krotkov, N. (2017). A decade of global volcanic SO2 emissions measured from space. *Scientific reports*, 7(1):1–12.

Cashman, K. V. and Scheu, B. (2015). Magmatic fragmentation. In *The encyclopedia of volcanoes*, pages 459–471. Elsevier.

Chaudhuri, A., Hadjadj, A., and Chinnayya, A. (2011). On the use of immersed boundary methods for shock/obstacle interactions. *Journal of Computational Physics*, 230(5):1731–1748.

Chicco, D. and Jurman, G. (2020). The advantages of the Matthews correlation coefficient (MCC) over F1 score and accuracy in binary classification evaluation. *BMC genomics*, 21(1):1–13.

Chojnicki, K., Clarke, A., Phillips, J., and Adrian, R. (2015). Rise dynamics of unsteady laboratory jets with implications for volcanic plumes. *Earth and Planetary Science Letters*, 412:186–196.

Chvyreva, A., Pancheshnyi, S., Christen, T., and Pemen, A. (2018). Raether–Meek criterion for prediction of electrodeless discharge inception on a dielectric surface in different gases. *Journal of Physics D: Applied Physics*, 51(11):115202.

Cigala, V. (2017). *The dynamics of starting gas-particle jets: a volcanic scenario.* PhD thesis, Ludwig-Maximilians-Universität München, Germany.

Cimarelli, C., Alatorre-Ibargüengoitia, M., Aizawa, K., Yokoo, A., Díaz-Marina, A., Iguchi, M., and Dingwell, D. (2016). Multiparametric observation of volcanic lightning: Sakurajima Volcano, Japan. *Geophysical Research Letters*, 43(9):4221–4228.

Cimarelli, C., Alatorre-Ibargüengoitia, M., Kueppers, U., Scheu, B., and Dingwell, D. B. (2014). Experimental generation of volcanic lightning. *Geology*, 42(1):79–82.

Cimarelli, C., Behnke, S., Méndez Harper, J., and Van Eaton, A. (2022). Volcanic electrification: recent advances and future perspectives. *Bulletin of Volcanology*. (In press).

Cimarelli, C. and Genareau, K. (2021). A review of volcanic electrification of the atmosphere and volcanic lightning. *Journal of Volcanology and Geothermal Research*, page 107449.

Clement, C. and Harrison, R. (1992). The charging of radioactive aerosols. *Journal of aerosol science*, 23(5):481–504.

Cole, P., Smith, P., Komorowski, J.-C., Alfano, F., Bonadonna, C., Stinton, A., Christopher, T., Odbert, H., and Loughlin, S. (2014). Ash venting occurring both prior to and during lava extrusion at Soufriere Hills Volcano, Montserrat, from 2005 to 2010. *Geological Society, London, Memoirs*, 39(1):71–92.

Colombier, M., Vasseur, J., Houghton, B. F., Cáceres, F., Scheu, B., Kueppers, U., Thivet, S., Gurioli, L., Montanaro, C., Soldati, A., et al. (2021). Degassing and gas percolation in basaltic magmas. *Earth and Planetary Science Letters*, 573:117134.

Coombs, M. L., Wech, A. G., Haney, M. M., Lyons, J. J., Schneider, D. J., Schwaiger, H. F., Wallace, K. L., Fee, D., Freymueller, J. T., Schaefer, J. R., et al. (2018). Short-term forecasting and detection of explosions during the 2016–2017 eruption of Bogoslof volcano, Alaska. *Frontiers in Earth Science*, page 122.

Cooray, V. (2003). The mechanism of the lightning flash. *Lightning Flash*, 34:127–240.

Cooray, V. (2015). *An introduction to lightning*. Springer.

Corradini, S., Spinetti, C., Carboni, E., Tirelli, C., Buongiorno, M. F., Pugnaghi, S., and Gangale, G. (2008). Mt. Etna tropospheric ash retrieval and sensitivity analysis using Moderate Resolution Imaging Spectroradiometer measurements. *Journal of Applied Remote Sensing*, 2(1):023550.

Dash, J., Mason, B., and Wettlaufer, J. (2001). Theory of charge and mass transfer in ice-ice collisions. *Journal of Geophysical Research: Atmospheres*, 106(D17):20395–20402.

De Angelis, S., Diaz-Moreno, A., and Zuccarello, L. (2019). Recent developments and applications of acoustic infrasound to monitor volcanic emissions. *Remote sensing*, 11(11):1302.

Del Negro, C. and Napoli, R. (2004). Magnetic field monitoring at Mt. Etna during the last 20 years. *Washington DC American Geophysical Union Geophysical Monograph Series*, 143:241–262.

Dickinson, J., Langford, S., Jensen, L., McVay, G., Kelso, J., and Pantano, C. (1988). Fractoemission from fused silica and sodium silicate glasses. *Journal of Vacuum Science & Technology A: Vacuum, Surfaces, and Films*, 6(3):1084–1089.

Dinger, J. and Gunn, R. (1946). Electrical effects associated with a change of state of water. *Terrestrial Magnetism and Atmospheric Electricity*, 51(4):477–494.

Drake, J. (1968). Electrification accompanying the melting of ice particles. *Quarterly Journal of the Royal Meteorological Society*, 94(400):176–191.

Duda, R. O. and Hart, P. E. (1972). Use of the hough transformation to detect lines and curves in pictures. *Communications of the ACM*, 15(1):11–15.

Durant, A. J., Shaw, R., Rose, W. I., Mi, Y., and Ernst, G. (2008). Ice nucleation and overseeding of ice in volcanic clouds. *Journal of Geophysical Research: Atmospheres*, 113(D9).

Dzurisin, D. (2006). *Volcano deformation: new geodetic monitoring techniques*. Springer Science & Business Media.

Fawcett, T. (2006). An introduction to ROC analysis. *Pattern recognition letters*, 27(8):861–874.

Fee, D. and Matoza, R. S. (2013). An overview of volcano infrasound: From Hawaiian to Plinian, local to global. *Journal of Volcanology and Geothermal Research*, 249:123–139.

Francalanci, L., Bertagnini, A., Métrich, N., Renzulli, A., Vannucci, R., Landi, P., Del Moro, S., Menna, M., Petrone, C. M., Nardini, I., et al. (2008). Mineralogical, geochemical, and isotopic characteristics of the ejecta from the 5 April 2003 paroxysm at Stromboli, Italy: Inferences on the Preeruptive Magma Dynamics. In *Geophysical Monograph Series*. American Geophysical Union.

Franquet, E., Perrier, V., Gibout, S., and Bruel, P. (2015). Free underexpanded jets in a quiescent medium: A review. *Progress in Aerospace Sciences*, 77:25–53.

Gambino, S. and Cammarata, L. (2017). Tilt measurements on volcanoes: More than a hundred years of recordings. *Italian Journal of Geosciences*, 136(2):275–295.

Garcés, M. A. and McNutt, S. R. (1997). Theory of the airborne sound field generated in a resonant magma conduit. *Journal of volcanology and geothermal research*, 78(3-4):155–178.

Gaudin, D. and Cimarelli, C. (2019). The electrification of volcanic jets and controlling parameters: A laboratory study. *Earth and Planetary Science Letters*, 513:69–80.

Gaudin, D., Taddeucci, J., Scarlato, P., Del Bello, E., Ricci, T., Orr, T., Houghton, B., Harris, A., Rao, S., and Bucci, A. (2017a). Integrating puffing and explosions in a general scheme for Strombolian-style activity. *Journal of Geophysical Research: Solid Earth*, 122(3):1860–1875.

Gaudin, D., Taddeucci, J., Scarlato, P., Harris, A., Bombrun, M., Del Bello, E., and Ricci, T. (2017b). Characteristics of puffing activity revealed by ground-based, thermal infrared imaging: the example of Stromboli Volcano (Italy). *Bulletin of Volcanology*, 79(3):1–15.

Genareau, K., Cloer, S. M., Primm, K., Tolbert, M. A., and Woods, T. W. (2018). Compositional and mineralogical effects on ice nucleation activity of volcanic ash. *Atmosphere*, 9(7):238.

Gidaspow, D. (1994). *Multiphase flow and fluidization: continuum and kinetic theory descriptions*. Academic press.

Gilman, B., Moser, B., et al. (2007). *Ashen Sky: The Letters of Pliny the Younger on the Eruption of Vesuvius*. Getty Publications.

Giordano, G. and De Astis, G. (2021). The summer 2019 basaltic Vulcanian eruptions (paroxysms) of Stromboli. *Bulletin of Volcanology*, 83(1):1–27.

Giudicepietro, F., López, C., Macedonio, G., Alparone, S., Bianco, F., Calvari, S., De Cesare, W., Delle Donne, D., Di Lieto, B., Esposito, A. M., et al. (2020). Geophysical precursors of the July-August 2019 paroxysmal eruptive phase and their implications for Stromboli volcano (Italy) monitoring. *Scientific reports*, 10(1):1–16.

Gottlieb, S. (2005). On high order strong stability preserving Runge-Kutta and multi step time discretizations. *Journal of scientific computing*, 25(1):105–128.

Gurioli, L., Harris, A. J., Colò, L., Bernard, J., Favalli, M., Ripepe, M., and Andronico, D. (2013). Classification, landing distribution, and associated flight parameters for a bomb field emplaced during a single major explosion at Stromboli, Italy. *Geology*, 41(5):559–562.

Hagelaar, G. and Pitchford, L. C. (2005). Solving the Boltzmann equation to obtain electron transport coefficients and rate coefficients for fluid models. *Plasma Sources Science and Technology*, 14(4):722.

Haney, M. M., Van Eaton, A. R., Lyons, J. J., Kramer, R. L., Fee, D., and Iezzi, A. M. (2018). Volcanic thunder from explosive eruptions at Bogoslof volcano, Alaska. *Geophysical Research Letters*, 45(8):3429–3435.

Haney, M. M., Van Eaton, A. R., Lyons, J. J., Kramer, R. L., Fee, D., Iezzi, A. M., Dziak, R. P., Anderson, J., Johnson, J. B., Lapierre, J. L., et al. (2020). Characteristics of thunder and electromagnetic pulses from volcanic lightning at Bogoslof volcano, Alaska. *Bulletin of Volcanology*, 82(2):1–16.

Hargie, K. A., Van Eaton, A. R., Mastin, L. G., Holzworth, R. H., Ewert, J. W., and Pavolonis, M. (2019). Globally detected volcanic lightning and umbrella dynamics during the 2014 eruption of Kelud, Indonesia. *Journal of Volcanology and Geothermal Research*, 382:81–91.

Harrison, R. G., Nicoll, K., Ulanowski, Z., and Mather, T. (2010). Self-charging of the Eyjafjallajökull volcanic ash plume. *Environmental Research Letters*, 5(2):024004.

Henry, P. (1953). Survey of generation and dissipation of static electricity. *British Journal of Applied Physics*, 4(S2):S6.

Hinzen, K.-G. (2012). Seismological analysis of a lightning strike. *Seismological Research Letters*, 83(3):492–497.

Houghton, B. F., Swanson, D., Rausch, J., Carey, R., Fagents, S., and Orr, T. R. (2013). Pushing the Volcanic Explosivity Index to its limit and beyond: Constraints from exceptionally weak explosive eruptions at Kīlauea in 2008. *Geology*, 41(6):627–630.

Houghton, B. F., Taddeucci, J., Andronico, D., Gonnermann, H., Pistolesi, M., Patrick, M. R., Orr, T. R., Swanson, D., Edmonds, M., Gaudin, D., et al. (2016). Stronger or longer: Discriminating between Hawaiian and Strombolian eruption styles. *Geology*, 44(2):163–166.

Houim, R. W. and Oran, E. S. (2016). A multiphase model for compressible granular–gaseous flows: formulation and initial tests. *Journal of fluid mechanics*, 789:166–220.

Hutchins, M., Holzworth, R., Brundell, J., and Rodger, C. (2012). Relative detection efficiency of the world wide lightning location network. *Radio Science*, 47(06):1–9.

Inoue, T. (1985). On the temperature and effective emissivity determination of semi-transparent cirrus clouds by bi-spectral measurements in the 10μm window region. *Journal of the Meteorological Society of Japan. Ser. II*, 63(1):88–99.

Irie, T., Kashimura, H., and Setoguchi, T. (2005). Hysteresis phenomena of mach disk in an underexpanded jet. *Nippon Kikai Gakkai Ronbunshu B Hen (Transactions of the Japan Society of Mechanical Engineers Part B)*, 17(2):412–419.

Istituto Nazionale di Geofisica e Vulcanologia (2019). Stromboli, Bollettino Settimanale 24/06/2019 - 30/06/2019 [weekly bulletin, N° 27/2019]. *INGVvulcani.* https://www.ct.ingv.it/index.php/monitoraggio-e-sorveglianza/prodotti-del-monitoraggio/bollettini-settimanali-multidisciplinari [Accessed 20 December 2021].

Istituto Nazionale di Geofisica e Vulcanologia (2020a). Stromboli, Bollettino Settimanale 13/07/2020 – 19/07/2020 [weekly bulletin, N° 30/2020]. *INGVvulcani.* https://www.ct.ingv.it/index.php/monitoraggio-e-sorveglianza/prodotti-del-monitoraggio/bollettini-settimanali-multidisciplinari [Accessed 20 December 2021].

Istituto Nazionale di Geofisica e Vulcanologia (2020b). Stromboli, Bollettino Settimanale 16/11/2020 – 22/11/2020 [weekly bulletin, N° 48/2020]. *INGVvulcani.* https://www.ct.ingv.it/index.php/monitoraggio-e-sorveglianza/prodotti-del-monitoraggio/bollettini-settimanali-multidisciplinari [Accessed 20 December 2021].

James, M., Lane, S., and Gilbert, J. S. (2000). Volcanic plume electrification: Experimental investigation of a fracture-charging mechanism. *Journal of Geophysical Research: Solid Earth*, 105(B7):16641–16649.

James, M., Wilson, L., Lane, S., Gilbert, J., Mather, T., Harrison, R., and Martin, R. (2008). Electrical charging of volcanic plumes. *Space Science Reviews*, 137(1):399–418.

James, M. R., Lane, S., and Gilbert, J. (1998). Volcanic plume monitoring using atmospheric electric potential gradients. *Journal of the Geological Society*, 155(4):587–590.

Jayaratne, E. (1998). Density and surface temperature of graupel and the charge separation during ice crystal interactions. *Journal of Geophysical Research: Atmospheres*, 103(D12): 13957–13961.

Jayaratne, E., Saunders, C., and Hallett, J. (1983). Laboratory studies of the charging of soft-hail during ice crystal interactions. *Quarterly Journal of the Royal Meteorological Society*, 109(461):609–630.

Jayaratne, R. and Saunders, C. (2014). Wet hail and thunderstorm electrification. In *15th International Conference on Atmospheric Electricity (ICAE 2014)*.

Johnson, P. C. and Jackson, R. (1987). Frictional–collisional constitutive relations for granular materials, with application to plane shearing. *Journal of fluid Mechanics*, 176:67–93.

Khalil, I. and Miller, D. R. (2004). The structure of supercritical fluid free-jet expansions. *AIChE Journal*, 50(11):2697–2704.

Kieffer, S. W. (1981). Blast dynamics at mount St Helens on 18 May 1980. *Nature*, 291(5816):568–570.

Kikuchi, K. (1965). On the Positive Electrification of Snow Crystals in the Process of Their Melting (III): The relationship between air bubble concentration and charge generated in ice specimen during their melting. *Journal of the Meteorological Society of Japan. Ser. II*, 43(6):343–350.

Kok, J. F. and Lacks, D. J. (2009). Electrification of granular systems of identical insulators. *Physical Review E*, 79(5):051304.

Laboratorio Geofisica Sperimentale (2019a). Bollettino settimanale dell'attività del vulcano Stromboli (21 giugno – 27 giugno 2019) [weekly bulletin]. http://lgs.geo.unifi.it/index.php/reports/stromboli-weekly [Accessed 15 December 2021].

Laboratorio Geofisica Sperimentale (2019b). Bollettino settimanale dell'attività del vulcano Stromboli (28 giugno – 4 luglio 2019) [weekly bulletin]. http://lgs.geo.unifi.it/index.php/reports/stromboli-weekly [Accessed 15 December 2021].

Laboratorio Geofisica Sperimentale (2020a). Bollettino settimanale dell'attività del vulcano Stromboli (13 – 19 novembre 2020) [weekly bulletin]. http://lgs.geo.unifi.it/index.php/reports/stromboli-weekly [Accessed 15 December 2021].

Laboratorio Geofisica Sperimentale (2020b). Bollettino settimanale dell'attività del vulcano Stromboli (16 luglio – 23 luglio 2020) [weekly bulletin]. http://lgs.geo.unifi.it/index.php/reports/stromboli-weekly [Accessed 15 December 2021].

Lacks, D. J. and Levandovsky, A. (2007). Effect of particle size distribution on the polarity of triboelectric charging in granular insulator systems. *Journal of Electrostatics*, 65(2):107–112.

Lane, S. and Gilbert, J. (1992). Electric potential gradient changes during explosive activity at Sakurajima volcano, Japan. *Bulletin of Volcanology*, 54(7):590–594.

Lapierre, J., Van Eaton, A. R., Stock, M., Haney, M. M., and Lyons, J. J. (2018). Remote Measurements of Volcanic Plume Electrification Using a Sparse Network Technique. In *AGU Fall Meeting 2018*. AGU.

Liger-Belair, G., Cordier, D., and Georges, R. (2019). Under-expanded supersonic CO2 freezing jets during champagne cork popping. *Science advances*, 5(9):eaav5528.

Liu, N., Dwyer, J. R., Tilles, J. N., Stanley, M. A., Krehbiel, P. R., Rison, W., Brown, R. G., and Wilson, J. G. (2019). Understanding the radio spectrum of thunderstorm narrow bipolar events. *Journal of Geophysical Research: Atmospheres*, 124(17-18):10134–10153.

Longpré, M.-A. and Felpeto, A. (2021). Historical volcanism in the Canary Islands; part 1: A review of precursory and eruptive activity, eruption parameter estimates, and implications for hazard assessment. *Journal of Volcanology and Geothermal Research*, 419:107363.

Lorenz, R. D., Neakrase, L. D., Anderson, J. P., Harrison, R. G., and Nicoll, K. A. (2016). Point discharge current measurements beneath dust devils. *Journal of Atmospheric and Solar-Terrestrial Physics*, 150:55–60.

Lowell, J. and Truscott, W. (1986a). Triboelectrification of identical insulators. I. An experimental investigation. *Journal of physics D: Applied physics*, 19(7):1273.

Lowell, J. and Truscott, W. (1986b). Triboelectrification of identical insulators. II. Theory and further experiments. *Journal of Physics D: Applied Physics*, 19(7):1281.

MacGorman, D. R. and Rust, W. D. (1998). *Observations of the Electrical Characteristics of Thunderstorms: Chapter 7 in The electrical nature of storms*. Oxford University Press on Demand.

Maters, E. C., Cimarelli, C., Casas, A. S., Dingwell, D. B., and Murray, B. J. (2020). Volcanic ash ice-nucleating activity can be enhanced or depressed by ash-gas interaction in the eruption plume. *Earth and Planetary Science Letters*, 551:116587.

Maters, E. C., Dingwell, D. B., Cimarelli, C., Müller, D., Whale, T. F., and Murray, B. J. (2019). The importance of crystalline phases in ice nucleation by volcanic ash. *Atmospheric Chemistry and Physics*, 19(8):5451–5465.

Mather, T. A. and Harrison, R. G. (2006). Electrification of volcanic plumes. *Surveys in Geophysics*, 27(4):387–432.

McNutt, S. R. and Davis, C. (2000). Lightning associated with the 1992 eruptions of crater peak, Mount Spurr volcano, Alaska. *Journal of Volcanology and Geothermal Research*, 102(1-2):45–65.

McNutt, S. R. and Roman, D. C. (2015). Volcanic seismicity. In *The encyclopedia of volcanoes*, pages 1011–1034. Elsevier.

McNutt, S. R. and Thomas, R. J. (2015). Volcanic lightning. In *The encyclopedia of volcanoes*, pages 1059–1067. Elsevier.

McNutt, S. R. and Williams, E. R. (2010). Volcanic lightning: global observations and constraints on source mechanisms. *Bulletin of Volcanology*, 72(10):1153–1167.

Méndez Harper, J., Cimarelli, C., Cigala, V., Kueppers, U., and Dufek, J. (2021). Charge injection into the atmosphere by explosive volcanic eruptions through triboelectrification and fragmentation charging. *Earth and Planetary Science Letters*, 574:117162.

Méndez Harper, J., Cimarelli, C., Dufek, J., Gaudin, D., and Thomas, R. J. (2018). Inferring compressible fluid dynamics from vent discharges during volcanic eruptions. *Geophysical Research Letters*, 45(14):7226–7235.

Méndez Harper, J., Courtland, L., Dufek, J., and McAdams, J. (2020). Microphysical effects of water content and temperature on the triboelectrification of volcanic ash on long time scales. *Journal of Geophysical Research: Atmospheres*, 125(14):e2019JD031498.

Méndez Harper, J. and Dufek, J. (2016). The effects of dynamics on the triboelectrification of volcanic ash. *Journal of Geophysical Research: Atmospheres*, 121(14):8209–8228.

Méndez Harper, J., Dufek, J., and McAdams, J. (2015). The electrification of volcanic particles during the brittle fragmentation of the magma column. In *Proceedings of the ESA Annual Meeting on Electrostatics*.

Mercalli, G. (1907). *I Vulcani Attivi Della Terra: Morfologia, Dinamismo, Prodotti, Distribuzione Geografica, Cause*. U. Hoepli.

Métrich, N., Bertagnini, A., Landi, P., and Rosi, M. (2001). Crystallization driven by decompression and water loss at Stromboli volcano (Aeolian Islands, Italy). *Journal of Petrology*, 42(8):1471–1490.

Métrich, N., Bertagnini, A., Landi, P., Rosi, M., and Belhadj, O. (2005). Triggering mechanism at the origin of paroxysms at Stromboli (Aeolian Archipelago, Italy): the 5 April 2003 eruption. *Geophysical Research Letters*, 32(10).

Métrich, N., Bertagnini, A., and Pistolesi, M. (2021). Paroxysms at Stromboli volcano (Italy): Source, genesis and dynamics. *Frontiers in Earth Science*, 9:45.

Min, C. and Gibou, F. (2007). A second order accurate level set method on non-graded adaptive cartesian grids. *Journal of Computational Physics*, 225(1):300–321.

Miura, T., Koyaguchi, T., and Tanaka, Y. (2002). Measurements of electric charge distribution in volcanic plumes at Sakurajima Volcano, Japan. *Bulletin of volcanology*, 64(2):75–93.

Montijn, C. and Ebert, U. (2006). Diffusion correction to the Raether–Meek criterion for the avalanche-to-streamer transition. *Journal of Physics D: Applied Physics*, 39(14):2979.

Morales Rivera, A. M., Amelung, F., Mothes, P., Hong, S.-H., Nocquet, J.-M., and Jarrin, P. (2017). Ground deformation before the 2015 eruptions of Cotopaxi volcano detected by InSAR. *Geophysical Research Letters*, 44(13):6607–6615.

Nakayama, K. and Hashimoto, H. (1992). Triboemission of charged particles and photons from wearing ceramic surfaces in various gases. *Tribology transactions*, 35(4):643–650.

Napoli, R., Currenti, G., Del Negro, C., Greco, F., and Scandura, D. (2008). Volcanomagnetic evidence of the magmatic intrusion on 13th May 2008 Etna eruption. *Geophysical research letters*, 35(22).

Netz, R. R. and Andelman, D. (1997). Roughness-induced wetting. *Physical Review E*, 55(1): 687.

Nicoll, K., Airey, M., Cimarelli, C., Bennett, A., Harrison, G., Gaudin, D., Aplin, K., Koh, K. L., Knuever, M., and Marlton, G. (2019). First in situ observations of gaseous volcanic plume electrification. *Geophysical Research Letters*, 46(6):3532–3539.

Nijdam, S., Teunissen, J., and Ebert, U. (2020). The physics of streamer discharge phenomena. *Plasma Sources Science and Technology*, 29(10):103001.

Ogden, D. E., Wohletz, K. H., Glatzmaier, G. A., and Brodsky, E. E. (2008). Numerical simulations of volcanic jets: Importance of vent overpressure. *Journal of Geophysical Research: Solid Earth*, 113(B2).

Orescanin, M., Austin, J., and Kieffer, S. (2010). Unsteady high-pressure flow experiments with applications to explosive volcanic eruptions. *Journal of Geophysical Research: Solid Earth*, 115(B6).

Orescanin, M. M. and Austin, J. (2010). Exhaust of underexpanded jets from finite reservoirs. *Journal of Propulsion and Power*, 26(4):744–753.

Pallister, J. and McNutt, S. R. (2015). Synthesis of volcano monitoring. In *The encyclopedia of volcanoes*, pages 1151–1171. Elsevier.

Pankhurst, M. J., Scarrow, J. H., Barbee, O. A., Hickey, J., Coldwell, B. C., Rollinson, G. K., Rodríguez-Losada, J. A., Lorenzo, A. M., Rodríguez, F., Hernández, W., et al. (2022). Rapid response petrology for the opening eruptive phase of the 2021 Cumbre Vieja eruption, La Palma, Canary Islands. *Volcanica*, 5(1):1–10.

Papale, P. (1999). Strain-induced magma fragmentation in explosive eruptions. *Nature*, 397 (6718):425–428.

Parfitt, E. and Wilson, L. (1995). Explosive volcanic eruptions—IX. The transition between Hawaiian-style lava fountaining and Strombolian explosive activity. *Geophysical Journal International*, 121(1):226–232.

Patrick, M. R., Harris, A. J., Ripepe, M., Dehn, J., Rothery, D. A., and Calvari, S. (2007). Strombolian explosive styles and source conditions: insights from thermal (FLIR) video. *Bulletin of volcanology*, 69(7):769–784.

Pattantyus, A. and Businger, S. (2014). On the interaction of Tropical Cyclone Flossie and emissions from Hawaii's Kilauea volcano. *Geophysical Research Letters*, 41(11):4082–4089.

Peltier, A., Bianchi, M., Kaminski, E., Komorowski, J.-C., Rucci, A., and Staudacher, T. (2010). PSInSAR as a new tool to monitor pre-eruptive volcano ground deformation: Validation using GPS measurements on Piton de la Fournaise. *Geophysical Research Letters*, 37(12).

Pengra, D., Zhu, D.-M., and Dash, J. (1991). Surface melting of strained and unstrained layers: Kr, Ar, and Ne. *Surface science*, 245(1-2):125–131.

Pierce, E. (1955). Electrostatic field-changes due to lightning discharges. *Quarterly Journal of the Royal Meteorological Society*, 81(348):211–228.

Pistolesi, M., Delle Donne, D., Pioli, L., Rosi, M., and Ripepe, M. (2011). The 15 March 2007 explosive crisis at Stromboli volcano, Italy: assessing physical parameters through a multidisciplinary approach. *Journal of Geophysical Research: Solid Earth*, 116(B12).

Pitchford, L. C., Alves, L. L., Bartschat, K., Biagi, S. F., Bordage, M.-C., Bray, I., Brion, C. E., Brunger, M. J., Campbell, L., Chachereau, A., et al. (2017). Lxcat: An open-access, web-based platform for data needed for modeling low temperature plasmas. *Plasma Processes and Polymers*, 14(1-2):1600098.

Powers, D. M. (2020). Evaluation: from precision, recall and F-measure to ROC, informedness, markedness and correlation. *arXiv preprint arXiv:2010.16061*.

Prata, A. (1989a). Infrared radiative transfer calculations for volcanic ash clouds. *Geophysical research letters*, 16(11):1293–1296.

Prata, A. (1989b). Observations of volcanic ash clouds in the 10-12 μm window using AVHRR/2 data. *International journal of Remote sensing*, 10(4-5):751–761.

Prata, A. and Bernardo, C. (2007). Retrieval of volcanic SO2 column abundance from Atmospheric Infrared Sounder data. *Journal of Geophysical Research: Atmospheres*, 112(D20).

Prata, A., Folch, A., Prata, A., Biondi, R., Brenot, H., Cimarelli, C., Corradini, S., Lapierre, J., and Costa, A. (2020). Anak Krakatau triggers volcanic freezer in the upper troposphere. *Scientific Reports*, 10(1):1–13.

Prata, A. and Grant, I. (2001). Retrieval of microphysical and morphological properties of volcanic ash plumes from satellite data: Application to Mt Ruapehu, New Zealand. *Quarterly Journal of the Royal Meteorological Society*, 127(576):2153–2179.

Prata, F. and Lynch, M. (2019). Passive earth observations of volcanic clouds in the atmosphere. *Atmosphere*, 10(4):199.

Raether, H. (1964). *Electron avalanches and breakdown in gases*. Butterworths.

Raizer, Y. P. and Allen, J. E. (1991). *Gas discharge physics*, volume 1. Springer.

Rakov, V. (2013). The physics of lightning. *Surveys in Geophysics*, 34(6):701–729.

Rakov, V. A. and Uman, M. A. (2003). *Lightning: physics and effects*. Cambridge university press.

Rebscher, D., Westerhaus, M., Welle, W., and Nandaka, I. (2000). Monitoring ground deformation at the decade volcano Gunung Merapi, Indonesia. *Physics and Chemistry of the Earth, Part A: Solid Earth and Geodesy*, 25(9-11):755–757.

Rison, W., Krehbiel, P. R., Stock, M. G., Edens, H. E., Shao, X.-M., Thomas, R. J., Stanley, M. A., and Zhang, Y. (2016). Observations of narrow bipolar events reveal how lightning is initiated in thunderstorms. *Nature communications*, 7(1):1–12.

Roche, O. and Carazzo, G. (2019). The contribution of experimental volcanology to the study of the physics of eruptive processes, and related scaling issues: A review. *Journal of Volcanology and Geothermal Research*, 384:103–150.

Romero, J., Andronico, D., Bonadonna, C., Taddeucci, J., Pistolesi, M., Burton, M., Polacci, M., Rodrígez, M., Martín Lorenzo, A., Scarlato, P., Hayer, C., and Pankhurst, M. (2022). Volume and stratigraphy of the Cumbre Vieja 2021 eruption tephra fallout, La Palma Island. In *VMSG Annual Meeting 2022*. VMSG.

Rose, W. I., Delene, D., Schneider, D., Bluth, G., Krueger, A., Sprod, I., McKee, C., Davies, H., and Ernst, G. G. (1995). Ice in the 1994 Rabaul eruption cloud: implications for volcano hazard and atmospheric effects. *Nature*, 375(6531):477–479.

Rosi, M., Bertagnini, A., and Landi, P. (2000). Onset of the persistent activity at Stromboli volcano (Italy). *Bulletin of volcanology*, 62(4):294–300.

Rosi, M., Pistolesi, M., Bertagnini, A., Landi, P., Pompilio, M., and Di Roberto, A. (2013). Stromboli volcano, Aeolian Islands (Italy): present eruptive activity and hazards. *Geological Society, London, Memoirs*, 37(1):473–490.

Saunders, C. (1994). Thunderstorm electrification laboratory experiments and charging mechanisms. *Journal of Geophysical Research: Atmospheres*, 99(D5):10773–10779.

Saunders, C., Bax-Norman, H., Emersic, C., Avila, E., and Castellano, N. (2006). Laboratory studies of the effect of cloud conditions on graupel/crystal charge transfer in thunderstorm electrification. *Quarterly Journal of the Royal Meteorological Society: A journal of the atmospheric sciences, applied meteorology and physical oceanography*, 132(621):2653–2673.

Saunders, C. and Peck, S. (1998). Laboratory studies of the influence of the rime accretion rate on charge transfer during crystal/graupel collisions. *Journal of Geophysical Research: Atmospheres*, 103(D12):13949–13956.

Scharff, L., Hort, M., Harris, A., Ripepe, M., Lees, J., and Seyfried, R. (2008). Eruption dynamics of the SW crater of Stromboli volcano, Italy — An interdisciplinary approach. *Journal of volcanology and geothermal research*, 176(4):565–570.

Schmid, M., Kueppers, U., Civico, R., Ricci, T., Taddeucci, J., and Dingwell, D. B. (2021). Characterising vent and crater shape changes at Stromboli: implications for risk areas. *Volcanica*.

Schneider, D. J., Van Eaton, A. R., and Wallace, K. L. (2020). Satellite observations of the 2016–2017 eruption of Bogoslof volcano: aviation and ash fallout hazard implications from a water-rich eruption. *Bulletin of Volcanology*, 82(3):1–20.

Schultz, C. J., Andrews, V. P., Genareau, K. D., and Naeger, A. R. (2020). Observations of lightning in relation to transitions in volcanic activity during the 3 June 2018 Fuego Eruption. *Scientific reports*, 10(1):1–12.

Sekine, T., Katsura, T., and Aramaki, S. (1979). Water saturated phase relations of some andesites with application to the estimation of the initial temperature and water pressure at the time of eruption. *Geochimica et Cosmochimica Acta*, 43(8):1367–1376.

Settle, M. (1978). Volcanic eruption clouds and the thermal power output of explosive eruptions. *Journal of Volcanology and Geothermal Research*, 3(3-4):309–324.

Shaw, P. (1926). The electrical charges from like solids. *Nature*, 118(2975):659–660.

Shen, Z., Yan, W., and Yuan, G. (2016). A robust HLLC-type Riemann solver for strong shock. *Journal of Computational Physics*, 309:185–206.

Shinbrot, T., Komatsu, T. S., and Zhao, Q. (2008). Spontaneous tribocharging of similar materials. *EPL (Europhysics Letters)*, 83(2):24004.

Smith, C. M., Gaudin, D., Van Eaton, A. R., Behnke, S. A., Reader, S., Thomas, R. J., Edens, H., McNutt, S. R., and Cimarelli, C. (2021). Impulsive volcanic plumes generate volcanic lightning and vent discharges: A statistical analysis of Sakurajima volcano in 2015. *Geophysical Research Letters*, 48(11):e2020GL092323.

Sod, G. A. (1978). A survey of several finite difference methods for systems of nonlinear hyperbolic conservation laws. *Journal of computational physics*, 27(1):1–31.

Song, W., Lavallée, Y., Hess, K.-U., Kueppers, U., Cimarelli, C., and Dingwell, D. B. (2016). Volcanic ash melting under conditions relevant to ash turbine interactions. *Nature communications*, 7(1):1–10.

Sparks, R., Biggs, J., and Neuberg, J. (2012). Monitoring volcanoes. *Science*, 335(6074):1310–1311.

Sparks, R. S. J., Bursik, M., Carey, S., Gilbert, J., Glaze, L., Sigurdsson, H., and Woods, A. (1997). *Volcanic plumes*. Wiley.

Starikovskiy, A. Y. and Aleksandrov, N. (2019). ‘Gas-dynamic diode’: Streamer interaction with sharp density gradients. *Plasma Sources Science and Technology*, 28(9):095022.

Starikovskiy, A. Y. and Aleksandrov, N. (2020). Blocking streamer development by plane gaseous layers of various densities. *Plasma Sources Science and Technology*, 29(3):034002.

Stern, S., Cimarelli, C., Gaudin, D., Scheu, B., and Dingwell, D. (2019). Electrification of experimental volcanic jets with varying water content and temperature. *Geophysical Research Letters*, 46(20):11136–11145.

Taddeucci, J., Cimarelli, C., Alatorre-Ibargüengoitia, M., Delgado-Granados, H., Andronico, D., Del Bello, E., Scarlato, P., and Di Stefano, F. (2021). Fracturing and healing of basaltic magmas during explosive volcanic eruptions. *Nature Geoscience*, 14(4):248–254.

Taddeucci, J., Edmonds, M., Houghton, B., James, M. R., and Vergniolle, S. (2015). Hawaiian and Strombolian eruptions. In *The encyclopedia of volcanoes*, pages 485–503. Elsevier.

Taddeucci, J., Palladino, D., Sottili, G., Bernini, D., Andronico, D., and Cristaldi, A. (2013). Linked frequency and intensity of persistent volcanic activity at Stromboli (Italy). *Geophysical Research Letters*, 40(13):3384–3388.

Takahashi, T. (1969). Electric potential of liquid water on an ice surface. *Journal of the Atmospheric Sciences*, 26(6):1253–1258.

Takahashi, T. (1978). Riming electrification as a charge generation mechanism in thunderstorms. *Journal of Atmospheric Sciences*, 35(8):1536–1548.

Tamburello, G., McGonigle, A. J., Kantzas, E. P., and Aiuppa, A. (2011). Recent advances in ground-based ultraviolet remote sensing of volcanic SO2 fluxes. *Annals of Geophysics*, 54(2).

Tharwat, A. (2020). Classification assessment methods. *Applied Computing and Informatics*.

Thomas, R. J., Krehbiel, P. R., Rison, W., Edens, H., Aulich, G., Winn, W., McNutt, S. R., Tytgat, G., and Clark, E. (2007). Electrical activity during the 2006 Mount St. Augustine volcanic eruptions. *Science*, 315(5815):1097–1097.

Thomas, R. J., Krehbiel, P. R., Rison, W., Hunyady, S. J., Winn, W. P., Hamlin, T., and Harlin, J. (2004). Accuracy of the lightning mapping array. *Journal of Geophysical Research: Atmospheres*, 109(D14).

Thomas, R. J., McNutt, S. R., Krehbiel, P. R., Rison, W., Aulich, G., Edens, H., Tytgat, G., and Clark, E. (2010). Lightning and electrical activity during the 2006 eruption of Augustine Volcano: Chapter 25 in The 2006 eruption of Augustine Volcano, Alaska. Technical report, US Geological Survey.

Townsend, J. (1910). *The theory of ionization of gases by collision*. Constable, Limited.

Tripathy-Lang, A. (2020). Taal's eruption illuminates volcanic lightning for scientists, Temblor.

Tzur, I., Roble, R., and Adams, J. (1985). Atmospheric electric field and current configurations in the vicinity of mountains. *Journal of Geophysical Research: Atmospheres*, 90(D4):5979–5988.

Van Eaton, A. R., Amigo, Á., Bertin, D., Mastin, L. G., Giacosa, R. E., González, J., Valderrama, O., Fontijn, K., and Behnke, S. A. (2016). Volcanic lightning and plume behavior reveal evolving hazards during the April 2015 eruption of Calbuco volcano, Chile. *Geophysical Research Letters*, 43(7):3563–3571.

Van Eaton, A. R., Muirhead, J. D., Wilson, C. J., and Cimarelli, C. (2012). Growth of volcanic ash aggregates in the presence of liquid water and ice: an experimental approach. *Bulletin of volcanology*, 74(9):1963–1984.

Van Eaton, A. R., Schneider, D. J., Smith, C. M., Haney, M. M., Lyons, J. J., Said, R., Fee, D., Holzworth, R. H., and Mastin, L. G. (2020). Did ice-charging generate volcanic lightning during the 2016–2017 eruption of Bogoslof volcano, Alaska? *Bulletin of Volcanology*, 82(3):1–23.

Visacro, S., Soares Jr, A., Schroeder, M. A. O., Cherchiglia, L. C., and de Sousa, V. J. (2004). Statistical analysis of lightning current parameters: Measurements at Morro do Cachimbo Station. *Journal of Geophysical Research: Atmospheres*, 109(D1).

Von der Linden, J., Kimblin, C., McKenna, I., Bagley, S., Li, H.-C., Houim, R., Kueny, C. S., Kuhl, A., Grote, D., Converse, M., et al. (2021). Standing shock prevents propagation of sparks in supersonic explosive flows. *Communications Earth & Environment*, 2(1):1–9.

Vossen, C. E. J. and Cimarelli, C. (2022). Electrical measurements of explosive volcanic eruptions from Stromboli volcano, Italy. *GFZ Data Services*.

Vossen, C. E. J., Cimarelli, C., Bennett, A. J., Geisler, A., Gaudin, D., Miki, D., Iguchi, M., and Dingwell, D. B. (2021). Long-term observation of electrical discharges during persistent Vulcanian activity. *Earth and Planetary Science Letters*, 570:117084.

Wang, C., Yang, P., Baum, B. A., Platnick, S., Heidinger, A. K., Hu, Y., and Holz, R. E. (2011). Retrieval of ice cloud optical thickness and effective particle size using a fast infrared radiative transfer model. *Journal of applied meteorology and climatology*, 50(11):2283–2297.

Wassermann, J. (2012). Volcano seismology. In *New manual of seismological observatory practice 2 (NMSOP-2)*, pages 1–77. Deutsches GeoForschungsZentrum GFZ.

Wen, S. and Rose, W. I. (1994). Retrieval of sizes and total masses of particles in volcanic clouds using AVHRR bands 4 and 5. *Journal of Geophysical Research: Atmospheres*, 99(D3):5421–5431.

Wettlaufer, J. (1999). Impurity effects in the premelting of ice. *Physical Review Letters*, 82(12):2516.

Williams, E. and McNutt, S. (2004). Are large volcanic eruptions just dirty thunderstorms? *Eos (Transactions, American Geophysical Union)*, 85(47).

Williams, E. R. (1989). The tripole structure of thunderstorms. *Journal of Geophysical Research: Atmospheres*, 94(D11):13151–13167.

Williams, E. R. and McNutt, S. R. (2005). Total water contents in volcanic eruption clouds and implications for electrification and lightning. *Recent progress in lightning physics*, 81:93.

Wilson, C. T. R. (1921). III. Investigations on lighting discharges and on the electric field of thunderstorms. *Philosophical Transactions of the Royal Society of London. Series A, Containing Papers of a Mathematical or Physical Character*, 221(582-593):73–115.

Wilson, L., Sparks, R., Huang, T., and Watkins, N. (1978). The control of volcanic column heights by eruption energetics and dynamics. *Journal of Geophysical Research: Solid Earth*, 83(B4):1829–1836.

Woodhouse, M. J. and Behnke, S. A. (2014). Charge structure in volcanic plumes: a comparison of plume properties predicted by an integral plume model to observations of volcanic lightning during the 2010 eruption of Eyjafjallajökull, Iceland. *Bulletin of Volcanology*, 76(8):1–21.

Yair, Y. (2008). Charge generation and separation processes. *Space science reviews*, 137(1): 119–131.

Yamanouchi, T., Suzuki, K., and Kawaguchi, S. (1987). Detection of clouds in Antarctica from infrared multispectral data of AVHRR. *Journal of the Meteorological Society of Japan. Ser. II*, 65(6):949–962.

Zhang, W., Almgren, A., Beckner, V., Bell, J., Blaschke, J., Chan, C., Day, M., Friesen, B., Gott, K., Graves, D., et al. (2019). AMReX: a framework for block-structured adaptive mesh refinement. *Journal of Open Source Software*, 4(37):1370–1370.

Declaration / Affidavit

München, 8 March 2022

I hereby confirm that my thesis entitled *"Exploring the conditions for the occurrence of volcanic lightning"* is the result of my own original work. Furthermore, I certify that this work contains no material that has been accepted for the award of any other degree or diploma in my name, in any university and, to the best of my knowledge and belief, contains no material previously published or written by another person, except where due reference has been made in the text. In addition, I certify that no part of this work will be used in a submission in my name in the future, for any other degree or diploma in any university or other tertiary institution without the prior approval of the Ludwig-Maximilians-Universität München.

Caron E.J. Vossen

Acknowledgements

Corrado, I do not even know where to start with thanking you. Thank you for giving me the opportunity to do this amazing PhD, for showing me how to do fieldwork on active volcanoes, and for guiding, teaching and motivating me every step of the way. I could not have wished for a better supervisor. I look forward to continue working with you and to observe and detect volcanic lightning during many more eruptions!

Thank you Don, for building a volcanology section full of wonderful people, which brought me to Munich as a Master student and led me to this PhD project. Thank you for your support and invaluable input.

Alec, many thanks for your help over the years with processing and interpreting the amazing results that we obtained at each volcano. Every time we have a Zoom meeting I learn something new about the BTD and lightning in general and I hope this will continue for many more years!

I wish to thank Matthias, André and Joachim for providing technical support in and out of the field and for their help with developing a new electrical system for my instruments.

A huge thanks to my two amazing office mates, Mat and Sidd! I am so happy I ended up sharing an office with you. Our tea breaks, Bollywood dances and salsa music made my work so much more fun. Thank you for always being there.
Markus, thank you for being my guide on Stromboli and for sharing my love for volcanoes and good food. Pancho, thank you for turning your office into the coffee break room, so we could drink an endless number of coffees, hang out and talk science. Jérémie, without you I would still be stuck in a Python error somewhere; thank you for always helping me fix my scripts, you are a genius. Joanna, Christina and Zeynep, thank you girls for always being there for me to talk to and to cheer me up. Vale, thank you for the fun moments we shared on Stromboli and La Palma, I really enjoyed working with you.
A big thanks to all of my colleagues for the nice UFO lunches, coffee breaks, volleyball and football matches, balcony breaks and 307 parties (hoping I did not forget anyone): Adrian, Ana, Arianna, Baha, Betty, Chris, Christina, Cristian, Damien, Daniel, Diana, Dirk, Eleonora, Iphi, Isabella, Jérémie, Joanna, Kai, Kai-Uwe, Lukas, Luiz, Markus, Michi, Mila, Omar, Pancho, Simon, Sönke, Steffi, Ulli, Vale, Wenja, Werner, Woife and Zeynep. Thank you Max and Markus for your help with my instruments and equipment, always right on time for the next

field campaign or lab experiment. And thanks to all the LMU staff, in particular Rike, Margot, Andre, Rosa, Nataliya and Isabel, for running everything smoothly and for providing such a nice work environment.

Agathe and Omar, I was so lucky to have you as my friends and roomies in Munich from the very beginning of my PhD. Thank you for making me feel at home through the countless dinners we enjoyed together, the long chats we had and the many laughs we shared.

Joëlle, ik ben zo blij dat je naar München bent gekomen! Het is super leuk om een tweede Dutchie hier te hebben. Dankje voor alle steun en de gezellige afspraakjes het afgelopen jaar.

Heel veel dank aan mijn vrienden thuis: Joran, Niels, Martijn, Iris, Andrés en Sam. Jor, dankjewel voor alle motivatie die je deze kant hebt opgestuurd via onze (vaak lange maar) gezellige telefoontjes. Niels en Martijn, ik hoop dat onze jaarlijkse pannenkoekenetentjes nog lang traditie zullen blijven.
Lieve Barbs - Mad, Jan, Kir, Sab, Miek, Lies en Noor - ik heb zoveel mazzel met jullie als vriendinnen. Ondanks dat ik 800 kilometer verderop woon, hebben jullie mij altijd gesteund en zijn we niet minder hecht geworden. Dankjewel dat jullie er altijd voor mij zijn.
Mad, ik had dit niet gekund zonder jou als mijn bestie. Het is zo lief dat je zo vaak naar München bent gekomen. Onze weekendjes samen vol kletsen, lekker eten en films kijken, zorgden ervoor dat ik iedereen in Nederland wat minder miste en gaven mij weer een boost om verder te gaan met mijn PhD.

Aan mijn familie: dankjewel dat jullie altijd zo geïnteresseerd zijn in mijn werk en mijn leven in München. Ondanks dat ik jullie weinig heb kunnen zien vanwege de pandemie, voelt het alsof jullie altijd dichtbij mij zijn.
Opa en oma, jullie hebben mij geleerd dat je hard werkt voor waar je van houdt en dat heb ik goed kunnen gebruiken tijdens mijn PhD, dankjewel daarvoor. Opie en omie, jullie hebben mijn leven gevuld met liefde en zorg, ik zal dat nooit vergeten.

Lieve papa, mama, Celine & Rick, het is de afgelopen jaren lastig geweest om zo ver weg te wonen van jullie en ik had het nooit gekund zonder jullie niet-aflatende liefde en steun. Dankjewel voor alles dat jullie voor me gedaan hebben, inclusief het sturen van kaarten en bloemen om te laten weten dat jullie aan me denken, de Google Meets en natuurlijk de vele bezoekjes. Ik heb het aan jullie te danken dat ik deze geweldige ervaring heb opgedaan en dat betekent de wereld voor me.

Nicola, you have been my rock, especially these last few months. Thank you for taking care of me, for motivating me throughout my PhD, for supporting me during my writing and for cheering me up whenever I needed it. I could not have done this without you! You made Munich my home and I will be forever grateful.